CRANFIELD UNIVERSITY

S. RAVINDRAN

Prediction of material damage in orthotropic metals for virtual structural testing

SCHOOL OF ENGINEERING

PhD THESIS

Academic year: 2009-2010

Supervisor: Dr. J. Campbell

December 2010

CRANFIELD UNIVERSITY

SCHOOL OF ENGINEERING

PhD THESIS

Academic Year 2009-2010

S. RAVINDRAN

Prediction of material damage in orthotropic metals for virtual structural testing

Supervisor: Dr. J Campbell

December 2010

This thesis is submitted in fulfilment of the requirement
for the degree of PhD

Dedicated to my teachers

ABSTRACT

Models based on the Continuum Damage Mechanics principle are increasingly used for predicting the initiation and growth of damage in materials. The growing reliance on 3-D finite element (FE) virtual structural testing demands implementation and validation of robust material models that can predict the material behaviour accurately. The use of these models within numerical analyses requires suitable material data. EU aerospace companies along with Cranfield University and other similar research institutions have created the MUSCA (non-linear MUltiSCale Analysis of large aero structures) project to develop virtual structural testing prediction. The MUSCA project focuses on static failure testing of large aircraft components. It aims to reduce laboratory tests using advanced numerical analysis to predict failure in order to save overall cost and development time. This thesis aims to improve the current capability of finite element codes in predicting orthotropic material behaviour, primarily damage. The Chow and Wang damage model has been implemented within ABAQUS as a VUMAT subroutine. This thesis presents the development of a numerical damage prediction model and an experimental study to develop a damage material characterisation process that can easily be performed using standard tensile test specimen and equipment already available in the aerospace industry. The proposed method makes use of Digital Image Correlation (DIC), a non-contact optical strain field measurement technique.

Experiments were conducted at Cranfield University material testing facility on aerospace aluminium alloy material AA-2024-T3 and AA-7010-T7651. After thorough literature survey a complete new method was formulated to implement Chow and Wang damage model in Abaqus Explicit numerical code. The damage model was successfully implemented for isotropic and orthotropic behaviour using single element model, multi-element coupon test model and a simple airframe structure. The simulation results were then verified with the similar experimental results by repeating the experimental procedure using simulation for each material type and found matching results. The model is then compared with experimentally determined orthotropic material parameter for AA2024 and AA7010 for validation and found agreeable results for practical use. The material characterisation of damage parameters from standard tensile specimen using DIC technique was also demonstrated and the procedures were established. In this research the combination of

experimental work and numerical analysis with clear and simpler calibration strategy for damage model is demonstrated. This is the important contribution of this research work and the streamlined procedures are vital for the industry to utilise the new damage prediction tools. The damage model implementation and test procedures developed through this research provide information and processes involved in fundamentally predicting the ductile damage in metals and metal alloys. The numerical damage model developed using the well-defined verification and validation procedures explained in this research work with new streamlined damage material characterisation using recent contact less DIC technique has wider implication in the material model development for ductile metals in general. The thesis ultimately delivered a fully verified, validated robust damage model numerical simulation code with a new DIC damage characterisation procedure for practical application. The model is now used by the aerospace industry for predicting damage of large aircraft structures.

Acknowledgements

I am indebted to my supervisor, Dr. James Campbell, for the guidance, help and support he gave me throughout this research work. Thanks James.

Thanks to Prof. Rade Vignjevic and Cranfield University for the opportunity and financial support during this work.

Thanks to Dr. Kevin Hughes for proof reading and correcting my thesis. Thanks to Mr. Barry Walker for the help in experimental tests.

Thanks to all the staff in School of Engineering and Cranfield University for their kind help.

Finally, thanks to my family who have supported me during my PhD.

Table of Contents

Table of Figures

List of Tables

Nomenclature

σ - Cauchy stress

S – deviatoric stress tensor

$\bar{\sigma}$ - virgin material stress

σ_{yield} - yield stress

ε - Strain

ε^{el} - elastic strain, $\dot{\varepsilon}^{el}$ - elastic strain increment

ε^{pl} - plastic strain, $\dot{\varepsilon}^{pl}$ - plastic strain increment

R - radius R

A - fourth order tensor

F, G, H. L, M, N – Hill's orhtoropic co-efficients

$R_{L,}$ *P,* Q_{xy}, Q_{yz}, Q_{zx} *– Lankford's co-efficient*

Q - plastic potential

$\bar{\varepsilon}^{pl}$ - Effective plastic strain

W_p - Plastic work

ε_p Plastic strain

p - Accumulated plastic strain

D – Damage variable

β - Overall damage

R_0 – strain hardening threshold initiation

R – increment of strain hardening threshold (in thermodynamic internal variable)

Y - Damage energy release rate

B_0 – damage strengthening threshold initiation

B – increment of damage strengthening threshold (in thermodynamic internal variable)

$\varepsilon_{e_{ij}}$ – elastic portion of the total strain

$\varepsilon_{p_{ij}}$– plastic portion of the total strain

$\boldsymbol{\sigma}$ - Cauchy stress tensor

***D* –** damage tensor

H^* - directional dependency of material properties at a material point x

x - material point at time "t"

$\boldsymbol{\varepsilon_{ij} = \varepsilon_{e_{ij}} + \varepsilon_{p_{ij}}}$ - total strain

F – is the thermodynamic flux vector (in thermodynamic domain)

P – is the thermodynamic conjugate force vector (in thermodynamic domain)

Ω - flow potential

H - Hills anisotropic co-efficient matrix

$\boldsymbol{J}$ – is the damage characteristic tensor which describes the anisotropic nature of damage growth.

$\tilde{\sigma}_d$ - effective damage stress

$(B_0 + B)$ - the damage resistance force from the material

$\tilde{\sigma}_d - (B_0 + B)$ - is the thermodynamic force conjugate to damage nucleation and propagation.

$\boldsymbol{E_{ijkl}}$ - the elastic stiffness tensor

$\boldsymbol{\varepsilon^e_{kl}}$ - the elastic strain tensor

S - element surface area

$\tilde{S}$ - damaged area

$\boldsymbol{M_{ij}(D)}$ - damage effective tensor proposed by Chow and Wang

$B(\beta) = \frac{dB}{d\beta}\beta$ increment of damage threshold depending on β

$\frac{dB}{d\beta}$ - damage evolution threshold

$\tilde{\sigma}_d$ - effective damage stress

S_E - is the engineering stress

F – is the force

A_0 - is the initial cross sectional area of the specimen

e_E - is the engineering stress

ΔL – is the difference in lengths

L_0 - is the initial length between two measurable points on the specimen

L - is the new length between two measurable points on the specimen after deformation

μ - damage potential matrix constant

D_{cr} - effective critical damage constants

R_{11}, R_{22}, R_{33}, R_{44}, R_{55}, R_{66} – Abaqus orthotropic coefficients (in terms of Hill's orthotropic coefficients F, G, H, L, M and N)

E is the Young's modulus of virgin material

$\tilde{E}$ is the Young's modulus of the damaged material (which is the new slope during reloading in cyclic test)

D_1, D_2, D_3 are damage variables in the respective direction

ν_{12}, ν_{13} are Poisson's ratio

$\boldsymbol{C_e}$ - elastic stiffness tensor

$\tilde{\boldsymbol{C}}_{\boldsymbol{e}}$ - effective elastic stiffness tensor

$\tilde{\boldsymbol{\varepsilon}}_{\boldsymbol{e}}$ - effective elastic strain tensor

$\dot{\lambda}_p$ - plastic multiplier

$\dot{\lambda}_d$ - damage multiplier

$\frac{dR}{dp}$ - material hardening parameter at that instance

a - current radius of the neck (in Zhang correction procedure)

R - the radius of curvature (in Zhang correction procedure)

b_0 – original width of the specimen

l_{ms} – length of the measuring surface in the longitudinal direction

ε - true strain measured from the surface

ε_{p-Pmax} - plastic strain from at P_{max} (Plastic strain at F_{max})

The following contracted notations of stress and strain in vector form are used in this report:

$$\{\sigma\} = \{\sigma_{11} \quad \sigma_{22} \quad \sigma_{33} \quad \tau_{23} \quad \tau_{31} \quad \tau_{12}\}^T = \{\sigma_{11} \quad \sigma_{22} \quad \sigma_{33} \quad \sigma_{23} \quad \sigma_{31} \quad \sigma_{12}\}^T,$$

$$\{\varepsilon^e\} = \{\varepsilon^e_{11} \quad \varepsilon^e_{22} \quad \varepsilon^e_{33} \quad \gamma^e_{23} \quad \gamma^e_{31} \quad \gamma^e_{12}\}^T = \{\varepsilon^e_{11} \quad \varepsilon^e_{22} \quad \varepsilon^e_{33} \quad 2\varepsilon^e_{23} \quad 2\varepsilon^e_{31} \quad 2\varepsilon^e_{12}\}^T,$$

$\{\sigma\} = [\boldsymbol{C}]\{\varepsilon^e\}$ and

$\{\varepsilon^e\} = [\boldsymbol{C}]^{-1}\{\sigma\}$

1 Introduction

In the early 18th century materials were selected for a particular application based on historical data of how long and how well they performed in that specific operational environment. As the understanding of material behaviour improved, simple stress strain relationships were used in selection of material, more recently improved computer based numerical codes started to emerge for simple analysis of material. The recent advances in computer capabilities are increasingly allowing designers to include material behaviour beyond the elastic and plastic region in design. This emerging "predictive materials technology" can be used to predict complex interactions of deformation processes such as impact, damage evolution and fracture of metals and alloys. These latest computer simulations use complex material models with the capability to predict material behaviour under extreme loading conditions. Nowadays these three-dimensional (3-D) computer simulations are used for design process alongside direct experimentation.

In the future virtual testing will increasingly replace some of the laboratory testing. Virtual testing can also be used to evaluate systems which are too difficult to investigate with experimental techniques such as impact on spacecraft by space debris. These simulations not only reduce the cost they also aid the process of product development using continuous virtual material test and improving upon existing design using these results until the development of superior final product. This combination of design, virtual testing and improvement interplay makes the new 3-D simulations a powerful engineering tool. The growing reliance on 3-D virtual structural testing demands implementation and validation of robust material models that can predict the material behaviour accurately within finite element (FE) software.

Today the automotive industry uses virtual prototyping techniques for design including crash test simulation even before manufacturing actual vehicles. A goal in the aerospace industry is to use virtual testing for complete prototyping like the automotive industry. However the complex nature of aerospace structure requires high level of accurate prediction of structural behaviour in order to design the aircraft prototypes before manufacturing. One of the aims of this project is to characterise

orthotropic metals using existing aerospace laboratory test facility and use the developed virtual test for advanced structural testing similar to the automotive industry.

The new capability will allow engineers to create reliable custom designed products with known material characteristics and predictable behaviour during their life cycles. In this research a form of predictive orthotropic material damage model is numerically evolved, implemented verified and validated to simulate the actual behaviour of orthotropic metals used in aerospace. The damage model is verified during each step of implementation using the numerical software Abaqus Explicit and validated using the physical experimental results obtained as a part of this research work at Cranfield University. The research work also aims to develop a procedure for damage material characterisation and demonstrate the method in relatively new Digital Image Correlation (DIC) technique available in the aerospace industry.

The ability to predict orthotropic material failure entirely depends on how accurately the selected material model can replicate the actual material behaviour when subjected to dynamic loading conditions. One such implementation performed by Gray, Maudlin et al. (2005) describes how these new predictive models can incorporate the results of strength experiments and modern theories of crystal defect interactions and strain localisations. They used various experimental facilities in small scale to conduct impact tests, tensile test and explosively driven fracture of metal shells. These experimental results of metal behaviour from strain hardening to fracture agreed with the advanced simulation results. The results produced by Gray, Maudlin et al. (2005) research team and other similar researches by Zurek et al (2003); De Vuyst (2003); Chow and Jie (2004); Mirkovic (2004); Campbell, Vignjevic and Mirkovic (2006); Panov (2006) encourage current numerical technologies in FE to improve further into the new area of advanced research namely predictive materials technology. Gray, Maudlin et al. (2005) say that a predictive model must be able to capture the basic relationships between the independent variables of stress, strain, strain rate and temperature to specific bulk material responses such as yield stress, strain hardening, texture evolution, evolution of global damage, subsequent heterogeneous damage, such as strain localisation and cracking and finally material failure.

In this research work the virtual structural testing is considered based on the EU funded research programme the MUSCA (non-linear MUltiSCale Analysis of large aersostructures) directives. This project aims to improve or to introduce new virtual testing technologies for virtual testing of large aircraft components. It also aims to reduce the laboratory tests by introducing advanced non-linear numerical analysis to predict failure in order to reduce cost and time.

A constitutive model will be selected and the damage material parameter will be characterised based on available latest laboratory tests used in the industry. The experiments will be conducted on aerospace aluminium alloy AA2024 and AA7010 specimens at Cranfield University testing facility using digital image correlation technique. The constitutive model will use ABAQUS explicit numerical software along with FORTRAN 99 to develop the material model. The verification and subsequent validation of the code will be done by repeating the similar virtual experiments to that of physical experiments numerically and comparing with experimental test data.

The selection and implementation of the explicit numerical code to predict damage must focus on identifying and streamlining the procedure for damage material characterisation in a way that it can be used in the industry without complex processes. The work also needs to address recent contact less technique such as Digital Image Correlation (DIC) for measurements. The important criteria here are to identify, develop and demonstrate simpler procedures to measure damage parameters with orthotropic behaviour for aerospace ductile metallic structures. It is also necessary to identify less complex and inexpensive general procedure for characterisation of damage for ductile metals so that it could be used for the other ductile metals used in aerospace structures.

In this research thesis supplement to the previous review reports findings, the literature review appears in two forms. The first one concentrates on previous work which forms the basis of this research work; the methods and results obtained in this category are presented without any change. The second form concentrates on the results produced by this research work and relates the findings to similar research objectives, methods, experimental set up, numerical analysis and results. In this

category wherever it is necessary the author's research results were verified with other similar results with appropriate comments, review and discussions.

1.1 Thesis structure

The overview of predictive material behaviour analysis and the 3D simulation technology and thesis structure are described in chapter 1.

The chapter 2 gives an overview of orthotropic metals, how it forms, grain microstructure in orthogonal directions**,** rolling process and influence in material orthotropy. Example of aerospace aluminium alloy AA-2024 with orthotropic behaviour is shown. Explanation of damage initiation, growth of damage, failure mechanisms and theoretical background by researchers are explained. Figures explaining the damage process and assumptions in continuum damage mechanics were also given. Introduction of the numerical methods, mesh and mesh descriptions, various time integration methods and discretization methods, finite element software with an emphasis on Abaqus software used in this work were discussed briefly.

The chapter 3 gives the overall project summary with design certification process and outline of the MUSCA project which forms the background of this thesis and how predictive numerical simulation could improve the present certification process. The project objectives and research methodologies were also explained in this chapter.

Chapter 4 briefly explains about plasticity flow rule, hardening anisotropic yield criteria summary and equations, Hills orthotropic co-efficient summary, Lankford co-efficient equations.

Chapter 5 provides information on the constitutive equations developed by researchers, their pros and cons. It also covers a literature review of the models developed. It also gives insight into developments on general principles of anisotropic damage model, continuum damage mechanics, accuracy of predictions , Chow and Wang damage model and its applicability and strain equivalence and energy equivalence damage models and selection of constitutive model.

Chapter 6 describes detailed procedure on application of DIC method, damage characterisation, orthotropic experimental tensile test results for standard tensile test

and cyclic test, establishment of damage characterisation procedure, characterisation of damage parameters and the advantage of using DIC for damage characterisation are explained.

Chapter 7 explains about Zhang-Bridgman-Le Roy correction procedure after necking, the application and test from the experimental parameters using Abaqus standard experiments. It also describes the difficulty in applying this procedure directly to DIC and new method to calculate empirical a/R are described.

Chapter 8 explains the formulation for implementation of damage model in the numerical code. It gives details of anisotropic elastic with damage, anisotropic elastoplasticity with damage, coupling of the elastoplasticity with damage and derivation of elastoplasticity plastic and damage multiplier for Chow and Wang damage model.

Chapter 9 provides information about orthotropic material failure modelling in Abaqus explicit code in this research work. It gives an overview of implementation of user subroutines and virtual tests for isotropic material algorithm for elastic plastic update, hardening implementation for isotropic and kinematic hardening and virtual test of orthotropic elasticity to ascertain material orientation. It also gives orthotropic material implementation schematic for elastic, plastic and damage update.

Chapter 10 describes the numerical testing methods, results and validation. It provides information on simulation test coupons and results and discussion of isotropic and orthotropic virtual simulations without damage and with damage using single elements and multi elements. It also explains the validation of virtual test results on standard tensile test and cyclic tests using the experimental test results.

Chapter 11 provides the conclusion of the thesis report and the future work. The references used in this thesis are given in chapter 12. The appendix in chapter 13 gives the other material properties used in initial virtual tests and additional virtual test result from the AA2024 and AA7010 experimental data useful for the reader. The chapter 13 also provides the numerical code and example input data for the users.

2 Overview of orthotropic metals, ductile damage and numerical methods

The metals manufactured during rolling process influence the material behaviour from isotropic condition and behave anisotropic. A simplified form of anisotropy evaluated in three mutually orthogonal directions of the material is called orthotropy. Examples of aerospace aluminium alloy AA-2024 with orthotropic behaviour show difference in yield and plastic prosperities in rolling direction and transverse direction. The explanations about orthotropy, damage initiation, growth of damage and failure mechanisms theoretical information provided by other researchers are discussed briefly in this chapter. Figures explaining the damage process and assumptions in continuum damage mechanics were also discussed. An overview of the numerical methods, mesh and mesh descriptions, various time integration methods and discretization methods and Abaqus finite element software which are used in this research work are summarised.

2.1 Orthotropy

This PhD research project focuses on damage and failure prediction for orthotropic metals. Metals are made up of many crystals or grains within each crystal atoms are stacked in a regular array. These grain boundaries demarcate regions of different crystallographic orientation (Dunne and Petrinic, 2005). The grains are initially oriented at random and as a result the bulk material behaviour is isotropic. When these metals are deformed during the manufacturing process, such as rolling to produce sheet metals, plastic deformation takes place. During this deformation the randomly orientated grains become elongated towards the direction of maximum tensile strain (Hill, 1948). Due to this process metals become fibrous, as shown in Figure 2-1, and the material properties become anisotropic. This non-random distribution of grains causes material macroscopic stress and strain properties to vary with direction (Figure 2-2). Experimental studies show that failures of initially isotropic material properties in structure are often associated with the development of anisotropic material damage during the life cycle loading conditions (Chow, 1987) and manufacturing process such as rolling.

Two most common types of anisotropy in metals are planar anisotropy and normal anisotropy. The planar anisotropy describes the variation in mechanical properties in the plane of the sheet and it is characterised by the amount of earrings that occur in the cylindrical cup drawing from a circular blank sheet. In planar anisotropy the strain in rolling direction and the strain in 90^0, 45^0 to rolling direction are not equal. The normal anisotropy or through thickness anisotropy describes the variation in mechanical properties between the plane and thickness. In metals both planar and normal anisotropy influence the behaviour. An orthotropic material is defined to have different mechanical properties in the three mutual axes.

Hill (1948) proposed a simplified form of anisotropic material to create orthotropic material by considering that there are three mutually orthogonal planes of symmetry exist at every point as shown in Figure 2-1. The rolling processes may produce materials having different properties such as tensile yield stress in transverse direction and through thickness direction compared to the rolling direction and thus induces orthotropic behaviour.

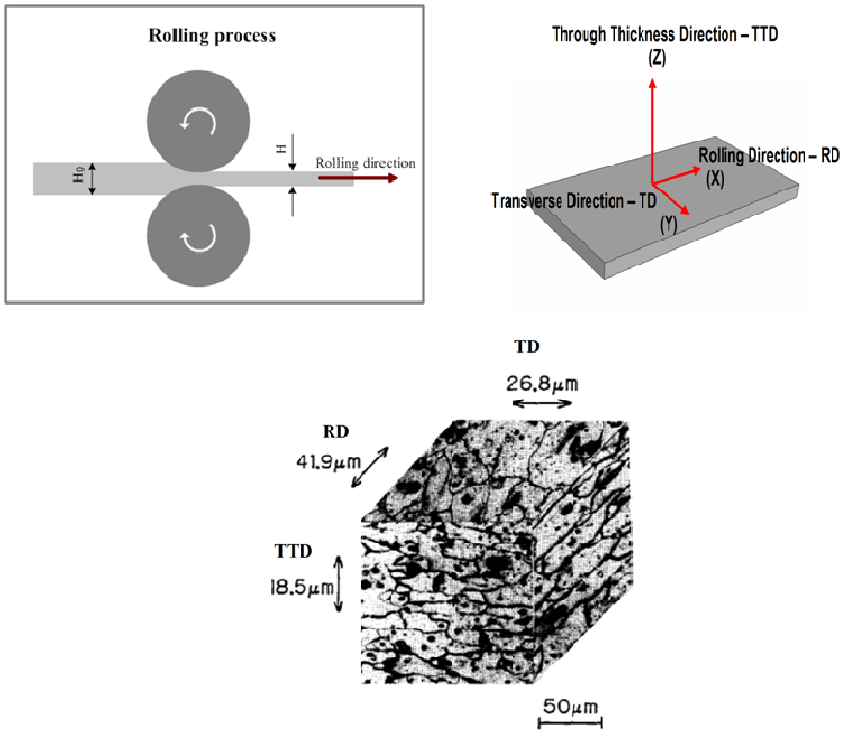

Figure 2-1 Aluminium 2024-T3 pancake shaped grain microstructure with their respective sizes in three mutually orthogonal directions after the rolling process - adapted from Akiniwa and Tanaka (1988)

Orthotropic metals, of various types, are used in the aerospace industry. Due to the wide use of these sheet metals, there is a need to investigate and include the orthotropic criterion into the current failure model. The identification and inclusion of orthotropic material behaviour for aerospace material failure mechanisms is important for better design of the structure. The orthotropic damage material characterisation and implementation within the finite element (FE) code will improve the current prediction capability to orthotropic materials as well.

In this research project material failure prediction using non-linear numerical techniques on orthotropic metals is being considered for application in virtual structural testing. The experimental tests and numerical simulations use orthotropic aerospace aluminium alloys AA-2024-T3 and AA-7010-T7651. The procedure and characterisation process determined in this thesis can be applied to other similar materials such as copper and tantalum.

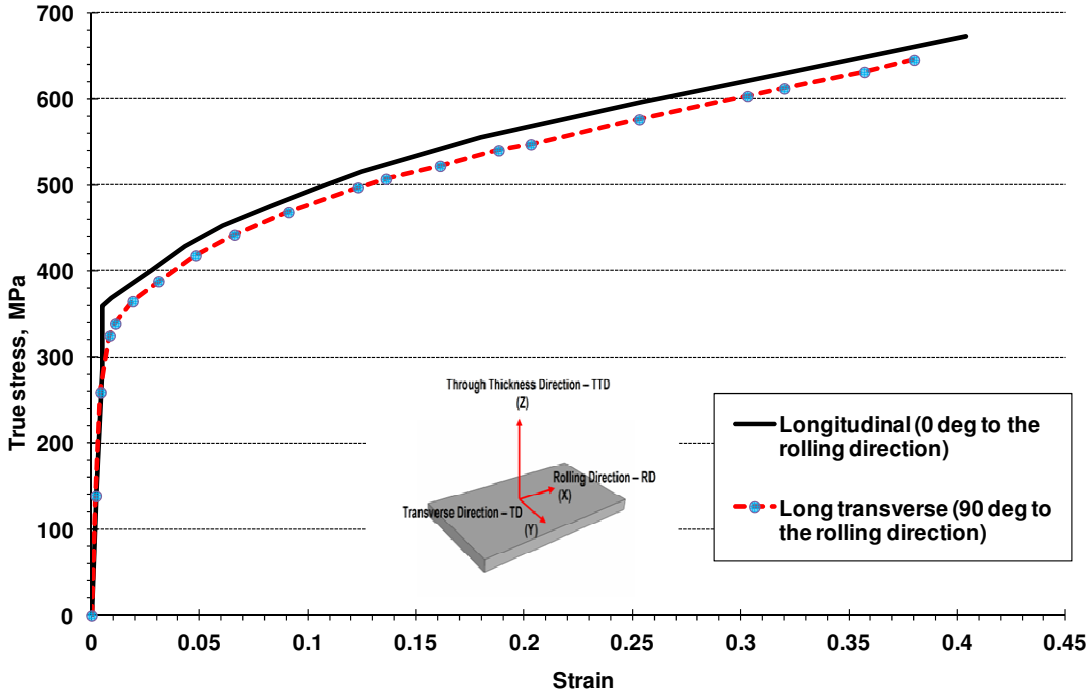

Figure 2-2 Uniaxial tensile test – specimens cut in 0^0 to rolling direction and 90^0 to rolling direction - Aluminium 2024-T3 experimental results (CU) showing orthotropy

2.2 Ductile damage growth

Damage occurs in material due to irreversible changes in microstructure of the material due to thermo-mechanical loading or unloading process. Slipping, micro-cracking and development of micro-cavity are the most common modes of

irreversible micro-structural rearrangements (Lu and Chow, 1990). These micro-structural rearrangements reflect on macroscopic level as inelastic material response which is known as plasticity. Damage mechanics principles should represent the process of initiation of damage, its growth and ultimately fracture. In material debonding between atoms imitates the damage process.

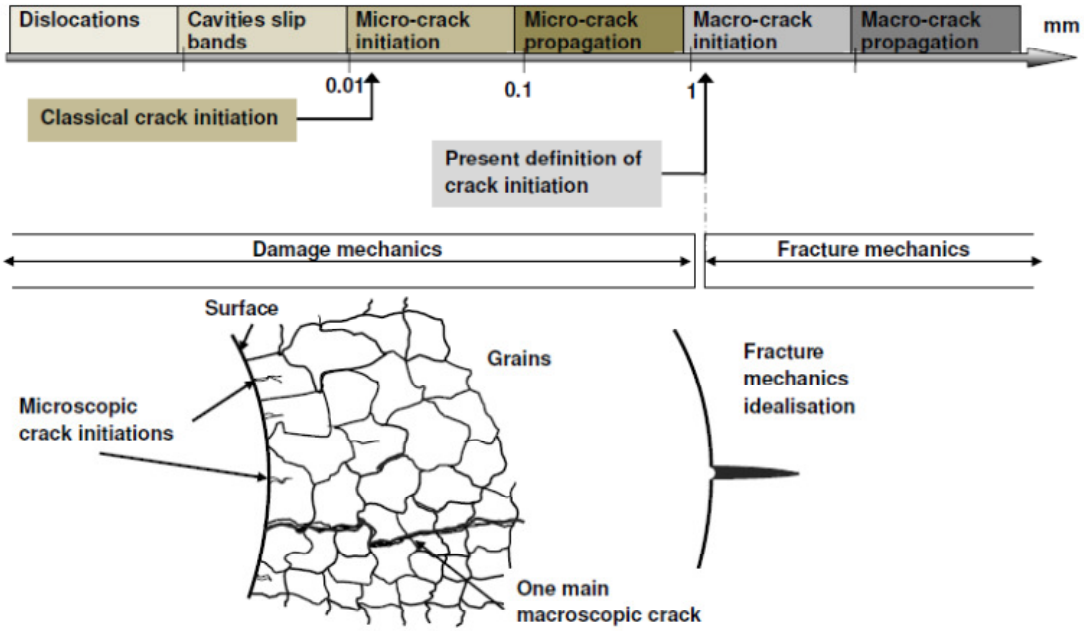

Figure 2-3 Illustration of damage process and macroscopic crack growth (adapted from Chaboche, 1986)

Metal have grain structure as shown in Figure 2-3, the grains are arranged in regular array of atoms but there are missing atoms which create lines of dislocation. In certain cases the dislocations are stopped by micro-defects. Several arrested dislocations nucleate a micro-crack. These micro cracks grow due to thermo-mechanical loading and unloading processes and combine to form a macro-crack that then grows as one main macroscopic crack. The overall process of this phenomenon is shown in Figure 2-3, which is modified from Chaboche's (1986) explanation of the process.

Ductile damage occurs due to nucleation of cavities and micro-cracks followed by the coalescence of voids, cavities, micro-cracks, other types of material defects and impurities. Generally ductile damage occurs along with the plastic deformation when damage gets initiated due to irreversible processes explained in pervious section.

However damage may also commence before or after plastic deformation begins, depending on the material properties. The damage process macroscopically reduces the load carrying capacity which is proportional to the reduction in area due to absence of material. Thus macroscopically damage could be measured from the reduction in an element's effective load carrying surface area when subject to thermo mechanical loading or unloading.

2.3 Numerical methods

2.3.1 Introduction

The complex engineering problems cannot be solved analytically; however they can be solved using numerical methods. The numerical methods solve equations based on approximate solution within acceptable error margins. The computational tool which models the behaviour of continuous media is known as hydrocode. In continuum damage mechanics the hydrocode numerically solve the differential equations of conservation laws and compatibility equations.

The finite element and finite difference computer program consist of pre-processor, solver or processor and post-processor. The pre-processor is used to generate computational mesh of the geometry along with material properties, boundary condition, loading conditions and other initial requirements for loading. The solver or processor numerically solves the conservation laws and compatibility equations using the information provided by the pre-processor. The post-processor then prepares the graphical representation of the information provided by the processor and displays as a results. Typical output data from post-processor will have stress, strain, displacement, velocity, strain rate, temperature at given time.

2.3.2 Mesh description

There are two types of mesh description available in hydrocodes. They are based on Lagrangian or Eulerian spatial discretization. In Lagrangian co-ordinate system every point in the deformed body is defined in some reference state and the discretization deforms with the material. In Lagrangian mass of element remains constant and only volume changes when material distorts. The advantages of Lagrangian method for mesh description are; it is simple, requires less computational time, history variables

are easily obtained and defining boundary conditions are much easier. The disadvantage is that the time step is controlled by smallest element, severe distortion of the smallest element could lead to divergence. In Eulerian co-ordinate system the points are fixed in space and discretization does not move with the material. The computational grid is fixed in space and the code calculates the quantities that flow into and out of each cells. The main advantage of Eulerian code is that it can be used for large deformation. The main disadvantages of Eulerian code are the boundary conditions cannot be well defined and the computational time is more compared to Lagrangian co-ordinate system (Hamouda, 1996). Lagrangian co-ordinate system is used in Abaqus explicit codes.

2.3.3 Time integration

There are two time integration methods used in numerical codes. They are called explicit scheme if the discretised equation of motion solution at some time $\boldsymbol{t + \Delta t}$ in computation is based on the knowledge of equilibrium conditions at previous time step $\boldsymbol{t}$. In the implicit method, the discretised equation of motion solution at time $\boldsymbol{t + \Delta t}$ is based at the knowledge of equilibrium condition at time the same time step $\boldsymbol{+\Delta t}$. The explicit scheme does not require calculation of stiffness and mass matrices for the complete system and previous step knowledge is sufficient to achieve the required accuracy. To implement explicit scheme the time step must be sufficiently small to get accurate results. The stability of the model depends on the time step hence it might take more time to solve the problem. It also suffers from the wave propagation problems if the time step is not chosen sufficiently small. The time steps in implicit method can be larger and unconditionally stable but at the expense of solving simultaneous equation at each time step.

2.3.4 Finite element software

One of the main objectives of this research is to develop a new material model using numerical code. The EU research project partners have identified that prediction of large scale structure with Abaqus explicit codes provide better results compared to implicit code. Hence Abaqus explicit code has been chosen to develop the numerical model. The Abaqus explicit code is based on Lagrangian code. The Abaqus FE software allows newly developed user material model to run within the existing

software code. The Abaqus CAE is used to develop the material coupons and airframe structures; the new damage model was implemented in the explicit VUMAT code using FORTRAN 99 programming language. The analysis were run in Cranfield University computational facility in Abaqus CAE solver and the results are observed using Abaqus CAE post processor.

3 Project summary

3.1 Project background

Design and certification of an aircraft today involve a number of structural tests ranging in complexity from simple coupon tests to the final full-scale aircraft structural test as illustrated in Figure 3-1. The MUSCA (non-linear MUltiSCale Analysis of large aerostructures) is an EU funded research project involves aerospace companies and research institutions (including Cranfield University funded under the 6th Framework programme).

- The aim of the project is to develop technologies to allow the virtual testing of large aircraft components.
- It aims to reduce laboratory tests using advanced numerical analysis to predict failure in order to save overall cost and development time.

The MUSCA project partners identified that the large structures simulation prediction were more accurate with explicit software in quasi-static regime.

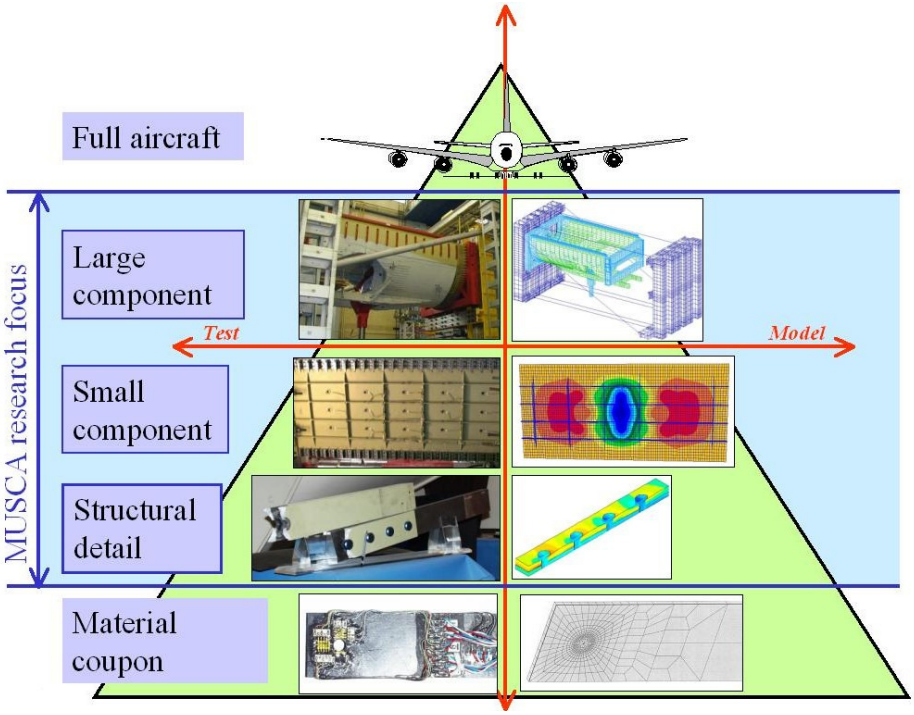

Figure 3-1 Test and analysis pyramid illustrating current engineering process for designing and certifying a new aircraft product (range of tests performed during aircraft design process adapted from MUSCA project, 2009)

Structural testing is carried out at different scales ranging from:

- **Full scale**: Complete aircraft scale
- **Large component**: Major parts of an aircraft like central wing box, fuselage section or partial wing tests
- **Small components**: Typical aircraft structural components like panels, ribs or passenger floor structure.
- **Structural detail**: Elements of a large aircraft component like wing to fuselage junctions or net-tension tests for skin and stringer assemblies.
- **Coupon**: Basic design verification tests like bolt and rivet joints or material coupon testing. Also for derivation of material properties.

At the top of the pyramid, **large components tests constitute more than 80 % of the overall cost of the aircraft certification process** (full aircraft test not included). Manufacturing and testing of large component structures is a time consuming and expensive process. If virtual testing similar to automotive industry are established in aerospace industry, it will significantly reduce the time and cost of designing and delivering new aircraft products.

3.2 Context of work

At the time of this research project MUSCA partners have identified explicit numerical model can predict material failure of large aircraft structure more accurately under quasi-static regime. Abaqus explicit offers a general capability to model progressive damage and failure of structures. It uses stiffness degradation using damage mechanics to predict the degradation of material. It assumes failure as complete loss of load carrying capacity of the structure. The progressive damage and failure can be used for ductile fracture of metals and necking instability in forming of sheet metals. The ductile fracture of metals uses void nucleation, coalescence and growth of voids and shear band localisation for damage modelling. The progressive damage model can be used in elastic, plastic with hardening by introducing damage evolution. In elastic, plastic material damage evolution the damage is depicted in two forms once is degradation of elasticity in elastic part and softening of yield stress in

plastic part. The damage evolution uses fracture energy per unit area or equivalent plastic displacement in this case. The damage evolution is updated based on the information of damage initiation point, damage evolution phase and removal of element when failure occurs. The progressive damage can be used in conjunction with Mises, Johnson-Cook, and Drucker-Prager plasticity models. Liu and Zheng (2010) in their recent paper observe that the major limitations of the Abaqus explicit progressive damage model are characterisation of damage parameters, unrealistic growth of damage during its evolution and complexity, time and test procedure required to determine the damage parameters. It also requires increased computational time for complex large aerospace structures.

Apart from the selection and implementation of the explicit numerical code to predict damage the work needs to focus on identifying and streamlining the procedure for damage material characterisation in a way that it can be used in the industry without complex processes. The work also needs to address recent contact less technique such as Digital Image Correlation (DIC) for measurements. The important criteria here are to identify, develop and demonstrate simpler procedures to measure damage parameters with orthotropic behaviour for aerospace ductile metallic structures. It is also necessary to identify less complex and inexpensive general procedure for characterisation of damage for ductile metals so that it could be used on the wider spectrum of ductile materials used in aerospace structures.

In this project the experimental set up for damage characterisation tests using DIC instruments need to be developed along with the procedure to verify and validate the numerical damage model through similar test procedure. Upon completion of coupon tests the numerical code should be test on simple aircraft structure to check the robustness.

3.3 Project objectives

The MUSCA project requires development of various technical capabilities for aircraft structure designing and engineering process. One of the requirements of MUSCA project is to develop virtual test models for aircraft structures. Based on the MUSCA project plan this research work focuses on developing virtual test models for predicting orthotropic metal behaviour within aircraft structures. The overall aim of

the research work is to improve the current capability of finite element codes in predicting orthotropic metallic material behaviour, including damage. The analysis of orthotropic behaviour in this research will use existing experimentally validated Chow and Wang (1987) damage model that can accurately predict initial elastic loading condition, plastic deformation, initiation of growth of damage and ultimately failure. The damage model will use elastoplasticity with damage into the user code to facilitate the orthotropic behaviour.

It is clear that the constitutive model that can predict accurate orthotropic behaviour should be selected to perform testing, in this kind of material. The constitutive model which controls the material behaviour will be characterised and improved through the typically available practical laboratory tests performed in the aerospace industry. The experiments will be conducted on aluminium material specimen AA2024 and AA7010 series to obtain damage variables at Cranfield University facility using digital image correlation technique. Constitutive model will be tested with ABAQUS explicit numerical software. Improvement, verification and validation of numerical test results will be performed using comparison of physical experimental results.

The project aims/objectives are as follows:

- Selection of suitable orthotropic constitutive model from literature.

- Implementation of it in non-linear explicit solver Abaqus, for prediction of elastic behaviour, plastic behaviour, initiation and growth of damage and failure of orthotropic metals.

- It also aims to improve the virtual techniques of orthotropic material failure prediction in metals where it is found inadequate with current practice.

- To conduct experimental tests on Aluminium alloys AA-2024-T3 and AA-7010-T7651 coupons to identify material parameters required for selected damage model for virtual testing.

- To develop a method to determine the damage parameters from the material.

- To conduct isotropic and orthotropic tests cases using the damage model developed in this research.
- Development and demonstration of damage material characterisation procedure using relatively new non-contact Digital Image Correlation (DIC) technique available in the aerospace industry.

- The DIC method will also be used to demonstrate the damage material characterisation using standard dog bone specimen.

- To be able to demonstrate considerable level of accuracy in predicting orthotropic material failure in large structural components under similar loading circumstances.

- To check the robustness of code when used in combination of Abaqus inbuilt and user VUMAT damage material model developed in this research.

3.4 Research methodologies

The research methodology is summarised in Figure 3-2. The mathematical model is first assessed and an implementation process will be developed, and then the model is verified for whether the numerical model effectively captures all aspects of the mathematical model. After this verification the numerical model is written in Fortran user code in as a user material model (VUMAT) for the Abaqus Explicit finite element package. During this process the code is checked from various aspects in such a way that it works along with the existing capability of Abaqus Explicit software without committing any errors. The results from this virtual simulation tests are then compared with a set of experimental test data performed during the first half of 2008 for validation. The feed back after this process is then updated into the mathematical model for further improvements to capture the true representation of physical behaviour of material when subject to virtual testing. This process cycle is repeated until each stage of implementation provides predictable accurate results as per our preset design requirements.

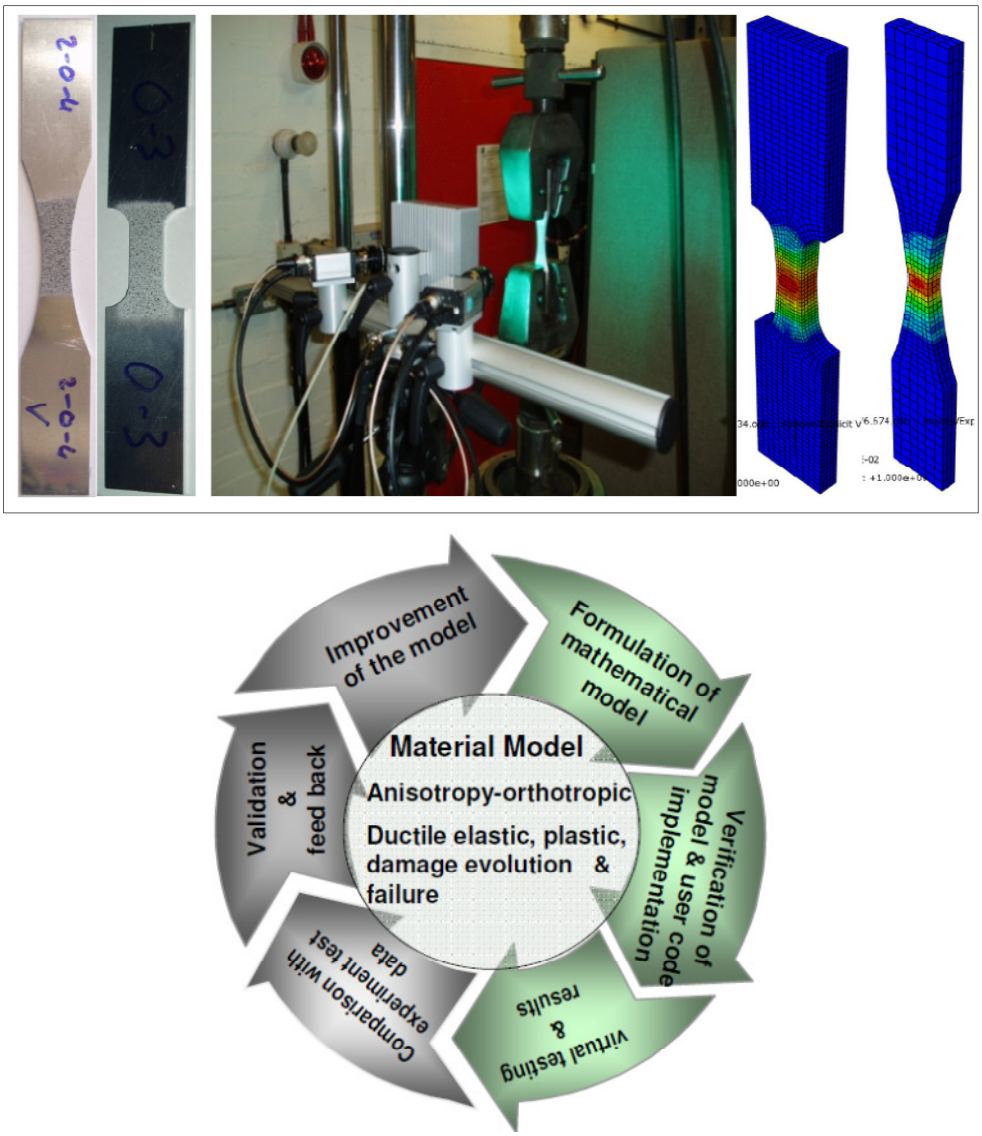

Figure 3-2 Research methodology – shows the experimental set-up and virtual test specimens similar to experimental test specimens. The circular diagram shows the evolution of damage model numerical implementation from formulation of mathematical model to improvement of the model

The implementation of material model in numerical code to represent real physical behaviour is done with several iterative steps. The overall iterative steps that have been followed in this method are used for characterisation of material model and implementation to achieve practical industrial level application. While implementing these iterative steps the cyclic process shown in Figure 3-2 is followed to achieve the best possible material model. The model is then used for practical application.

- First iterative step in developing this model is to implement the model for a simple isotropic case with elastic and plastic characteristics and compare it with the Abaqus Explicit inbuilt model.
- Second iterative step is to implement the model with orthotropic elastic case.
- Third iterative step is to implement the model with orthotropic elastic plastic case and check with Abaqus Explicit inbuilt model.
- Fourth iterative step is to implement the damage in isotropic case; from here on the behaviour of the model was checked using our physical experimental test results and Chow's experimental results.
- Fifth iterative step is to implement the damage for an orthotropic case and check the behaviour and results of the model using experimental test results.
- Finally the results obtained in the simulation tests are used to calculate the damage parameters similar to experimental test. The simulation damage parameters and material data were verified and validated with experimental results.
- The DIC non-contact strain field measurement technique will be used to do the experimental damage characterisation of the material. The procedure will be checked and developed for practical application for damage material characterisation. The use of DIC technique in standard tensile specimen coupon will also be thoroughly investigated for practical application.

4 Isotropic and anisotropic metal plasticity

To develop advanced material model with anisotropy first the basic elastic plastic material model for an isotropic material should be developed and then it should be extended to anisotropic material and later on the damage model should be incorporated. The consistence condition for yield, hardening and flow rule required for defining plasticity are briefly described in this chapter. The isotropic material plasticity and anisotropic plasticity using Hill's co-efficient are also summarised in this chapter; for detailed description the following books and papers could be referred Malvern (1969); Dunne and Petrinic (2005); Mendelson (1968); Abaqus version 6.7 documentation (2007) and Armen (1979). The hardening process explained in this chapter is used in development of numerical model. The kinematic and isotropic hardening behaviour were developed in Abaqus explicit VUMAT code and the results are shown in chapter 9. For the damage model implementation in this research isotropic hardening parameter has been selected.

4.1 Plasticity consistency condition

Metals are subject to various loading condition. When loaded the metal initially behaves elastically and the deformation of metals beyond elasticity leads to plastic deformation. To define the plastic deformation the point at which yield occurs should be defined. The plasticity is defined by consistency condition, hardening and evolution of plastic strain. In general the yield can be defined in the following form.

$F(\sigma_{ij}, \alpha) < 0$ Yielding has not occurred

$F(\sigma_{ij}, \alpha) = 0$ Yielding has occurred (Eq. 4.1)

The yield function "*F*" dependents on the stress tensor σ_{ij},initial yield stress σ_Y and α is the effective plastic strain. The consistence condition can be expressed based on yielding of material.

$$dF(\sigma_{ij}, \alpha) = 0 \quad \text{(Eq. 4.2)}$$

4.2 Hardening

During the plastic deformation process the shape of the material changes and shows increased amount of strength properties; hence called as work hardening. Work hardening occurs when material deform during cold work, it is also referred as strain

hardening. Yield surface is referred to maximum flow stress the material can withstand. Experimental studies show under uniform tension when the material is loaded in tension and then load is removed and reloaded for compression the yield point obtained in compression is less than the yield point obtained in tension. Based on material hardening two mathematical theories were formed one is isotropic hardening where the shape and position remain same (Figure 4-1) and second one kinematic hardening shifting of stress space (Figure 4-2) is done to correct for Baushinger effect. The hardening rule is used to describe how the yield surface changes during the plastic deformation.

Strain hardening and work hardening are classified based on following calculation methods;

Effective plastic strain - $\bar{\varepsilon}^{pl}$ (if this term is used to calculate the yield surface then it is called **strain hardening**)

Plastic work - W_p (if we use this term to calculate the yield surface then it is called **work hardening**)

The numerical equation form explained in this section can be used for computer codes.

4.2.1 Isotropic hardening

The evolution of the radius $\dot{R}$ of the yield surface is assumed to be proportional to the measure for the plastic deformation.

$$\dot{R} = K_i \dot{\bar{\varepsilon}}^{pl} \qquad \text{(Eq. 4.3)}$$

The constant $K_i = \sqrt{\frac{2}{3}} H'$ (Eq. 4.4)

H' is the hardening modulus

The value of constant describing the isotropic hardening behaviour will be determined next; in case of isotropic hardening the virgin material stress is

$$\bar{\sigma} = \sqrt{\frac{3}{2}(\boldsymbol{A} : \boldsymbol{\sigma}) : \boldsymbol{\sigma}} \qquad \text{(Eq. 4.5)}$$

substitute equation (4.5) in the following equation $f(\boldsymbol{\sigma}_{ij}) = \sqrt{(\boldsymbol{A} : \boldsymbol{\sigma}) : \boldsymbol{\sigma}} - R = \mathbf{0}$

$\boldsymbol{A}$ is a forth order tensor

$\boldsymbol{\sigma}_{ij} = \boldsymbol{\sigma}$ stress tensor

R is the radius of yield surface

The value for R by rewriting the equation and substituting the terms equal to the virgin material stress

$$\left(\sqrt{\frac{2}{3}}\sqrt{\frac{3}{2}}\right)\left(\sqrt{(\boldsymbol{A}:\boldsymbol{\sigma}):\boldsymbol{\sigma}}\right)-R=\mathbf{0}\ \Rightarrow\left(\sqrt{\frac{2}{3}}\right)\bar{\sigma}-R=0\ \Rightarrow\left(\sqrt{\frac{2}{3}}\right)\bar{\sigma}=R \qquad \text{(Eq. 4.6)}$$

Radius in the rate form

$$\dot{R}=\sqrt{\frac{2}{3}}\dot{\bar{\sigma}} \qquad \text{(Eq. 4.7)}$$

The stress $\boldsymbol{\sigma_{ij}}$ is related to the plastic strain $\boldsymbol{\varepsilon_{ij}^{pl}}$ by the hardening modulus H'; when expressed in rate form

$$\dot{\boldsymbol{\sigma}}_{\boldsymbol{ij}}=H'\dot{\boldsymbol{\varepsilon}}_{\boldsymbol{ij}}^{\boldsymbol{pl}} \qquad \text{(Eq. 4.8)}$$

The equation (4.8) could be used for equivalent stress $\dot{\bar{\sigma}}$ and the equivalent plastic $\dot{\bar{\varepsilon}}^{pl}$ strain provided f is homogeneous.

$$\dot{\bar{\sigma}}=H'\dot{\bar{\varepsilon}}^{pl} \qquad \text{(Eq. 4.9)}$$

Substitute the equation 4.9 in 4.7 and finding out radius in rate form

$$\dot{R}=\sqrt{\frac{2}{3}}H'\dot{\bar{\varepsilon}}^{pl} \qquad \text{(Eq. 4.10)}$$

The constant $K_i=\sqrt{\frac{2}{3}}H'$ (Eq. 4.11)

For isotropic hardening the equivalent plastic strain rate could be calculated from

$$\frac{\partial \boldsymbol{f}}{\partial \boldsymbol{\sigma}}=\sqrt{\frac{3}{2}}\frac{\boldsymbol{A\sigma}}{\bar{\sigma}} \qquad \text{(Eq. 4.12)}$$

and the plastic multiplier $\dot{\lambda}$ can be calculated from the equation 4.13

$$\dot{\lambda}=\frac{\frac{\partial \boldsymbol{f}}{\partial \boldsymbol{\sigma}}:(\boldsymbol{C}:\boldsymbol{d\varepsilon})}{\frac{\partial \boldsymbol{f}}{\partial \boldsymbol{\sigma}}:\left(\boldsymbol{C}:\frac{\partial \boldsymbol{f}}{\partial \boldsymbol{\sigma}}\right)+\sqrt{\frac{2}{3}}K_i} \qquad \text{(Eq. 4.13)}$$

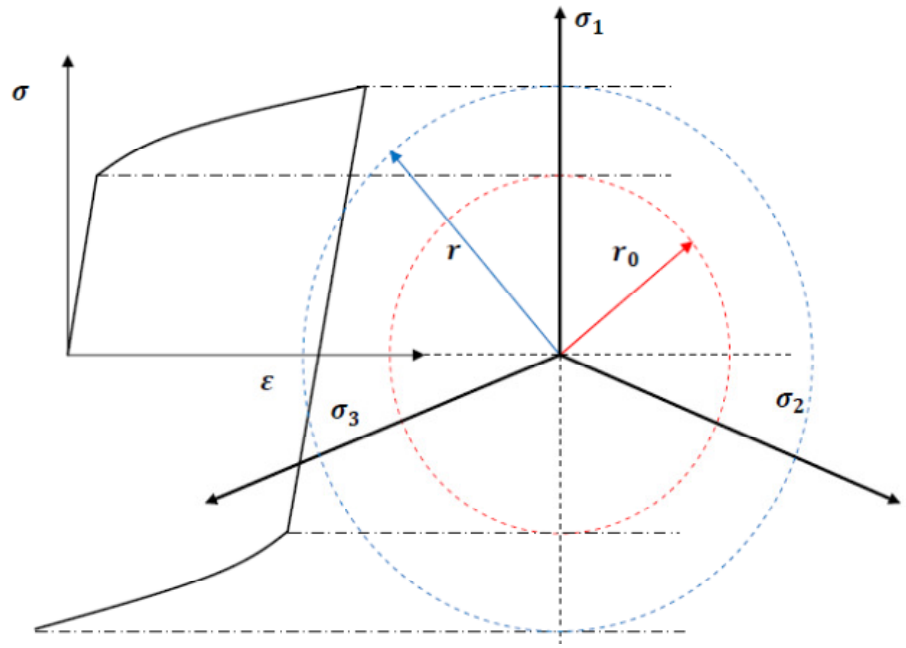

Figure 4-1 Illustration of approximate linear isotropic hardening (σ_1, σ_2 and σ_3 are the principle stresses; r_0 – is the radius of initial yield surface, r is the radius subsequent yield surface)

4.2.2 Kinematic Hardening

Kinematic hardening consists of shifting the initial yield surface in the stress space. Prager assumed that the translation of the yield surface is in the direction of the plastic strain-rate tensor (Prager, 1972).

$$\dot{\alpha} = K_k \dot{\varepsilon}^{pl} \qquad \text{(Eq. 4.14)}$$

In 1-D the movement of the yield surface = $\overline{\sigma} \sim \sigma_0$ (current virgin material stress ~ initial yield stress). The plastic strain-rate tensor is defined by;

$$\dot{\varepsilon}^{pl} = \dot{\lambda}\frac{\partial f}{\partial \sigma} \qquad \text{(Eq. 4.15)}$$

and equivalent plastic strain rate $\dot{\bar{\varepsilon}}^{pl} = \sqrt{\frac{2}{3}}\dot{\lambda}$ or $\dot{\lambda} = \sqrt{\frac{3}{2}}\dot{\bar{\varepsilon}}^{pl}$ (Eq. 4.16)

Therefore the rate of change of α can be written as $\dot{\alpha} = K_k \dot{\lambda}\frac{\partial f}{\partial \sigma}$ (Eq. 4.17)

And the kinematic hardening constant K_k can be written as

$$K_k = \sqrt{\frac{2}{3}} \frac{\mathbf{1}}{\sqrt{\left(\boldsymbol{A} : \frac{\partial f}{\partial \sigma}\right) : \frac{\partial f}{\partial \sigma}}} H' \qquad \text{(Eq. 4.18)}$$

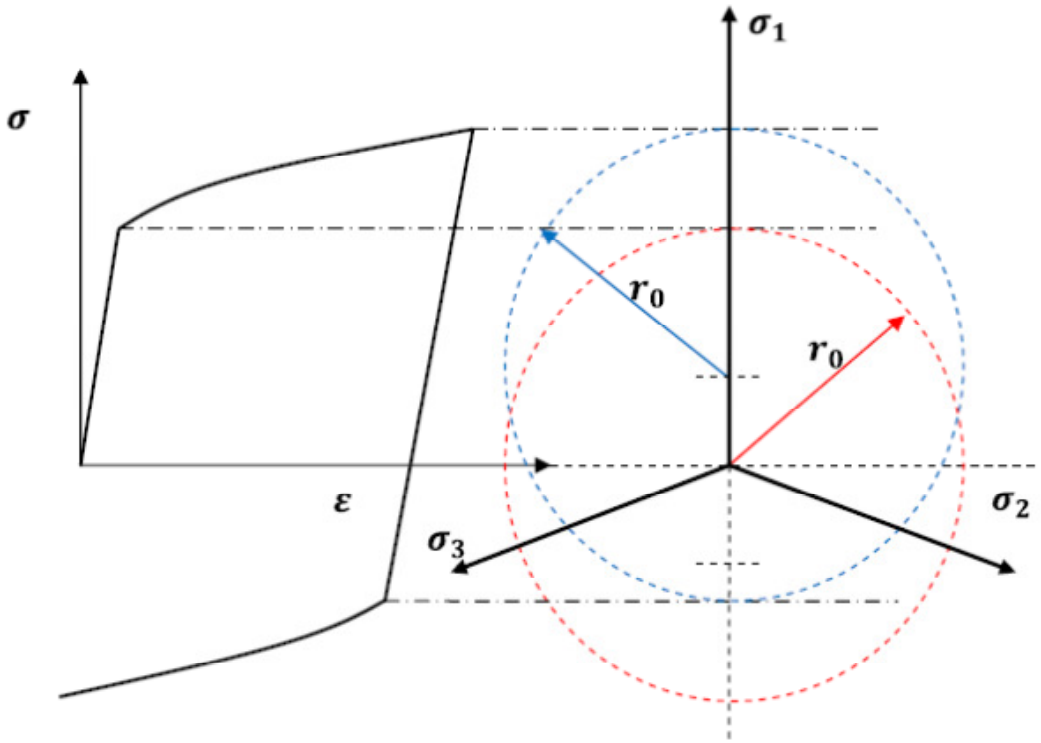

Figure 4-2 Illustration of approximate linear kinematic hardening (σ_1, σ_2 and σ_3 are the principle stresses; r_0 is the radius of yield surface)

Combining the isotropic and kinematic hardening to obtain general equation for $\dot{\lambda}$ by introducing m = 1 for isotropic hardening m = 0 for kinematic hardening.

$$\dot{\boldsymbol{\lambda}} = \frac{\frac{\partial \boldsymbol{f}}{\partial \boldsymbol{\sigma}} : (\boldsymbol{C} : d\boldsymbol{\varepsilon})}{\frac{\partial \boldsymbol{f}}{\partial \boldsymbol{\sigma}} : \left(\boldsymbol{C} : \frac{\partial \boldsymbol{f}}{\partial \boldsymbol{\sigma}}\right) + (1-m) K_k \frac{\partial \boldsymbol{f}}{\partial \boldsymbol{\sigma}} : \frac{\partial \boldsymbol{f}}{\partial \boldsymbol{\sigma}} + \sqrt{\frac{2}{3}} m K_i} \qquad \text{(Eq. 4.19)}$$

Calculation of elastic plastic matrices C_{ep}

$$C_{ep} = \boldsymbol{C} - \boldsymbol{C} : \frac{\partial \boldsymbol{f}}{\partial \boldsymbol{\sigma}} \frac{\frac{\partial \boldsymbol{f}}{\partial \boldsymbol{\sigma}} : \boldsymbol{C}}{\frac{\partial \boldsymbol{f}}{\partial \boldsymbol{\sigma}} : \left(\boldsymbol{C} : \frac{\partial \boldsymbol{f}}{\partial \boldsymbol{\sigma}}\right) + (1-m) K_k \frac{\partial \boldsymbol{f}}{\partial \boldsymbol{\sigma}} : \frac{\partial \boldsymbol{f}}{\partial \boldsymbol{\sigma}} + \sqrt{\frac{2}{3}} \beta K_i} \qquad \text{(Eq. 4.20)}$$

The equations described in this section are used for initially developing isotropic hardening and kinematic hardening behaviour in the material model.The user defined Abaqus VUMAT material model for isotropic hardening and kinematic hardening were derived and the numerical simulation results are shown in Figure 9-2 in the later Chapter 9.

4.3 Plasticity flow rule

The material behaviour in plastic region is defined by the plastic strain. Depending on the assumption made in plastic strain rate flow theory is classified into associative and non-associative. The non-associative plastic flow theory is applied in work softening material such as soil. The associative plastic theory is used for the research work.

The total strain can be decomposed the strain into elastic and plastic parts in the current assumption;

$$\varepsilon = \varepsilon_{el} + \varepsilon_{pl} \qquad \text{(Eq. 4.21)}$$

Once the material is loaded beyond plastic limit the material will yield and plastic strain will increase. The flow rule relates the change of plastic strain tensor to the change of stress state. If "Q is assumed to be the plastic potential which is a function of the stress tensor and hardening variable, then the evolution of the plastic strain is assumed to be proportional to the gradient of the plastic potential Q"

$$\dot{\varepsilon}_{pl} = \dot{\lambda}\frac{\partial Q}{\partial \sigma} \qquad \text{(Eq. 4.22)}$$

In general case the plastic strain rate increment tensor is independent of the plastic potential which is known as non-associative plasticity. The Prandtl Reuss equation assumes that the increment in the plastic strain tensor is in direction normal to plastic potential Q for associative flow rule.

The general case where $f \neq Q$ is known as non associative plasticity. (Eq. 4.23)

A special case where the yield function is equal to the plastic potential that is known as associative plasticity where

$$f = Q \qquad \text{(Eq. 4.24)}$$

A variation on this is the Mises-Levy flow rule which relates the total strain, rather than the plastic strain, to the gradient of plastic potential.

$$\dot{\varepsilon} = \dot{\lambda}\frac{\partial Q}{\partial \sigma} \qquad \text{(Eq. 4.25)}$$

$d\varepsilon_{ij}$ = (scalar factor $d\lambda$) x (deviatoric stress σ'_{ij})

$$d\varepsilon_{ij} = d\lambda \sigma'_{ij} \quad \text{(Eq. 4.26)}$$

The equation (4.26) is extended to allow for the elastic strain which would take the form

Total strain increment $d\varepsilon_{ij}$ = elastic strain increment $d\varepsilon_{el_{ij}}$ + plastic strain increment $d\varepsilon_{pl_{ij}}$

$$d\varepsilon_{ij} = d\varepsilon_{el_{ij}} + d\varepsilon_{pl_{ij}} \quad \text{(Eq. 4.27)}$$

with the plastic strain increment

$$d\varepsilon_{pl_{ij}} = d\lambda \sigma'_{ij} \quad \text{(Eq. 4.28)}$$

Assumption made for the Prandtl Reuss equation is that principal axes of plastic strain increment and deviatoric stress are coincident.

4.4 Isotropic metal plasticity

The continuum mechanics for elastic, plastic behaviour of material makes following general assumption on evaluation of isotropic material.

- Material is homogenous (it has same properties throughout the material)
- Material is isotropic (its properties are independent of direction)
- When subjected to moderate strain rate and temperature the material behaves like inviscid material; the sum of plastic strains is zero ($\varepsilon_{pl_x} + \varepsilon_{pl_y} + \varepsilon_{pl_z} = 0$).
- When subjected to moderate pressure the volume remains same

The above assumption leads to a conclusion that the deformation depends only on deviatoric part of the stress tensor σ'_{ij} . where δ_{ij} is Kronecker delta.

$\sigma'_{ij} = \sigma_{ij} - \delta_{ij}\sigma_{mean}$; for shell element σ_{mean} = $S_{mean} = \frac{1}{3}(\sigma_x + \sigma_y + \sigma_z)$ and

The principal deviatoric stress components are obtained from the equation based on Dieter (1988).

$$\sigma'^3 - J_1\sigma'^2_2 - J_2\sigma'_1 - J_3 = 0 \quad \text{(Eq. 4.29)}$$

σ'- stress deviator,

σ'_1, σ'_2, -σ'_3 stress deviator in principal stress direction 1, 2 and 3 respectively

J_1, J_2, J_3 are the first, second and third invariants of stress deviator

The von Mises flow theory is related to the second invariant of the equation (4.29) and thus referred as J_2 theories. To reduce the multi axial complexity the concept of equivalent or effective values are proposed by von Mises to assess plastic flow. The equivalent stress is given as

$$\bar{\sigma}_{VM} = \sqrt{\frac{3}{2}\boldsymbol{\sigma}'_{ij}\boldsymbol{\sigma}'_{ij}} = \frac{1}{\sqrt{2}}\left[(\sigma'_x - \sigma'_y)^2 + (\sigma'_y - \sigma'_z)^2 + (\sigma'_z - \sigma'_x)^2 + 6(\tau^2_{xy} + \tau^2_{yz} + \tau^2_{zx})^2\right]^{\frac{1}{2}}$$

(Eq. 4.30)

σ_x , σ_y , σ_z are the principal stress in xx, yy and zz directions respectively and τ_{xy}, τ_{yz}, τ_{zx} are the shear stresses in xy, yz and zx directions respectively.

which implies $3J_2 = \bar{\sigma}^2_{VM}$

The equivalent plastic strain is given as

$$\dot{\bar{\varepsilon}}_{pl} = \sqrt{\frac{2}{3}\dot{\boldsymbol{\varepsilon}}_{\boldsymbol{pl}_{ij}}\dot{\boldsymbol{\varepsilon}}_{\boldsymbol{pl}_{ij}}} \qquad \text{(Eq. 4.31)}$$

$$\dot{\bar{\varepsilon}}_{pl} = \frac{\sqrt{2}}{3}\left[(\dot{\varepsilon}_{pl_x} - \dot{\varepsilon}_{pl_y})^2 + (\dot{\varepsilon}_{pl_y} - \dot{\varepsilon}_{pl_z})^2 + (\dot{\varepsilon}_{pl_z} - \dot{\varepsilon}_{pl_x})^2 + 6[(\dot{\varepsilon}_{pl_{xy}})^2 + (\dot{\varepsilon}_{pl_{yz}})^2 + (\dot{\varepsilon}_{pl_{xz}})^2]\right]^{\frac{1}{2}}$$

(Eq. 4.32)

$\dot{\varepsilon}_{pl_x}$, $\dot{\varepsilon}_{pl_x}$, $\dot{\varepsilon}_{pl_x}$ - plastic strain increment in xx, yy and zz directions respectively

$\dot{\varepsilon}_{pl_{xy}}$, $\dot{\varepsilon}_{pl_{yz}}$, $\dot{\varepsilon}_{pl_{zx}}$ - plastic strain increment in xy, yz and zx directions respectively

The equivalent plastic strain and equivalent stress terms are used in defining behaviour of materials in the numerical VUMAT code.

4.5 Hill anisotropy plasticity

Hill from his observation proposed a quadratic yield criterion for anisotropic materials based on preferred orientation. He assumed that the grains in the metals gradually elongate and become fibrous in the direction which has most strain and show anisotropic behaviour after loading. He also assumed that it has three mutually orthogonal directions. These orthogonal directions are called principal axes of anisotropy. However these axes may vary in directions within a bulk material based on the grain orientation. The preferred orientation in principal axes allowed him to simplify anisotropy in a form of homogenous quadratic function "***f***" to represent associative plastic potential. Based on the assumptions Hill (1948) proposed a

quadratic yield criterion as an extension to von Mises criterion for isotropic plasticity case. The Hill's orthotropic case is explained here briefly along with von Mises yield criterion. The implementation of Hill's orthotropic co-efficient is done with Lankford co-efficient in the numerical code inline with earlier work carried out at Cranfield University by Mirkovic (2004) and Panov (2006).

The von Mises yield criterion for isotropic material is

$$f(s) = \sqrt{\boldsymbol{s} : \boldsymbol{s}} - R = 0 \qquad \text{(Eq. 4.33)}$$

"$\boldsymbol{s}$" is deviatoric stress tensor and the R is radius. The radius can be written as

$$R = \sqrt{\frac{3}{2}}\sigma_{yield} \qquad \text{(Eq. 4.34)}$$

Using the general form used by Lemaitre (1983)

$$(\boldsymbol{A}_{ijkl} : \boldsymbol{s}_{kl}) : \boldsymbol{s}_{ij} = 1 \qquad \text{(Eq. 4.35)}$$

where A is a forth order tensor with the following symmetries:

$$\boldsymbol{A}_{ijkl} = \boldsymbol{A}_{klij} = \boldsymbol{A}_{jikl} = \boldsymbol{A}_{ijkl} \qquad \text{(Eq. 4.36)}$$

Using this notation the yield surface can be expressed as

$$\boldsymbol{f}(\boldsymbol{\sigma}_{ij}) = \sqrt{(\boldsymbol{A} : \boldsymbol{s}) : \boldsymbol{s}} - \boldsymbol{R} = \boldsymbol{0} \qquad \text{(Eq. 4.37)}$$

and the equivalent stress is:

$$\bar{\sigma} = \sqrt{\frac{\boldsymbol{3}}{\boldsymbol{2}}(\boldsymbol{A} : \boldsymbol{s}) : \boldsymbol{s}} \qquad \text{(Eq. 4.38)}$$

The anisotropic yield criterion proposed by Hill (1948) could be used to calculate the anisotropic behaviour by assuming anisotropy has three mutually orthogonal planes of symmetry at every point in the material. The intersections of these planes are the principal axes of anisotropy. The anisotropic yield criterion can be expressed in the similar for of von Mises equation by including the orthotropy co-efficient *F, G, H ,L, M, N* proposed by Hill. The orthotropic yield criterion will have the following form.

$$f(\sigma_{ij}) = \frac{1}{\sqrt{F+G+H}}\left[F(\sigma_y - \sigma_z)^2 + G(\sigma_z - \sigma_x)^2 + H(\sigma_x - \sigma_y)^2 + 2L\sigma_{yz}^2 + 2M\sigma_{zx}^2 + 2N\sigma_{xy}^2\right]^{\frac{1}{2}} - R = 0$$

(Eq. 4.39)

$$\bar{\sigma} = \left[\frac{3}{2} \left(\frac{F(\sigma_y - \sigma_z)^2 + G(\sigma_z - \sigma_x)^2 + H(\sigma_x - \sigma_y)^2 + 2L\sigma_{yz}^2 + 2M\sigma_{zx}^2 + 2N\sigma_{xy}^2}{F+G+H} \right) \right]^{\frac{1}{2}} \quad \text{(Eq. 4.40)}$$

In the plane stress case the equation (4.40) reduces to

$$\left[\left(\frac{F\sigma_y^2 + G\sigma_x^2 + H(\sigma_x - \sigma_y)^2 + 2N\sigma_{xy}^2}{F+G+H} \right) \right]^{\frac{1}{2}} - R = 0 \quad \text{(Eq. 4.41)}$$

The yield criterion can also be expressed in Lankford's coefficients which are written as follows, here R_L is used for one of the parameters to distinguish it from Radius R:

$$F = \frac{1}{R_L + 1} \frac{R_L}{P} \quad \text{(Eq. 4.42)}$$

$$G = \frac{1}{R_L + 1} \quad \text{(Eq. 4.43)}$$

$$H = \frac{1}{R_L + 1} R_L \quad \text{(Eq. 4.44)}$$

$$2L = 2Q_{xy} + 1 \quad \text{(Eq. 4.45)}$$

$$2M = (2Q_{xy} + 1) \frac{PR_L + R_L}{P(R_L + 1)} \quad \text{(Eq. 4.46)}$$

$$2N = (2Q_{xy} + 1) \frac{P + R_L}{P(R_L + 1)} \quad \text{(Eq. 4.47)}$$

Yield function in Lankford's coefficients takes the following form

$$\boldsymbol{f(\sigma_{ij})} = \sqrt{R_L + P + R_L P} \left[\begin{array}{l} R_L(\sigma_y - \sigma_z)^2 + P(\sigma_z - \sigma_x)^2 + PR_L(\sigma_x - \sigma_y)^2 \\ + (2Q_{yz} + 1)(PR_L + P)\sigma_{yz}^2 + (2Q_{zx} + 1)(PR_L + R_L)\sigma_{zx}^2 \\ + (2Q_{xy} + 1)(P + R_L)\sigma_{xy}^2 \end{array} \right]^{\frac{1}{2}} - R = \mathbf{0}$$

(Eq. 4.48)

Anisotropic yield criterion proposed by Hill could be very well expressed in simple equation form similar to von Mises.

$$\boldsymbol{f(\sigma_{ij})} = \sqrt{(\boldsymbol{A} : \boldsymbol{\sigma}) : \boldsymbol{\sigma}} - R = \mathbf{0} \quad \text{(Eq. 4.49)}$$

R is the yield stress in one of the principal axes of anisotropy. Using Voigt notation the equation (4.49) could be rewritten in the following form

$$f(\sigma) = \sqrt{(A\sigma)^t \sigma} - R = 0 \qquad \text{(Eq. 4.50)}$$

Where the stress vector could be expressed in the following form:

$$\sigma^t = \begin{bmatrix} \sigma_{xx} & \sigma_{yy} & \sigma_{zz} & \sigma_{yz} & \sigma_{xz} & \sigma_{xy} \end{bmatrix} \qquad \text{(Eq. 4.51)}$$

Where A is with the coefficients takes the following 6x6 matrix form

$$A = \frac{1}{F+G+H} \begin{bmatrix} G+H & -H & -G & 0 & 0 & 0 \\ -H & F+H & -F & 0 & 0 & 0 \\ -G & -F & F+G & 0 & 0 & 0 \\ 0 & 0 & 0 & 2N & 0 & 0 \\ 0 & 0 & 0 & 0 & 2L & 0 \\ 0 & 0 & 0 & 0 & 0 & 2M \end{bmatrix} \qquad \text{(Eq. 4.52)}$$

For an isotropic case using following reduces the equation (4.52) to Von mises isotropic

$$F = G = H = \frac{1}{2},\ L = M = N = \frac{3}{2}$$

The anisotropic co-efficient derivation and assumption are explained in Hill's book (1964). The level of orthotropy in a material were measured from uniaxial tensile tests on specimens cut at 0 degrees, 90 degrees and 45 degrees to the rolling direction. The strain ratios obtained through these results are assumed to remain constant and they are called r values. In sheet metals the r values are assessed for longitudinal strains greater than 0.05. Hence it is assumed that the elastic strains are negligible and the metal can be considered as incompressible so that the algebraic sum of the total principal natural strains is zero.

The characterisation of orthotropic co-efficient for AA2024 and AA7010 aluminium alloy materials were completed by Panov in his research work during 2006 at Cranfield University. He used Lankford co-efficient to determine the orthotropic parameters. Detailed procedures for characterising the orthotropic co-efficient and experimental methods are explained in his thesis (Panov, 2006).

4.6 Conclusion

The isotropic and anisotropic basic material modelling assumptions are briefly reviewed in this chapter. The main assumption for plasticity consistency criterion,

hardening criterion and flow theory especially associative plasticity theory were also briefly discussed. The isotropic and kinematic hardening assumption and their numerical equation forms were also discussed. The Hill's assumption on developing orthotropic material from anisotropic theory, Hill's orthotropic co-efficient and equivalent Lankford co-efficient and their numerical implementation equation forms were also described in this chapter.

5 Material models

5.1 Introduction

The term damage is commonly referred in material science and applied mechanics to describe irreversible changes to the microstructure of the material by a thermo-mechanical loading and unloading process (Lu and Chow, 1990). Slipping, micro cracking and or micro cavitations are the most common modes of irreversible micro structural rearrangement of material during this process. In a macroscopic scale these irreversible processes result in plastic response of the materials. The damage coupled theory with plasticity should cover two sets of material characterisation variables; first nucleation and propagation of dislocation and second micro cracking. In the creep region Kachanov (1958) defined reduction in load carrying capacity of the cross sectional area as a scalar measure of damage. Kachanov postulated this loss of load carrying capacity of the material as it damages, is responsible for accelerating creep strain rate leading to fracture (tertiary creep). Experiments carried out by Chaboche (1984), Onat and Leckie (1988) and Murakami (1988) showed strong evidence that creep damage in the form of planar microvoids usually nucleates and grows on grain boundaries whose planes are perpendicular to the maximum tensile stress direction. This confirms that the orientation independent isotropic damage variable is not accurate to define material damage. The isotropic damage based measurement predicted by Chow and Wang (1987) and (Jansson and Stigh, 1985) predict lower strength of materials compared to experimental results.

Lemaitre (1972) introduced another scalar measure of damage as decrease of elastic modulus. He used virgin material stress concept along with strain equivalence principle to derive the damage coupled elastic constitutive equations. Although this method is extensively used by many researchers, it suffers from not being able to influence the Poisson's ratio during damage (Lu and Chow, 1990). The theoretical analysis done by Case (1984) and Rabier (1989) and experimental measurements taken by Cordebois and Sidoroff (1982) and Chow and Wang (1987) revealed, there is substantial damage induced changes in Poisson's ratio due to reduction in elastic modulus. Trampczynski, Hayhurst and Lecki (1981) work on creep rupture of copper and aluminium under non-proportional loading and Davison and Stevens (1973) work on thermo-mechanical constitution of spalling elastic bodies showed the directional

nature of material damage influencing the final rupture. These research works reveal the significance of damage induced material anisotropy for predicting material damage. The above research works suggest that any prediction damage model developed for material with a form of anisotropy behaviour during loading must include damage induced anisotropy. Otherwise it might lead to inaccurate results (Lu and Chow, 1990).

5.2 Review of other constitutive models

In crashworthiness and metal processing application the strain rate is in the range of 0.01 to 100 s^{-1}. The effect of the strain rate in this range cannot be neglected (Zukas, 1982). Strain rate dependency varies from material to material. However if the application of material in dynamic case shows dependency of strain rate then the material model should allow inclusion of strain rate parameters. Other than strain rate dynamic material models which capture material deformation process should also include strain hardening, working hardening and thermal effects.

The rate dependant models define the yield stress as a function of strain, strain rate and thermal effects. The material models are broadly classified into two groups based on the assumption; one group is based on empirical relationship and the other is based physical relationships. Based on these assumption material models have been developed for the use of computer simulations. The most widely used models for crashworthiness applications are Johnson-Cook, Zerilli-Armstrong and Mechanical threshold stress models. These models are used only when material show considerable dependency on strain rate and temperature. The material constants for these models should be obtained accurately for practical application. There are considerable amount of difficulty in obtaining the material constants accurately.

5.2.1 Johnson- Cook model

Johnson-Cook (1983) model relates the equivalent von Mises flow stress as a function of equivalent plastic strain, strain rate and temperature. Johnson and Cook (1983) combined the hardening of material at low constant strain rate condition and strain rate effect due to thermal softening in an adiabatic heating condition and proposed a strength model. It is an empirical model.

$$\sigma = \left[A + B\left(\varepsilon_{pl}\right)^{n}\right][1 + C\ ln(\dot{\varepsilon}^{*})][1 - (T^{*})^{m}] \quad \text{(Eq. 5.1)}$$

A, B, C, n, m are material constants to be determined by experiments, ε_{pl} is the effective plastic strain, $\dot{\varepsilon}^{*}$ is the dimensionless strain rate

$$\dot{\varepsilon}^{*} = \frac{\dot{\varepsilon}_{pl}}{\dot{\varepsilon}_{0}} \quad \text{(Eq. 5.2)}$$

$\dot{\varepsilon}_{pl}$ - is the plastic strain rate and

$\dot{\varepsilon}_{0}$ - is the reference strain rate)

T^{*} - homologues temperature which is a ratio of current temperature T to the melting temperature T_m

$$T^{*} = \frac{T - T_r}{T_m - T_r} \quad \text{(Eq. 5.3)}$$

where T_r is the reference temperature at initiation of yield stress (σ_0)

Johnson-Cook model can be used for strain rates of 0.001 to 1000 s^{-1} typically the model is used for explosive forming, ballistic and impact application. Some of the desirable features of this model are;

- Simple to implement
- Requires less computational time and memory
- Applicable to wide range of metals
- Material constants can be obtained from limited number of experimental tests

The material constants are obtained using dynamic Hopkins bar tensile test, torsion tests and static tensile tests.

The main disadvantage of the model is that the thermal effect and strain rate on the flow stress are uncoupledJohnson and Cook (1983). This implies that the strain rate sensitivity is independent of temperature. But in general most metals at high strain rate do not behave this way. Moreover empirical based equations are curve fitting procedures. Exceptional care must be taken when extrapolating for the values for strains and temperature which are out of observed zone while determining material constants.

The damage model of Johnson-Cook is given by the following equation; the strain fracture is given by

$$\varepsilon_f = [D_1 + D_2 exp(D_3 \sigma^{*})][1 + D_4\ ln(\dot{\varepsilon}^{*})][1 - (D_5 T^{*})] \quad \text{(Eq. 5.4)}$$

D_1, D_2, D_3, D_4, D_5 are damage model parameters

σ^* is the ratio of pressure divided by virgin material stress $\sigma^* = \frac{p}{\bar{\sigma}}$

Fracture occurs when damage parameter D reaches a value of 1

$$D = \sum \frac{\Delta\varepsilon}{\varepsilon^f} \quad \text{(Eq. 5.5)}$$

Johnson-Cook model have also been modified for some simple applications

- Simplified Johnson-Cook model

Simplified form of this model is used for applications where thermal effects are negligible at large strain range. Then the flow stress is defined as;

$$\sigma = \left[A + B\left(\varepsilon_{pl}\right)^n\right][1 + C\ ln(\dot{\varepsilon}^*)] \quad \text{(Eq. 5.6)}$$

5.2.2 Zerilli-Armstrong model

Zerilli and Armstrong (1987) model was developed based on improving the Johnson-Cook model by additionally including the crystalline structure of the material. The model was developed for face-centred-cubic (*fcc*) and body-centred-cubic (*bcc*) (Zerilli and Armstrong, 1987; Johnson and Holmquist, 1988) based on the observation of dislocation process controlling the plastic flow. Compared to *fcc* metals the *bcc* metal tend to have strong dependency of plastic yield stress on the temperature and strain rate.

$$\sigma_Y = C_0 + C_2(\sqrt{\bar{\varepsilon}_{pl}})\ e^{-C_3T + C_4Tln(\dot{\bar{\varepsilon}})}, \text{ for } (fcc) \quad \text{(Eq. 5.7)}$$

$$\sigma_Y = C_0 + C_1\left(\sqrt{\bar{\varepsilon}_{pl}}\right)e^{-C_3T + C_4Tln(\dot{\bar{\varepsilon}})} + C_5(\bar{\varepsilon}_{pl})^n, \text{ for } (bcc) \quad \text{(Eq. 5.8)}$$

$C_0, C_1, C_2, C_3, C_4, C_5$ and n are the material constants, $\bar{\varepsilon}_{pl}$ is the total plastic strain and T is the absolute temperature.

The difference between Johnson-Cook and Zerilli-Armstrong model is the athermal stress is divided in to two components. The *fcc* and *bcc* formulation also differ based on work hardening law. The *fcc* work hardening is coupled with the temperature and strain rate but for *bcc* the rule assumes work hardening is independent of temperature and strain rate.

5.2.3 Steinberg-Guinan model

The Steinberg-Guinan model relates the shear stress (G) with pressure, temperature and effective plastic strain in addition to the yield strength definition (Y) (Steinberg,

Cochran and Guinan, 1980). The main assumption in this model is that the strain rate $\dot{\varepsilon}$ has minimal effect on Y beyond certain strain rate value ($\dot{\varepsilon} = 10^5\ s^{-1}$). At this higher dynamic strain rate the constitutive relation for G and Y with strain, pressure and temperature are provided by the equation;

$$G = G_0\left[1 + \left(\frac{G_p'}{G_0}\right)\frac{P}{\eta^{1/3}} + \left(\frac{G_T'}{G_0}\right)[T - 300]\right] \quad \text{(Eq. 5.9)}$$

$$Y = Y_0\left(1 + \beta(\varepsilon + \varepsilon_i)\right)^n\left[1 + \left(\frac{Y_p'}{Y_0}\right)\frac{P}{\eta^{1/3}} + \left(\frac{Y_T'}{Y_0}\right)[T - 300]\right] \quad \text{(Eq. 5.10)}$$

Subject to $Y_{max} \geq Y_0\left(1 + \beta(\varepsilon + \varepsilon_i)\right)^n$ (Eq. 5.11)

where η is compression = $\frac{v_0}{v}$; v_0 is the initial specific volume and v specific volume, β and n are the hardening parameters, ε_i is the initial plastic strain (which is normally zero). Subscripts "p" and "T" are used to identify the derivatives obtained from pressure and temperature respectively. The subscript "0" is used for reference state.

Steinberg-Lund improved the model to (Steinberg and Lund, 1988) to lower strain rates of $\dot{\varepsilon} = 10^{-4}\ s^{-1}$. The modified model is given as;

$$\sigma_y = \left\{Y_T\left(\dot{\varepsilon}_p, T\right) + Y_A f\left(\varepsilon_p\right)\right\}\left[\frac{G(P,T)}{G_0}\right] \quad \text{(Eq. 5.12)}$$

Here $Y_T\left(\dot{\varepsilon}_p, T\right)$ is the thermally activated form of the yield strength as a function of plastic strain and temperature. The $Y_A f\left(\varepsilon_p\right)$ term is the athermal portion of the equation, which is a function of plastic strain and the final term $\frac{G(P,T)}{G_0}$ is the shear modulus term in which $G(P,T)$ is pressure and temperature dependent shear form and G_0 is the shear modulus at the standard pressure and temperature condition.

5.2.4 Mechanical threshold stress model

The mechanical threshold stress (MTS) model uses differential mathematical form to depict experimental results (Follansbee, 1988; Maudlin, foster and Jones, 1997). It has been observed that when metallic materials are subject to large strains they move towards a finite saturation stress. This saturation stress is not included in the other models discussed in this section. However the MTS model includes this in the formulation. The results obtained through the MTS model provide better correlation with the experimental results (Chen, 1996). The MTS flow stress is defined by athermal (Gourdin and Lassila, 1991) and thermal parts.

$$\sigma_Y = \sigma_a + \frac{\mu}{\mu_0}\sum_i S_{T,i}\,\hat{\sigma}_i \qquad \text{(Eq. 5.13)}$$

μ is the temperature dependent shear modulus and μ_0 is the shear modulus at absolute zero temperature.

where $\sigma_a = k_y d^{-n}$ (Eq. 5.14)

σ_a is the athermal part, k_y is determined from Hall-Pletch plot (Gourdin and Lassila, 1991), *d* is the grain size and *n* is a constant (1/3<n<1).

The thermal portion $S_{T,i}$ is defined by the following equation; The thermal part considers the rate dependent interaction of forest dislocations, interstitials, solutes and other barriers that are overcome by thermal initiation.

$$S_{T,i} = \left[1 - \left(\frac{kT\ln\left(\frac{\dot{\varepsilon}_{oi}}{[\dot{\varepsilon}]^p}\right)}{\mu b^3 g_{oi}}\right)^{\frac{1}{q_i}}\right]^{\frac{1}{p_i}}$$

(Eq. 5.15)

Where *k* is the Boltzmann's constant, *T* is the temperature, $\dot{\varepsilon}_o$ is the reference strain rate b is the magnitude of Burger's vector, g_o is the normalised activation energy for given dislocation and obstacle interaction, q and p are the material constants and $\hat{\sigma}$ is the differential hardening law for forest dislocation.

The main advantage of Johnson-Cook model over MTS model is the numbers of parameters need to be determined for running a simulation. However the MTS model is based on physical processes which deform the material during loading hence MTS model can be a better representation of the behaviour of material. Moreover the Johnson-Cook model lacks the representation of saturation stress as an integral part of the model compared to MTS model. The Zerrili-Armstrong model gives satisfactory macroscopic description of the deformation during the strain rate in the order of 10^4 s^{-1} and the Steinberg-Guinan model can be used for large strain rates as well as low strain rates by using Steinberg and Lund (1988) improvement. This chapter explains the various material models available for study. However these models are based on higher strain rate and work well for the specified strain rates. The model choice for specific application depends mainly on the acceptable level of accuracy in prediction material behaviour at that specific strain rate. In this research work a quasi-static strain rate independent model should be used in order to achieve the required results proposed by MUSCA partners.

5.3 Developments on general principles of anisotropic damage models

Anisotropic damage models have been developed using vectors and tensors with state variables characterising the damage. The damage models based on Kachanov's principle were developed by Davison and Stevens (1973), Krajcinovic and Fonseka (1981) and Krajcinovic (1985). The scalar damage variable in this case is the magnitude of projected area density of planar micro-voids onto a given cross section defined by its normal (Lu and Chow, 1990). The dot product of the normal is defined as an appropriate average of the direction normal to the micro-cracks distributed over a representative volume element V_m or also defined by Krajcinovic (1985) as statistically significant sample. The drawback with this model is that the damage is a vector variable and inclusion of newly created micro-cracks in the direction different from earlier micro-crack direction becomes difficult.

To accommodate the newly created micro-cracks in analysis of creep problems Lecki and Onat (1981, 1985) introduced a sequence of even ranking irreducible tensorial damage variable $\hat{V} = [\hat{V}_0, \hat{V}_{i,j}, \hat{V}_{i,j,k,l}, \dots\dots]$ representing the total volume of cavities within a unit volume material element and the cavity distribution of this volume among the grain boundaries and $\hat{N} = [\hat{N}_0, \hat{N}_{i,j}, \hat{N}_{i,j,k,l}, \dots\dots]$ representing the number of locations available for void growth on grain boundaries perpendicular to a specified direction. This model represents the complete mathematical input of microstructure, however it has not been developed to normal practical application due to the fact that it lacks the explicit treatment of damage coupled constitutive equation. Lu and Chow (1990) point out that this may be due the ambiguous physical meaning of higher rank damage tensors $\hat{V}_{i,j,k,l}$, $\hat{N}_{i,j,k,l}$ this model is unable to represent practical applications.

Lu and Chow noticed the shortcoming on the physical and mathematical representation of the previous damage models. Lu and Chow (1990) conducted a study to examine best way to represent thermodynamically acceptable damage coupled constitutive equations of inelasticity. The damage tensor $\boldsymbol{D}$ has been used to study elasticity and elasto-plastic ductile anisotropic theory, creep problems, theory of cracks, damage mechanics theory, fatigue and the thermomechanics in various research based experimental works by authors Chow and Wang (1982, 1987), Rabotnov , Vakulenko and Kachanov (1971), Betten (1983), Kawamot, Ichikawa

Kyoya (1988), Litewka (1986), and Weitsman (1988), Allen, Harris and Groves (1988).

The extensive use of damage tensors by the authors is due to the mathematical simplicity and it represents the three main orthotropic directions and the corresponding axes values. Lu and Chow (1990) acknowledged the damage induced material anisotropy could be characterised by a second order symmetric damage tensor ***D***. Lu and Chow also emphasise from the work completed by Murakami (1988) that ***D*** can describe the damage state corresponding to an arbitrary distribution of microcracks and/or microvoids however complicated it might be, as long as the net area reduction due to these defects characterises the material damage over a representative volume element. The experiments by Chow and Wang (1987, 1988) on ductile fracture of aluminium alloy 2024-T3 showed the theoretical predictions of anisotropic damage model with damage tensor ***D*** gave agreeable results with experimental test results. The damage tensor ***D*** was also used by Mirkovic (2004) for modelling non-linear behaviour of metallic structure and Panov (2006) for modelling metal behaviour at high strain rate during their research at Cranfield University.

5.4 Summary of thermodynamic analysis done by Lu and Chow

The general thermodynamic analysis was considered by Lu and Chow (1990) damage model and the result are summarised here. The assumptions made in their paper are;

- Infinitesimal deformation is usually considered unless otherwise stated.
- Isothermal conditions are assumed; the effect of temperature enters the constitutive equations only through material parameters.
- At the start when time is zero the material damage is considered zero (D=0) and the material is considered to be in virgin state

The internal variables used in this thermodynamic analysis are listed in the Table 5-1. Lu and Chow considered only isotropic hardening for simplicity and they also assert that the proposed formulations can be readily extended to other hardening models without difficulty. The thermodynamic assumption and complete derivation can be found in Lu and Chow (1990) paper.

Table 5-1 Chow and Wang (1990) general thermodynamic internal variables

Internal variables	**Associated generalised forces**
Plastic strain ε_p	Cauchy stress σ
Accumulated plastic strain p	Strain hardening threshold $R_0 + R$ R_0 – strain hardening threshold initiation R – increment of strain hardening threshold
Damage variable D	Damage energy release rate Y
Overall damage β	Damage strengthening threshold $B_0 + B$ (sum of virgin material stress when damage initiates (B_0) and the additional virgin material stress (B) required to continue the damage evolution) B_0 – damage strengthening threshold initiation (virgin material stress at which damage starts occurring) B – increment of damage strengthening threshold (virgin material stress required for damage evolution after damage has intiated at B_0)

5.4.1 Thermodynamic restriction on damage constitutive equations

The theory of irreversible process of thermodynamics assumption iterates that; the number of internal variables can be determined adequately by using instantaneous values of internal variable which represent the reversible process while the necessary constrains keep the state under thermodynamic equilibrium.

Lu and Chow proposed when the rate of increment of the internal variables represents the current state of damaged material and depends only on their respective conjugate forces, it is possible to prove that scalar flow potential "Ω" exists. From this scalar flow potential it is possible to derive the rate of increment of each internal variable (Lu and Chow, 1990).

5.4.2 Thermodynamic function for damage model

The elasticity is assumed to be not dependant on plastic strain $\boldsymbol{\varepsilon_p}$ the elastic properties depend on damage variables only. To accommodate damage in plastic region, energy based plastic flow and damage processes were introduced in the

postulate. This postulate assumes the plastic flow and damage processes induced by heat or stored in material through hardening are independent to each other. This postulate should be understood as there is no direct coupling between plasticity and damage (Lu and Chow, 1990). In contrast to the above assumption Lu and Chow also showed that plastic flow also contributes to nucleation and growth of damage.

Based on Lu and Chow (1990) thermodynamic assumptions they provided an uncoupled form of plastic dissipative potential and damage dissipative potential in the following equations.

$$\boldsymbol{\sigma}: \dot{\boldsymbol{\varepsilon}}_{\boldsymbol{p}} - (R_0 + R)\dot{p} \geq 0 \qquad \text{(Eq. 5.16)}$$

$$\widehat{\boldsymbol{Y}}: \dot{\boldsymbol{D}} - (B_0 + B)\dot{\beta} \geq 0 \qquad \text{(Eq. 5.17)}$$

where $\widehat{\boldsymbol{Y}} = -\boldsymbol{Y}$

The equations (5.16) and (5.17) imply that there exist a plastic dissipative potential and a damage dissipative potential. It means that the non-negative convex closed function or flow potential Ω can be decomposed into two independent components.

$$\Omega(\boldsymbol{P}) = \Omega_{\mathrm{p}}\,(\boldsymbol{\sigma},\ R_0 + R) + \Omega_{\mathrm{d}}\,(\widehat{\boldsymbol{Y}},\ B_0 + B) \qquad \text{(Eq. 5.18)}$$

Here when

$\Omega_{\mathrm{p}} = 0$ represents yield surface in generalised force space and

$\Omega_{\mathrm{d}} = 0$ represents damage surface in generalised force space

Introduce the equivalent plastic stress $\tilde{\sigma}_p$ and an equivalent damage $\tilde{\sigma}_d$ or damage dissipation potential described by Chow and Wang (1988) instead of equivalent energy release rate Y_d (Lu and Chow, 1990) to overcome certain anomalies associated with the energy release rate tensor $\boldsymbol{Y}$.

$$\boldsymbol{\sigma}: \dot{\boldsymbol{\varepsilon}}_{\boldsymbol{p}} = \tilde{\sigma}_p\dot{p} \text{ and} \qquad \text{(Eq. 5.19)}$$

$$\widehat{\boldsymbol{Y}}: \dot{\boldsymbol{D}} = \tilde{\sigma}_d\dot{\beta} \qquad \text{(Eq. 5.20)}$$

The two inequalities in equations (5.16) and (5.17) can be written as

$$\tilde{\sigma}_p - (R_0 + R)\dot{p} \geq 0 \qquad \text{(Eq. 5.21)}$$

$$\tilde{\sigma}_d - (B_0 + B)\dot{\beta} \geq 0 \qquad \text{(Eq. 5.22)}$$

In the absence of damage the approximate representation of the yield surface for an anisotropic material depicts von Mises yield criterion.

$$\Omega_{\mathrm{p}}\,(\boldsymbol{\sigma},\ R_0 + R) = \left\{\tilde{\sigma}_p\right\}^2 - \{(R_0 + R(p)\}^{\mathbf{2}} \qquad \text{(Eq. 5.23)}$$

Or equivalently

$$F_p\ (\boldsymbol{\sigma},\ R_0 + R) = \{\tilde{\sigma}_p\} - \{(R_0 + R(p)\} \quad \text{(Eq. 5.24)}$$

where $\tilde{\sigma}_p = \left\{\frac{1}{2}\tilde{\boldsymbol{\sigma}}:\boldsymbol{H}:\tilde{\boldsymbol{\sigma}}\right\}^{\frac{1}{2}}$ (Eq. 5.25)

$\boldsymbol{H}$ - Hills anisotropic co-efficient matrix

Similarly for damage growth rate under damage dissipation potential

$$\Omega_{\mathrm{d}}\ (\widehat{\boldsymbol{Y}},\ B_0 + B) = \{\tilde{\sigma}_d\}^2 - \{(B_0 + B(\beta)\}^{\mathbf{2}} \quad \text{(Eq. 5.26)}$$

Or equivalently

$$F_d\left(\widehat{\boldsymbol{Y}},\ B_0 + B\right) = \{\tilde{\sigma}_d\} - \{(B_0 + B(\beta)\} \quad \text{(Eq. 5.27)}$$

where $\tilde{\sigma}_d = \left\{\frac{1}{2}\tilde{\boldsymbol{\sigma}}:\boldsymbol{J}:\tilde{\boldsymbol{\sigma}}\right\}^{\frac{1}{2}}$ (Eq. 5.28)

$\boldsymbol{J}$ – is the damage characteristic tensor which describes the anisotropic nature of damage growth.

In a physical sense the functions describing the plasticity and damage can be called as follows;

$\tilde{\sigma}_d$ - damage driving force from the external loading mechanisms

$(B_0 + B)$ - the damage resistance force from the material

$\tilde{\sigma}_d - (B_0 + B)$ - is the thermodynamic force conjugate to damage nucleation and propagation.

$\{(B_0 + B(\beta)\}$ - is related to damage evolution and it is a material property. Physically it may be recognized as specific work required for a unit damage growth.

As per Lu and Chow all inelastic constitutive equation for solids can be traced back into two non-negative convex closed functional form of the thermodynamic potential ψ and the dissipative potential Ω. However the formulation of explicit forms within the general thermodynamic rules still remains unsolved. The thermodynamic potential ψ is decomposed into three components to simplify the problem and obtain agreeable solution. Nevertheless this simplification supports the rational examination and subsequent experimental evidence of research work done by notable authors Chaboche's (1984) research work, Krajcinaovic (1985) and Lemaitre (1987).

5.5 Overview of damage model

Continuum damage mechanics represents a class of methods for modelling the effect of material damage within the framework of continuum mechanics. The common features are that the effect of damage within a material is averaged over a volume and

represented by a continuous variable that is related to the density of the defects within the material. The models require material parameters derived from experiment to characterise a particular material, and the quality of these parameters directly influences the accuracy of the numerical results. If the process for obtaining these parameters from experiment is complex or time consuming then this limits the use of these models.

A generalised anisotropic theory of ductile fracture using the above scenarios is presented by Chow and Wang. This is achieved by developing a constitutive equation of plasticity based on the damage effect tensor $\underline{\boldsymbol{M}}(\boldsymbol{D})$. The damage tensor proposed by them can be used for a general coordinate system. Chow and Wang derived the damage evolution equations based on the virgin material stress tensor $\tilde{\sigma}$, and proposed that the virgin material stress tensor give physical representation of material degradation. Chow and Wang proposed a general anisotropic damage evolution model and verified and validated the model from the experimentally obtained damage parameters. The determination of experimental results based on general anisotropic damage model can then be used on the constitutive equations to solve the practical problem in orthotropic metal. Their proposed model includes the equation of elasticity, plasticity and damage. The Chow and Wang damage model provides a comprehensive theory of anisotropic continuum damage mechanics capable of solving practical engineering problems. In the context of this research work the simplicity in this model is that the damage variables could be easily determined under present laboratory set up.

5.6 Strain equivalence and energy equivalence damage models

In continuum damage mechanics the prediction of material damage uses the concept originally proposed by Kachanov (1958) for creep; he used a damage variable term D to assess the material degradation. Though the micro mechanics material degradation Kachanov (1993) is due to nucleation and coalescence of voids, cavities, and micro-cracks, the damage variable D reflects the average degradation of material at the macro (continuum) scale. Present prediction methods use this theory to develop theory of fracture mechanics and use it effectively to predict practical failure scenarios. The advantage here is it allows to approximate macro scale damages using

the micro-mechanics damage variables. This enables researchers to measure the average degradation of materials using conventional specimen testing methods and use the data for practical problems with the aid of finite element methods (Benallal et al. 1985).

There are two principles used in evaluating the damage variable, one is the strain equivalence principle and the other is the energy equivalence principle. Lemaitre and Chow's models vary in the way they use the equivalence principles. Lemaitre (2000) model uses strain equivalence principle and Chow's model uses energy equivalence principle.

5.6.1 Strain equivalence principle

Lemaitre (1971) used the virgin material stress concept and proposed a strain equivalence principle that Any strain constitutive equation for a damaged material may be derived in the same way as for a virgin material except that the usual stress σ is replaced by the effective $\tilde{\sigma}$ stress .

For one dimensional case it implies the following:

Undamaged material	Damaged material
$D = 0$	$0 < D < 1$
$\varepsilon = f(\sigma,....)$	$\varepsilon = f(\tilde{\sigma},....) \Rightarrow \varepsilon = f\left(\frac{\sigma}{1-D},....\right)$

and the damage variable could be derived as $D = 1 - \frac{E}{E}$ (Eq. 5.29)

where $\tilde{E}$ is the effective young's modulus and E is the Young's modulus

5.6.2 Energy equivalence principle

Sidoroff (1981) proposed an elastic energy equivalence concept the complementary elastic energy for a damage material is the same in form as that of an undamaged material, except that the stress is replaced by the virgin material stress in the energy formulation.

This implies that the complementary elastic energy for a damaged material could be equated to fictitious undamaged material by replacing the stress with virgin material stress in the energy equation. Since the complementary elastic energy $W_e(\sigma,0)$ of an undamaged material (where D = 0) is

$$\mathrm{W_e}(\boldsymbol{\sigma},0) = \frac{1}{2}\boldsymbol{\sigma}^{\mathbf{T}} : \mathbf{C_e^{-1}} : \boldsymbol{\sigma} \qquad \text{(Eq. 5.30)}$$

from the above hypothesis the complementary energy of a damage material is expressed as

$$\mathrm{W_e}(\boldsymbol{\sigma},\mathbf{D}) = \mathrm{W_e}(\tilde{\boldsymbol{\sigma}},\mathbf{0}) = \frac{1}{2}\tilde{\boldsymbol{\sigma}}^{\mathbf{T}} : \mathbf{C_e^{-1}} : \tilde{\boldsymbol{\sigma}} = \frac{1}{2}\boldsymbol{\sigma} : (\mathbf{M}^{\mathbf{T}} : \mathbf{C_e^{-1}} : \mathbf{M}) : \boldsymbol{\sigma} \qquad \text{(Eq. 5.31)}$$

where C_e is the elastic stiffness tensor and the effective elastic stiffness tensor could be expressed as

$$\tilde{\mathbf{C}}_{\mathbf{e}} = \mathbf{M^{-1}} : \mathbf{C_e} : \mathbf{M^{-T}} \qquad \text{(Eq. 5.32)}$$

similarly using the hypothesis of energy equivalence the effective elastic strain vector is

$$\tilde{\boldsymbol{\varepsilon}}_{\mathbf{e}} = \mathbf{M^{-1}} : \boldsymbol{\varepsilon}_{\mathbf{e}} \qquad \text{(Eq. 5.33)}$$

5.7 Chow and Wang anisotropic damage variables

Materials deteriorate at different stages of loading due to formation and realignment of dislocations, micro-cracks, voids and other types of material defects and impurities. Chow and Wang (1987) proposed an anisotropic damage tensor based on the theory of continuum mechanics to address the progressive material degradation. Chow and Wang (1987) used virgin material stress tensor $\tilde{\sigma}$ and second order damage tensor ***D***, to represent damage state of material under service loading conditions. The damage tensor ***D*** may be experimentally determined.

Assumption considered by Chow and Wang for the proposed damage effect tensor ***M*(*D*)**;

- The element considered is large enough to contain numerous defects but sufficiently small as a material point that the concept of damage mechanics may be applied within the scope of continuum mechanics.
- The damage may be calculated at macro-scale level based on the reduction of cross sectional area during loading.

- The cracks and cavities formed during damage are uniformly distributed in all directions.
- The concept of proportional loading (Sidoroff, 1981) used to approximate the damage effect 4th order tensor; and the assumption allows prediction of material damage for general structural analysis under arbitrary loading conditions.

Prior to loading the cross-sectional area S orientation is defined by $\underline{n}$. The cross-sectional area originally resisting the material before damage S changes to effective resisting area $\tilde{S}$ after degradation of material due to loading. A damage variable D could be depicted as shown in Figure 5-1 as a measure of the change of an element surface area S to $\tilde{S}$ after loading.

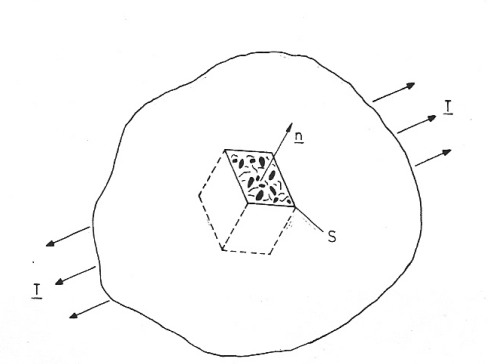

Figure 5-1 Damaged material element Chow and Wang (1986, 1987)

$$D = \frac{S - \tilde{S}}{S} \qquad \text{(Eq. 5.34)}$$

The effective Cauchy stress tensor $\tilde{\sigma}$ related to the effective resisting area $\tilde{S}$ could be written in the form

$$\tilde{\sigma} = \sigma \frac{S}{\tilde{S}} = \frac{\sigma}{1 - D} \qquad \text{(Eq. 5.35)}$$

which may be expressed in a generalised form of anisotropic damage as

$$\tilde{\boldsymbol{\sigma}} = \boldsymbol{M(D)} : \boldsymbol{\sigma} \qquad \text{(Eq. 5.36)}$$

If the material damage direction assumed to coincide with the principal axes of virgin material stresses then the components of ***M(D)*** can be expressed in the principal co-ordinate system. The damage effect tensor proposed by Chow and Wang (1987) in

this theory is a symmetric 4th order tensor taking into account the anisotropic material damage in the principal coordinate system as

$$M_{ij}(D) = \begin{bmatrix} \frac{1}{1-D_1} & 0 & 0 & 0 & 0 & 0 \\ 0 & \frac{1}{1-D_2} & 0 & 0 & 0 & 0 \\ 0 & 0 & \frac{1}{1-D_3} & 0 & 0 & 0 \\ 0 & 0 & 0 & \frac{1}{\sqrt{(1-D_1)(1-D_2)}} & 0 & 0 \\ 0 & 0 & 0 & 0 & \frac{1}{\sqrt{(1-D_2)(1-D_3)}} & 0 \\ 0 & 0 & 0 & 0 & 0 & \frac{1}{\sqrt{(1-D_3)(1-D_1)}} \end{bmatrix}$$

(Eq. 5.37)

The damage variables D_1, D_2, D_3 are in their respective principal co-ordinate system. For isotropic condition this damage effect tensor readily reduces to scalar $D_1 = D_2 = D_3 = D$. The damage effect tensor proposed in equation 5.37 is expressed in principal stress direction and the general co-ordinate system can be derived using the transformation of co-ordinate system laws.

For one dimensional case it implies the following:

Undamaged material	Damaged material
$D = 0$	$0 < D < 1$
$W^e = \frac{1}{2}\sigma\varepsilon$	$W^e = \frac{1}{2}\tilde{\sigma}\tilde{\varepsilon}$

and the damage variable could be derived as $D = 1 - \sqrt{\frac{\tilde{E}}{E}}$ (Eq. 5.38)

where $\tilde{E}$ is the degraded or damaged material Young's modulus and E is the undamaged material's Young's modulus.

The damage variable D is useful to characterise the degradation of the elastic modulus in continuum damage mechanics. We have to differentiate two cases, one for the isotropic materials and one for the anisotropic materials.

Although other expressions for the damage variable can be found, the experimentation shows that the change in elastic modulus is the most convenient way to calculate damage in metals and composites. From the equation 5.38 the degraded Young's

modulus and Poisson's ratio and through the experiment and the damage variables D_1, D_2, D_3 could be calculated (Chow and Wang, 1987).

5.7.1 Constitutive equations for plasticity

Chow and Wang (1987) had shown in their paper that using von Mises yielding criterion the yielding of material with damage could be derived and effective plastic strain for orthotropic material could be calculated using Hill's orthotropic virgin material stress.

$$F_p(\sigma, D, R) = F_p(\tilde{\sigma}, R) = \tilde{\sigma}_p - \{R_0 + R(p)\} = 0 \qquad \text{(Eq. 5.39)}$$

$\tilde{\sigma}_p$ = effective plastic equivalent stress, R_0 = initial strain hardening threshold, $R(p)$ = increment of strain hardening threshold

$$\tilde{\sigma}_p = \left\{ \frac{1}{2} \sigma^T : \tilde{H} : \sigma \right\}^{\frac{1}{2}} \qquad \text{(Eq. 5.40)}$$

where $$\tilde{H} = M^T(D) : H : M(D) \qquad \text{(Eq. 5.41)}$$

If the vector notation for stress and strain is used, the positive semi-definite tensor H for orthotropic material is represented by 6 x 6 matrices as in principal coordinate system and it is called as the Hill's anisotropic coefficient matrix.

The increment of strain hardening threshold may be represented by power law

$$R(p) = Kp^n$$

where p is the accumulative plastic strain and K and n are material constants.

5.7.2 Damage Evolution

Damage evolution is depicted by introducing an effective damage stress similar to the effective plastic stress.

$$F_d = \tilde{\sigma}_d - (B_0 + B(\beta)) = 0 \qquad \text{(Eq. 5.42)}$$

$\tilde{\sigma}_d$ = effective damage equivalent stress, B_0 = initial damage threshold, β = overall damage, $B(\beta)$ = increment of damage threshold depending on β

$$\tilde{\sigma}_d = \left\{ \frac{1}{2} \sigma^T : \tilde{J} : \sigma \right\}^{\frac{1}{2}} \qquad \text{(Eq. 5.43)}$$

where $\tilde{J} = M^T : J : M$ (Eq. 5.44)

$\tilde{J}$ is the fourth order damage characteristic tensor.

A generalised anisotropic theory of ductile fracture using the above scenarios is presented by Chow and Wang.

5.8 Lemaitre's anisotropic damage law of evolution

Lemaitre (2000) in his recent paper formulated anisotropic damage based on the principle of strain equivalence; it is based on his earlier work on isotropic damage (Lemaitre, 1983).

In summary, Lemaitre (2000) in his recent paper describes his anisotropy damage law of evolution in the following paragraph. Based on the strain equivalence principle anisotropic damage has been formulated. The damage variable is based on the surface density of material due to microcracks and microvoids. The damage evolution is governed by the plastic strain. The plastic strain is represented by an orthotropic second order tensor. . The damage in elastic part is introduced by a tensor on the deviatoric part of the energy along with a scalar which is a trace from the hydrostatic part. The kinetic law of evolution of damage is an extension of isotropic case. In this assumption the damage rate tensor is proportional to the absolute value of the principal components of the plastic strain rate tensor and it is a non-linear function of effective elastic strain energy. In this theory there are no other material parameter are introduced. Several experiments were conducted on metals to validate the theory. From virgin material stress concept the coupling of damage with plasticity along with quasi-unilateral conditions of partial closure of microcracks are derived. To determine the critical value of damage at mesocrack initiation a strain localisation study is done.

5.9 Limitations of strain equivalence postulate

Lu and Chow (1990) argue that the strain equivalence postulate is based on a weak argument and it is empirical in nature. The nucleation of damage and growth of damage is directly related to drop in stress due to reduction in stiffness of the material. However in reality the material damage occurs due to micro-cracks and micro-cavities which affect both stress and strain distribution (Hutchinson, 1987). Similar to fracture mechanics, crack extension is usually accompanied by a reduction in stiffness and increase in deformation except for two special boundary conditions namely fixed grip and dead load. Krajcinovic and Fonseka (1987) redefined the damage variable to keep the model linearly dependable to stress. Lu and Chow (1990) differ that there is no physical justification for this ad hoc adjustment. Chow and Wang (1987) also emphasise that apart from the above shortcomings the postulate lacks thermodynamically acceptable damage coupled elastic constitutive equation when damage is not orientation dependable. Lu and Chow (1990) extensively discuss the experimental and thermodynamic limitations of strain equivalence postulate.

5.10 Selection of constitutive models

Lemaitre and Chow's models vary in the way they use the equivalence principles. Lemaitre model uses strain equivalence principle and Chow's model uses energy equivalence principle. The selection of a suitable constitutive model now depends on which one of these models can predict the results accurately. Moreover it directly affects accuracy of the selected material behaviour which would in turn affect results in the implementation methods and further improvement upon it.

Chow and Wang (1987) after careful evaluation found that Lemaitre's proposed hypothesis (1978) with strain equivalence principle for isotropic damage by replacing the conventional stress with the virgin material stress in the constitutive equation unfortunately lead to asymmetry of stiffness matrix when anisotropic damage is considered. To overcome this inconsistency Chow and Wang used the energy equivalence concept. The Chow and Wang energy based model is widely used for research and analysis (Chow and Lu, 1992; Chow and Yu, 1997; Chow and Yang, 2003).

Based on his previous strain equivalence for isotropic damage theory Lemaitre extended it to anisotropy. He also argues that the energy equivalence based method followed by Chow and Wang (1987) and Ju (1989) yields existence of the elastic potential but the physical definition of the damage variable is lost. He also elaborates further that the damage is no longer directly related to the surface density of defects but is a mathematical variable defined by its coupling with elasticity. Then, no more rules exists to describe the coupling with plasticity or the conditions of partial closure of microcracks (Ladeveze, 1983; Ladeveze and Lemaitre, 1984; Chaboche, 1993) nor to define the critical value of the damage at mescocrack initiation. He also reveals that micromechanics used by Kachanov (1993) is also restricted to brittle failure and does not yield a closed form constitutive equation. But Lemaitre's (2000) new theory does not solve the problem completely. Lemaitre's comparison between his proposed theory and experiments show significant discrepancies (Lemaitre, 2000) and he states that due to experimental discrepancy it is not possible to conclude that the proposed theory exactly fits the experimental results. The evaluation by the Lemaitre (2000) that his proposed model needs further modification to obtain agreeable results makes this theory not suitable for this research work. But this theory could be suitably researched once agreeable results are obtained or published.

The Chow and Wang damage model used in computer simulations using LS-DYNA3D code was recently completed and deliver agreeable results for sheet metals (Chow, Tai and Chu, 2003). This model is also widely used for comparative study of continuum damage models for crack propagation and measuring the formability of ductile metals (Chow and Lu, 1992; Chow and Yu, 1997; Chow and Yang, 2003). In the context of this research project which predominately investigates on developing damage model in Abaqus/Explicit code for prediction of damage in the aerospace structures, in quasi-static regime as required by MUSCA partners, the Chow and Wang damage model was selected for immediate further research.

6 Material characterisation

6.1 Introduction

The damage growth model requires material parameters derived from experiments. The influence of damage on the elastic modulus, offers a convenient technique for the experimental measurement of damage growth (Lemaitre and Desmorat, 2005; Chow and Wang, 1987). This technique uses low cyclic test where the change in elastic modulus with permanent deformation can be measured. Damage measurement techniques using conventional instrumentation (Lemaitre and Desmorat, 2005; Chow and Wang, 1987) are time consuming and require either specific test specimens to be used (Lemaitre and Desmorat, 2005) or careful specimen preparation (Chow and Wang, 1987). This additional time, specific specimen preparation and measurement inaccuracies in the damage characterisation of a specific material limit the industrial application of the conventional test approach to damage modelling. For practical industrial application it is very important to obtain accurate material characterisation with less cumbersome process. This thesis introduces the procedures on how Digital Image Correlation (DIC) technique can be used to characterise damage parameters for industrial application. The procedures to use existing industrial DIC experimental set up along with standard test specimen are also investigated in this thesis. This chapter briefly explains the quasi-static material testing, drawback of damage characterisation using conventional methods, new DIC experimental set up, procedure for preparation of specimen, test procedures and how to calculate damage parameters from the DIC test data.

6.2 Dynamic aspects of material testing

The deformations of materials differ based on the strain rate of the material hence the mechanism of deformation also changes. Figure 6-1 shows the overall picture of the dynamic aspects of material behaviour at increasing strain rates. The experiments conducted should also follow the necessary strain rate regime at which the material characterisation needs to be established. The strain rate regime is chosen based on the material's application and life cycle.

Creep is observed when material deforms at isothermal state and when the material is loaded at elevated temperatures. Creep law is used to establish the material behaviour

in this region; typical creep strain rate is up to 10^{-5} s^{-1}. The next region is quasi-static and the strain rates are of the range of 10^{-4} s^{-1} to 10^{-1} s^{-1}. In this region stress strain curves are obtained using constant strain rate, uniaxial tensile test and compression tests are done in this region to establish material characterisation. After this region the intermediate strain rate is observed, it ranges between 10^{-1} s^{-1} to 10^{2} s^{-1}. In this region strain rate effect should be considered during the material characterisation. However in some cases the strain rate effect might be small. Next to intermediate region the strain rate is known as high strain rate and it is typically beyond 10^{3} s^{-1} to 10^{4} s^{-1}. In this region inertia forces, thermal and wave propagation through the material is considered. Beyond intermediate range is called higher strain rate. Higher strain rates are observed typically beyond 10^{5} s^{-1}. Shock wave loading, thermal effects and transition states are also considered at this state.

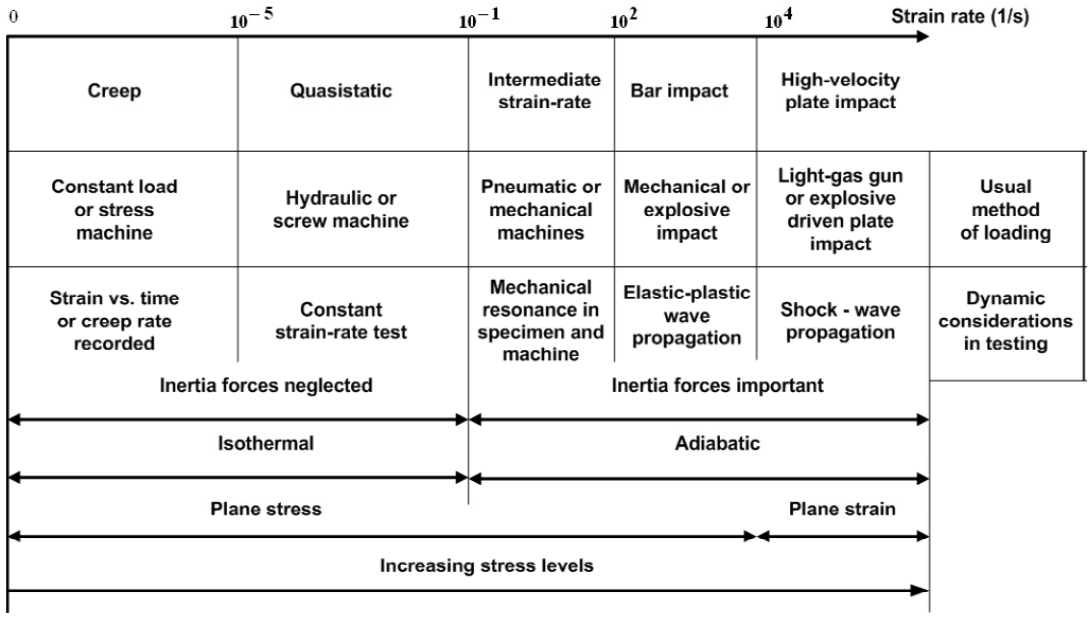

Figure 6-1 Dynamic aspects of mechanical testing, Zukas (1982)

It is an established fact from the past research works and experiments conducted in this area that material deformation mechanism significantly changes with the strain rate. The change in material deformation mechanism based on the strain rate introduces several challenges to interpret the response of material behaviour for the entire range of strain rates. Development of a general constitutive law should cover the entire range of material behaviour at various strain rates. However most of the constitutive equations only cover certain range of strain rates. It will be a great

accomplishment to establish a single general constitutive law governing the material behaviour at different strain rates. However the material deformation mechanism is not unique for entire strain rate range. The different physical behaviour of material under different strain rates makes it difficult to establish a single general constitutive law.

6.3 Quasi-static range and experiments

The main focus in this research work is based on quasi-static range. Chow and Wang ductile damage model is not a rate dependent model and it has been used for numerical model development and simulations in this research work. The stress-strain relationships are obtained based on the constant strain rate. The material parameters obtained in this category are used as inherent property of the materials, but they are valid only in this range of strain rate; higher strain rate should use the higher level strain rate test to obtain material parameters.

Typical constant strain rate tests are uniaxial tension and compression tests. In these experiments the uniaxial simple tensile test or standard tensile test and cyclic tests are carried out. The experimental results are used to validate the numerical model developed based on Chow and Wang's ductile damage model.

To characterise the material parameters for the virtual test, series of physical experiments have been performed. The widely used aerospace Aluminium alloy AA2024 and AA7010 materials tested in this research. Uniaxial tensile tests were performed on the cut specimen of the Aluminium alloy in three different material directions 0^0 (rolling direction or longitudinal direction), 90^0 (transverse direction or long transverse direction) and 45^0 to rolling direction. The material data collected from the experimental tests are used to validate the virtual test model.

The results obtained from quasi-static experiments from this research work augment Panov (2006) tensile tests for same material (AA7010 and AA2024) at Cranfield University. In his experiments the strain rate range was of 6 per second subjecting the specimen to temperature between -50^0 C to $+200^0$ C. He also conducted Taylor cylinder impact test for high strain rate. The combined results form a complete ductile metal characterisation data for material AA7010 and AA2024. These

combined experimental results data can be used for simulating aerospace material when subject to different strain rates in that regime.

6.4 Lemaitre and Chow & Wang damage measurement methods

Lemaitre (2005) and Chow and Wang (1987) identified that the damage can be obtained from elastic modulus degradation.

Lemaitre's procedure for depicting the damage was to produce a varying cross section model as show in Figure 6-2. The varying cross section of specimen allows the maximum deformation to concentrate at the centre of the specimen. Here the assumption is made that the material failure will occur at the centre of the specimen. This allowed the strain gauges to be mounted at the maximum strain point. The measurements were obtained during a uniaxial cyclic test. However this method requires special preparation of specimen. The strain measurement for damage parameter measurements requires strain gauges with range from a very small percentage to 40% and more. This requires frequent change of strain gauges due to limitations of strain gauge operating ranges and failure of foil type strain gauges. These frequent stops during the cyclic test to change strain gauges reduce the precision of strain measurement and disturb the continuous cyclic test requirement for obtaining good damage parameters. These imprecise methods reduced the accuracy of calculation of damage parameters.

Chow and Wang used micrometer to measure the strain. Chow and Wang used standard tensile test specimen for testing. Chow and Wang prepared the specimen by engraving thin straight lines on the major area of deformation and failure (Figure 6-2). Then Chow and Wang used micrometer to measure the displacement between the lines from the previous position to new position at various intervals during the cyclic test to calculate the strain. But this method required the knowledge of failure location prior to the start of experiment. This method also required frequent stops to obtain the measurement using micrometer as well as disruption of the experimental set up during the measurement. Similar to Lemaitre's method this method also inherits the inaccuracies due to frequent stops of the continuous cyclic testing procedure.

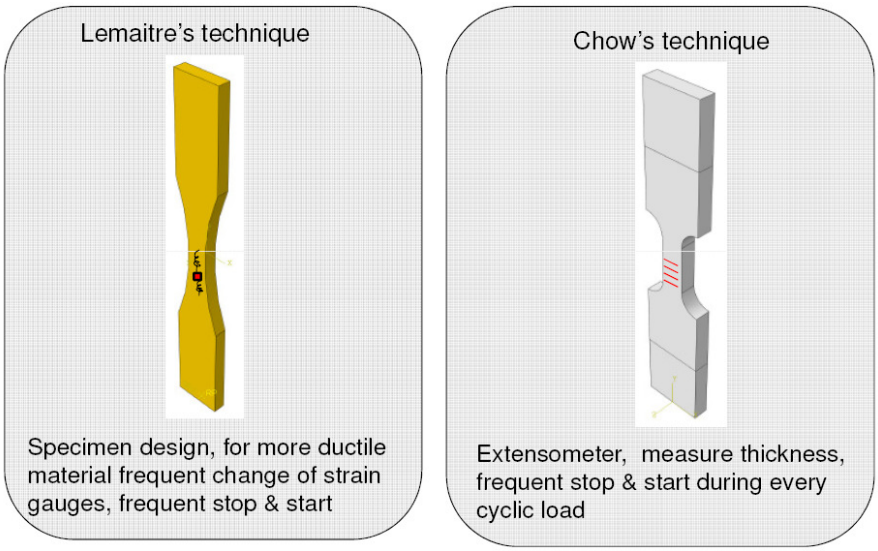

Figure 6-2 Coupons cyclic testing - Lemaitre and Chow techniques for characterisation of damage from experiments

6.5 Overview of Digital Image Correlation (DIC)

The conventional extensometer and resistance foil strain gauges measurement method experimental set up and techniques are time consuming and cumbersome. Moreover it cannot capture the full field area of interest. This additional difficulty in the characterisation of a specific material limits the industrial application of conventional approach to determine damage parameters. The objective of the work presented here is to demonstrate that a modern measurement technique using non-contact digital image correlation for ductile damage material characterisation.

A relatively new strain measurement technique that is now increasingly used within industry is digital image correlation (DIC) (Dantec Dynamics, 2006). This is a non-contact optical technique that uses one or more cameras to take a series of images during the test. These images can then be post-processed to give full field deformation information allowing the strain field to be calculated. This method requires a stochastic pattern to be applied onto the surface of the test object. The advantages of DIC for damage characterisation are that it is now increasingly used in industry as a strain measurement technique within the material characterisation process, and so the necessary specimen preparation is already done. It does not require the use of special test specimens where the location of the minimum cross-section and maximum deformation should be identified prior to test. The maximum

deformation location can be identified in DIC technique during the image processing. Hence standard specimens can be used. Therefore determination of damage parameters can be incorporated within the existing material characterisation test campaign without the requirement for special techniques or specimens.

6.5.1 3D digital image correlation basics

The digitised light intensity values are captured and stored in a CCD (Charged Coupled Device) camera as grey scale values ranging from 0 to 255 depending on the intensity of light reflected off the object. To observe good image quality a random grey pattern of high contrast speckle is applied on the surface area of the object of interest.

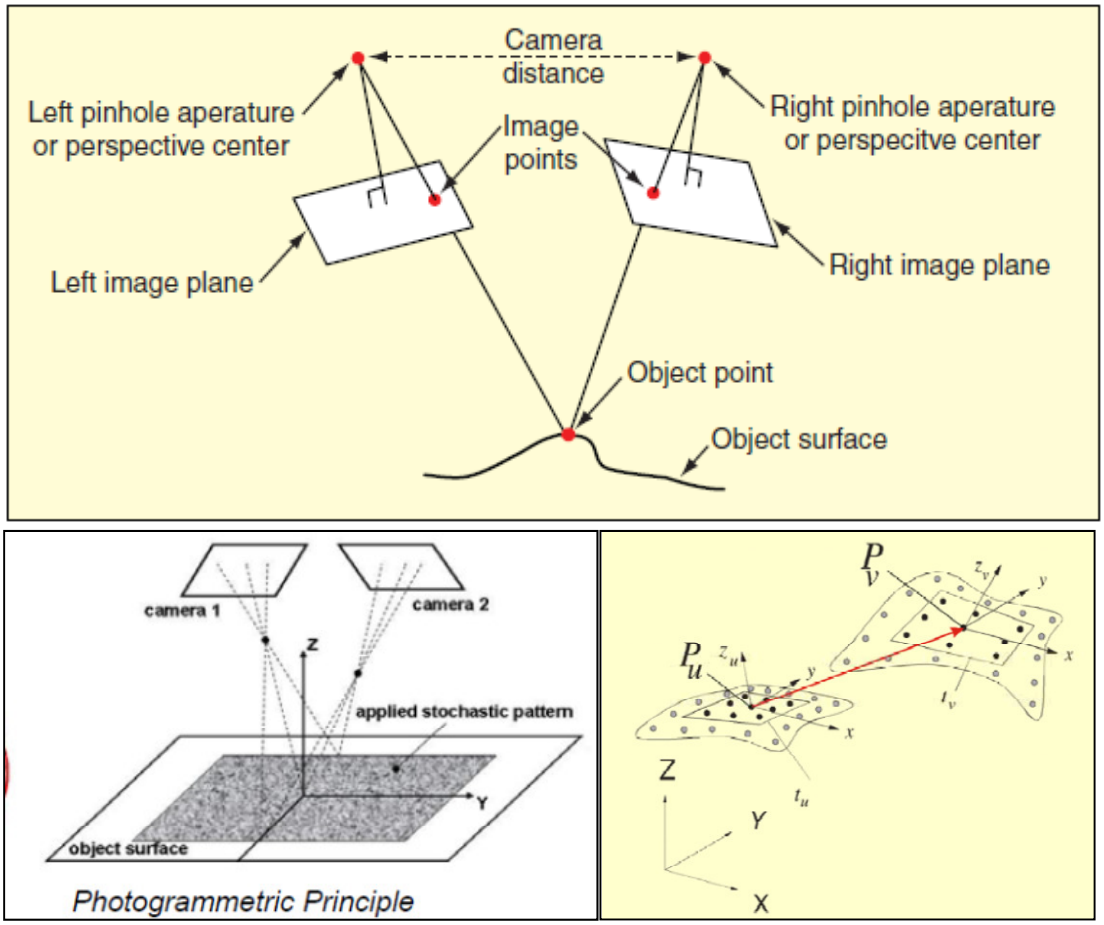

Figure 6-3 Photogrammetric principle and determination of three dimensional displacement vector (Avitablile, 2010; Dantec, 2006)

The images obtained by a pair of camera are divided into overlapping facets with unique finger print of the greyscale light intensity values. The reference facets are

compared with the overlapping facets and the displacement vector for each facet is calculated. A correlation algorithm to tack the grey value patterns in small local neighbourhoods is used by Dantec (2006) to correlate identical points from both cameras.

In Figure 6.3 the displacement vector of a surface element is shown. The centre point P_u has been displaced form the reference state to deformation state P_v. With the known displacement vectors of each surface point and reference contour, the strains can be calculated by the analysis of the distortion of each local facet.

The DIC works on the basis of relating images obtained successively. As deformation takes place the relative position of the points are captured by a camera or set of cameras. Use of one camera allows the determination of object deformation in a plane parallel to the image plane of the camera (Avitablile, 2010). Using the two cameras relative to each other allows capture of specific pixel in that camera's image plane. Two cameras are required to capture 3-D position of any point on the object surface from different directions. If the position of each camera, magnification of the lenses and all image parameters are known; the absolute 3D coordinates of any surface point in the space can be calculated (Dantec, 2006). If this calculation is done for every point of the object surface, then 3D surface contour of the object can be determined. Once the 3D contour of surface is determined, the correlation of the images taken by both cameras with the reference surface images allows three dimensional deformations to be calculated.

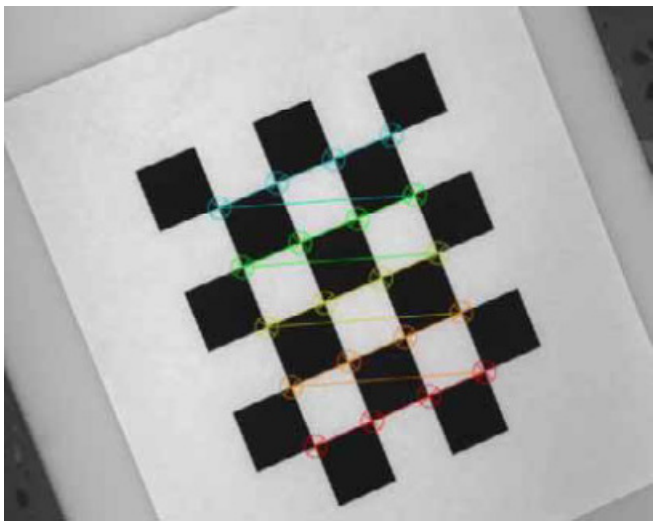

Figure 6-4 Calibration plate with determined nodal points (Dantec, 2006)

6.5.2 Calibration of cameras

To calibrate the cameras the intrinsic parameters such as focal length of the lenses, principle point of the lenses, radial distortions of the lenses, tangential distortion of the lenses and extrinsic parameters such as translation vector and rotation matrix (Dantec, 2006) should be determined. Once the camera is calibrated using the ISTRA-4D software the whole system can be integrate for useful measurement.

A calibration plate (Figure 6-4) provided by Dantec is manually moved in front of the camera at different angles and position from the specimen location. The ISTRA-4D software registers the nodal points of the test blade and automatically captures different images. The captured images are calibrated against the pre-set calibration plate dimensions and the parameters are used for determining the intrinsic values. The main parameters such as focal length and principal point are displayed on the monitor for control by user. For calibrating the extrinsic parameters the test plate is positioned in front of both cameras and the image is captured. The ISTRA-4D software then calculated the extrinsic parameters. Upon completion of the calibration the system is ready to measure the displacement data.

6.5.3 DIC displacement and strain measurement example

An example from the actual DIC technique is shown in Figure 6-5. A grey scale pattern is applied on the surface. The cameras capture images of the test specimen and produce a 3D contour of the surface. The screen shots are then evaluated by the software and the surface map of the test specimen is produced. One such grey scale facet pixels set focused by the camera is highlighted on Figure 6-5. The highlighted box shows the change in relative distance of the speckle pattern from step=0 at reference state (t=0), to intermittent step=50 ($t=t+dt_{50}$) and just before failure step=112 ($t=t+dt_{112}$). The literature provided by the Dantec Dynamics (2006) describes the measuring principle. A stochastic pattern is applied onto the surface of the test object. The surface is observed with two cameras. In each image pair homologous points of the patterns are identified using a specific pattern matching algorithm. The three-dimensional position of each object point is determined by triangulation performed by the Dantec Dynamics software. If image sequences are

recorded during the displacement of the object, the deformation of each object point is calculated automatically. From displacement the strain can be calculated.

Once the deformation starts the grey scale pattern of the reference image is compared with the successive images. The correlation process then determines the shift and/or rotation and distortion of the little facet elements in the reference surface. The displacement vector calculated by comparing the current image to reference image is then used to calculate the strain values. The Figure 6-5 shows the displacement and strain with respect to time for reference image when t=0 to a mid level displacement and strain at step 50 and just before failure data at step 112.

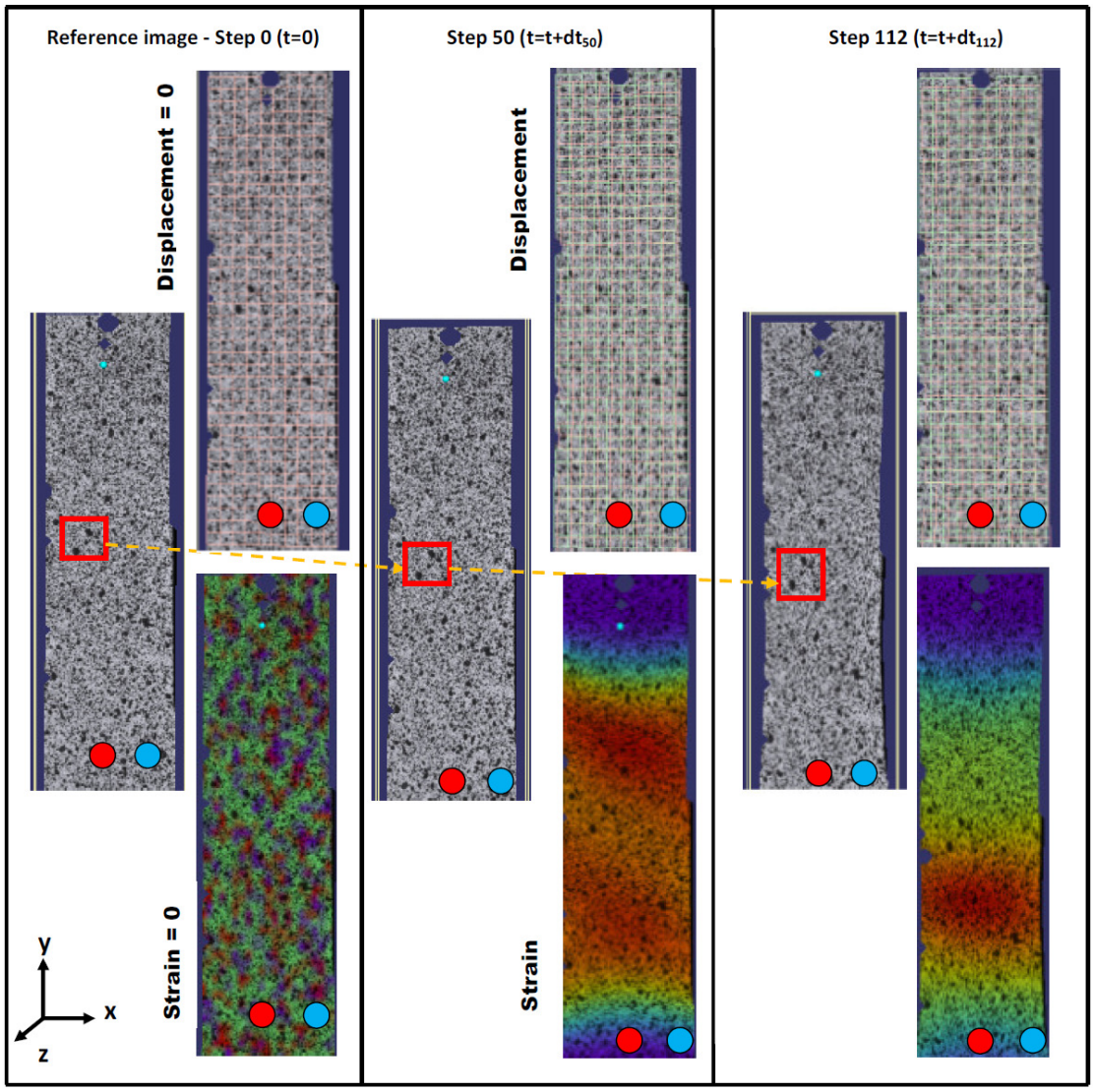

Figure 6-5 DIC displacement and strain example Cranfield University tensile test of Aluminium AA-2024-T3

To obtain meaningful data from the DIC a co-ordinate system must be defined. The Figure 6-5 shows the co-ordinate system defined by two sets of pins; the pin at the left defines the origin and pin at the right defines the local x-axis with respect to the origin. The local xy plane is defined by the tangential plane of the origin. The measured value from the DIC is then used for material characterisation. The displacement and strain data can be obtained by measuring over the surface area of interest (Figure 6-6). Alternatively the extensometer type displacement can be obtained by using two reference points on the surface area (Figure 6-6). From the displacement, force and original cross-sectional area of the specimen, the strain and stress can be calculated using equation 6.1 to 6.7. For detailed theoretical information on the measurement technique please refer to Dantec (2006) technical information and ISTRA-4D software instruction guide.

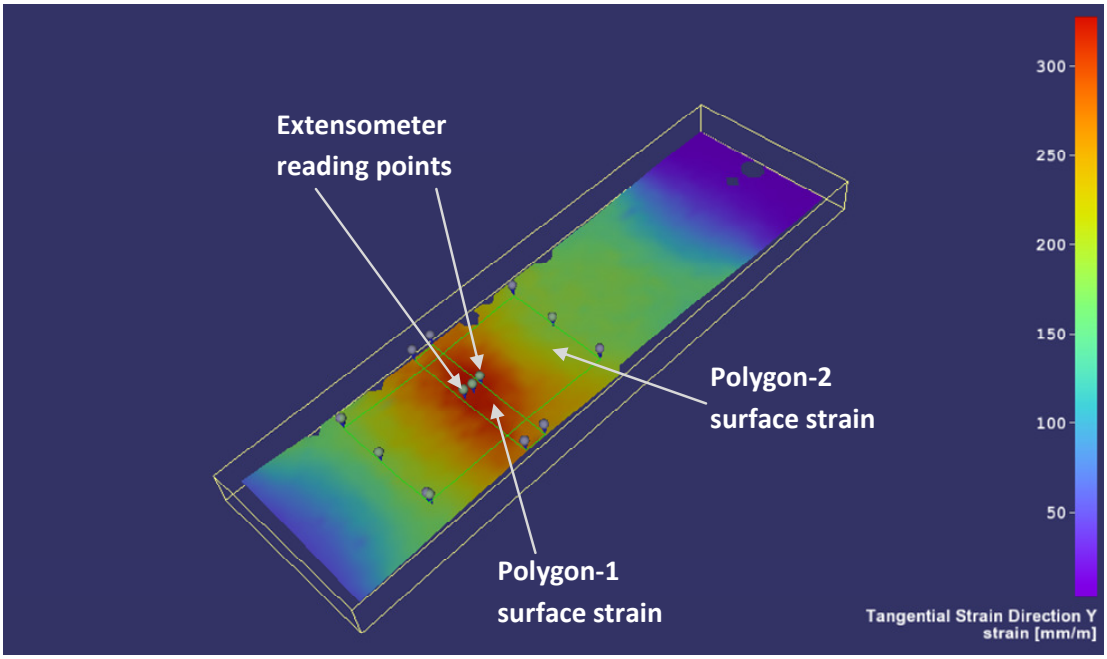

Figure 6-6 DIC strain measurement example Cranfield University tensile test of Aluminium AA-2024-T3

6.5.4 Use of digital image correlation and limitations

The digital image correlation is widely used in the industry for measurement of surface deformation. However there are limitations of its use. This section describes a brief overview of sources of errors, uncertainties in the measuring techniques and accuracy levels of DIC. The pattern required for camera to observe the specimen are

applied using paint. The area of interest on the specimen is thoroughly cleaned and prepared by spraying chemically inactive matt spray paint. The matt finish with white colour is first applied and then speckles of black patterns are applied after the white paint has dried. A sample specimen is shown in the Figure 6-10. The pattern formed by the paint before deformation is used as reference pattern and the deformation are measured based on the movement of patterns on the surface from the initial reference position during loading. The cameras used for observation are calibrated and the patterns checked for quality by the inbuilt ISTRA-4D software. The system provides a smart calibration tool with an online feedback of calibration quality. The inbuilt algorithm is capable of estimating the uncertainties of the resulting calibration parameters. The estimated error from the quality check should less than 0.001 of a millimetre.

However the observation made by the camera is influenced by the errors and it alters the quantities like contours, displacement and thus strain. The error sources of DIC are intrinsic noise of the acquired images, statistical and errors introduced by the system calibration, subpixel effects resulting from the limited camera resolution and intrinsic uncertainties of correlation algorithm (Schreier, Braasch and Sutton, 2006). The errors introduced during the erroneous system calibration cannot be reduced by the post-processing. Thus once systematic errors are made they hard limit the system resolution and increase the error. The errors are classified into two categories according to their impact on the evaluation process.

- Correlation errors – describe uncertainties for the correlation of corresponding facet positions in different image frames. Correlation errors are divided into statistical error and systematical error. Statistical error occurs because of the limited number of pixels and corresponding grey values in each facet. Other potential error sources are statistical noise of the grey values, different illumination conditions for the two cameras, image contrast and size of the speckle pattern on the specimen surface. Systematical errors are introduced by subpixel effects. Correlation errors influence the accuracy of image correlation.

- 3D reconstruction errors – which have a direct impact on reconstruction of the 3D co-ordinates of the correlated image facets. Uncertainties of the calibration parameters lead to errors when reconstruction of 3D coordinates from correlated facets of the two cameras.

The error estimations of 3D digital image correlation measurement are presented by Dantec for Q-400 instrument in their paper by Schreier, Braasch and Sutton (2006). Displacement errors are in the order of less than 0.02 pixel, strain errors are limited to 0.05 m strain when using a lens with 50 mm focal length.

The digital image correlation used by Dantec Dynamics can determine the maximum of the displacement with an accuracy of up to 1/100 pixel (Dantec Dynamics, 2006). Once calibration is completed the accuracy levels of each specimen pattern is given by the algorithm automatically. The acceptability of the speckle pattern is one where sufficient data points can be identified to define a displacement. During this process high contrast speckle should not exceed the resolution of the imaging cameras. The Q-400 camera displacement accuracy is stated as 2% of a pixel (Dantech Dynamics, 2006). There were occasions in this experimental research work where the specimens with unacceptable speckle patterns were identified using ISTRA-4D software during post processing of data and the specimens were omitted during the test. In this research work the ISTRA-4D software was used to identify good speckle pattern of the short listed specimen for the experimental work. The short listed specimen speckle patterns were within the specified error range by Dantech Dynamics (2006).

6.6 Experimental work

6.6.1 Tensile test

The tensile test experiments are performed on AA-2024-T3 and AA-7010-7651 aluminium alloys at quasi-static strain rate. The aim of the test is to determine the Chow's damage material constants. These material constants are measured with respect to the input parameter required in Abaqus general orthotropic material model. Hill proposed (1948) orthotropic material constants measurement through series of uniaxial tensile tests. The tensile tests are performed in two principal axes of the

material grain orientation and one test at 45^0 to principal axes to determine the material constants.

Standard tensile test are performed on tensile testing machine by holding one end of the specimen stationary on the actuator grip and moving the other end at constant speed until the specimen is fractured. The cyclic test is also performed in similar fashion but for every 2% to 5% of the strain the specimen is unloaded almost to zero load and reloaded to next 2% to 5% of the strain. This process is continued until the specimen is fractured. The values obtained using initial specimen geometry are known as engineering variables. The measurements are obtained by digital image correlation process using Dantec digital 3D correlation system Q400. The obtained images are processed to calculate the true strain of the material using an algorithm provided with the image correlation system software.

Engineering stress

$$S_E = \frac{F}{A_0} \qquad \text{(Eq. 6.1)}$$

Where S_E is the engineering stress, F is the force and A_0 is the initial cross sectional area of the specimen

Engineering strain

$$e_E = \frac{\Delta L}{L_0} = \frac{L\text{-}L_0}{L_0} \qquad \text{(Eq. 6.2)}$$

Where e_E is the engineering stress, ΔL is the difference in lengths, L_0 is the initial length between two measurable points on the specimen and L is the new length between two measurable points on the specimen after deformation

The total true strain

$$\varepsilon = = \int_{L_0}^{L} \frac{\Delta L}{L} = \int_{L_0}^{L} \frac{L-L_0}{L} = ln\left[\frac{L}{L_0}\right] \qquad \text{(Eq. 6.3)}$$

Similarly the true stress of the material is the ratio between the force and current cross-sectional area of the specimen after deformation

$$\sigma = \frac{F}{A} \qquad \text{(Eq. 6.4)}$$

A is the current cross sectional area of the specimen after deformation

Using the assumption that during plastic deformation there is no net change in volume, the true strain and true stress variables can be easily measured from the experiments.

The true strain in terms of engineering strain

$$\varepsilon = ln\,[1 + e_E] \quad \text{(Eq. 6.5)}$$

The true stress in terms of engineering stress and true strain

$$\sigma = S_E exp^{\varepsilon} \quad \text{(Eq. 6.6)}$$

Or the true stress in terms of engineering strain

$$\sigma = S_E[1 + e_E] \quad \text{(Eq. 6.7)}$$

6.7 Chow and Wang damage model material constants

The uniaxial tensile test at controlled environment allows the measurement of Young's modulus, the Poisson's ratios and shear modulus. Please note there is a change in notation of Chow and Wang (1987) original damage model parameter $B(\beta)$ (damage evolution threshold) – equation (5.27) in order to aid clarity this symbol has been replaced with $B(\beta) = \frac{dB}{d\beta}\beta$ where $\frac{dB}{d\beta}$ is the slope of virgin material true stress versus overall damage β.

Further to the above measurements, the Chow's ductile material model constants μ (damage potential matrix constant), $\frac{dB}{d\beta}\beta$ (damage evolution threshold), B_o (damage evolution initiation stress) and D_{cr} effective critical damage constants should be calculated. Accurate determination of these constants allows the implementation of damage model in Abaqus explicit simulation using user VUMAT code. The material parameters or material constants are shown in the **Table 6-1**. Hill's orthotropic coefficients F, G, H, L, M and N in terms of Abaqus internal material constants R_{11}, R_{22}, R_{33}, R_{44}, R_{55}, R_{66} were calculated using Panov's experimental test results on the same materials during 2005. In continuum damage mechanics it is assumed that materials deteriorate at different stages of loading due to formation and realignment of dislocations, micro-cracks, voids and other types of material defects and impurities. The common assumption is that the damage variable D represents the reduction in effective element surface area S to $\tilde{S}$ due to the presence of voids within the material (Lemaitre, Desmorat, 2005). From this assumption effective Cauchy stress tensor $\tilde{\sigma}$ related to the effective resisting area $\tilde{S}$ is written in the form

$$\tilde{\sigma} = \sigma\frac{S}{\tilde{s}} = \frac{\sigma}{1-D} \quad \text{(Eq. 6.8)}$$

The concept of elastic energy equivalence can then be used to derive the constitutive equations of elasticity (Chow and Wang, 1987) as:

$$\sigma = \tilde{E}\varepsilon \quad \text{(Eq. 6.9)}$$

$$\tilde{E} = E(1-D)^2 \quad \text{(Eq. 6.10)}$$

$$D = 1 - \sqrt{\frac{\tilde{E}}{E}} \quad \text{(Eq. 6.11)}$$

In an elastic-plastic material the damage also influences the plastic constitutive equations (Lemaitre & Desmorat, 2005 Chow and Wang, 1987). Here E is the Young's modulus of virgin material, Ẽ is the Young's modulus of the damaged material (which is the new slope during reloading in cyclic test as shown in Figure 6-20), D is the damage variable.

Many different damage evolution laws have been proposed in literature. Within this paper we consider the linear evolution model proposed by Chow and Wang (1987) where damage evolution is depicted by introducing an effective damage stress similar to the effective plastic stress.

$$f_d = \tilde{\sigma}_d - \left(B_0 + \frac{dB}{d\beta}\beta\right) = 0 \quad \text{(Eq. 6.12)}$$

Here $\tilde{\sigma}_d$ is the equivalent effective damage stress, B_0 is the initial damage threshold, $\boldsymbol{\beta}$ is the equivalent damage and $\boldsymbol{dB/d\beta}$ is the slope of damage threshold curve. The parameters B_0 (the damage initiation stress) and B (The virgin material stress during evolution of damage) are material properties that must be derived from experiment.

$$\frac{dB}{d\beta}\beta = \tilde{\sigma}_d - B_0 \quad \text{(Eq. 6.13)}$$

The damage can be calculated from the current value of the elastic modulus using equation 6-11. The equivalent damage, β, under uniaxial case is defined as

$$\beta = D\left(1 - \frac{D}{2}\right). \quad \text{(Eq. 6.14)}$$

Chow damage potential constant μ can be calculated from following relationship

$$\mu = \frac{D_2\left[1 - \frac{D_2}{2}\right]}{D_1\left[1 - \frac{D_1}{2}\right]} \quad \text{(Eq. 6.15)}$$

μ is used in the damage characteristic tensor $\boldsymbol{J}$ which describes the anisotropic nature of the damage growth.

The current damage threshold stress is then the effective Cauchy stress that can be calculated from the measured stress using equation (6.8). A plot of the measured values of B and β allows the material parameters B_0 and B to be obtained from a linear fit (Figure 6-23 and Figure 6-31). These figures also show that the assumption of a linear of B vs β relationship is appropriate for this material.

Table 6-1 Material parameter characterised

Parameter	Description
E_1	Young's modulus – longitudinal or direction-1 or (0^0)
E_2	Young's modulus – transverse or direction-2 or (90^0)
E_3	Young's modulus – through thickness or direction-3
v_{21}	Poisson ratio between 2-1 direction
v_{31}	Poisson ratio between 3-1 direction
v_{32}	Poisson ratio between 3-2 direction
G_{12}	Shear modulus between 1-2 direction
G_{23}	Shear modulus between 2-3 direction
G_{31}	Shear modulus between 3-1 direction
F, G, H, L, M, N	Hill's orthotropic coefficients - in terms of Abaqus internal material constants (orthotropic potentials) **R_{11}, R_{22}, R_{33}, R_{44}, R_{55}, R_{66}** (Characterised along with Panov (2005) experiments on same material)
μ	Chow's damage potential constant
$\frac{dB}{d\beta}$	Chow's damage threshold constant
B_0	Chow's damage initiation stress
D_{cr}	Chow's effective critical damage value

6.7.1 Test specimen geometry

In general "flat" or "dog bone" or "standard" test specimen are used for tensile testing (Davis and Troxell, 1982; John, 1992). The standard tensile test specimens are uniform in cross-section. The ratios of the specimen geometry are taken from the standards (Davis and Troxell, 1982; John, 1992). Apart from the dog bone specimen

alternative specimen with varying cross section were specially made based on Alves and Jones (2000) suggested in their paper. These varying cross-section specimens were manufactured because the maximum plastic deformation is concentrated on the centre of the specimen due to its shape. The varying specimen results are compared with the standard tensile specimen results. To determine the specimen geometry, maximum strain location, displacement boundary condition and to determine tensile testing machine cross velocity, similar simulation to experimental tests were performed with Abaqus standard model..

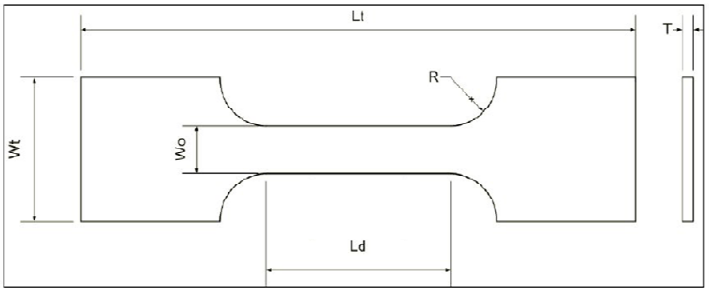

Description	AA-2024-T3	AA-7010-T7651
Total length, L_t	170 mm	170 mm
Total width, W_t	25 mm	25 mm
Thickness, T	2.5 mm	6.35 mm
Deforming Length, L_d	20 mm	20 mm
Test width, W_o	10 mm	10 mm
Radius, R	8 mm	8 mm

Figure 6-7 Uniform cross section (UCS) specimen dimension details

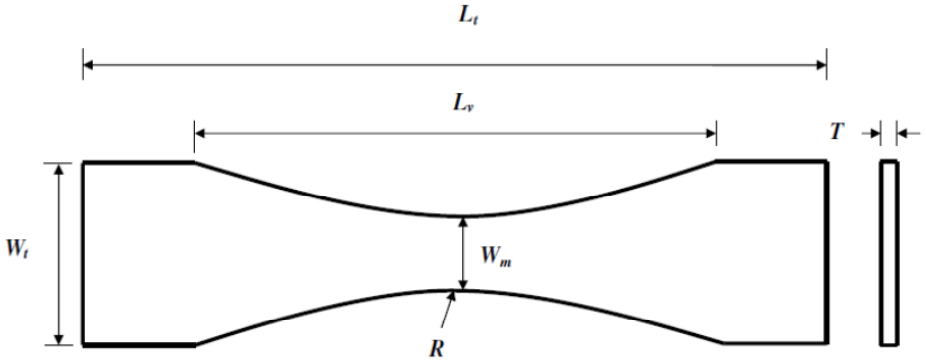

Description	AA-2024-T3	AA-7010-T7651
Total length, L_t	170 mm	170 mm
Total width, W_t	25 mm	25 mm
Thickness, T	2.5 mm	6.35 mm
Minimum width, W_m	10 mm	10 mm
Varying cross section Length, L_v	77 mm	77 mm
Radius, R	105 mm	105 mm

Figure 6-8 Varying cross section (VCS) specimen dimension details

Researchers Lemaitre (2000) and Alves & Jones (2000) used varying cross section specimen along with strain gauges to measure the strain as the location of maximum plastic deformation is well defined. However it is time consuming as the gauges are small and needs to be replaced quite often during the experiment. One of the research objectives is to identify whether standard dog bone test specimen can be used as an alternate to varying cross section in damage material characterisation with a non contact type DIC measuring technique. The use of standard dog bone type specimen will reduce the cost and complication of manufacturing special varying cross section specimen to characterise damage in the industrial experimental facilities.

Dog bone or uniform cross section (UCS) test specimens are produced based on Panov (2006) specimen geometry. Panov modified standard ISO specimens to obtain intermediate strain rate condition using standard servo hydraulic fatigue machine at Cranfield University. The diagram of the specimen and the measurements are shown in Figure 6-7. The total length is based on the requirement to hold the specimen in servo hydraulic machine grips. The deformation length is based on the cross section of the specimen. Similar to UCS specimen the varying cross (VCS) section specimens were also produced to for this research work. The specimen dimensions are shown in Figure 6-8.

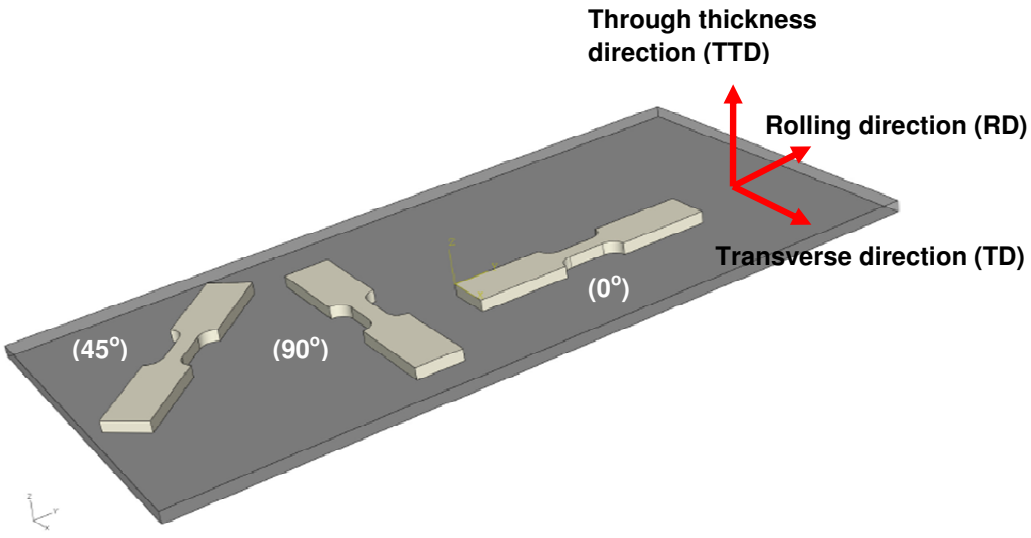

Figure 6-9 Uniform cross section (UCS – shown in picture) and Varying cross section (VCS) specimen cut at angles of 0°, 90° and 45°

The specimens were cut from the blank of hot rolled material in 0^o, 90^o and 45^o with respect to the rolling direct as show in Figure 6-9. The specimens were cut in uniform cross section shapes and varying cross section shapes. The cut and prepared specimens are coded with three characters during testing procedures. It allows identifying the samples from each test and material characterisation at later stages. Examples with the starting coupon test serial numbers are "**2-0-1", "7-0-1", "2-90-1", "7-90-1", "2-45-1", "7-45-1"**. The coupon tests which were not able to produce better results using the DIC method post-processing were omitted from the material characterisation process.

First character	**Second character**	**Third character**
Alloy material first character number **"2"** for 2024 series **"7"** for 7010 series	**"0"** for 0^o wrt rolling direction **"90"** for 90^o wrt rolling direction **"45"** for 45^o wrt rolling direction	Specimen test coupon number, starting with **"1, 2, 3,…"**

The samples were coded with specific numbers before the start of experiments. In certain cases if the sample did not produce accurate results and those samples were omitted and additional samples were tested by giving a fourth character for continuity, e.g. 7-0-2-2.

6.7.2 Preparation of test specimen

The aerospace aluminium alloy materials were supplied by commercial supplier. They are supplied as hot rolled plates. Their dimensions and chemical composition are;

2024-T3 (2.5 mm thick) – 2642 mm (Length) x 1270 mm (Wide)

7010-T7651 (6.35 mm thick) – 1475 mm (Length) x 1200 mm (Wide)

These materials were selected specifically from the same manufacturer as Panov's supplier during 2005 to determine the material parameters at quasi-static strain rate. The specimens are cut to the required shape at Cranfield University facility from rolled sheet without altering the mechanical properties. The specimens were prepared without any damage material, the finished surface of the specimen is at least 3 mm sheared line and 6 mm away from the flame cut faces. The final specimens were machine finished without altering the mechanical and thermal properties of the material.

Table 6-2 Composition of chemical elements in the aluminium alloy

Other chemical elements	Aluminium alloy AA2024-T3 (2.5 mm thick) in %	Aluminium alloy AA7010-T7651 (6.35 mm thick) in %
Si	0.09%	0.04%
Fe	0.19%	0.08%
Cu	4.71%	1.66%
Mn	0.57%	0.01%
Mg	1.38%	2.26%
Cr	0.01%	0.78%
Ni	-	0.81%
Zn	0.06	6.08%
Zr	-	0.11%
Ti	0.02	0.03%
V	0.02%	-

The machine finished specimens are then sprayed with white paint with speckle of black as shown in Figure 6-10. Specimens are painted with patterns as per procedure provided by the Dantec Dynamics, 2006. The paints selected were free from any erosion or chemical degradation of material when applied. These stochastic patterns form a reference for the specimen's initial pattern before any deformation occurs. The patterns are optically recorded and followed throughout the test and compared against reference image and previous deformation position and thus displacements are measured using an algorithm provided by Dantec Dynamics. In total 14 samples in each specimen (Table 6-3) were prepared in uniform cross-section and varying cross-section as shown in the Figure 6-10.

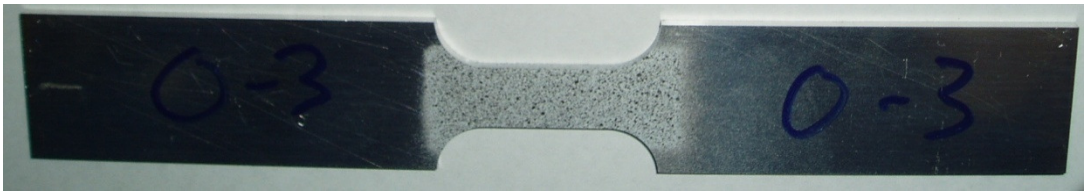

a) Specimen of uniform cross-section

b) Specimen of varying cross-section, so plastic deformation restricted to small zone

Figure 6-10 Prepared Aluminium specimen

Table 6-3 No of samples for uniaxial cyclic test and standard tensile test in each series

Uniaxial cyclic test

Direction with respect to rolling direction	AA2024 T3 series	UCS	VCS	AA7010 T7651 series	UCS	VCS
0^0	5 samples	2	3	4 samples	4	-
90^0	2 samples	-	2	3 samples	3	-
45^0	3 samples	-	3	-	-	-
Total	**10 samples**	**2**	**8**	**7 samples**	**7**	**-**

Uniaxial standard tensile test

Direction with respect to rolling direction	AA2024 T3 series	UCS	VCS	AA7010 T7651 series	UCS	VCS
0^0	3 samples	1	2	5 samples	2	3
90^0	1 sample	1	-	2 samples	1	1
45^0	-	-	-	-	-	-
Total	**4 samples**	**2**	**2**	**7 samples**	**3**	**4**

6.8 Experimental set up

The tensile tests were carried out using Instron 8032 Servo hydraulic machine along with the data logger to measure the displacement. Along with the tensile testing machine Dantec digital 3D correlation system Q400 was used to do the non-contact optical measurement of displacement and strain. The tensile tests were performed on specimen of two different materials AA2024-T3 with 2.5 mm thickness and AA7010-T7651 with 6.35 mm thickness. The Cranfield University experimental set up of machinery is shown in Figure 6-11. The cut specimen is prepared with spray paint to produce a stochastic pattern (as shown in our experimental test specimen in Figure 6-10 and then a pair of cameras was calibrated using calibration plate provided by Dantec. Cyclic tensile test were also performed to measure the change of elastic modulus with increasing strain.

The pair of cameras takes digital images at uniform intervals, these images are then processed using the Dantec software and actual material parameters are determined.

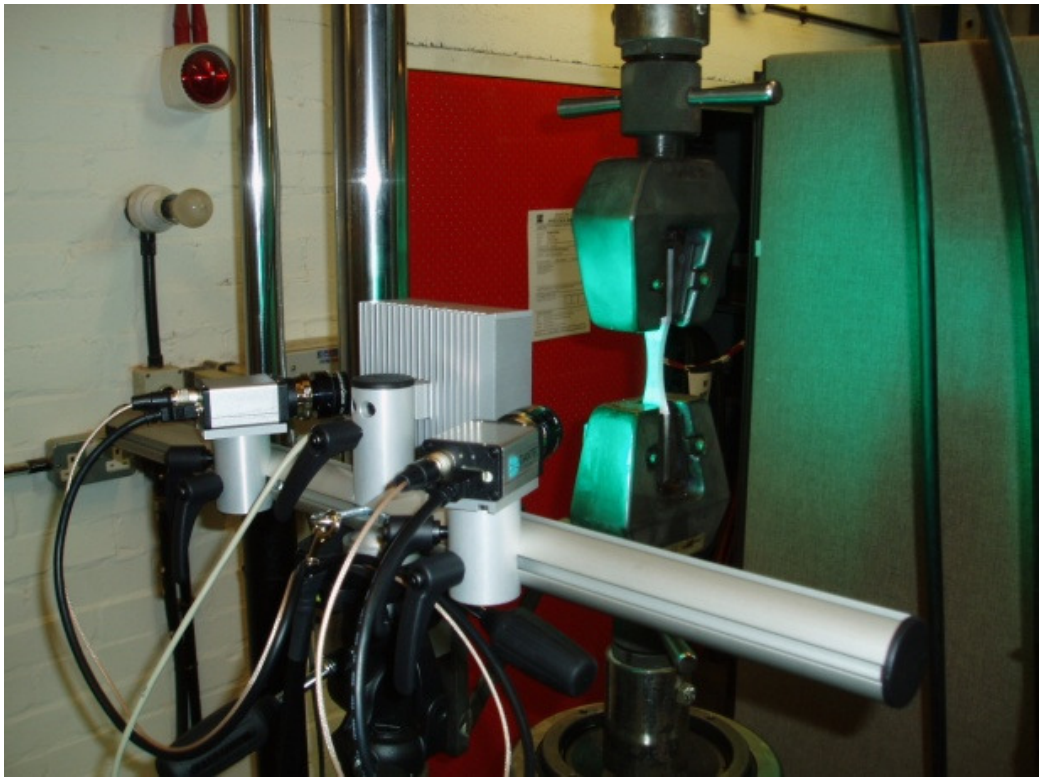

Figure 6-11 Instron 8032 Servo hydraulic test machine with tensile test specimen and optical measuring instrument - Dantec digital 3D correlation system Q400

The material parameters are obtained using Dantec Dynamics digital 3D correlation system Q-400 optical measuring instrument acquired in SOE during early 2008. The instrument works on the principle of digital image correlation.

The digital image correlation (DIC) method could be used to measure the strain without any contact and continuous imaging allows obtaining continuous data. Compare to extensometer and strain gauge techniques the DIC allows the data to be collected continuously after necking starts and until the specimen fails. It also allows us to use a standard specimen of uniform cross-section shown in Figure 6-10 compared to varying cross-section form which is expensive to produce. The DIC could also be used to characterise some of the material data in anisotropy and orthotropy using the present laboratory experimental facilities and sensible measurement could be obtained, which is not possible with conventional methods.

6.9 Test procedure and measurements

The specimen material characterisation overall procedure is explained in this section. The specimens were prepared and measurements were obtained based on Dantec Dynamics (2006) procedure. The summarised test procedure for preparation and measurement of strain is shown below; for detailed procedure please refer to Dantec Dynamics (2006) technical literature.

- Prepare the sample with the pattern as explained in chapter 6.7.2 and Dantec Dynamics (2006) detailed procedure. Example of prepared sample is shown in Figure 6-10 with white and black paint speckles.
- Prepare the tensile testing machine and fit the sample for initial adjustments and calibration.
- Set up Dantec digital 3D correlation system Q400 along with the tensile testing machine as shown in Figure 6-11
- The specimen deformation length should be focused well within the field view of pair of cameras.
- Calibrate the cameras using calibration plate as per Dantec procedure.
- Record the image sequence from the start continuously at small equal intervals to track the deformation points. The camera shutter can be opened manually at specified intervals to capture the image.

The Instron 8032 servo hydraulic test machine is calibrated with 0.5% for 100 kN load cell and the uncertainty is 0.5 KN. This uncertainty is too small and was not used in experimental measurement.

- Process the data using Dantec software ISTRA as per the technical procedure
    - Measure the average surface true strain at the area of interest (where it shows maximum strain at the centre of the specimen) by selecting the area of interest or measure the displacement of two reference point by placing two pins on the area of interest using ISTRA-4D software.
    - Measure the engineering stress from the Force and initial cross-sectional area of the specimen
    - From the measured true strain calculate the true stress based on equations (6.1) to(6.7)
    - Alternatively the average strain and displacement can be measured over the surface area of interest as well

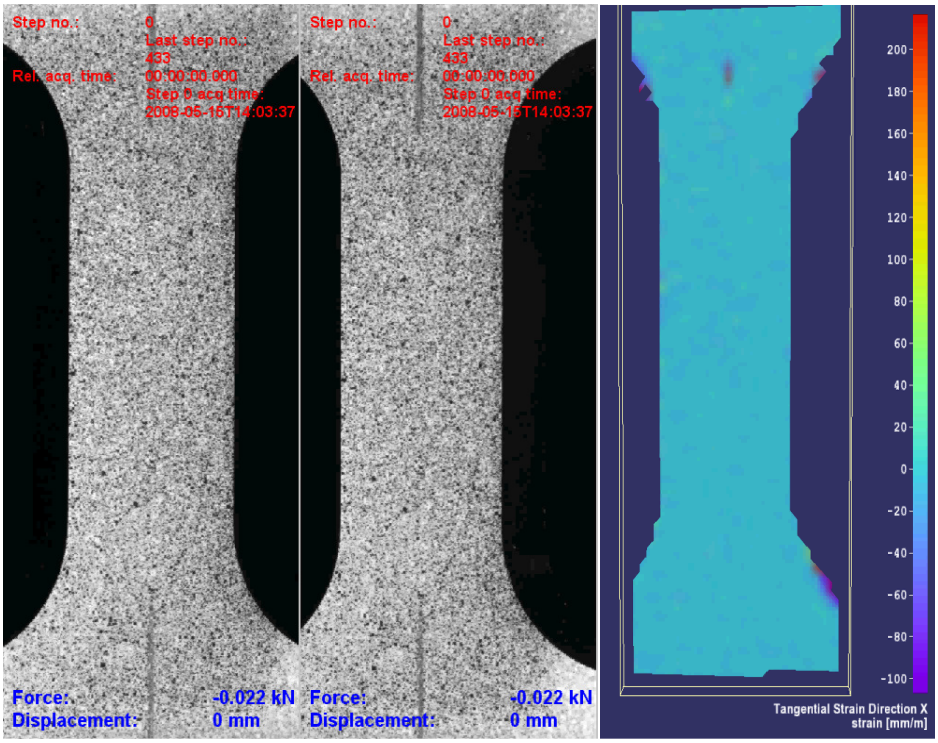

(a) UCS Specimen camera images and surface strain at the beginning of the experiment (Scale of tangential strain mm/m on the right side ranges from (-)100 to +200)

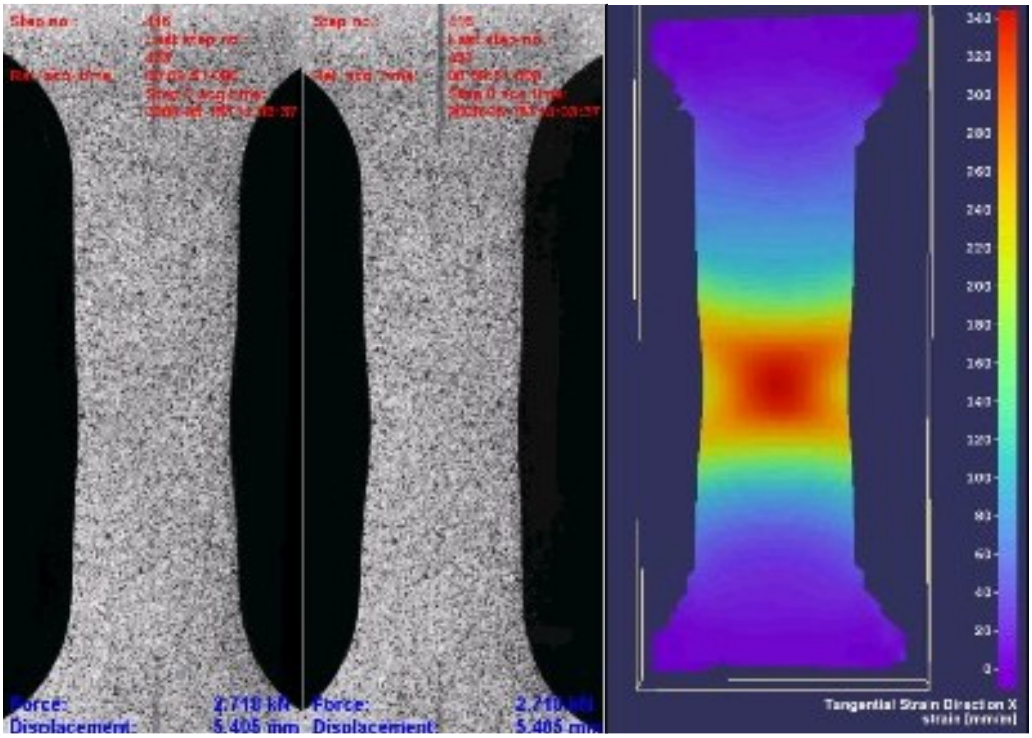

(b) UCS Specimen camera images and surface strain just before failure (Scale of tangential strain mm/m on the right side ranges from 0 to 240)

Figure 6-12 AA7010 uniform cross section specimen experimental test –sample images of optical measurement using Dantec digital 3D correlation system Q400

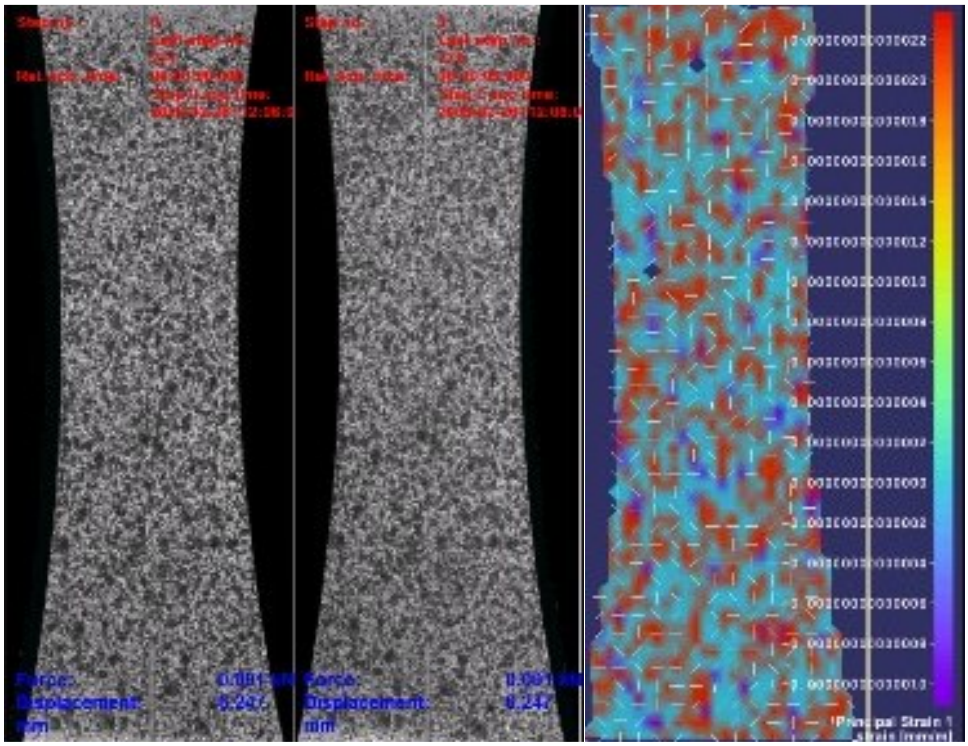

a) VCS Specimen camera images and surface strain at the beginning of the experiment

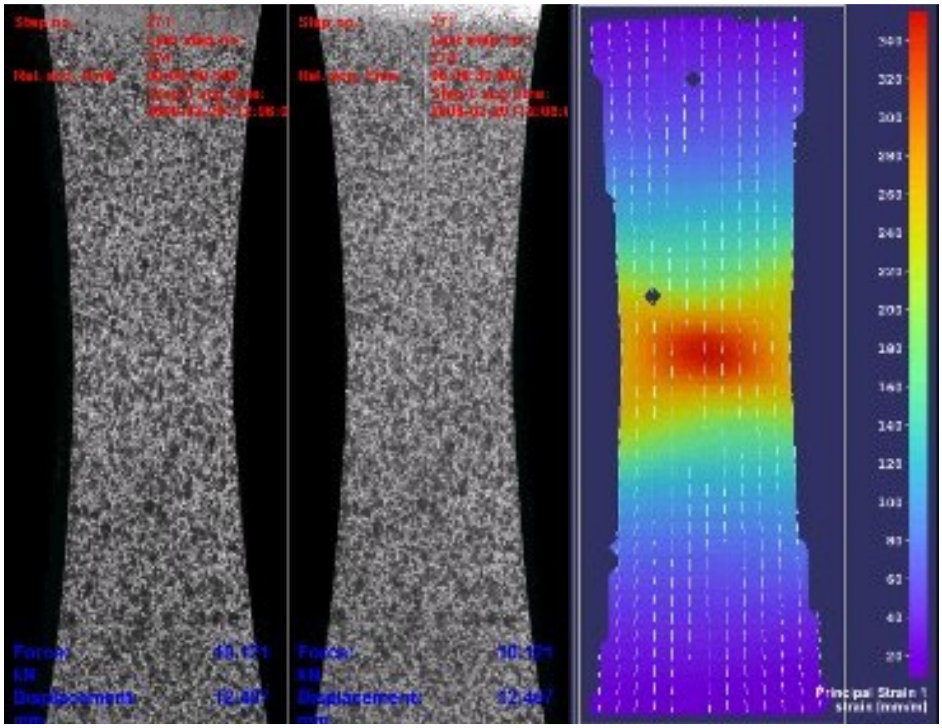

(b) VCS Specimen camera images and surface strain just before failure (Scale of tangential strain mm/m on the right side ranges from 21 to 343)

Figure 6-13 AA2024 varying cross section specimen experimental test –sample images of optical measurement using Dantec digital 3D correlation system Q400

The tensile test specimen test images obtained during one of the coupon test case is shown in Figure 6-12 along with the measured strain proportional to the deformation using DIC method. Figure 6-12 shows the specimen deformation of a uniform cross section at initial, before failure and immediately after total failure stages. Similarly Figure 6-13 shows the varying cross section initial, before failure and immediately after total failure stages.

6.9.1 UCS and VCS results comparison using DIC technique

Uniaxial tensile tests were performed to compare the results of Uniform Cross Section (UCS) coupons and Varying Cross Section (VCS) coupons. The results were obtained using the DIC method explained in Chapter 6. The results were collated and compared against each other for similar test cases. The results for AA2024 and AA7010 materials are shown in Figure 6-14 and Figure 6-15 respectively. The coupon tests using UCS and VCS specimens produce same results. Hence prior knowledge of maximum strain location area is eliminated and the need for VCS specimen is not required. The non-contact DIC technique processes the data after measurement and identification of maximum strain area can be done after the experiment is completed. The maximum strain areas for a UCS obtained after post processing the data is shown Figure 6-12 and for VCS specimen is shown in Figure 6-13.

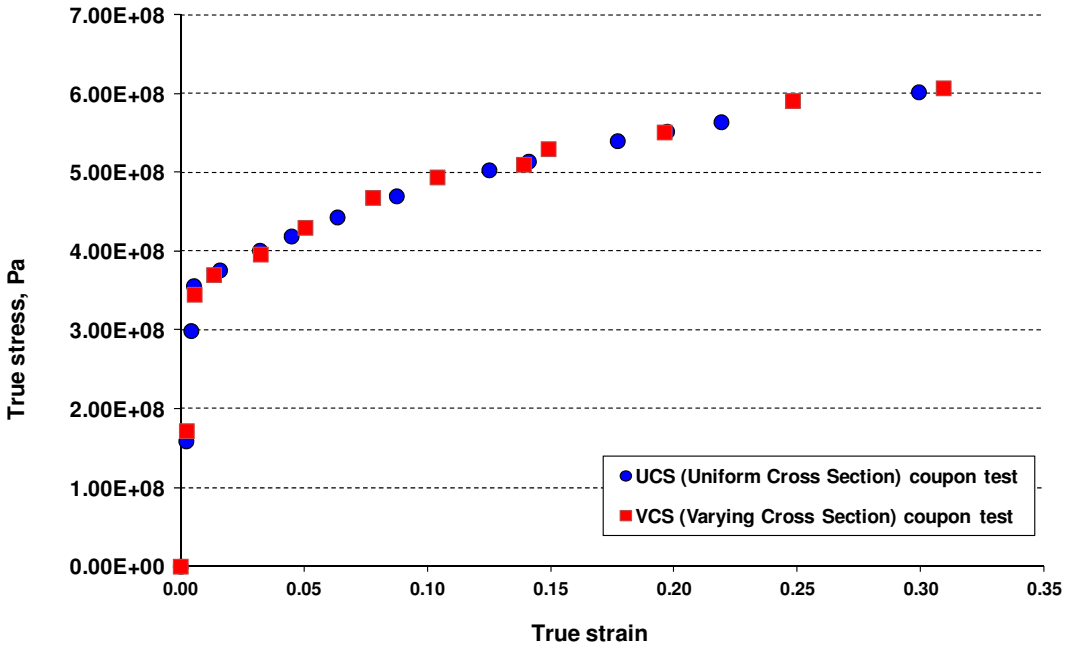

Figure 6-14 AA7010 uniaxial tensile test results for Uniform Cross Section (UCS) coupon test results comparison with Varying Cross Section (VCS) coupon test results

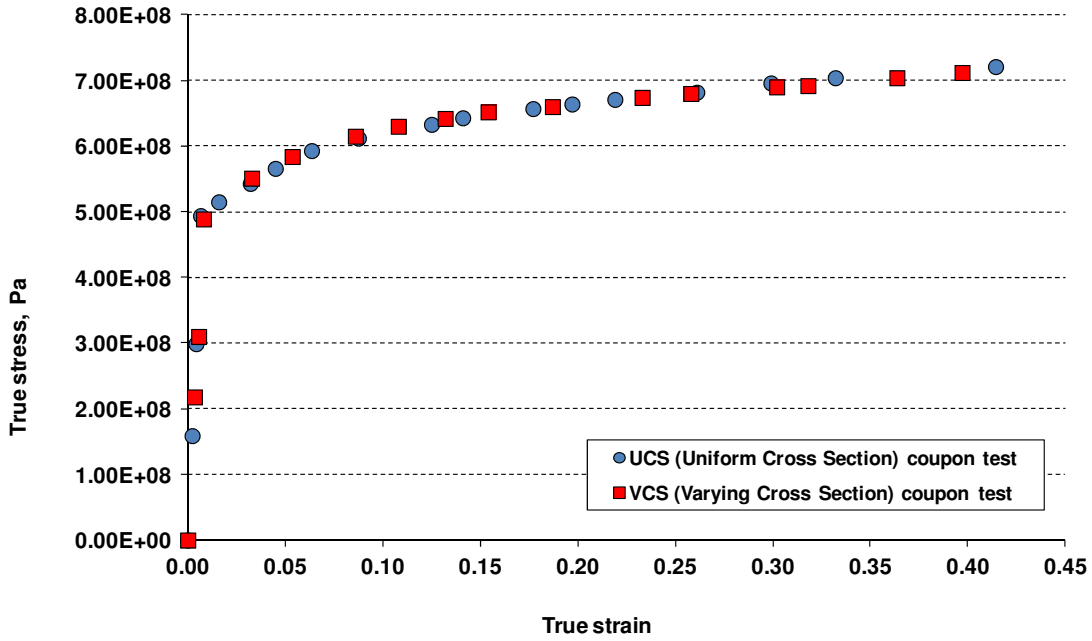

Figure 6-15 AA2024 uniaxial tensile test results for Uniform Cross Section (UCS) coupon test results comparison with Varying Cross Section (VCS) coupon test results

The tests reveal that there is no need for using VCS coupons in DIC measurement technique. Therefore the time consuming costlier preparation VCS specimen can be replaced with standard dog bone specimen for characterisation procedure.

6.10 Aluminium 2024-T3 Experimental results

In this work a Dantec Dynamics Q-400 DIC (2006) system was used to measure the strain on a series of standard tensile tests and low cycle tension tests of aluminium alloy AA-2024-T3. The stress strain curves are obtained from standard tensile tests and cyclic tests. The data obtained by coupon test sets on 0^0, 90^0 and 45^0 to rolling directions are compiled together. The procedure for calculation of damage parameter from cyclic test is established in this section. The aluminium AA2024-T3 experimental results and material characterisation are shown from Figure 6-16 to Figure 6-25. The isotropic material parameters calculated from this section are summarised in Table 6-4. The orthotropic material parameter are summarised in Table 6-5. This section demonstrates that DIC measurement techniques allow characterisation of ductile damage in metals to be simply incorporated within an existing material characterisation process available in the aerospace industry.

6.10.1 AA2024 standard tensile test and cyclic tests coupon results

Uniaxial tensile tests were performed using UCS and VCS coupons. Both UCS and VCS specimen results were used in finding out the average values of true stress and true strain. The standard tensile tests experimental results are complied together and shown in Figure 6-16 and average values are obtained.

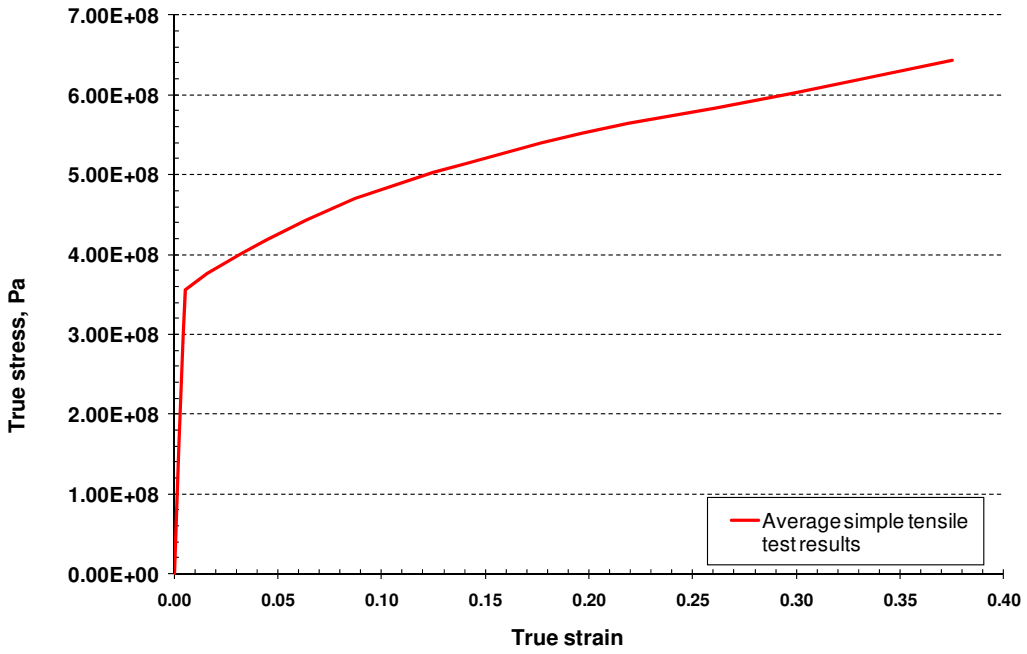

Figure 6-16 Simple uniaxial tensile test of Aluminium AA2024-T3 specimen experimental data

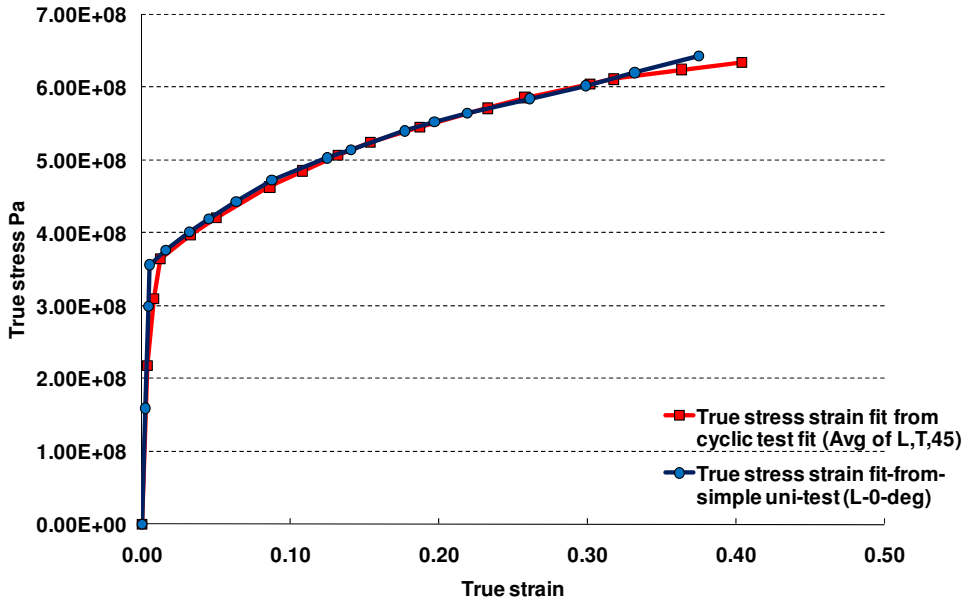

Figure 6-17 Comparison of average true stress strain curve from simple uniaxial tensile test and cyclic test for Aluminium AA2024-T3 series experimental data

Similar to the standard tensile test the uniaxial cyclic test experiments were performed on longitudinal, transverse and 45^0 to longitudinal directions. The results are complied together and average values of stress strain data were obtained. Both standard and cyclic tensile data were compared to check the consistence of results (Figure 6-17). The results obtained through both methods produce similar results.

6.10.2 Orthotropic behaviour of AA2024-T3

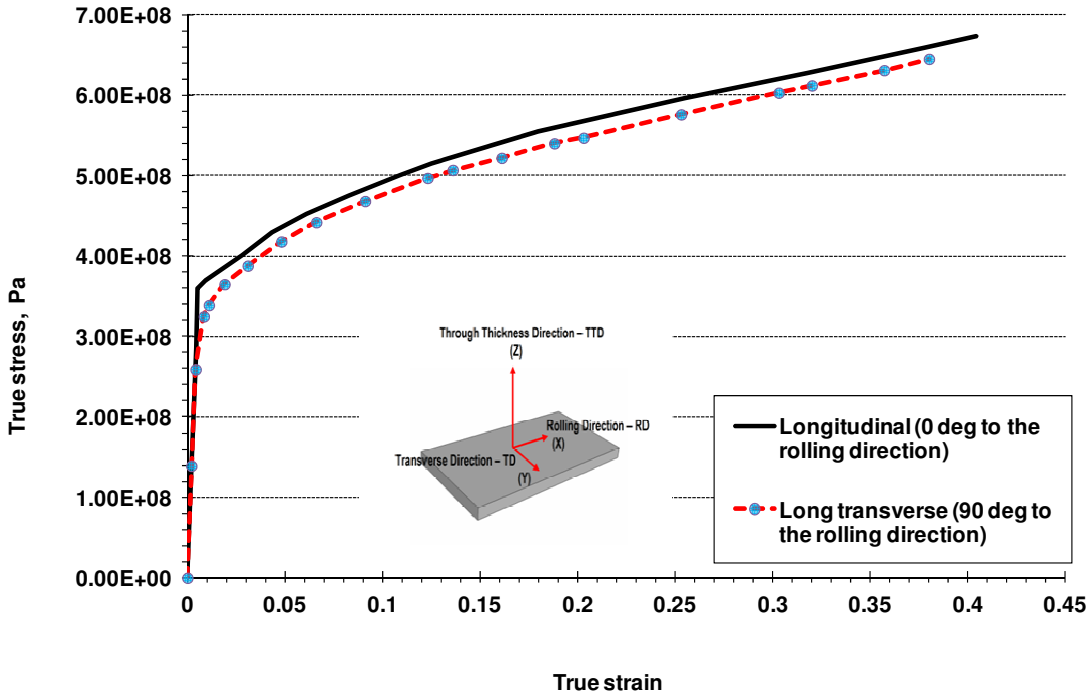

Figure 6-18 Uniaxial tensile test for AA2024 Aluminium material – specimen cut in 0^0 to rolling direction and 90^0 to rolling direction- Experimental results show orthotropy for standard tensile test results

The test results provided in Figure 6-18 show the behaviour of AA2024 material in longitudinal direction (rolling direction or 0^0 to rolling direction) and in long transverse direction (transverse direction or 90^0 to rolling direction). It is evident from the graph that Aluminium alloy AA2024 specimens used in this research work in tensile testing experiments are slightly orthotropic. The material data between longitudinal direction and long transverse direction show the yield criteria and plasticity slightly vary between them and show orthotropic behaviour.

6.10.3 AA-2024 damage parameter calculations

During the uniaxial cyclic test shown in Figure 6-20, the material is subject to repeated loading/unloading cycle above 2% to 5% of plastic strain from the previous loading. This low cyclic process allows measurement of degradation of elastic modulus. This process is done until the specimen fractures. To achieve this low cycle process the cross-head displacement versus time was obtained from the Instron 8032 servo hydraulic test machine. Sample cyclic tests were performed to obtain approximate values of cross-head displacement and time. The cross-head displacement and time were obtained for noticeable level of plastic deformation during loading process and zero stress level during unloading process at each cycle. A typical cross-head displacement versus time curve is show in Figure 6-19 for AA-2024 cyclic test. The signal from the tensile testing machine cross-head displacement against time is used to carry out the loading and unloading sequence for the cyclic test.

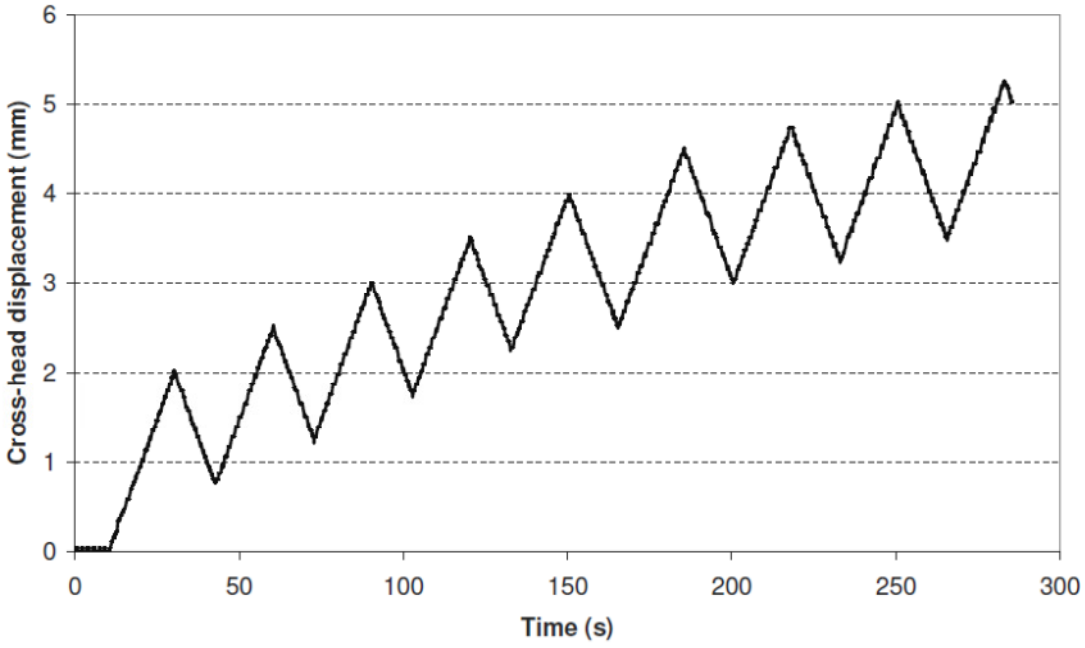

Figure 6-19 Instron 8032 servo hydraulic machine cyclic test input value for AA-2024-T3 material (cross-head displacement versus time)

In this process the micro cracks and voids form in the virgin material and thus reduce its load carrying capacity and as a result the materials Young's modulus reduces to lower level. These reductions in Young's modulus are shown in Figure 6-20. Using this data along with energy equivalence principle explained in Chapter 5 and Chow's

anisotropic theory of elasticity for continuum damage mechanics (1987) damage parameters are calculated. The experimental procedure and damage parameter measurement techniques explained in this chapter for Chow and Wang damage model can be used for other models as well.

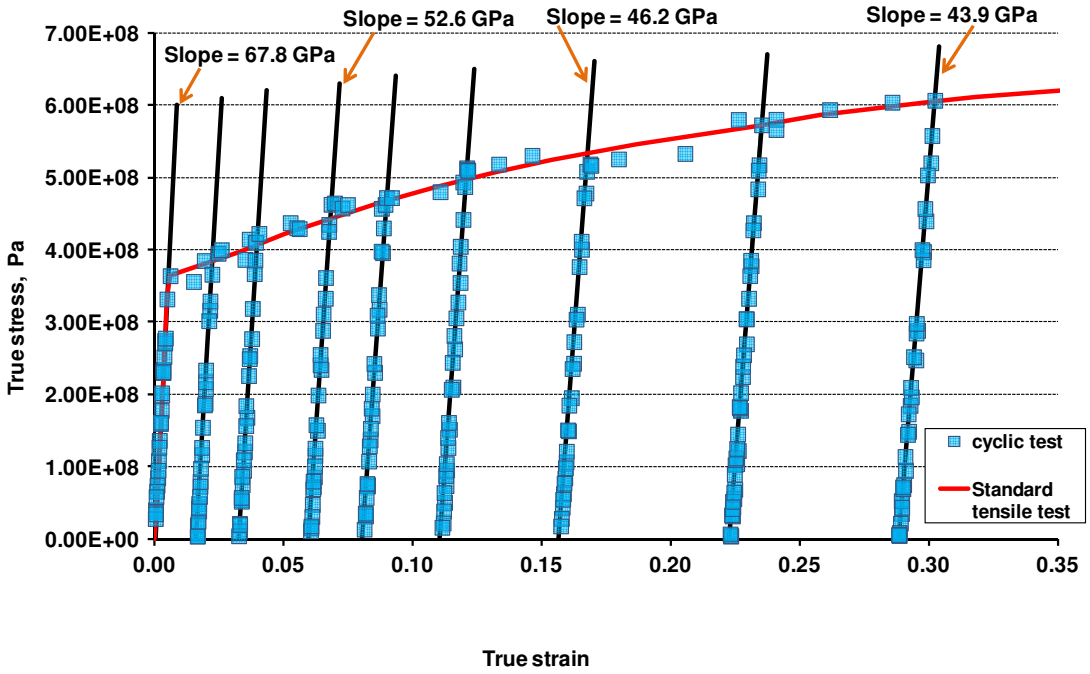

Figure 6-20 Aluminium AA2024-T3 cyclic test data along with standard uniaxial tensile test, slopes reveals elastic modulus degradation due to damage present; black lines are used to highlight the Young's modulus degradation due to damage

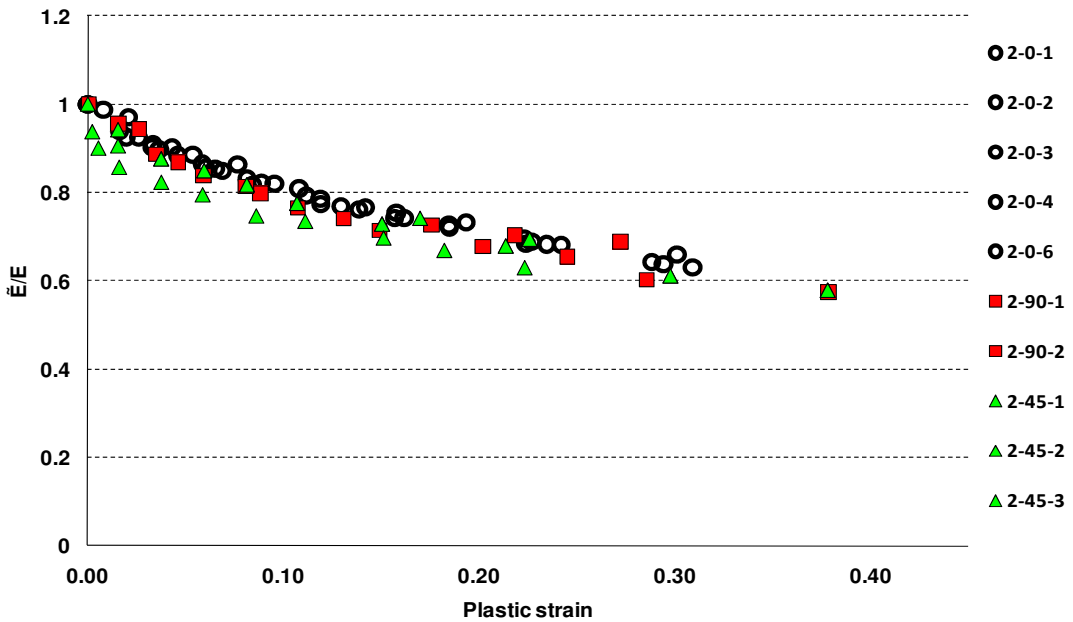

Figure 6-21 Aluminium AA2024-T3 uniaxial cyclic test data from coupons for damage characterisation

One of the cyclic test results is shown in Figure 6-20. From the cyclic test Figure 6-20 the elastic modulus ratios can be obtained by dividing the new degraded elastic modulus ($\tilde{E}$) at each cyclic test instance (highlighted with straight line slopes) with the elastic modulus (E). The plastic strain is obtained from the intersection of straight line slopes at the strain axis. From equation (6.11) the damage variable D can be calculated for that instance. The damage value at each instance of the cycle is calculated until the specimen completely fails. The

Figure 6-21 shows the complete coupons test results of AA-2024-T3 material on elastic modulus degradation ratio versus plastic strain. The graph of elastic modulus ratio versus plastic strain for rolling direction (2-0-X), transverse direction (2-90-X) and 45 degree to rolling direction (2-45-X) show only small variation. It implies that the batch of Aluminium AA-2024-T3 material used in this test shows slight orthotropy.

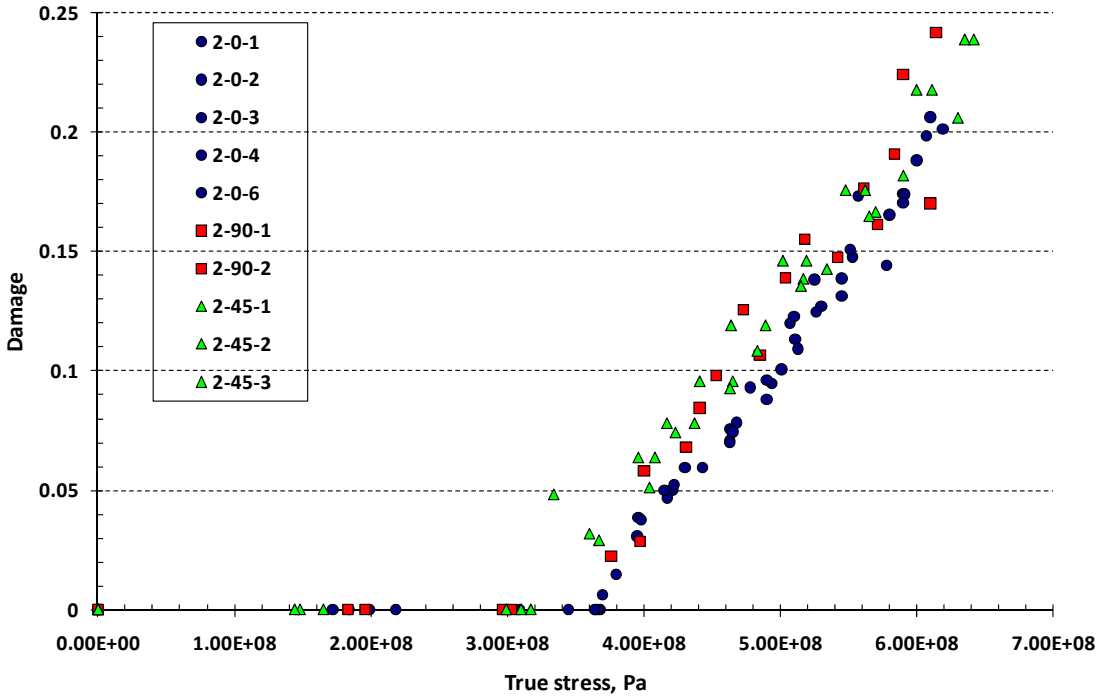

Figure 6-22 Cyclic test of Aluminium AA2024-T3 uniaxial experimental data, true stress vs damage

6.10.4 AA-2024 damage versus true stress

The damage parameters calculated from the experimental results are plotted against true stress data. The coupon true stress and damage test results obtained from rolling direction (2-0-X), transverse direction (2-90-X) and 45 degree to rolling direction (2-45-X) were complied together and plotted in Figure 6-22. The coupon true strain

versus damage graph is available in appendix Figure 13-1 for reference. The data points obtained from rolling direction, transverse direction and 45 degree to rolling direction show slight variation.

6.10.5 AA-2024 B versus β and Bo calculation

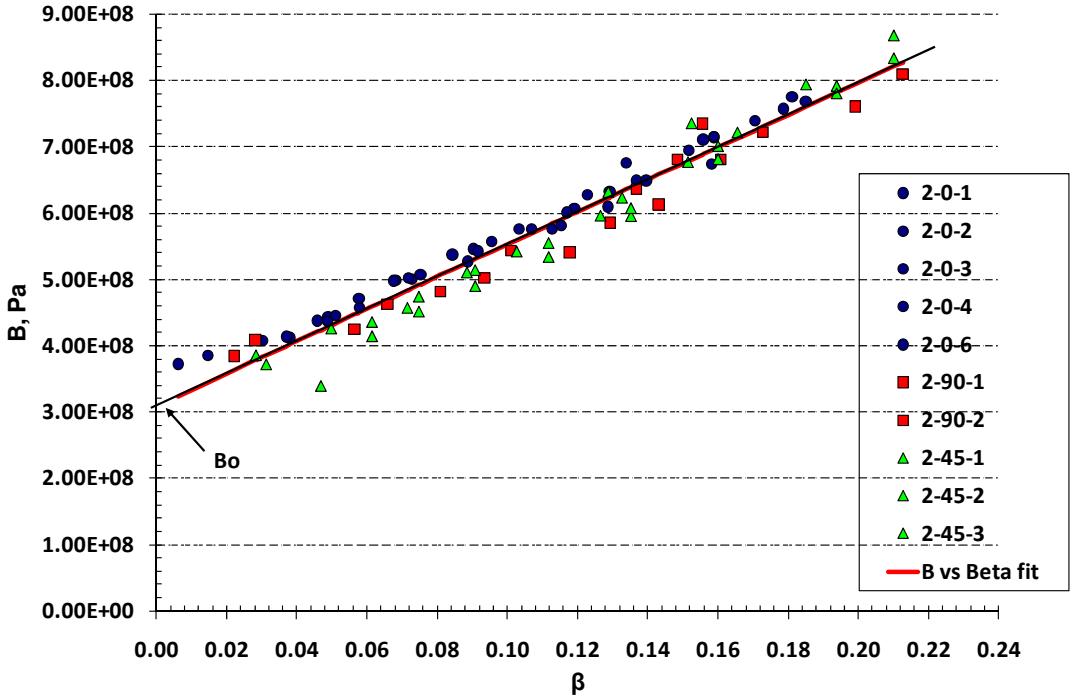

Figure 6-23 B vs β fit from uniaxial experimental results of AA-2024 material coupon cyclic test, the R^2 value of B vs β fit is $R^2 = 1$

From the true stress data obtained, the virgin material stress data are calculated using equation (6.8). The damage parameter calculated from the cyclic test is used to calculate the B and β parameter from equation (6.13) and (6.14). The B versus β curve fit was calculated from the data. The results show linear relationship between B and β. The slope of this curve $dB/d\beta$ is directly obtained from the curve fitting. This implies that the linear assumption of damage growth suggested by Chow and Wang (1987) is sufficient to define the damage evolution. The value of Bo (the damage initiation stress) is obtained from the curve fitting; which is the value of B where β is zero.

6.10.6 AA2024 Virgin material stress & virgin material strain calculation from damage parameters

The virgin material true stress and true strain are defined as the effective stress and effective strain by Chow and Wang (1987). The virgin material true stress and virgin

material true strain are calculated from the damage value *D* using the equation (6.8) and (6.10) . The data obtained from the coupon test are compiled in Figure 6-24 and Figure 6-25. The average values obtained from these graphs and data from the Table 6-4 and Table 6-5 are used in Abaqus for damage model simulation.

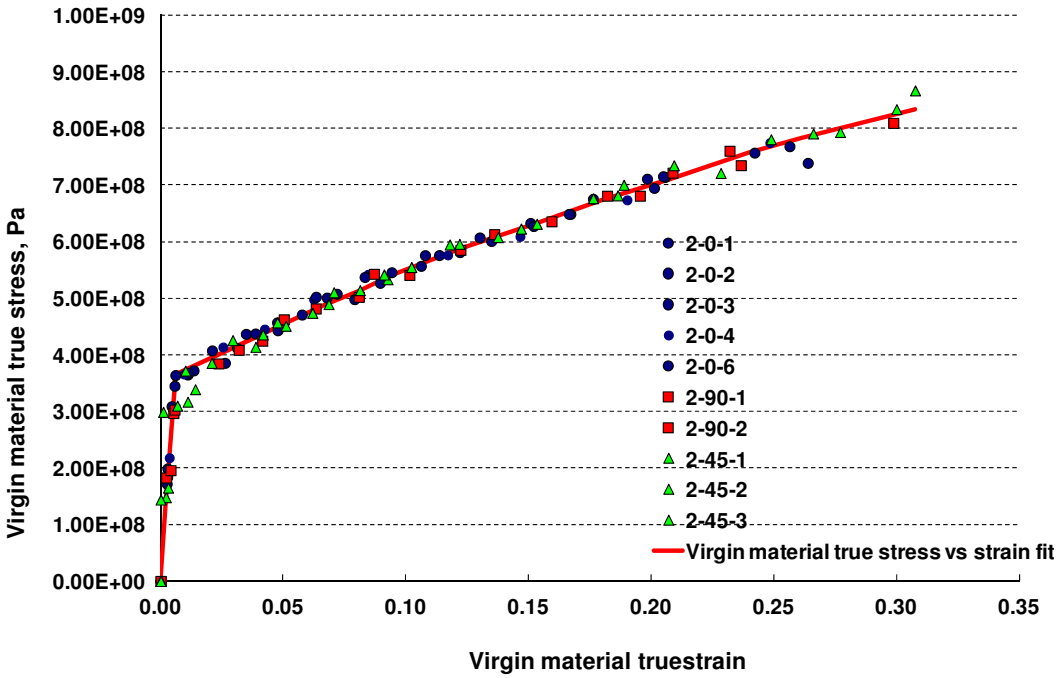

Figure 6-24 Virgin material true stress and virgin material true strain for Aluminium AA2024-T3 series calculated from the uniaxial experimental data

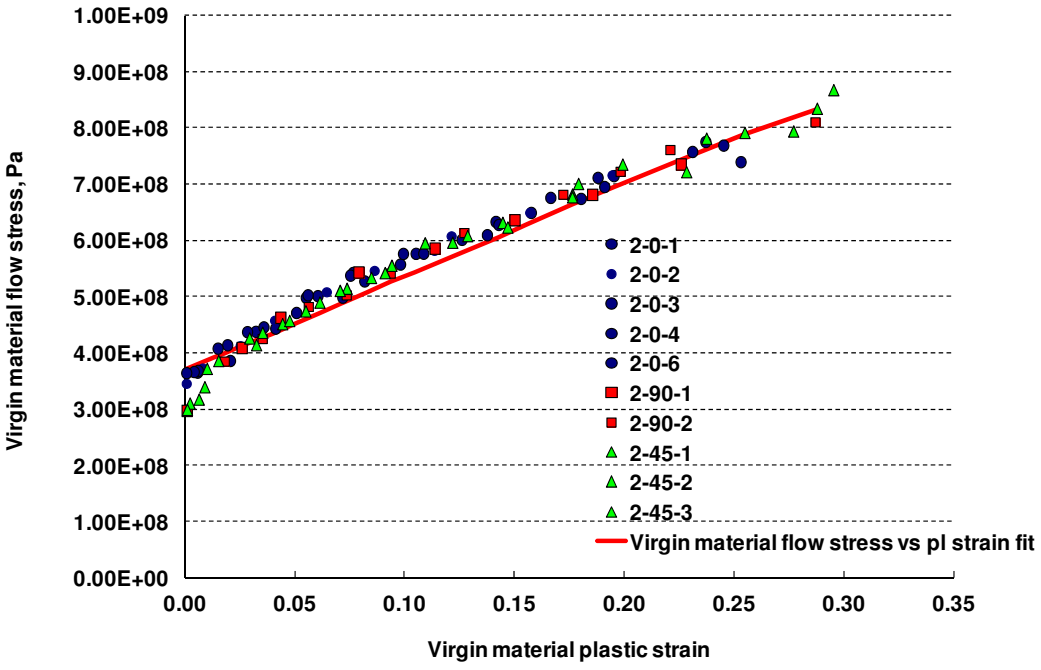

Figure 6-25 Virgin material flow stress Virgin material stress and virgin material plastic strain for Aluminium AA2024-T3 series calculated from the uniaxial experimental data

In summary the following parameters should be determined from the uniaxial cyclic test experimental data to determine the material constants for Chow and Wang damage model.

i. Damage

$$D = 1 - \sqrt{\frac{\tilde{E}}{E}}$$

ii. Virgin material true stress (effective stress – Chow and Wang , 1987)

$$\tilde{\sigma} = \frac{\sigma}{(1-D)}$$

iii. Virgin material true strain (effective strain – Chow and Wang, 1987)

$$\tilde{\varepsilon} = (1 - D)\varepsilon$$

iv. B_0 is the stress at which damage start to evolve

v. $\frac{dB}{d\beta}\beta = \tilde{\sigma}_d - B_0$ additional stress required for damage evolution after damage initiated. ε

vi. $\tilde{\sigma}_d$ is effective damage stress once damage initiates

vii. $$\beta = D_1\left(1 - \frac{D_1}{2}\right)$$

viii. β vs B curve and calculation of $\frac{dB}{d\beta}$

ix. $$\mu = \frac{D_2\left[1 - \frac{D_2}{2}\right]}{D_1\left[1 - \frac{D_1}{2}\right]}$$

x. D_{cr} (Damage critical) – is the damage value just before the specimen completely fails during uniaxial tensile test. The damage critical value for longitudinal direction is denoted by dcr_1, transverse direction is denoted by dcr_2 and through thickness direction is denoted by dcr_3. The effective damage value D_{cr} is the value of β just before the specimen fails. The damage critical values are the observed damage values during the specimen failure in the experiment with respect to the orthotropic directions (longitudinal and transverse direction). The value for dcr_3 (through thickness direction) is not determined in these experiments. The critical damage value is used to initiate damage failure in the simulation mode.

Once the material constants are obtained the simulation results using Abaqus explicit code based on Chow and Wang damage model can be scrutinised and validated.

The degradation of elastic modulus forms the basis for both energy equivalence principle and strain equivalence principle. The ratio of elastic modulus from
Figure 6-21 can be used for strain equivalence principle as well. But additional testing and determination of other parameters should be completed based on Lemaitre's (2006) work. The DIC measurement technique can be used for either energy equivalence principle or strain equivalence principle for damage parameter measurements.

6.10.7 AA-2024 damage parameter results summary

Table 6-4 AA2024 Material constants for Chow's isotropic damage model

Parameter	**Description**	**Experimental value**
E	Young's modulus – longitudinal or direction-1 or (0^0)	68.5 GPa
v	Poisson ratio	0.327
G	Shear modulus	25.81 GPa
R	Hill's isotropic coefficient	1
μ	Chow's damage potential matrix constant	1
$\frac{dB}{d\beta}$	Chow's damage threshold constant	2.44 GPa
B_0	Damage initiation stress under uniaxial tensile test	309 MPa
D_{cr}	Critical effective damage value	0.213

The experimental data collected were obtained for AA2024. Typical results and characterisation of AA2024 specimens are shown in Figure 6-18 to Figure 6-25. Figure 6-18 gives the details of relationship between stress and strain for a uniaxial tensile test case, Figure 6-20 provides the information on uniaxial cyclic tensile test and
Figure 6-21, Figure 6-22 and Figure 13-1 gives the information on degradation of elastic modulus damage in relation to plastic strain, true stress and true stress. The

Figure 6-23 establishes the relationship between B and β and determines the slope of the curve $dB/d\beta$. Based the damage calculated virgin material stress and virgin material strain curves (Figure 6-24) and virgin material stress versus effective plastic strain were obtained (Figure 6-25). The damage parameters determined from the experiments are summarised in Table 6-4 (isotropic case) and Table 6-5 (orthotropic case).

Table 6-5 AA2024 Material constants for Chow's orthotropic damage model

Parameter	**Description**	**Experimental value**
E_1	Young's modulus – longitudinal or direction-1 or (0^0)	67.8 GPa
E_2	Young's modulus – transverse or direction-2 or (90^0)	66.6 GPa
E_3	Young's modulus – through thickness or direction-3	67.8 GPa
v_{21}	Poisson ratio between 2-1 direction	0.326
v_{31}	Poisson ratio between 3-1 direction	0.347
v_{32}	Poisson ratio between 3-2 direction	0.326
G_{12}	Shear modulus between 1-2 direction	25.81 GPa
G_{23}	Shear modulus between 2-3 direction	25.81 GPa
G_{31}	Shear modulus between 3-1 direction	25.81 GPa
R_{11}	Hill's anisotropic coefficient	1.0
R_{22}	Hill's anisotropic coefficient	0.9364
R_{33}	Hill's anisotropic coefficient	0.8877
R_{12}	Hill's anisotropic coefficient	0.9015
R_{13}	Hill's anisotropic coefficient	0.9515
R_{23}	Hill's anisotropic coefficient	0.9683
μ	Chow's damage potential matrix constant	0.945
$\frac{dB}{d\beta}$	Chow's damage threshold constant	2.44 GPa
B_0	Damage initiation stress under uniaxial tensile test	309 MPa
dcr_1	Critical damage value in longitudinal direction	0.217
dcr_2	Critical damage value in transverse direction	0.242
D_{cr}	Critical effective damage value	0.213

6.11 Aluminium AA-7010-T7651 experimental results

Similar to AA2024-T3 results the aluminium AA7010-T7651 experimental results and material characterisation are shown from Figure 6-26 to Figure 6-31. The isotropic material parameters are summarised in Table 6-6 this section. The orthotropic material parameter are summarised in Table 6-7.

6.11.1 AA7010-T651 standard tensile test and cyclic tests coupon results

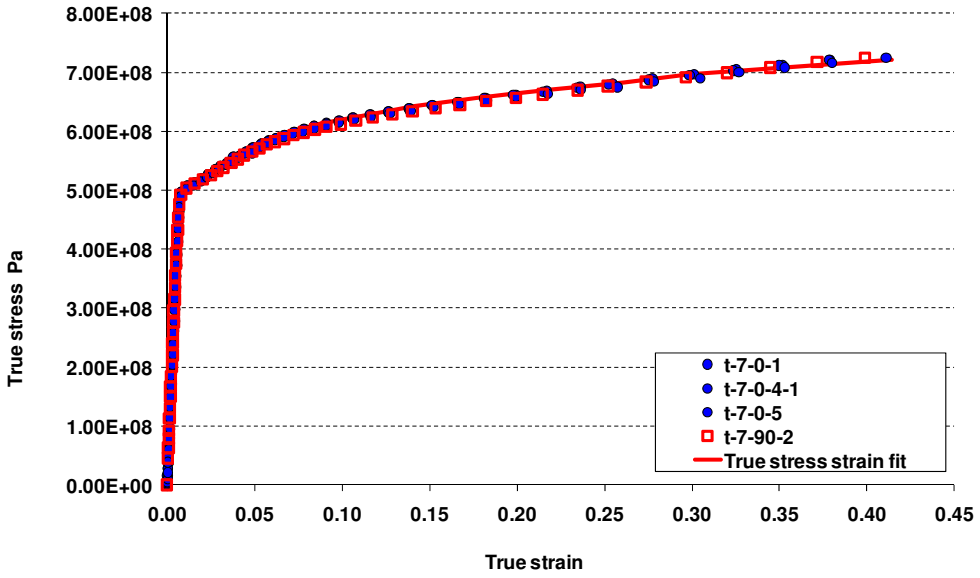

Figure 6-26 Uniaxial standard tensile test of Aluminium AA7010 experimental data

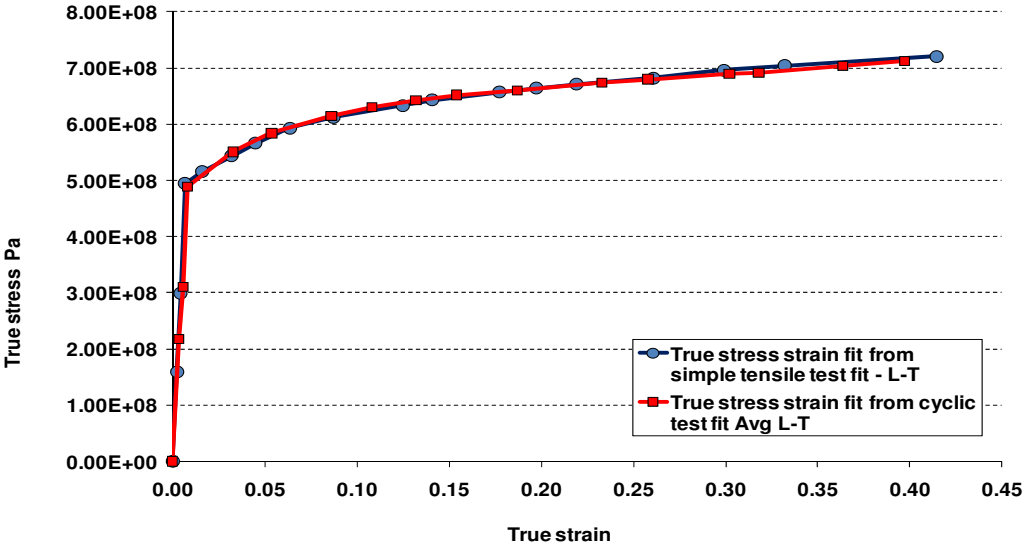

Figure 6-27 True stress strain curve for uniaxial tensile test cases - comparison between cyclic tensile test and simple tensile test of Aluminium AA7010 experimental data

Several uniaxial tensile tests were performed using AA7010 UCS and VCS coupons. From the standard tensile experimental results the data were compiled together and graphs were plotted as shown in Figure 6-26. The average values were obtained and plotted on Figure 6-26. Similar to the standard tensile test the uniaxial cyclic test experiments were performed on 0^0 and 90^0 to rolling directions. The results are compiled together and average values of stress strain data were obtained. Both standard and cyclic tensile data were compared to check the consistence of results (Figure 6-28). The results obtained through both methods produce similar results.

6.11.2 Orthotropic behaviour of AA7010-T7651

The test results provided in Figure 6-26 and

Figure 6-27 show the behaviour of AA7010 material in longitudinal direction (rolling direction or 0^0 to rolling direction) and in long transverse direction (transverse direction or 90^0 to rolling direction). The material data between longitudinal direction and long transverse direction do not show any difference yield criteria. It is evident from the graph that Aluminium alloy AA7010 specimens used in these tensile testing experiments do not show appreciable level of orthotropy.

6.11.3 AA7010-T7651 cyclic tests and damage parameter calculations

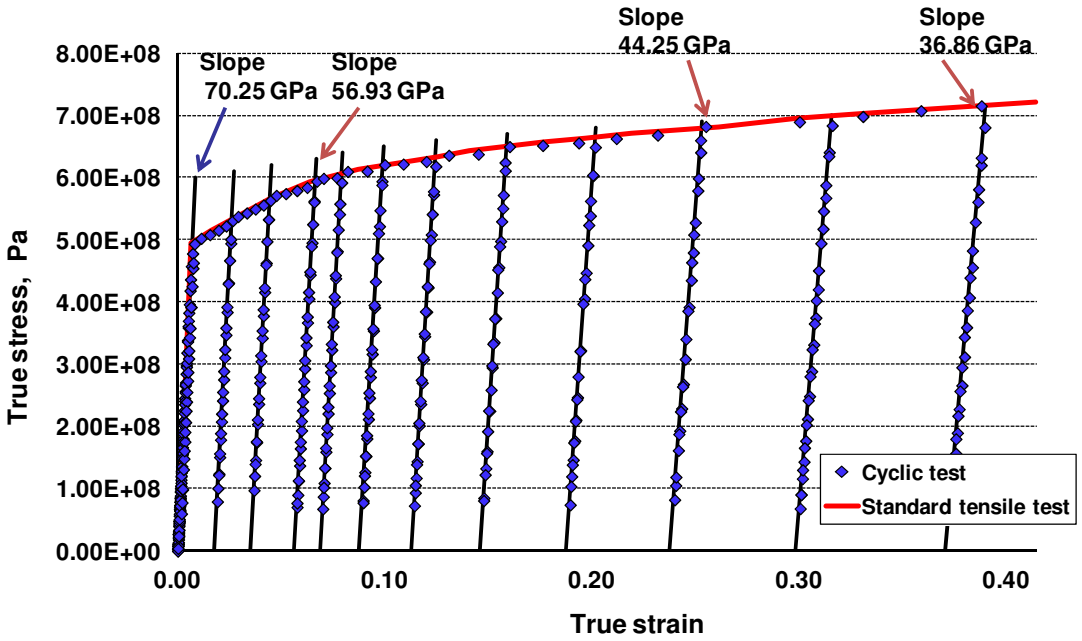

Figure 6-28 Aluminium AA7010 uniaxial cyclic test data along with standard tensile test (test number 7-0-6) elastic modulus degradation due to damage, black lines are used to highlight the Young's modulus degradation due to damage

Similar to the calculation of AA-2024 material the AA7010 elastic modulus degradation ratio versus plastic strain are calculated. From the cyclic test Figure 6-28 the elastic modulus ratios can be obtained by dividing the new degraded elastic modulus ($\tilde{E}$) at each cyclic test instance (highlighted with straight line slopes) with the elastic modulus (E). The plastic strain is obtained from the intersection of straight line slopes at the strain axis. From equation (6.11) the damage variable D was calculated for that instance. The damage value at each instance of the cycle is calculated until the specimen completely fails.

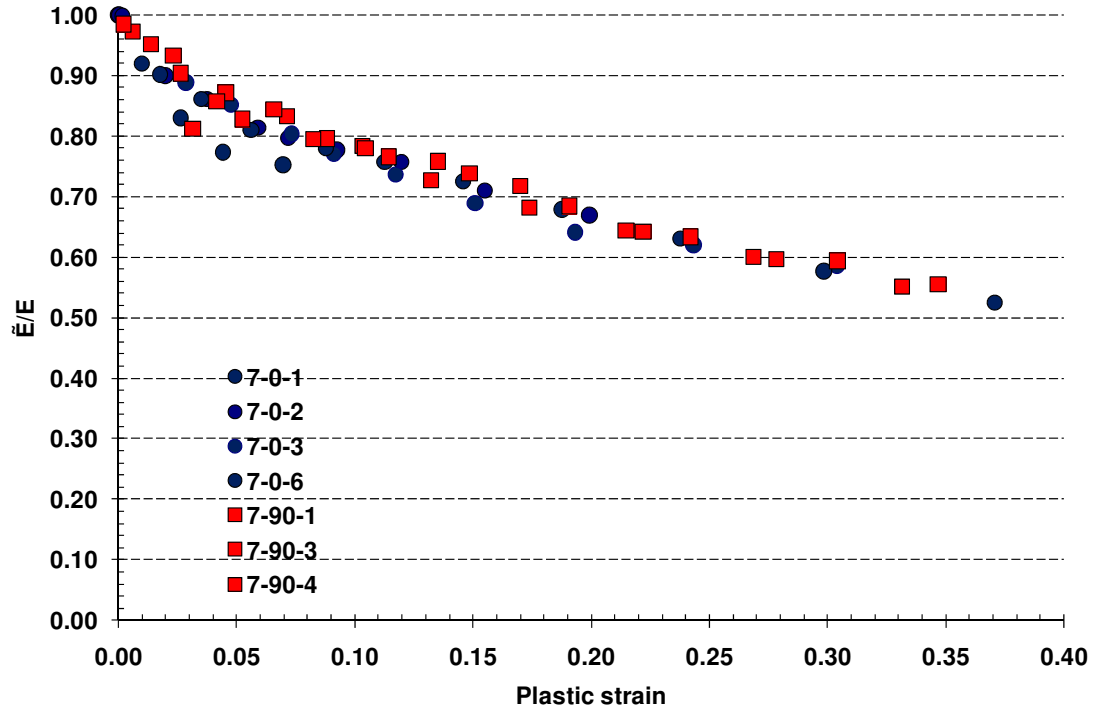

Figure 6-29 Aluminium AA7010 uniaxial cyclic test data from coupons for damage characterisation

The graph (Figure 6-29) of elastic modulus ratio versus plastic strain for rolling direction (7-0-X), and transverse direction (7-90-X) show only small variation. It implies that the batch of Aluminium AA7010-T7651 material used in this test shows slight orthotropy.

6.11.4 AA-7010 tests damage versus true stress

The true stress data were compared against damage parameters calculated from the experimental results. The results are shown in Figure 6-30. The data points obtained from rolling direction and transverse direction do not show appreciable variation.

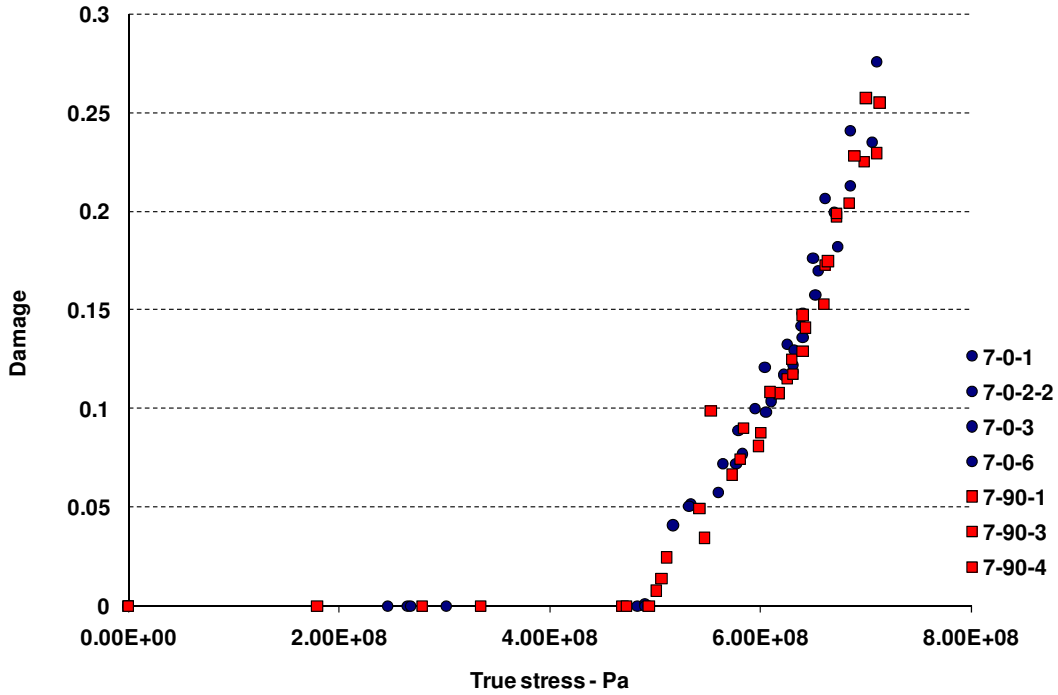

Figure 6-30 Stress versus damage curve extracted from uniaxial cyclic tensile test of Aluminium AL7010 experimental data

6.11.5 AA-7010 B versus β and Bo calculation

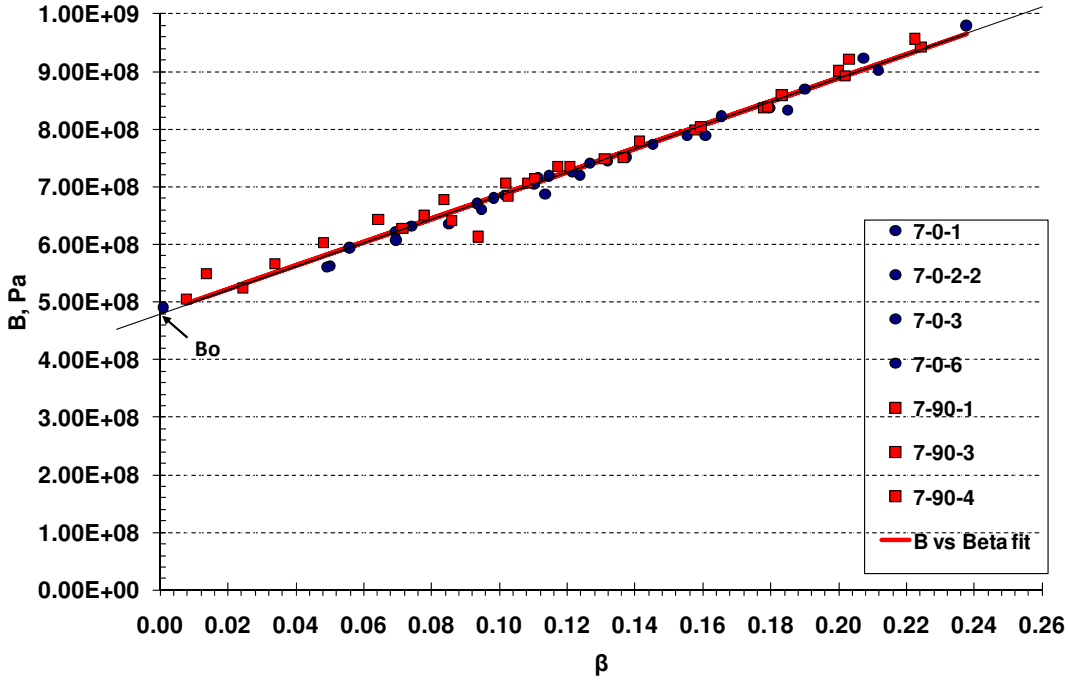

Figure 6-31 B versus β curve fit from uniaxial cyclic tensile test of Aluminium AA7010 experimental data and damage initiation point identification, the R^2 value of B vs β fit is $R^2 = 1$

From the true stress data the virgin material stress data are determined from equation 6-8. The virgin material stress and damage parameters calculated from the cyclic test

were used to calculate the B and β parameter from equation 6.13 and 6.14. The results show linear relationship between B and β. The slope of this curve $dB/d\beta$ is directly obtained from the curve fitting. This implies that the linear assumption of damage growth suggested by Chow and Wang (1987) is sufficient to define the damage evolution. The value of Bo is obtained from the curve fitting; which the value of B where β is zero. The value of Bo is when the damage starts evolving. The graph of B versus β is shown in Figure 6-31.

Table 6-6 AA7010 Material constants for Chow's isotropic damage model

Parameter	**Description**	**Experimental value**
E	Young's modulus – longitudinal or direction-1 or (0^0)	70.4 GPa
v	Poisson ratio	0.327
G	Shear modulus	26.7 GPa
R	Hill's isotropic coefficient	1
μ	Chow's damage potential matrix constant	1
$\frac{dB}{d\beta}$	Chow's damage threshold constant	2.034 GPa
B_0	Damage initiation stress under uniaxial tensile test	481.7 MPa
D_{cr}	Critical effective damage value	0.238

6.11.6 Uniaxial cyclic tests virgin material stress & virgin material strain calculation from damage parameters

The effective true stress and virgin material strain are calculated from the damage value D using the equation (6.8) and (6.10) . The data obtained from the coupon test were compiled in Figure 6-32 and Figure 6-33. The virgin material stress and virgin material strain curve (Figure 6-32) provides the information on virgin (undamaged) material true stress and true strain as defined by Chow and Wang (1987). From the virgin material strain the virgin (undamaged) material effective plastic strain values are obtained from the relationship $\tilde{\varepsilon}_{pl} = \tilde{\varepsilon} - \frac{\tilde{\sigma}}{E}$. The average values of effective plastic strain and virgin material stress (that is virgin material plastic strain and virgin material true stress) obtained from experimental data (Figure 6-32) . The average data

obtained from Figure 6-33 along with the data in Table 6-6 and Table 6-7 are used as an input data in Abaqus for isotropic and orthotropic damage model simulation.

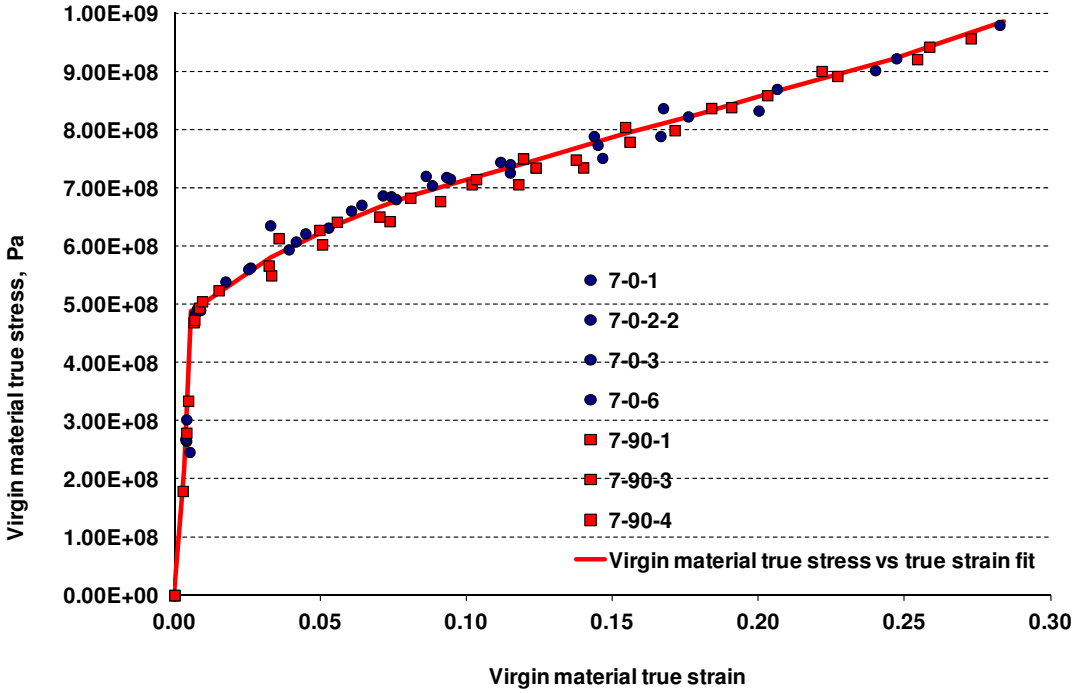

Figure 6-32 Virgin material stress virgin material strain curve from uniaxial cyclic tensile test experimental data obtained using damage parameters for Aluminium AA7010

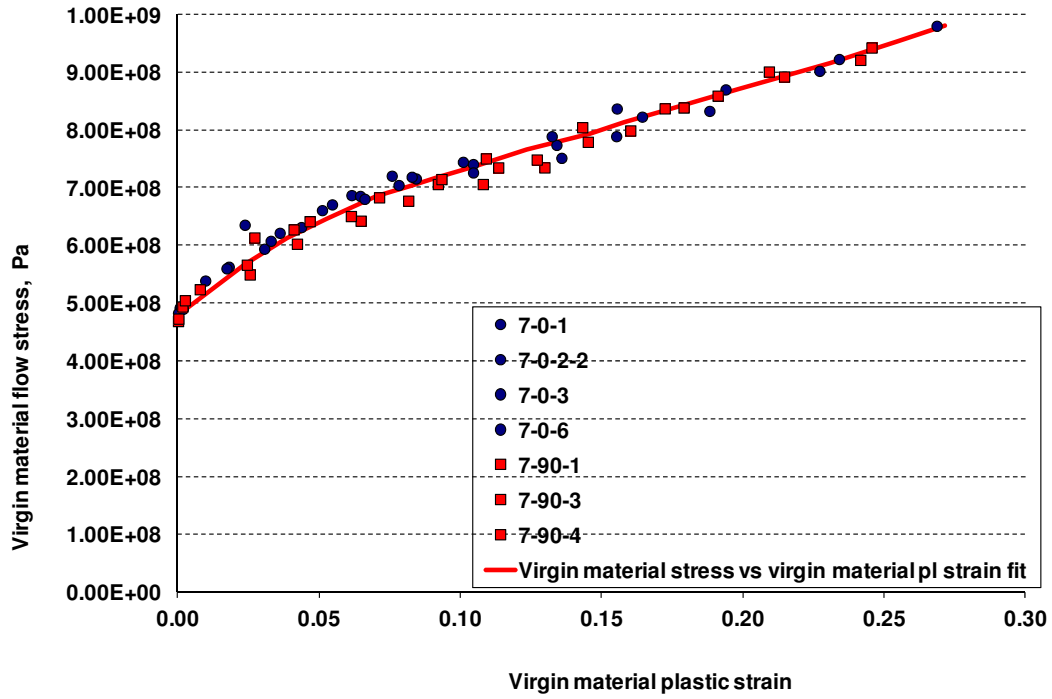

Figure 6-33 Virgin material stress effective plastic strain curve from uniaxial cyclic tensile test experimental data obtained using damage parameters for Aluminium AA7010

The virgin material data are then used in Abaqus simulation similar to experimental simulation. The use of virgin material data allows the determination of damage parameter continuously. The elastic modulus degradation values and subsequent damage values obtained by the simulation results are compared with experimental tests in Chapter 10 - Numerical test results and validation.

Table 6-7 AA7010 Material constants for Chow's orthotropic damage model

Parameter	**Description**	**Experimental value**
E_1	Young's modulus – longitudinal or direction-1 or (0^0)	70.4 GPa
E_2	Young's modulus – transverse or direction-2 or (90^0)	70.4 GPa
E_3	Young's modulus – through thickness or direction-3	70.4 GPa
v_{21}	Poisson ratio between 2-1 direction	0.327
v_{31}	Poisson ratio between 3-1 direction	0.327
v_{32}	Poisson ratio between 3-2 direction	0.327
G_{12}	Shear modulus between 1-2 direction	26.7 GPa
G_{23}	Shear modulus between 2-3 direction	26.7 GPa
G_{31}	Shear modulus between 3-1 direction	26.7 GPa
R_{11}	Hill's anisotropic coefficient	1
R_{22}	Hill's anisotropic coefficient	0.9961
R_{33}	Hill's anisotropic coefficient	0.9547
R_{12}	Hill's anisotropic coefficient	0.9547
R_{13}	Hill's anisotropic coefficient	0.9838
R_{23}	Hill's anisotropic coefficient	1
μ	Chow's damage potential matrix constant	0.995
$\frac{dB}{d\beta}$	Chow's damage threshold constant	2.034 GPa
B_0	Damage initiation stress under uniaxial tensile test	481.7 MPa
dcr_1	Critical damage value in longitudinal direction	0.276
dcr_2	Critical damage value in transverse direction	0.257
D_{cr}	Critical effective damage value	0.238

6.11.7 AA-7010 damage parameter results summary

The experimental data collected were obtained for AA7010. Typical results and characterisation of AA7010 specimens are shown in Figure 6-26 to Figure 6-33. Figure 6-26 gives the details of relationship between stress and strain for a uniaxial tensile test case, Figure 6-28 provides the information on uniaxial cyclic tensile test and Figure 6-29, and Figure 13-2 gives the information on degradation of elastic modulus and damage in relation to plastic strain, true stress and true stress. The Figure 6-31 establishes the relationship between B and β and determines the slope of the curve $dB/d\beta$. Based the damage calculated virgin material stress and virgin material strain curves (Figure 6-32) and virgin material stress versus effective plastic strain were obtained (Figure 6-33). The damage parameters determined from the experiments are summarised in Table 6-6 (isotropic case) and Table 6-7 (orthotropic case).

6.12 Conclusion of experimental results

The damage characterisation using the digital image correlation (DIC) for Chow and Wang damage model is demonstrated. The procedures were established to determine the damage parameter using DIC technique in this thesis. The results obtained using standard tensile specimen test show that the measurement of strain using DIC technique using standard tensile specimen is more than sufficient to characterise damage parameters. This proves that the special varying cross section specimens are not required for damage parameter characterisation. These results characterise the aluminium alloy material in quasi-static region. The data will be used as a basis to compare the virtual test results using the proposed Chow's damage model. The direct comparison between the physical experimental tests is very vital in validating the virtual simulation test model. The direct comparisons of the experimental results with virtual tests are explained in Chapter 10 - Numerical test results and validation.

The damage parameter calculated using the DIC method may not be accurate after 20% of the strain due to necking. Though DIC optical measurement are obtained after necking, it is better to consider these data as less accurate due to the complex geometrical deformation or cushioning effect of the rectangular specimen. The DIC

techniques do not address this issue clearly (Dantec, 2006). However the linear nature of the relationship of B versus β for Aluminium alloy AA-2024-T3 (Figure 6-23) and AA-7010-T7651 (Figure 6-31) can be conveniently used to calculate damage parameter for simulation until material fails. This linear relationship allow determination of damage from simulation even after necking starts and minimise the error after necking starts.

The digital image correlation techniques could be used not only in academic research facility but it could also be used by engineers for practical characterisation of material along with the existing laboratory techniques used in the aerospace industry. The industry could use the experimental methods and characterisation techniques established in this thesis with the existing digital image correlation equipment to widen their simulation test and predictions of damage. DIC instrumentation is already in use in most of the industry for standard characterisation tests. The present DIC equipment available in the industry can be used to characterise the damage parameters explained in this research work without much modification.

7 Determination of true stress-strain curve correction procedure

The determination of true stress-strain curve for rectangular tensile specimen tests after necking is very important for accurate prediction of damage. The material test stress-strain curve measurement using extensometer reading using the minimum cross-section has been proposed by Zhang et al (1999, 2001) based on Bridgman (1952) correction procedure. While the Zhang-Bridgman correction procedure works well for finite element (FE) analysis, it does not produce good results for experimental simple tensile test and cyclic test cases. The tests were carried out to check and analyse the data obtained from this experiments with standard tensile cases and subsequent FE analysis to establish the method. The cyclic test cases analysed using FE simulation Zhang correction produced good result because the minimum thickness point of the FE specimen is well defined. However when the same method was applied to standard tensile test and experimental cyclic test data obtained by DIC it didn't produce the expected results. A new method has been proposed using the measurement width ratio between the extensometer points. The FE model has been used to establish the new method and the verification has been done using the experimental cyclic test data.

7.1 Experimental data and correction methods

The simple tensile test is tested in Abaqus inbuilt explicit material model using AA7010 experimental data. The virtual model was created with multi-elements with one mm sized mesh, 3D with 8 node C3D8R isoparametric elements with reduced integration type. The tests are conducted under uniaxial simple tensile test case. This test is devised to highlight the extensometer type reading using nodal pairs from 2 mm apart to 20 mm apart from the centre. The true stress and true strain are calculated using the extensometer type reading and compared with the input data given in inbuilt Abaqus simulation. The Nodal displacement and reaction force were obtained from the FE model for the set of nodes distanced from the centre point starting from 2 mm up to 20 mm. The true stress-strain curves were calculated using the extensometer method using equations 6.1 to 6.7. The results obtained from the various sets of nodes show variation in true stress strain curves (Figure 7-1). The variation in true stress strain determination is because of the cushioning effect (Zhang et al, 1999) of the rectangular specimen as shown in Figure 7-2.

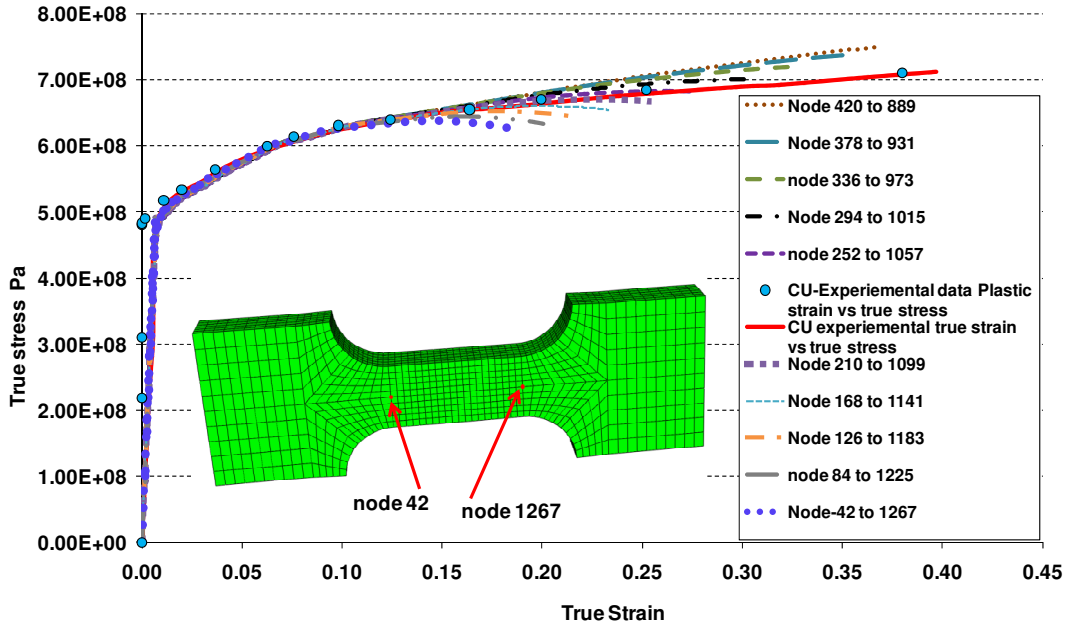

Highlights of specimen node pairs used for extensometer type measurement from the centre (first node pair 420 & 889; last two node pairs 42 & 1267)

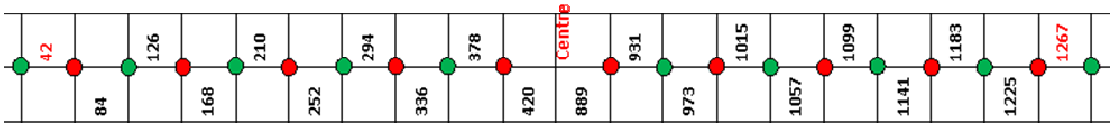

Figure 7-1 Uniaxial simple tensile test using explicit model in FE without damage (extensometer reading at nodal pairs from centre point 2 mm to 20 mm)

Under uniaxial loading the area of cross-section of a rectangular specimen takes the shape of a cushion. The cushion shape term is obtained from the shape of a cushion when seated. Figure 7-2 shows the cushion shape during the uniaxial loading condition. This curved cross-section makes it difficult to calculate actual minimum cross-sectional area of the rectangular specimen. The simulated results shown Figure 7-1 highlights the variation in predicting the true stress strain curve using extensometer type reading. The simulation test shows that prediction of damage after necking may be affected by the cushion effect in rectangular specimen. However the linear relationship of damage threshold stress *(B)* versus overall damage β and subsequent calculation of $^{dB}/_{d\beta}$ (Figure 6-23 and Figure 6-31) will produce satisfactory simulation results on prediction of damage beyond necking for AA2024 and AA7010 materials.

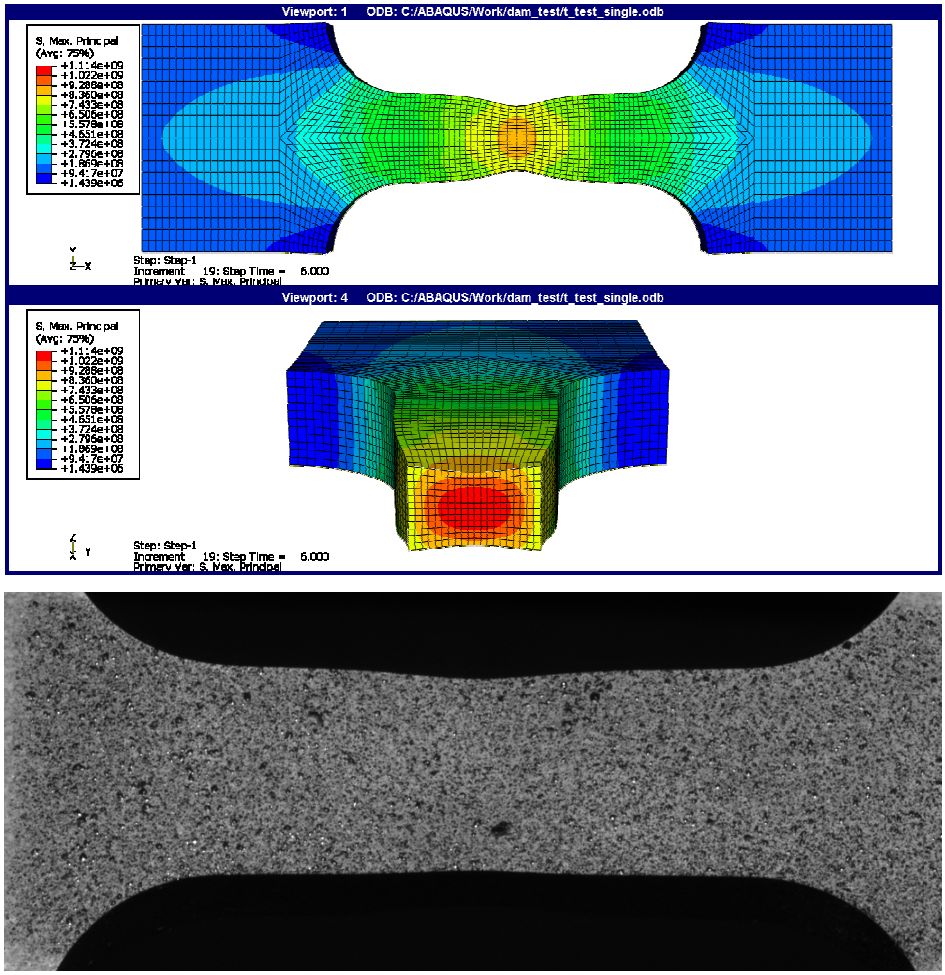

Figure 7-2 Numerical study of material characterisation shown here is exaggerated level of necking to highlight the cushioning effect compared to experimental necking, the stress units are Pascal

The cushion type necking behaviour in rectangular specimen reduces the accuracy of measurement actual cross sectional area compare to cylindrical specimen. Hence direct application of Bridgman correction was not possible. Figure 7-2 gives the exaggerated level of necking to highlight the cushioning effecting compared to experimental result necking.

7.2 Zhang Bridgman correction methods

Zhang introduced a correction procedure based on calculation of actual areas of the rectangular specimen after necking. The implementation of Zhang-Bridgman-Le Roy is briefly discussed in this section. The correction method proposed by Zhang et al (1999) was used along with Le Roy (1981) empirical expression for neck geometry parameter for a/R in this work. The calculations for determining the true stress-strain are summarised here:

$$\boldsymbol{S = \frac{w_0}{t_0}} \quad \text{(Eq. 7.1)}$$

where w_0 and t_0 are the initial width and thickness of the rectangular specimen.

Calculate the thickness reduction ratio $\boldsymbol{\frac{\Delta t}{t_0}}$

$$\frac{\Delta t}{t_0} = \frac{t_0 - t}{t_0} \quad \text{(Eq. 7.2)}$$

Identify P_{max} thickness at the point where necking starts; the load versus thickness reduction should give the P_{max} where the rectangular specimen thickness at the center is less than the ends.

Then calculate shape function

$$f_t(x) = c_0 + c_1 x + c_2 x^2 + c_3 x^3 + c_4 x^4 \quad \text{(Eq. 7.3)}$$

where C_0= *-0.03069*, C_1 = *1.09016*, C_2 = *11.1512*, C_3 = *-25.1*, C_4 = *14.8718 and*

$$x = \frac{\Delta t}{t_0} - P_{max} \quad \text{(Eq. 7.4)}$$

Then calculate total area reduction ratio

$$\frac{\Delta A}{A_0} = \left(2\frac{\Delta t}{t_0}\right) - \left(\frac{\Delta t}{t_0}\right)^2 - (0.1686 + 0.6\ln(S))f_t(x)\left(0.2845 - 0.956\left(\frac{\Delta t}{t_0}\right)_{P_{max}}\right) \quad \text{(Eq. 7.5)}$$

$\left(\frac{\Delta t}{t_0}\right)_{P_{max}}$ is the thickness reduction ratio when necking starts

Then calculate the actual area

$$A = \left[1 - \frac{\Delta A}{A_0}\right] A_0 \quad \text{(Eq. 7.6)}$$

where A_0 is the initial cross-sectional area

Once the actual area is calculated, the ratio of current radius of the neck "a" to the radius of curvature "R" of the neck surface (Figure 7-3) is calculated using Le Roy empirical equation.

$$\frac{a}{R} = 1.1(\varepsilon - \varepsilon_{P_{max}}) \quad \text{(Eq. 7.7)}$$

Where ε is the total strain and $\varepsilon_{P_{max}}$ is the plastic strain at the load P_{max}

Then calculate actual thickness from the measurements "t" after the necking starts

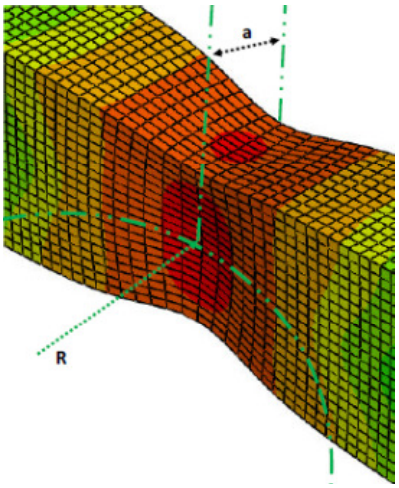

a = current radius of the neck here for rectangular specimen it is the current thickness at the minimum section

R = Radius of curvature of the neck surface in the longitudinal plane at the minimum section

Figure 7-3 Bridgman Zhang correction measurement of current thickness "a" and radius of curvature "R" at the minimum section thickness on the rectangular specimen

From the actual area calculate the true strain

$$\varepsilon = ln\left(\frac{A_0}{A}\right) \quad \text{(Eq. 7.8)}$$

From the actual area calculate the approximate true stress σ_a without Bridgman correction

$$\sigma_a = \frac{F}{A} \quad \text{(Eq. 7.9)}$$

From the relationship Bridgman proposed correction equation (1952)

$$\frac{\sigma_b}{\sigma} = \frac{1}{\left(1+\frac{2R}{a}\right)ln\left(1+\frac{a}{2R}\right)}$$

$$\sigma_b = \frac{\sigma}{\left(1+\frac{2R}{a}\right)ln\left(1+\frac{a}{2R}\right)} \quad \text{(Eq. 7.10)}$$

7.2.1 Implementation of Bridgman-Zhang-Le Roy correction for tensile test with the aide of Abaqus Standard

Tensile test specimens of uniform cross sections were created with half mm sized mesh of C3D8 with 8 node 31680 linear brick elements with AA7010 properties and one mm sized mesh of C3D8R with 8 node 3960 linear brick elements with reduced integration. Tensile test specimen of varying cross section with one mm sized mesh of C3D8R with 8 node 6364 linear brick elements for AA2024 material and a coarse model of C3D8R with 8 node 568 linear brick elements with reduced integration were created. The model boundary conditions are same as the models explained in Figure 10-7. The method proposed by Zhang, Bridgman and Le Roy were used for standard

tensile test and cyclic test. The coarse model was initially tested to ascertain the boundary and cyclic loading conditions. The fine meshed models are then tested to check the correction procedure for rectangular specimens. Isotropic material properties determined from the experimental tests were used for the simulations.

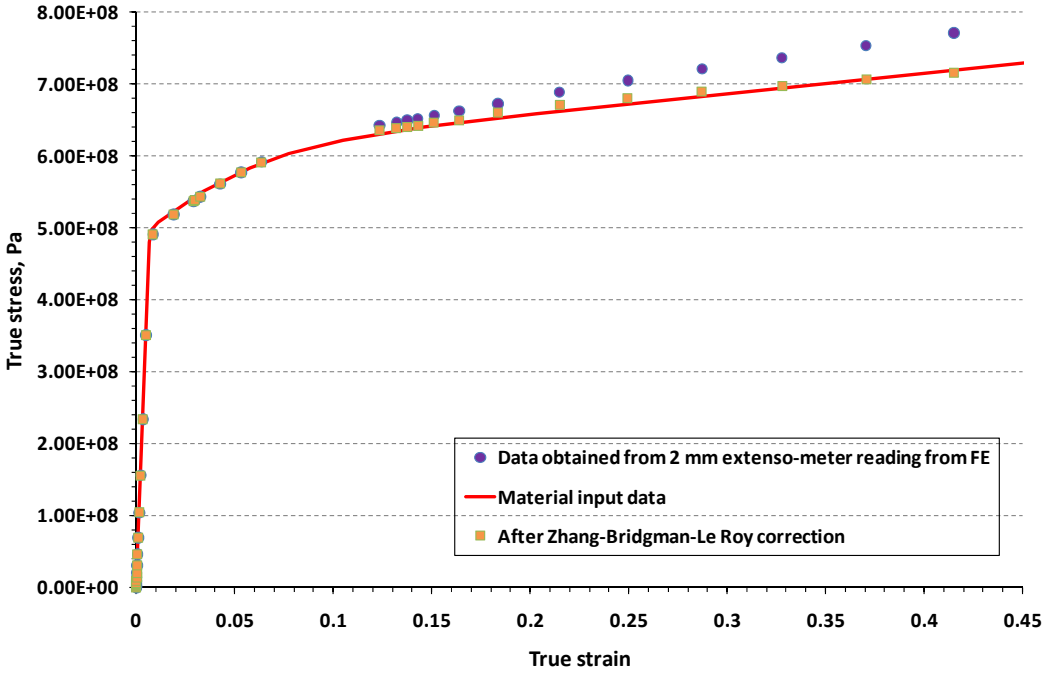

Figure 7-4 Bridgman-Zhang-Le Roy correction using numerical analysis for uniaxial standard test for AA7010 isotropic material parameters

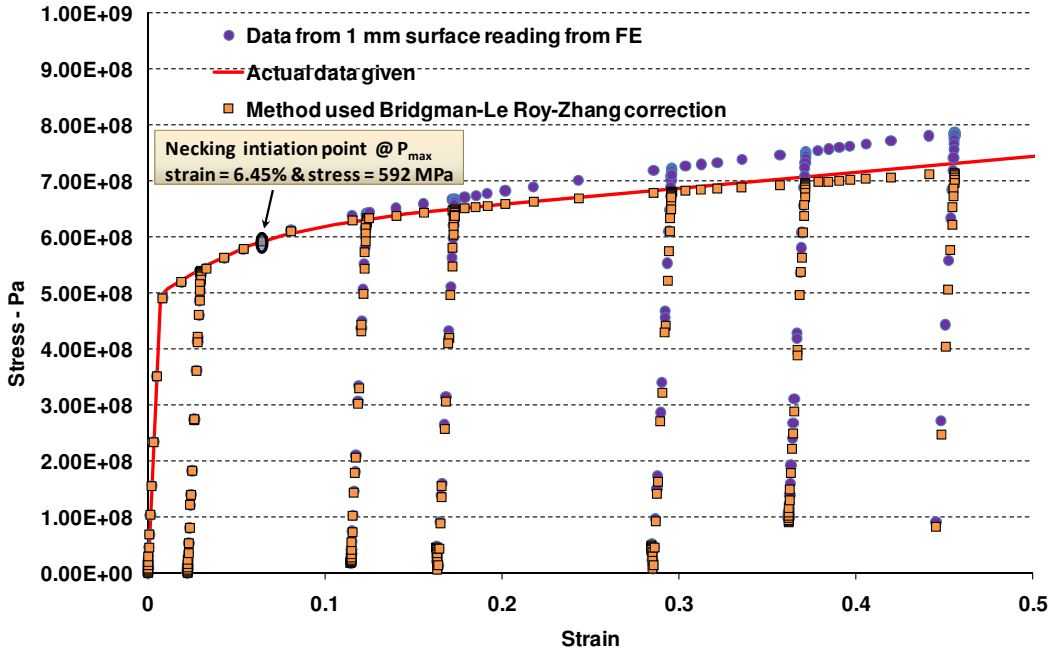

Figure 7-5 Bridgman-Zhang-Le Roy correction using numerical analysis for uniaxial cyclic test for AA7010 isotropic material parameters

The standard tensile tests were first performed using the simulation coupons and then the cyclic tests were performed. Using the correction procedure the true stress-strain curves were obtained. The extensometer reading and direct surface strain measurements were used to study the correction procedure by simulating the coupons on Abaqus inbuilt implicit code. The minimum thickness has been identified using reference point shown in Figure 7-7. The reference points were chosen at location where the specimen does not deform.

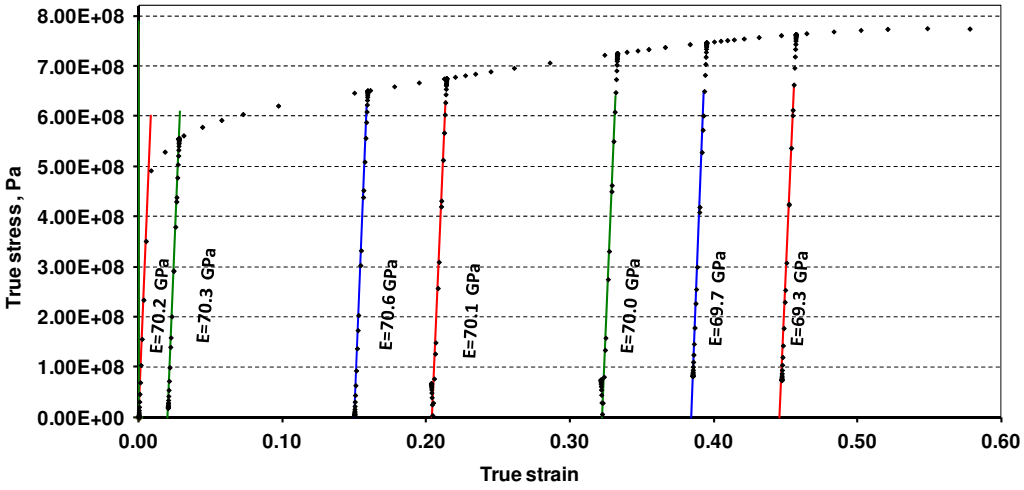

Figure 7-6 Young's modulus check after Bridgman, Zhang & Le Roy correction for AA7010 isotropic material parameters under uniaxial loading condition; the slope lines are highlighted with red, green and blue to show the Young's modulus clearly

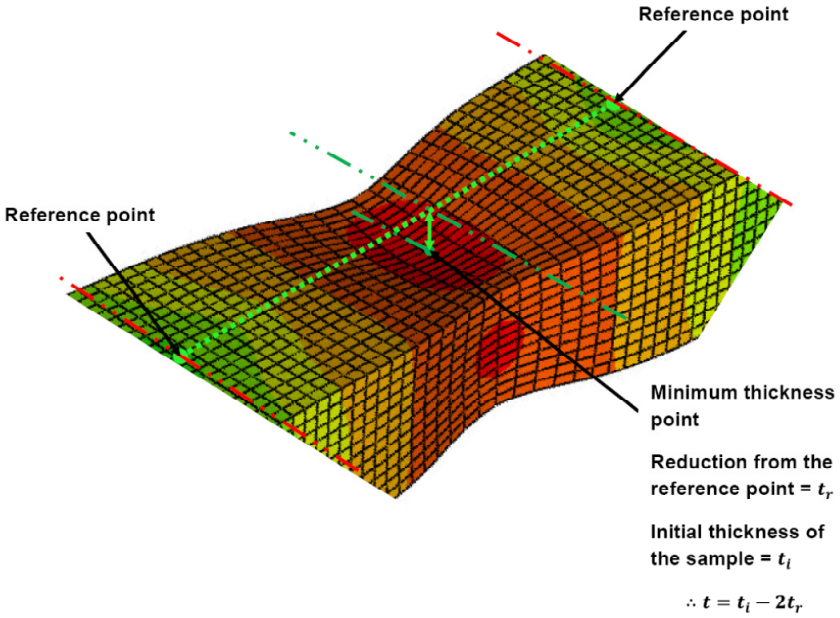

Figure 7-7 Bridgman Zhang correction measurement of current thickness "t" (for rectangular specimen) for simulation and ISTRA-3D experimental data

The results prior to correction and after the corrections are presented in Figure 7-4 to Figure 7-6. The results from cyclic test simulations surface strain reading is presented in Figure 7-5 and Figure 7-6 show that the correction procedure proposed by Zhang can be successfully implemented for cyclic test simulation cases using FE software. The cyclic test data were checked for elastic modulus to verify whether there are any changes in modulus due to anomalies in the procedure. The modulus check results shown in Figure 7-6 are consistently same for the operating strain (40%) of the AA7010 aluminium material. These tests prove that the methods and procedure used here establish acceptable correction after necking.

7.2.2 Implementation of Bridgman-Zhang-Le Roy correction for DIC

The Bridgman-Zhang-Le Roy method was implemented in the present form to determine true stress-strain data from the DIC measurements. From the ISTRA-4D tensile test data the minimum thickness point was identified, two reference points were identified as shown in Figure 7-7 to measure the reduction in thickness.

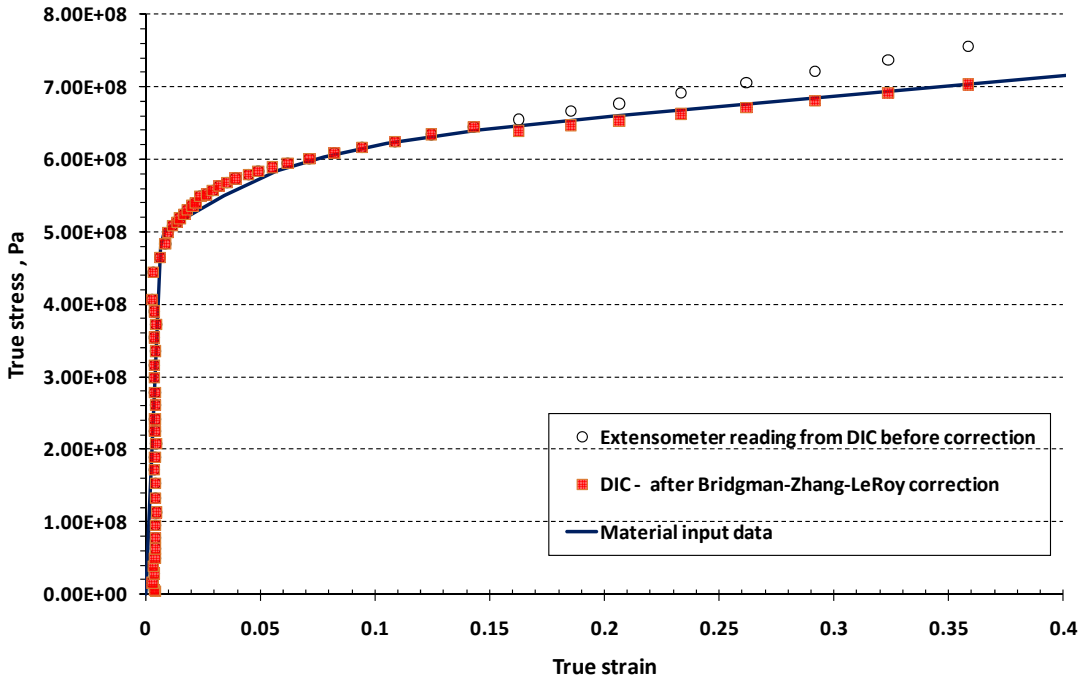

Figure 7-8 Bridgman-Zhang-Le Roy correction for uniaxial standard tensile test with AA7010 material properties obtained using DIC technique

The displacement measurement of the thickness axis (Z) and reference points were obtained from the ISTRA-4D output data. The data were plotted and compared with

FE simulation results. The results obtained form the ISTRA-4D for standard tensile test result is shown in Figure 7-8 and it can be noticed that the extensometer reading and are not accurate after necking. The extensometer reading measurement from DIC is then corrected using Bridgman, Zhang and Le-Roy procedure to get accurate results.

The cyclic test data from ISTRA-4D measurements were then obtained. It can be observed from the Figure 7-9 the reference points Z displacement from ISTRA-4D cyclic data is not constant as in FE simulation. The result obtained from this method is shown in Figure 7-10; the variation in the results is due the shifting of reference point. Several DIC test data were checked and reference points were determined in this study; however the shifting of reference point in the present DIC field of view made it difficult to apply the present Bridgman-Zhang-Le Roy correction method.

The DIC results were checked for rigid body movement as shown in Figure 7-9 though the midpoint stays in straight line the reference points keep shifting. The results obtained from the reference point and minimum thickness are then used to calculate the corrected true stress-strain curve. The results are shown in Figure 7-10, it is evident that the correction procedure from data obtained from the DIC technique for a cyclic test does not produce expected result. It also shows that the method used by Zhang cannot be applied for present DIC measurement technique. The possibility of using fixed reference point can only be achieved from the present DIC instrument is, to observe three or four fixed points within the field of view which does not alter. This can be achieved by using an external fixed pointer which is not a part of deformation area or the non-varying reference point in the specimen should be marked with some special identification and observed along with the measurement field of view. Alternatively three optical cameras can be used instead of two, one dedicated to observe the variation in thickness. From the actual minimum thickness measured using the third camera Zhang correction procedure can be implemented successfully.

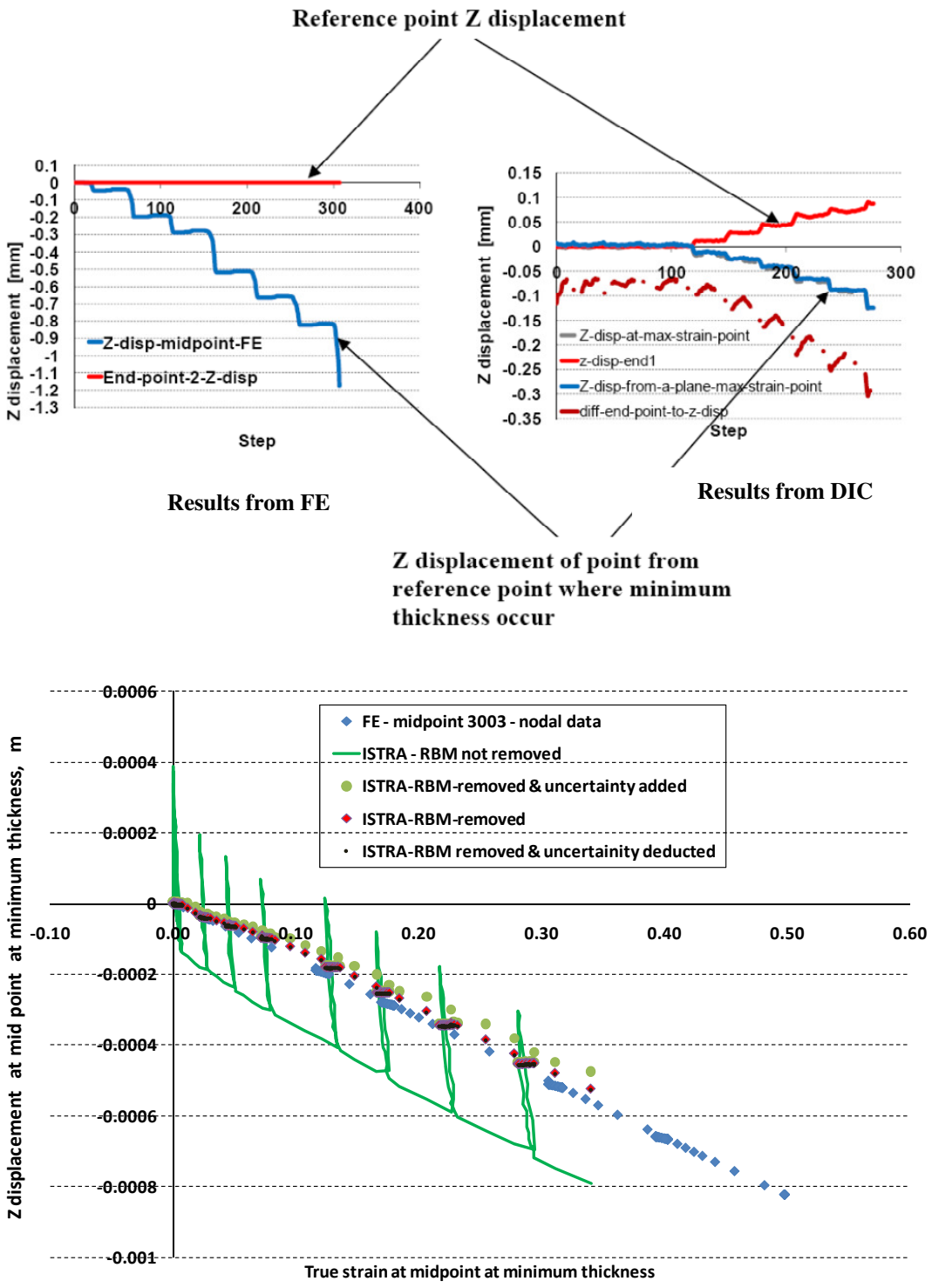

Figure 7-9 True strain vs displacement at midpoint for uniaxial cyclic test on AA7010 – comparison with FE test data

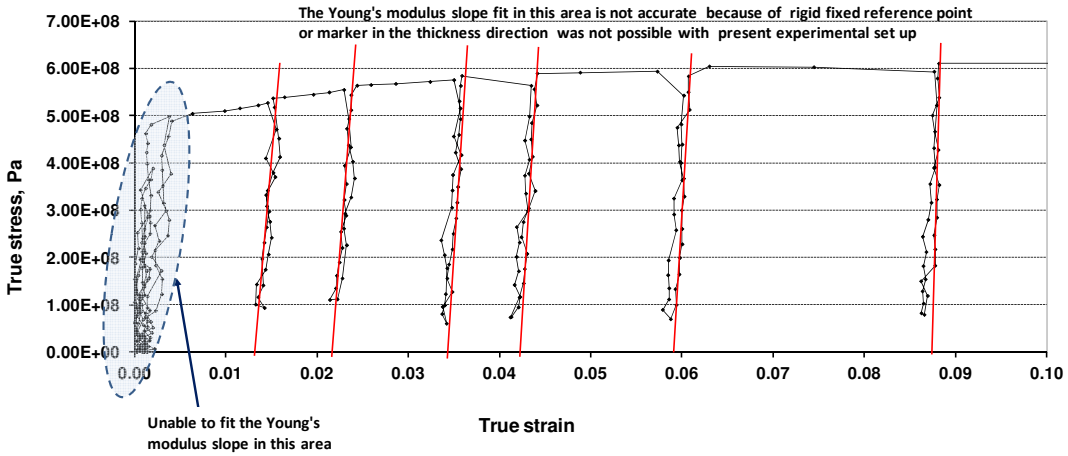

Figure 7-10 Zhang correction procedure for AA7010 uniaxial experimental results using DIC, the thickness measurement is not accurate in DIC due to reference point with respect to thickness is not stationary in the current experimental set up

7.3 Proposal of width ratio based correction methods

A new procedure for correcting the data obtained from DIC cyclic test has been proposed here. A correction method with true strain obtained from the ISTRA-4D is used in this correction procedure. From the true strain provided by DIC measurement approximate stress is calculated and the correction were made using Bridgman proposed method. A newly identified empirical equation called "measurement width ratio" is used for the calculation of *a/R*. The determination of a/R is shown in Figure 7-11. The "measurement width ratio" is also referred as "width ratio" in this thesis report. The width ratio correction is used in place of Le Roy empirical equation (7.7) to improve the correction results. The proposed new method has been implemented using Abaqus standard model for standard tensile test and cyclic test results. The new method was also implemented for a cyclic test results obtained from Dantec ISTRA-4D software.

From the experimental result using ISTRA-4D the true strain has been measured from selected area (Figure 7-11) Along with the reaction forces. These two measurements are then used to calculate the approximate stress, correction and true stress. The procedure to calculate the true stress from the ISTRA-4D data is explained here. To apply this correction procedure the original width (breadth) of the specimen b_0 should be greater than measurement length l_{ms} (Figure 7-11).

Calculate engineering stress

$$\sigma_{eng} = \frac{F}{A_0} \quad \text{(Eq. 7.11)}$$

where σ_{eng} is the engineering stress, F is the total reaction force at the end of the specimen, A_0 is the original cross-sectional area of the specimen.

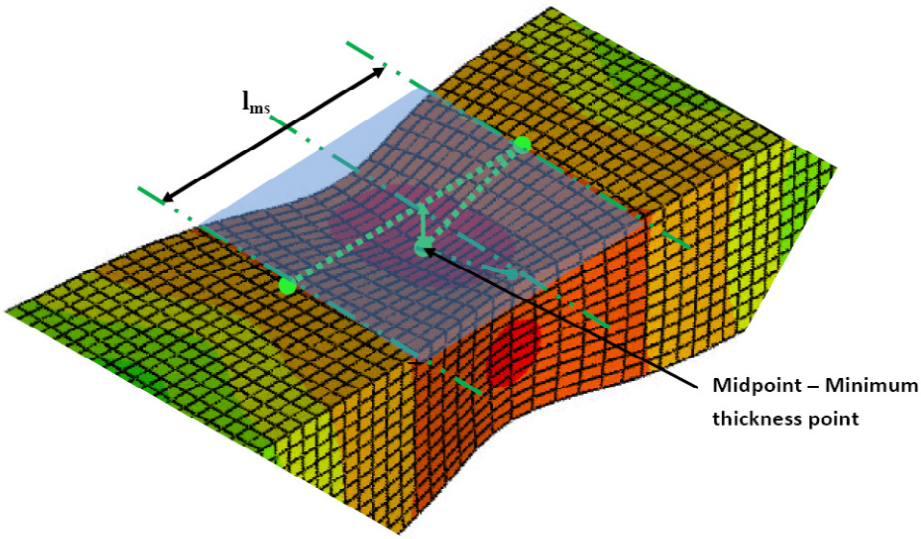

$\mathbf{b_0}$ – original width of the specimen

$\mathbf{l_{ms}}$ – length of the measuring surface in the longitudinal direction

$\boldsymbol{\varepsilon}$ - true strain measured from the surface

$\boldsymbol{\varepsilon_{p-Pmax}}$ - plastic strain from at P_{max} (Plastic strain at F_{max})

$$\frac{\mathbf{a}}{\mathbf{R}} = \left[\frac{\mathbf{b_0 - l_{ms}}}{\mathbf{b_0}}\right]\left(\boldsymbol{\varepsilon} - \boldsymbol{\varepsilon_{p-Pmax}}\right) \quad \text{where} \quad \mathbf{b_0 > l_{ms}}$$

Figure 7-11 New empirical equation for a/R calculation using measurement surface

From the true strain obtained from the ISTRA-4D calculate approximated true stress

$$\sigma_{appx-true} = \sigma_{eng} e^{\varepsilon} \quad \text{(Eq. 7.12)}$$

Calculate the ratio of radius of curvature for rectangular specimen a/R (Figure 7-11)

$$\frac{a}{R} = \left[\frac{b_0 - l_{ms}}{b_0}\right]\left(\varepsilon - \varepsilon_{p-Pmax}\right) \quad \text{where} \quad b_0 > l_s \quad \text{(Eq. 7.13)}$$

Use Bridgman correction to calculate the true stress.

$$\sigma_{true} = \sigma_{appx-true}\left[\frac{1}{\left(1+\frac{2R}{a}\right)ln\left(1+\frac{a}{2R}\right)}\right] \quad \text{(Eq. 7.14)}$$

7.3.1 Implementation of width ratio correction procedure

Similar to the implementation of Zhang correction procedure the width ratio correction procedure was checked using FE models. The FE model with AA7010 properties and AA2024 properties were checked. Initially from the FE simulation 2 mm average surface reading was measured as shown in Figure 7-11. The proposed width ratio correction was calculated using equations from 7.11 to 7.14. The results were compared with Le Roy correction method. Additional measurements were made using 1 mm, 2 mm, and 5 mm surfaces. In the new method, calculation of a/R uses plastic strain "ε_p" at P_{max} (necking initiation point) instead of true strain "ε". This improves the prediction of the true stress-strain curve.

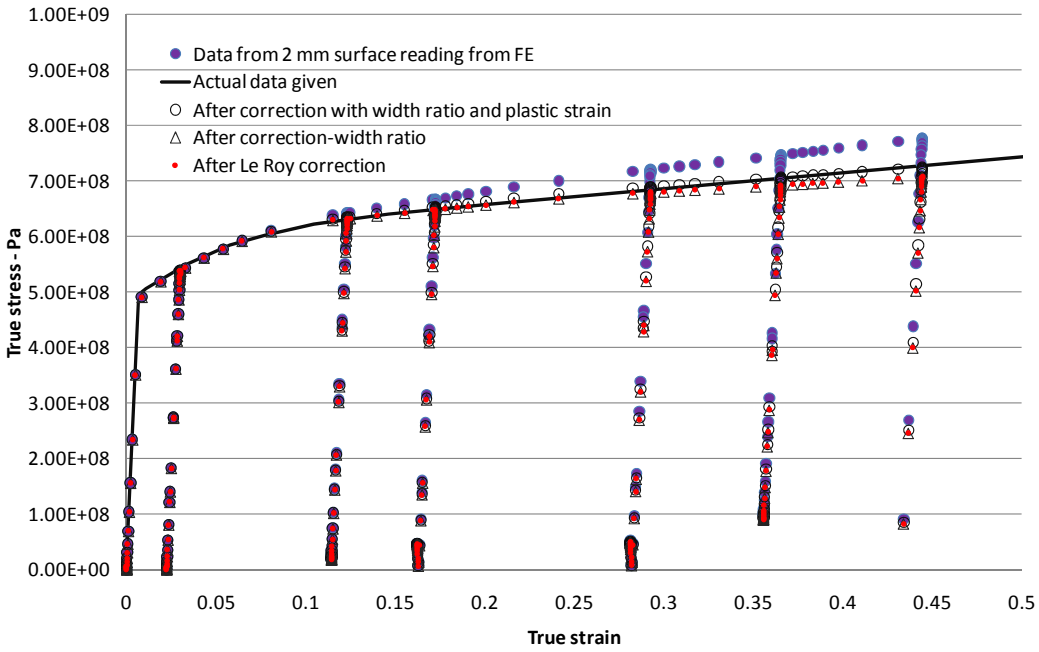

Figure 7-12 Surface true stress and true strain measurement for 2 mm surface strip for uniaxial loading case

The comparison of these results shown in Figure 7-12, Figure 7-13 and Figure 7-14 prove that new method proposed in this research predict the true stress-strain data better.

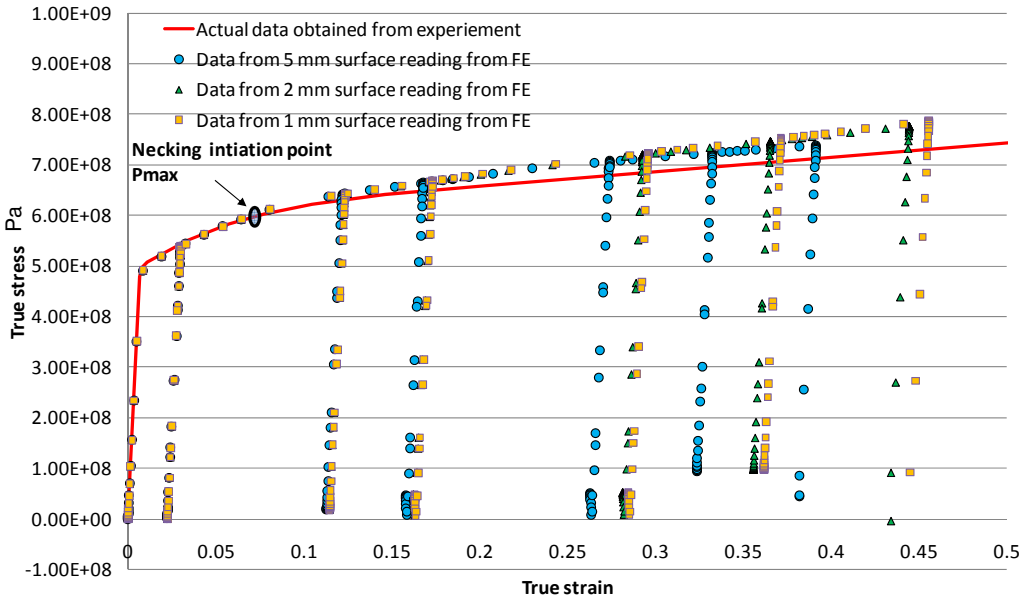

Figure 7-13 Measurement of surface strain and calculation of stress from the FE model to check the applicability for extracting uniaxial experimental data from optical technique

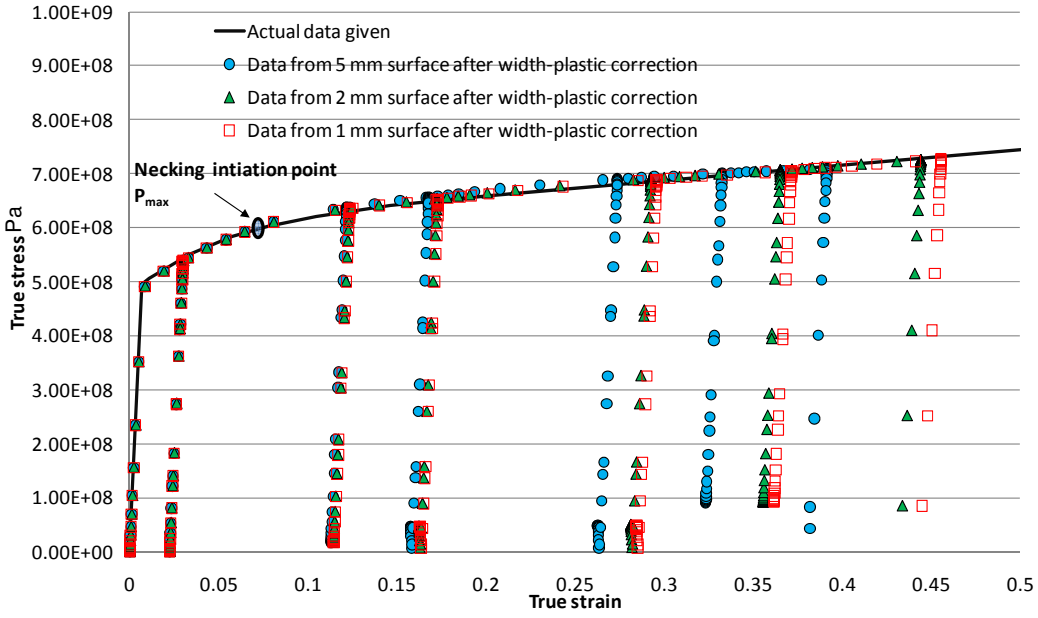

Figure 7-14 Corrected surface true stress-strain curve from FE model (AA7010) under uniaxial loading condition

The tests were then used directly to check the applicability to optical measurements. The average surface strain was measured for the surface area as shown in Figure 7-11.

The equation from 7.11 to 7.14 was used to calculate the correction. The results are shown in Figure 7-15. The results show that this method can be used for measuring the data from the ISTRA-3D using surface strain measurement.

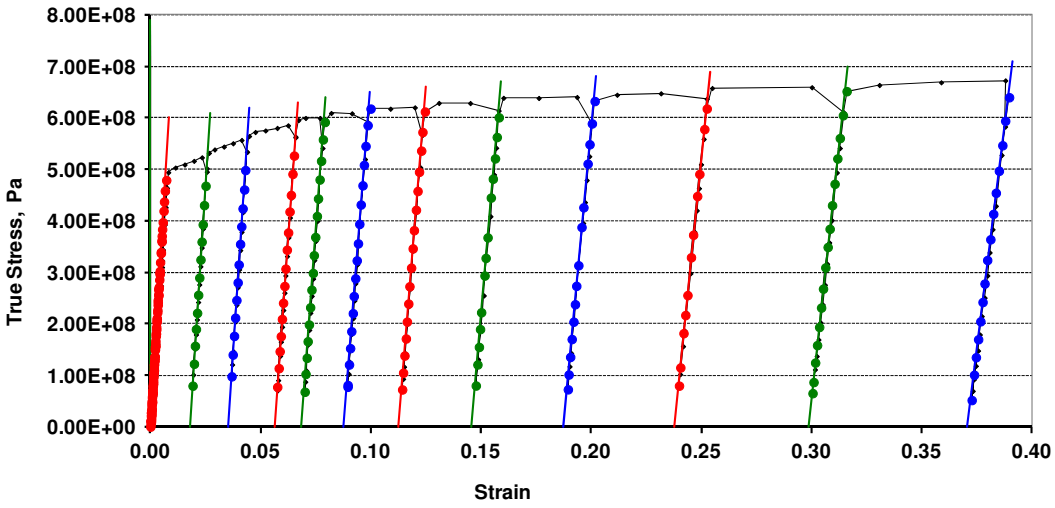

Figure 7-15 AA7010 material measurements after correction to get the modulus degradation and subsequent damage under uniaxial loading condition; the slope lines are highlighted with red, green and blue with dots to show the Young's modulus clearly

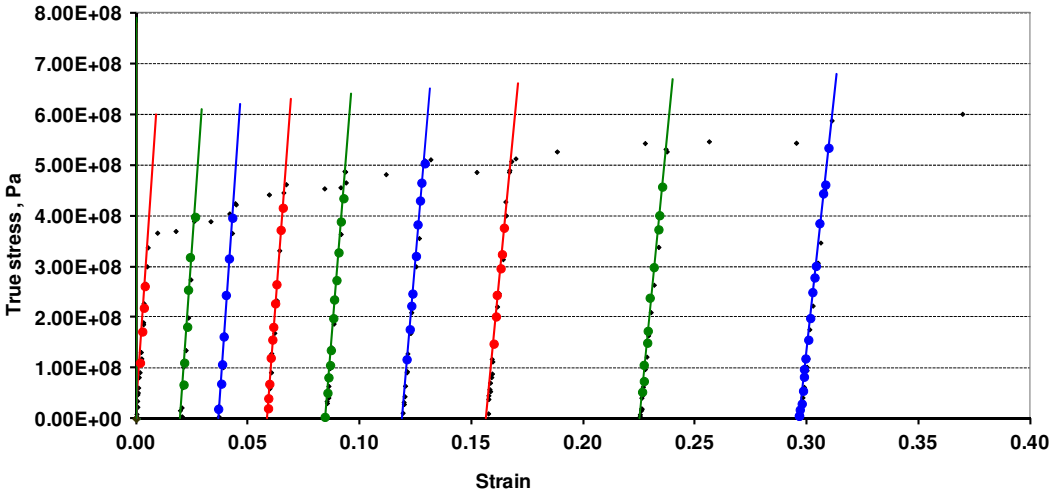

Figure 7-16 AA2024 material parameter results after width-ratio correction procedure for uniaxial loading condition; the slope lines are highlighted with red, green and blue and dots to show the slopes clearly

The true stress-strain curve obtained through the new method was tested for elastic modulus degradation using FE simulation. One of the results is shown for AA2024 material in Figure 7-16. Surface stress strain measurement for AA-2024 without damage was used and new width ratio correction method was applied. The results

obtained from the new method shows the Young's modulus degradation form the true stress-strain curve is within the acceptable limits.

7.4 True stress-strain correction methods conclusion

The Zhang-Bridgman-Le Roy correction procedure has been checked for AA7010 and AA2024 experimental results using FE simulations. The correction procedure was then directly applied to experimental results obtained from DIC technique. But it didn't produce acceptable results cyclic test case with DIC test data, due to the shifting of reference points in DIC. A new correction method called "width ratio" has been proposed and tested using FE simulation. The new method has been successfully tested for plastic deformation on thin aluminium specimen for cyclic data obtained from DIC technique. In this research the new width ratio correction procedure works well for 2.5 mm and 6.5 mm thick dog bone specimens. However the new width ratio method results do not calculate the true strain directly from the shape function and geometry of the specimen at that instant. Without the data of minimum thickness it is difficult to calculate actual area after necking accurately. The new method has not been tested for thick specimens and large plastic deformation cases and it might not produce very accurate results when large plastic deformation occurs.

The limitations of this method are described in this paragraph and alternate method of fixed point reference and additional camera to measure the thickness are proposed to calculate minimum thickness of specimen at particular instance. For better application of the Zhang-Bridgman-Le Roy correction procedure, fixed reference points need to be incorporated into the measurement field. This fixed reference points should be within the visibility of camera. The fixed reference point data from the DIC measurement point can be used to calculate the minimum thickness of the specimen during deformation. This can be achieved by using external fixed pointer with in the field of view. Another method is to use an additional camera dedicated to measure the thickness of the specimen. The measured specimen thickness can be used for the correction procedure. The new empirical width-ratio procedure to obtain a/R can also be utilised in Zhang-Bridgman correction method instead of Le Roy empirical equation to improve the results.

8 Damage model implementation

The damage model defined by Chow and Wang (1987) and Lu and Chow (1999) provide the theoretical background of the model. The damage model based on their assumption is used to formulate the numerical damage calculation for implementation in the explicit code. The plastic potential function and damage potential function are used for the new derivation of plastic multiplier and damage multiplier. The derivation of these multipliers facilitates the calculation of numerical plastic parameter from the flow stress and plastic strain and the numerical damage parameter from the damage initiation stress B_o and the slope of $dB/d\beta$ data provided as material input in the FE code. The derived equations are successfully implemented in Abaqus explicit VUMAT code and validated using experimental test data for AA-2024 and AA-7010. The Chow and Wang (1987) damage model is implemented in Abaqus VUMAT explicit code. Hence the present implementation is valid for very small increment where damage increment in current step has an insignificant effect on the plastic part. It should be emphasised that if the user want to use the present code for prediction of material damage then one should use only with explicit integration method.

In this chapter implementation of orthotropic behaviour using a damage model was described in brief. The material model should be able to predict elastic-plastic behaviour with strain-hardening including orthotropic behaviour for both elasticity and plasticity. Rate dependency and thermal softening were not included in the model, but the implementation should not prevent their inclusion in the future if necessary. Various methods of implementing orthotropic behaviour were extensively reviewed from papers (Hill 1948, 1964, 1990, 1993; Oller, Car and Lubliner, 2002; DYNA3D user manual, 1998; Borst and Feenstra,1990; Barlat, Lege and Brem, 1991; Barlat and Lian, 1989; Aretz, Hopperstad and Lademo, 2007; Brunig, 2003 and De Vuyst, 2003).

8.1 Damage model and numerical implementation in Abaqus

Chow and Wang (1987) proposed a generalised anisotropic damage theory in elasticity and extended it to plasticity and evolution of damage in ductile fracture using continuum damage mechanics based on the energy equivalence principle

(Sidoroff (1981); Sidoroff and Cordebois (1982); Cordebois, (1983); Ju (1989)). Chow and Wang introduced a modified damage effect tensor **M(D)** for the virgin material stress equations which can be applied for general structural analysis. This damage model is used in this research for numerical implementation in Abaqus explicit VUMAT code. Detailed theoretical review of the assumption are provided in Chow and Wang (1987) and Lu and Chow (1999); the derivation of the plastic multiplier and damage multiplier are based on theories of these two papers. The application of damage effect tensor **M(D)** was used by earlier researcher Mirkovic (2004) and Panov (2006) at Cranfield university for modelling damage. The damage effect tensor is used in this thesis with the Chow and Wang damage growth model to simulate Aluminium AA2024 and AA7010.

8.1.1 Plastic multiplier $\dot{\lambda}_p$ calculation

The determination of plastic multiplier can be derived based on Lu and Chow (1990) proposed theory summarised in chapter 5. The plastic potential is defined by the equation (5.24) in chapter 5 is;

$$F_p(\sigma_H, D, R) = F_p(\tilde{\sigma}_H, R) = \tilde{\sigma}_H - \left\lfloor \sigma_{y_0} + R(p) \right\rfloor = 0$$

From the plasticity consistency relation $\dot{F}_p = 0$ the plastic multiplier under loading could be derived as under

$$\dot{F}_p = \frac{\partial F_p}{\partial \sigma}\dot{\sigma} - \frac{\partial F_p}{\partial R}\dot{R} = 0 \qquad \text{(Eq. 8.1)}$$

here

$$\frac{\partial F_p}{\partial R} = -1 \qquad \text{(Eq. 8.2)}$$

Therefore the consistence condition can be written as

$$\dot{F}_p = \frac{\partial F_p}{\partial \sigma}\dot{\sigma} + \dot{R} = 0 \qquad \text{(Eq. 8.3)}$$

The constitutive equation for the damaged material

$$\sigma = \tilde{C}_e \varepsilon_e \qquad \text{(Eq. 8.4)}$$

And the strain decomposition can be written as

$$\varepsilon = \varepsilon_e + \varepsilon_p \qquad \text{(Eq. 8.5)}$$

$$\dot{\sigma} = \tilde{C}_e(\dot{\varepsilon} - \dot{\varepsilon}_p) \qquad \text{(Eq. 8.6)}$$

Using isotropic hardening rule

$$\dot{R} = \frac{dB}{dt} \qquad \text{(Eq. 8.7)}$$

$$\dot{R} = \frac{dR}{dp}\frac{dp}{dt} = \frac{dR}{dp}\dot{\lambda}_p \qquad \text{(Eq. 8.8)}$$

Substitute this equation (8.8) in equation (8.3) where $\frac{dR}{dp}$ material hardening parameter at that instance.

$$\dot{\boldsymbol{F}}_p = \frac{\partial \boldsymbol{F}_p}{\partial \boldsymbol{\sigma}}\dot{\boldsymbol{\sigma}} + \frac{dR}{dp}\dot{\lambda}_p = \mathbf{0} \qquad \text{(Eq. 8.9)}$$

Substitute $\dot{\sigma} = \tilde{C}_e(\dot{\varepsilon} - \dot{\varepsilon}_p)$ in the equation (8.9) then

$$\dot{\boldsymbol{F}}_p = \frac{\partial \boldsymbol{F}_p}{\partial \boldsymbol{\sigma}}\tilde{\boldsymbol{C}}_e(\dot{\boldsymbol{\varepsilon}} - \dot{\boldsymbol{\varepsilon}}_p) + \frac{dR}{dp}\dot{\lambda}_p = \mathbf{0} \qquad \text{(Eq. 8.10)}$$

$$\dot{\boldsymbol{F}}_p = \frac{\partial \boldsymbol{F}_p}{\partial \boldsymbol{\sigma}}\tilde{\boldsymbol{C}}_e\dot{\boldsymbol{\varepsilon}} - \frac{\partial \boldsymbol{F}_p}{\partial \boldsymbol{\sigma}}\tilde{\boldsymbol{C}}_e\dot{\boldsymbol{\varepsilon}}_p + \frac{dR}{dp}\dot{\lambda}_p = \mathbf{0} \qquad \text{(Eq. 8.11)}$$

From the plastic stain rate provided by Chow and Wang (1987) substitute the plastic strain rate in equation (8.11) with following expression in equation (8.12) to get equation (8.13)

$$\dot{\varepsilon}_p = \frac{\partial \boldsymbol{F}_p}{\partial \boldsymbol{\sigma}}\dot{\lambda}_p \qquad \text{(Eq. 8.12)}$$

$$\dot{\boldsymbol{F}}_p = \frac{\partial \boldsymbol{F}_p}{\partial \boldsymbol{\sigma}}\tilde{\boldsymbol{C}}_e\dot{\boldsymbol{\varepsilon}} - \frac{\partial \boldsymbol{F}_p}{\partial \boldsymbol{\sigma}}\tilde{\boldsymbol{C}}_e\frac{\partial \boldsymbol{F}_p}{\partial \boldsymbol{\sigma}}\dot{\boldsymbol{\lambda}}_p + \frac{dR}{dp}\dot{\lambda}_p = \mathbf{0} \qquad \text{(Eq. 8.13)}$$

and solve for $\dot{\lambda}_p$

$$\dot{\lambda}_p = \frac{\frac{\partial \boldsymbol{F}_p}{\partial \boldsymbol{\sigma}}\tilde{\boldsymbol{C}}_e\dot{\boldsymbol{\varepsilon}}}{\frac{\partial \boldsymbol{F}_p}{\partial \boldsymbol{\sigma}}\tilde{\boldsymbol{C}}_e\frac{\partial \boldsymbol{F}_p}{\partial \boldsymbol{\sigma}} - \frac{dR}{dp}} \qquad \text{(Eq. 8.14)}$$

Here substitute the following equations to calculate plastic multiplier $\dot{\lambda}_p$

$$\frac{\partial \boldsymbol{F}_p}{\partial \boldsymbol{\sigma}} = \frac{\boldsymbol{1}}{2\tilde{\boldsymbol{\sigma}}_p}\tilde{\boldsymbol{H}} : \boldsymbol{\sigma} \qquad \text{(Eq. 8.15)}$$

$\frac{dR}{dp}$ is a material hardening parameter at that instance

$\tilde{\mathbf{C}}_{\mathbf{e}}$ is the damaged elastic coefficient matrix

$$\dot{\lambda}_p = \frac{\frac{1}{2\tilde{\sigma}_H}\left[\{\tilde{H}\}\{\sigma\}\right]\left[\{\tilde{C}_e\}\{\dot{\varepsilon}\}\right]}{\frac{1}{4\tilde{\sigma}_H^2}\left[\{\tilde{H}\}\{\sigma\}\right]\left[\{C\}\{\tilde{H}\}\{\sigma\}\right]-\frac{dR}{dp}} \qquad \text{(Eq. 8.16)}$$

Numerically this is solved in Abaqus explicit code as

$$\dot{\varepsilon}_p = \frac{\tilde{\sigma}_H - \sigma_{flow}}{\frac{1}{\tilde{\sigma}_H^2}\{\tilde{H}\}\{\sigma\}\}\{C\}\{\tilde{H}\}\{\sigma\}\}-\frac{dR}{dp}} \qquad \text{(Eq. 8.17)}$$

8.1.2 Damage multiplier $\dot{\lambda}_d$ calculation

Similarly the damage potential can be calculated from the equation (5.27) defined in chapter 5.

$$F_d(\tilde{\sigma}_d, B) = \tilde{\sigma}_d - \left[B_0 + B(\beta)\right] = 0$$

From the damage consistency relation the damage multiplier could be derived as under

$$\dot{\boldsymbol{F}}_{\boldsymbol{d}} = \frac{\partial \boldsymbol{F}_{\boldsymbol{d}}}{\partial \boldsymbol{\sigma}}\dot{\boldsymbol{\sigma}} + \frac{\partial \boldsymbol{F}_{\boldsymbol{d}}}{\partial \boldsymbol{B}}\dot{B} = \mathbf{0} \qquad \text{(Eq. 8.18)}$$

here

$$\frac{\partial \boldsymbol{F}_{\boldsymbol{d}}}{\partial \boldsymbol{B}} = -1 \qquad \text{(Eq. 8.19)}$$

therefore

$$\dot{\boldsymbol{F}}_{\boldsymbol{d}} = \frac{\partial \boldsymbol{F}_{\boldsymbol{d}}}{\partial \boldsymbol{\sigma}}\dot{\boldsymbol{\sigma}} - \dot{B} = \mathbf{0} \qquad \text{(Eq. 8.20)}$$

The damage stress rate can be written as

$$\dot{B} = \frac{dB}{dt} \qquad \text{(Eq. 8.21)}$$

Rewriting the equation (8.21) in terms of overall damage rate $d\beta$

$$\dot{B} = \frac{dB}{d\beta}\frac{d\beta}{dt} = \frac{dB}{d\beta}\dot{\lambda}_d \qquad \text{(Eq. 8.22)}$$

Substitute the equation (8.22) in equation (8.20) to get equation (8.23)

$$\dot{F}_d = \frac{\partial \boldsymbol{F_d}}{\partial \boldsymbol{\sigma}} \dot{\sigma} - \frac{dB}{d\beta} \dot{\lambda}_d = 0 \qquad \text{(Eq. 8.23)}$$

Substitute $\dot{\sigma} = \tilde{C}_e(\dot{\varepsilon} - \dot{\varepsilon}_p)$ in the equation (8.23) then

$$\dot{F}_d = \frac{\partial \boldsymbol{F_d}}{\partial \sigma} \tilde{\boldsymbol{C}}_e(\dot{\varepsilon} - \dot{\varepsilon}_p) - \frac{dB}{d\beta} \dot{\lambda}_d = 0 \qquad \text{(Eq. 8.24)}$$

$$\dot{F}_d = \frac{\partial F_d}{\partial \sigma} \tilde{C}_e \dot{\varepsilon} - \frac{\partial F_d}{\partial \sigma} \tilde{C}_e \dot{\varepsilon}_p - \frac{dB}{d\beta} \dot{\lambda}_d = 0 \qquad \text{(Eq. 8.25)}$$

From the plastic rate provided by equation (8.12) substitite for plastic strain rate $\dot{\varepsilon}_p$ in equation (8.25) and solve for $\dot{\lambda}_d$

$$\dot{\lambda}_d = \frac{\frac{\partial \boldsymbol{F_d}}{\partial \boldsymbol{\sigma}} \tilde{\boldsymbol{C}}_e \dot{\boldsymbol{\varepsilon}} - \frac{\partial \boldsymbol{F_d}}{\partial \boldsymbol{\sigma}} \tilde{\boldsymbol{C}}_e \frac{\partial \boldsymbol{F_p}}{\partial \boldsymbol{\sigma}} \dot{\boldsymbol{\lambda}}_p}{\frac{dB}{d\beta}} \qquad \text{(Eq. 8.26)}$$

By substituting the equations (8.15), (8.16) and (8.27) the damage multiplier can be calculated.

$$\frac{\partial \boldsymbol{F_d}}{\partial \boldsymbol{\sigma}} = \frac{1}{2\tilde{\boldsymbol{\sigma}}_d} \tilde{\boldsymbol{J}} : \boldsymbol{\sigma} \qquad \text{(Eq. 8.27)}$$

Here $\frac{dB}{d\beta}$ is a material constant, $\tilde{\boldsymbol{C}}_e$ is the damaged elastic coefficient matrix. The damage matrices $\boldsymbol{D}$ can be calculated from the following damage rate equation (8.28).

$$\dot{\boldsymbol{D}} = \frac{\dot{\lambda}_d}{2\tilde{\boldsymbol{\sigma}}_d} \tilde{\boldsymbol{J}} : \boldsymbol{\sigma} \qquad \text{(Eq. 8.28)}$$

To apply the damage model from the damage potential equation 5.27, the damage evolution is determined.

$$f_d = \tilde{\sigma}_d - \left(B_0 + \frac{dB}{d\beta}\beta\right) = 0 \qquad \text{(Eq. 8.29)}$$

Check for damage being evolved using the following equation

$$f_d = \tilde{\sigma}_d - \left(B_0 + \frac{dB}{d\beta}\beta\right) \leq 0 \quad \text{damage not evolving} \qquad \text{(Eq. 8.30)}$$

$$f_d = \tilde{\sigma}_d - \left(B_0 + \frac{dB}{d\beta}\beta\right) \geq 0 \qquad \text{damage evolving} \qquad \text{(Eq. 8.31)}$$

For a linear damage evolution

$$\dot{B} = \frac{dB}{d\beta}\dot{\beta} \qquad \text{(Eq. 8.32)}$$

B_0 is a material constant and it should be determined from the experimental results. The effective damage rate $\dot{\tilde{\beta}}$ can be calculated from the derivation using following relationship:

$$\dot{\tilde{\beta}} = \frac{\dot{\tilde{\sigma}}_d - \dot{B}}{\frac{dB}{d\beta}} \qquad \text{(Eq. 8.33)}$$

Using Crisfield's (2000) method similar to the calculation of plastic multiplier $\dot{\lambda}_p$ the damage multiplier $\dot{\lambda}_d$ can be calculated numerically

$$Y_{dam} = B_0 + \frac{dB}{d\beta}\beta^n \qquad \text{(Eq. 8.34)}$$

$$\beta^{n+1} = \lambda_d^{n+1} = \beta^n + \frac{\tilde{\sigma}_d - Y_{dam}}{\frac{dB}{d\beta}} \qquad \text{(Eq. 8.35)}$$

Substituting the equation (8.33) in equation (8.28) the damage rate is calculated numerically.

$$\dot{\boldsymbol{D}} = \frac{1}{2\tilde{\sigma}_d}\tilde{\boldsymbol{J}} : \sigma\frac{\tilde{\sigma}_d - \dot{B}}{\frac{dB}{d\beta}} \qquad \text{(Eq. 8.36)}$$

Thus $\dot{\boldsymbol{D}}$ is calculated using the new method. Update the damage using the calculated D_1, D_2 & D_3. The results obtained through the above method match the Chow and Wang (1987 & 1988) experimental results. The overall numerical implementation procedure is given in Figure 8-1. The trial stress is calculated using the FE code from the strain increment. Then the trial stress is corrected using normal return scheme (De Borst and Feenstra, 1990; Crisfield, 2000). The corrected stress is then used to calculate the damage and damage is updated. The complete iterative steps for elastic with damage and elastoplastic with damage numerical models are explained in the next chapter 9.

Orthotropic damage implementation in Abaqus explicit code

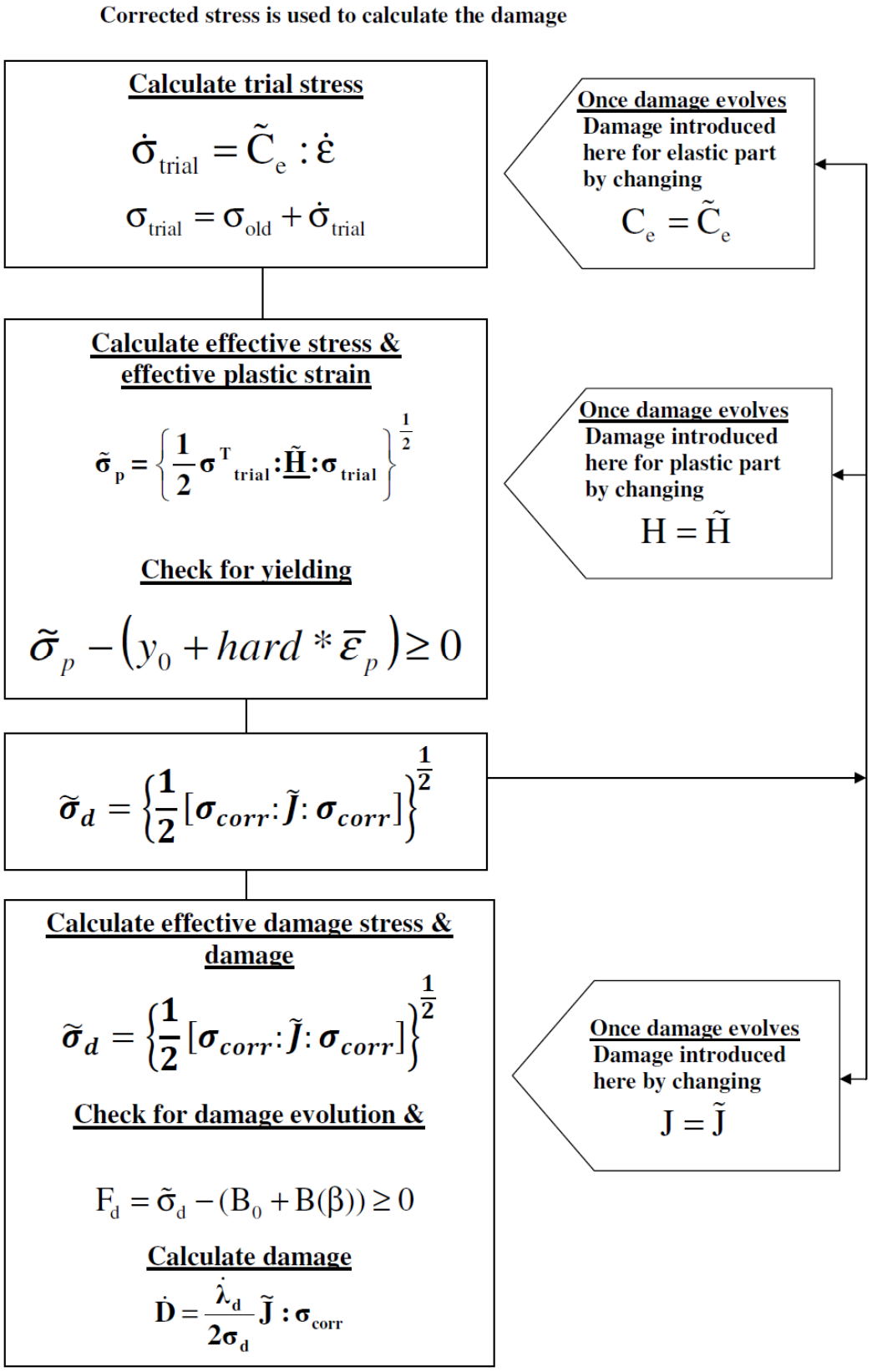

Figure 8-1 Orthotropic damage numerical implementation

8.2 Damage model implementation conclusion

The Chow and Wang damage model plastic multiplier and damage multiplier were derived in this chapter. The numerical form of calculation of plastic strain $\dot{\varepsilon}_p$ and the damage rate $\dot{D}$ are given in this chapter. The calculation of effective damage $\dot{\beta}$, damage stress $\dot{B}$, and the application of effective damage stress $\tilde{\sigma}_d$ to calculate the damage parameters are also described in this chapter. The equations provided in this chapter can be used directly for explicit numerical application in Abaqus VUMAT code.

9 Orthotropic material failure modelling in Abaqus/Explicit code

9.1 Introduction

The implementation algorithm is based on the numerical equation derived in chapter 8. At the start of the project the user material model implementation with the aid of FORTRAN 90 code in the Abaqus finite element explicit package for simulation was studied. Once it was ascertained that the Chow and Wang's damage model would be the candidate model for immediate research, the process of learning focused towards the implementation from start to finish.

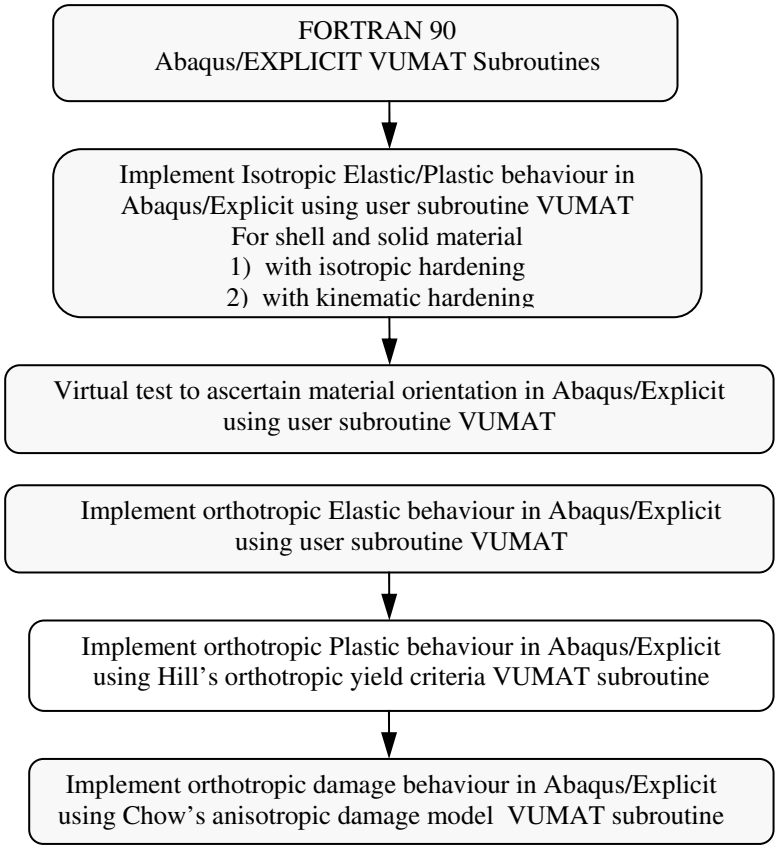

Figure 9-1 Orthotropic material failure modelling process for Abaqus/Explicit user subroutine

To start with isotropic material parameters were used to do the coding; the existing kinematic example from Abaqus has been implemented to understand the subroutine. A completely new isotropic hardening subroutine has been coded in Abaqus/Explicit VUMAT by the author. The implementation of user subroutines for Abaqus explicit simulation are discussed here in elastic with damage implementation and elastic with plastic and damage implementation. The various steps involved in implementing orthotropic material behaviour to get satisfactory results are given in Figure 9-1.

The implementation of material modelling in Abaqus explicit subroutines were completed in three phases the implementation phase, examination phase and validation phase. This procedure was applied on isotropic single element for elastic case and then the plastic behaviour was introduced into the code. Once the code was successfully implemented in single element case the isotropic behaviour was tested for multi-element models. The next level of complexity was introduced with orthotropic behaviour without damage and this was scrutinised and validated for single element case and multi-element cases. The orthotropic damage was introduced into the code and single element and multi-element models were studied and validated. The algorithm involved in the implementation is explained in this section. The Abaqus explicit model calculates "***trial stress***" from the strain increment due to loading; then the trial stress is used to calculate plastic parameters. The trial stress is then corrected based on normal return procedure (De Borst, 1990; Crisfield, 2000) the new stress is called "***corrected stress***". The corrected stress is then used to calculate the damage parameters and updated in the iterative steps. The Abaqus gives the corrected stress as output data.

9.2 Elastic and plastic region algorithm with damage

9.2.1 Anisotropic elastic and damage

The elastic tensor C_e is symmetric and thus the $\tilde{C}_e$ is also symmetric. The elastic tensor using the orthotropic 6x6 stiffness matrix is defined as:

$$C_e^{-1} = \begin{bmatrix} \frac{1}{E_1} & -\frac{v_{21}}{E_2} & -\frac{v_{31}}{E_3} & 0 & 0 & 0 \\ -\frac{v_{12}}{E_1} & \frac{1}{E_2} & -\frac{v_{32}}{E_3} & 0 & 0 & 0 \\ -\frac{v_{13}}{E_1} & -\frac{v_{23}}{E_2} & \frac{1}{E_3} & 0 & 0 & 0 \\ 0 & 0 & 0 & \frac{1}{G_{12}} & 0 & 0 \\ 0 & 0 & 0 & 0 & \frac{1}{G_{23}} & 0 \\ 0 & 0 & 0 & 0 & 0 & \frac{1}{G_{31}} \end{bmatrix} \qquad \text{(Eq. 9.1)}$$

The material parameter can be written in following form

$$C_e = \begin{bmatrix} \frac{E_1(1-v_{32}v_{23})}{\Delta} & \frac{E_2(v_{12}+v_{13}v_{32})}{\Delta} & \frac{E_3(v_{13}+v_{12}v_{23})}{\Delta} & 0 & 0 & 0 \\ \frac{E_1(v_{21}+v_{23}v_{31})}{\Delta} & \frac{E_2(1-v_{13}v_{31})}{\Delta} & \frac{E_3(v_{23}+v_{21}v_{13})}{\Delta} & 0 & 0 & 0 \\ \frac{E_1(v_{31}+v_{21}v_{32})}{\Delta} & \frac{E_2(v_{32}+v_{12}v_{31})}{\Delta} & \frac{E_3(1-v_{21}v_{12})}{\Delta} & 0 & 0 & 0 \\ 0 & 0 & 0 & G_{12} & 0 & 0 \\ 0 & 0 & 0 & 0 & G_{23} & 0 \\ 0 & 0 & 0 & 0 & 0 & G_{13} \end{bmatrix}$$

(Eq. 9.2)

where E_1, E_2, E_3 are Young's modulus in the respective direction

$v_{12}, v_{21}, v_{23}, v_{32}, v_{13}, v_{31}$ are Poisson's ratio and G_{12}, G_{23}, G_{13} are shear modulus

$$\Delta = 1 - v_{21}v_{12} - v_{31}v_{13} - v_{32}v_{23} - v_{12}v_{23}v_{31} - v_{21}v_{13}v_{32} \quad \text{(Eq. 9.3)}$$

$$\frac{v_{12}}{E_1} = \frac{v_{21}}{E_2}, \frac{v_{31}}{E_3} = \frac{v_{13}}{E_1}, \frac{v_{32}}{E_3} = \frac{v_{23}}{E_2} \quad \text{(Eq. 9.4)}$$

$$E_1(v_{21}+v_{23}v_{31}) = E_2(v_{12}+v_{13}v_{32})$$

$$E_1(v_{31}+v_{21}v_{32}) = E_3(v_{13}+v_{12}v_{23}) \quad \text{(Eq. 9.5)}$$

$$E_2(v_{32}+v_{12}v_{31}) = E_3(v_{23}+v_{21}v_{13})$$

In the Abaqus user code the trial stress increment can be calculated from the equation (9.6) with damage included in the elastic region. The constitutive equation (9.6) gives the trial stress without damage which is used in the numerical calculation. The trial stress constitutive equation with damage is given by the equation (9.7)

$$\boldsymbol{\sigma}_t = \boldsymbol{C}_e \boldsymbol{\varepsilon}_{\mathbf{e}} \quad \text{(Eq. 9.6)}$$

$$\boldsymbol{\sigma}_t = \tilde{\boldsymbol{C}}_e \boldsymbol{\varepsilon}_{\mathbf{e}} \quad \text{(Eq. 9.7)}$$

If damage does not exist that is when $D_1 = D_2 = D_3 = 0$ the equation (9.7) simply reduces to elastic stiffness tensor C_e. The damage compliance $\tilde{C}_{\mathbf{e}}$ matrix is given in equation (9.18). The following notations are used in the explanation of the algorithm;

$\sigma -$ is the damaged material stress

$\tilde{\boldsymbol{\sigma}} -$ is the stress in undamaged material

$\boldsymbol{C_e = C = C_{ijkl}}$ - is the stiffness co-efficient constitutive tensor for damaged material

$\tilde{C}_e = \tilde{C} = \tilde{C}_{ijkl}$ - is the stiffness co-efficient constitutive tensor for undamaged material

$\dot{\boldsymbol{\varepsilon}} = \dot{\boldsymbol{\varepsilon}}_{\boldsymbol{ij}}$ - is the strain rate tensor

$\dot{\boldsymbol{\varepsilon}}_{\boldsymbol{e}} = \dot{\boldsymbol{\varepsilon}}_{\boldsymbol{e_{ij}}}$ - is the elastic strain rate tensor

$\dot{\boldsymbol{\varepsilon}}_{\boldsymbol{p}} = \dot{\boldsymbol{\varepsilon}}_{\boldsymbol{p_{ij}}}$ - is the plastic strain rate tensor

9.2.2 Elastic region algorithm with trial damage calculation

The Abaqus explicit code is first implemented for elastic behaviour. The increment in trial stress is assumed to be in the elastic region.

$$\boldsymbol{\sigma^{t_{n+1}} = \sigma^{t_n} + C\Delta\sigma_e^{t_{n+\frac{1}{2}}}} \quad \text{(Eq. 9.8)}$$

Calculation of damage in elastic region

Calculate the effective damage stress from the trial stress

$$\tilde{\boldsymbol{\sigma}}_{\boldsymbol{D}}^{\boldsymbol{t_{n+1}}} = \sqrt{\frac{1}{2}\{\boldsymbol{\sigma^{t_{n+1}}}\}[\tilde{\boldsymbol{J}}]\{\boldsymbol{\sigma^{t_{n+1}}}\}} \quad \text{(Eq. 9.9)}$$

$$\tilde{\boldsymbol{J}} = 2\begin{bmatrix} \frac{1}{(1-D_1)^2} & \frac{\mu}{(1-D_1)(1-D_2)} & \frac{\mu}{(1-D_1)(1-D_3)} & 0 & 0 & 0 \\ \frac{\mu}{(1-D_1)(1-D_2)} & \frac{1}{(1-D_2)^2} & \frac{\mu}{(1-D_2)(1-D_3)} & 0 & 0 & 0 \\ \frac{\mu}{(1-D_3)(1-D_1)} & \frac{\mu}{(1-D_3)(1-D_2)} & \frac{1}{(1-D_3)^2} & 0 & 0 & 0 \\ 0 & 0 & 0 & \frac{2(1-\mu)}{(1-D_1)(1-D_2)} & 0 & 0 \\ 0 & 0 & 0 & 0 & \frac{2(1-\mu)}{(1-D_2)(1-D_3)} & 0 \\ 0 & 0 & 0 & 0 & 0 & \frac{2(1-\mu)}{(1-D_3)(1-D_1)} \end{bmatrix}$$

(Eq. 9.10)

Calculate the increment in damage threshold stress

$$\Delta B^{t_{n+\frac{1}{2}}} = B^{t_{n+1}} - B^{t_n} = \sigma_{\text{dtrial}}^{\text{t}_{\text{n+1}}} - \sigma_{\text{dtrial}}^{\text{t}_{\text{n}}} \quad \text{(Eq. 9.11)}$$

Calculate total damage threshold stress from equation (9.12)

$$Y_{dam}^{t_{n+1}} = B_o + \sum\Delta B = Y_{flow}^{t_{n+1}} \quad \text{(Eq. 9.12)}$$

Check for whether damage has occurred or not

$\sigma_{\text{d-virgin-trial}}^{\text{t}_{\text{n+1}}} - Y_{flow}^{t_{n+1}} < 0$ then damage is zero

$\sigma_{\text{d-virgin-trial}}^{\text{t}_{\text{n+1}}} - Y_{flow}^{t_{n+1}} \geq 0$ then damage has occurred calculate damage

If damage has occurred then calculate equivalent damage

$$\Delta\beta^{t_{n+\frac{1}{2}}} = \Delta\lambda_{\mathrm{d}}^{t_{n+\frac{1}{2}}} = \frac{\Delta B}{dB/_{d\beta}} = \frac{B^{t_{n+1}} - B^{t_n}}{dB/_{d\beta}} = \frac{Y_{flow}^{t_{n+1}} - Y_{flow}^{t_n}}{dB/_{d\beta}} \quad \text{(Eq. 9.13)}$$

where $dB/_{d\beta}$ is the slope of β vs Y_{dam} or β vs Y_{flow} curve

Y_{dam} or Y_{flow} is the effective flow stress or damage threshold stress from the uniaxial experimental test

β is the effective damage from the uniaxial experimental test

If damage condition satisfy then

$$\Delta \boldsymbol{D}^{\boldsymbol{t}_{n+1}} = \frac{\Delta \boldsymbol{\beta}^{\boldsymbol{t}_{n+1}}}{\tilde{\boldsymbol{\sigma}}_{\mathbf{D}}} [\tilde{\boldsymbol{J}}][\boldsymbol{\sigma}^{\mathbf{t}_{n+1}}] \quad \text{(Eq. 9.14)}$$

Now the damage is in terms current step are

$$\begin{Bmatrix} D_1 \\ D_2 \\ D_3 \\ D_4 \\ D_5 \\ D_6 \end{Bmatrix} = \begin{Bmatrix} D_1^{n+1} \\ D_2^{n+1} \\ D_3^{n+1} \\ D_4^{n+1} \\ D_5^{n+1} \\ D_6^{n+1} \end{Bmatrix} \quad \text{(Eq. 9.15)}$$

From the equation (9.15) the calculation of Chow's damage D_1, D_2, D_3 can be determined.

Update damage parameters

$$\boldsymbol{D}^{\boldsymbol{t}_{n+1}} = \boldsymbol{D}^{\boldsymbol{t}_n} + \Delta \boldsymbol{D}^{\boldsymbol{t}_{n+\frac{1}{2}}} \quad \text{(Eq. 9.16)}$$

The updated damage D^{n+1} is used in the beginning of the next step to update the parameters in terms of damage in Elastic part and the stress is updated.

9.2.3 Elastic region with inclusion of damage in current step

Initially the damage is zero as it evolves the damage calculated in each step is updated in elastic region when the material is damaged. The damage is calculated in the same iteration and updated again in the calculation of stress from the elastic strain increment. The relation between stress and strain could be derived using the energy equivalence hypothesis

$$\boldsymbol{\sigma} = \tilde{\mathbf{C}} \ : \boldsymbol{\varepsilon}_{\mathbf{e}} \quad \text{(Eq. 9.17)}$$

$$\tilde{\mathbf{C}} = \begin{bmatrix} C_{11}(1-D_1)^2 & C_{12}(1-D_1)(1-D_2) & C_{13}(1-D_1)(1-D_3) & 0 & 0 & 0 \\ C_{21}(1-D_1)(1-D_2) & C_{22}(1-D_2)^2 & C_{23}(1-D_2)(1-D_3) & 0 & 0 & 0 \\ C_{31}(1-D_1)(1-D_3) & C_{32}(1-D_2)(1-D_3) & C_{33}(1-D_2)^3 & 0 & 0 & 0 \\ 0 & 0 & 0 & C_{44}(1-D_1)(1-D_2) & 0 & 0 \\ 0 & 0 & 0 & 0 & C_{55}(1-D_2)(1-D_3) & 0 \\ 0 & 0 & 0 & 0 & 0 & C_{66}(1-D_3)(1-D_1) \end{bmatrix}$$

(Eq. 9.18)

Update the stress as stressNew in the current step

$$\sigma^{t_{n+1}} = \sigma^{t_n} + \tilde{C}\Delta\varepsilon_e^{t_{n+\frac{1}{2}}}$$

9.2.4 Elastic plastic algorithm with trial damage calculation

Constitutive equation for the undamaged material

$$\sigma = C_e\varepsilon_e \qquad \text{(Eq. 9.19)}$$

And the strain decomposition can be written as

$$\varepsilon = \varepsilon_e + \varepsilon_p$$

$$\boldsymbol{\sigma^{t_{n+1}} = \sigma^{t_n} + C\Delta\sigma^{t_{n+\frac{1}{2}}} - C\Delta\varepsilon_p^{t_{n+\frac{1}{2}}}} \qquad \text{(Eq. 9.20)}$$

Calculate Trial stress (Abaqus automatically initialises the stressNew to zero at the beginning of the trial stress).

$$\boldsymbol{\sigma_{trial}^{t_{n+1}} = \sigma^{t_n} + C\Delta\sigma^{t_{n+\frac{1}{2}}}} \qquad \text{(Eq. 9.21)}$$

The corrected stress calculation after damage has occurred

$$\boldsymbol{\sigma^{t_{n+1}} = \sigma^{t_n} + \tilde{C}\Delta\varepsilon^{t_{n+\frac{1}{2}}} - \tilde{C}\Delta\varepsilon_p^{t_{n+\frac{1}{2}}}} \qquad \text{(Eq. 9.22)}$$

Calculate damage trial stress

$$\sigma_{trial}^{t_{n+1}} = \sigma^{t_n} + \tilde{C}\Delta\varepsilon^{t_{n+\frac{1}{2}}}$$

$$H = \begin{bmatrix} G+H & -H & -G & 0 & 0 & 0 \\ -H & F+H & -F & 0 & 0 & 0 \\ -G & -F & F+G & 0 & 0 & 0 \\ 0 & 0 & 0 & 2N & 0 & 0 \\ 0 & 0 & 0 & 0 & 2L & 0 \\ 0 & 0 & 0 & 0 & 0 & 2M \end{bmatrix} \qquad \text{(Eq. 9.23)}$$

Calculate Hills stress from trial stress to incorporate orthotropic material character to satisfy the following equation. Now the material need to switch from damaged material to VIRGIN material domain hence (Because the material input data are in VIRGIN material domain).

$$\widetilde{\boldsymbol{H}}^{\boldsymbol{t}_{n+1}} = \frac{\mathbf{1}}{\{\mathbf{1}-\boldsymbol{D}^{\boldsymbol{t}}n+1\}}[\boldsymbol{H}]\frac{\mathbf{1}}{\{\mathbf{1}-\boldsymbol{D}^{\boldsymbol{t}}n+1\}} \quad \text{(Eq. 9.24)}$$

$$\widetilde{\boldsymbol{\sigma}}_{\boldsymbol{H}}^{\boldsymbol{t}_{n+1}} = \sqrt{\{\boldsymbol{\sigma}_{\boldsymbol{trial}}^{\boldsymbol{n+1}}\}[\widetilde{\boldsymbol{H}}^{\boldsymbol{t}_{n+1}}]\{\boldsymbol{\sigma}_{\boldsymbol{trial}}^{\boldsymbol{n+1}}\}} \quad \text{(Eq. 9.25)}$$

Calculate the flow stress in the reference direction (material's rolling direction) from the given material data input

$$\widetilde{\boldsymbol{\sigma}}_{\boldsymbol{flow}} = \widetilde{\boldsymbol{\sigma}}_{\boldsymbol{yield}} + \left(\frac{\boldsymbol{dR}}{\boldsymbol{dp}}\right)\Delta\bar{\boldsymbol{\varepsilon}}_{\boldsymbol{p}}^{\boldsymbol{t}_{n+\frac{1}{2}}} \quad \text{(Eq. 9.26)}$$

Check for yield using following equation

$\tilde{\sigma}_H - \tilde{\sigma}_{flow} < 0$ then yield has not occurred and it is still in elastic region

$\tilde{\sigma}_H - \tilde{\sigma}_{flow} \geq 0$ then yield has occurred and it has moved from elastic to plastic region

Calculate incremental equivalent plastic strain

$$\overset{\Delta}{\lambda}_{\rho}^{t_{n+1}} = \Delta\bar{\varepsilon}_{\rho} = \frac{\tilde{\sigma}_H - \tilde{\sigma}_{flow}}{\frac{1}{\tilde{\sigma}_H^2}\{[\tilde{H}][\sigma]\}\{[\tilde{C}][\tilde{H}][\sigma]\} - \frac{dR}{dp}} \quad \text{(Eq. 9.27)}$$

Substituting $\Delta\varepsilon_{\mathrm{p}}^{\mathrm{t_{n+1}}}$ in the equation (9.27) with Switch back from virgin material to damage material domain,

$\{\dot{\varepsilon}^p\} = \frac{\lambda_p}{2\tilde{\sigma}_H}[\tilde{H}]\{\sigma\}$ one can write

$$\Delta\boldsymbol{\sigma}_{\boldsymbol{p}}^{\boldsymbol{t}_{n+\frac{1}{2}}} = \frac{\Delta\boldsymbol{\lambda}_{\boldsymbol{p}}^{\boldsymbol{t}_{n+\frac{1}{2}}}}{\widetilde{\boldsymbol{\sigma}}_{\boldsymbol{H}}^{\boldsymbol{t}_{n+\frac{1}{2}}}}\left[\widetilde{\boldsymbol{H}}^{\boldsymbol{t}_{n+\frac{1}{2}}}\right]\left\{\boldsymbol{\sigma}_{\boldsymbol{trial}}^{\boldsymbol{n+\frac{1}{2}}}\right\} \quad \text{(Eq. 9.28)}$$

Switch back from virgin material to damage material domain with the correction is given by the equation;

$$\boldsymbol{\sigma}^{\boldsymbol{t}_{n+1}} = \boldsymbol{\sigma}^{\boldsymbol{n}} + \left\{\widetilde{\boldsymbol{C}}\Delta\boldsymbol{\sigma} - \frac{[\widetilde{\boldsymbol{C}}][\widetilde{\boldsymbol{H}}]\{\boldsymbol{\sigma}_{\boldsymbol{trial}}\}\Delta\boldsymbol{\lambda}_{\boldsymbol{p}}}{\widetilde{\boldsymbol{\sigma}}_{\boldsymbol{H}}}\right\}^{\boldsymbol{t}_{n+\frac{1}{2}}} \quad \text{(Eq. 9.29)}$$

Update equivalent plastic strain

$$\boldsymbol{\varepsilon_p}^{\boldsymbol{t}_{n+\frac{1}{2}}} = \boldsymbol{\varepsilon_p^n} + \boldsymbol{\Delta\sigma_p}^{\boldsymbol{t}_{n+\frac{1}{2}}} \qquad \text{(Eq. 9.30)}$$

Now the stress is in the corrected Hill's yield surface

When damage occurs the Hill's parameters will change to from $[H]$ to $\left[\widetilde{H}\right]$

$$\tilde{\sigma}_H = \sqrt{\frac{1}{2}\{\sigma\}\left[\widetilde{H}\right]\{\sigma\}}$$

$$\tilde{\boldsymbol{H}} = \begin{bmatrix} \frac{G+H}{(1-D_1)^2} & \frac{-H}{(1-D_1)(1-D_2)} & \frac{-G}{(1-D_1)(1-D_3)} & 0 & 0 & 0 \\ \frac{-H}{(1-D_1)(1-D_2)} & \frac{F+H}{(1-D_2)^2} & \frac{-F}{(1-D_2)(1-D_3)} & 0 & 0 & 0 \\ \frac{-G}{(1-D_1)(1-D_3)} & \frac{-F}{(1-D_2)(1-D_3)} & \frac{F+G}{(1-D_3)^2} & 0 & 0 & 0 \\ 0 & 0 & 0 & \frac{2N}{(1-D_1)(1-D_2)} & 0 & 0 \\ 0 & 0 & 0 & 0 & \frac{2L}{(1-D_2)(1-D_3)} & 0 \\ 0 & 0 & 0 & 0 & 0 & \frac{2M}{(1-D_1)(1-D_3)} \end{bmatrix}$$

(Eq. 9.31)

In the numerical implementation the ½ is already included hence

$$\tilde{\sigma}_H = \sqrt{\{\sigma^{t_{n+1}}\}\left[\widetilde{\boldsymbol{H}}\right]\{\sigma^{t_{n+1}}\}}$$

Similarly the damage characteristics tensor changes from [J] to [J̃]

$$\tilde{\sigma}_D^{t_{n+1}} = \sqrt{\frac{1}{2}\{\sigma^{t_{n+1}}\}[\tilde{\boldsymbol{J}}]\{\sigma^{t_{n+1}}\}}$$

$$\tilde{\boldsymbol{J}} = 2\begin{bmatrix} \frac{1}{(1-D_1)^2} & \frac{\mu}{(1-D_1)(1-D_2)} & \frac{\mu}{(1-D_1)(1-D_3)} & 0 & 0 & 0 \\ \frac{\mu}{(1-D)(1-D_2)} & \frac{1}{(1-D_2)^2} & \frac{\mu}{(1-D_2)(1-D_3)} & 0 & 0 & 0 \\ \frac{\mu}{(1-D_3)(1-D_1)} & \frac{\mu}{(1-D_3)(1-D_2)} & \frac{1}{(1-D_3)^2} & 0 & 0 & 0 \\ 0 & 0 & 0 & \frac{2(1-\mu)}{(1-D_1)(1-D_2)} & 0 & 0 \\ 0 & 0 & 0 & 0 & \frac{2(1-\mu)}{(1-D_2)(1-D_3)} & 0 \\ 0 & 0 & 0 & 0 & 0 & \frac{2(1-\mu)}{(1-D_3)(1-D_1)} \end{bmatrix}$$

(Eq. 9.32)

Calculate the increment in Damage threshold stress

$$\Delta B^{t_{n+\frac{1}{2}}} = B^{t_{n+1}} - B^{t_n} = \sigma_{\text{dtrial}}^{t_{n+1}} - \sigma_{\text{dtrial}}^{t_n}$$

From Chow and Wang's equation (1988 – page 96), calculate total damage threshold stress

$$Y_{dam}^{t_{n+1}} = B_o + \sum \Delta B = Y_{flow}^{t_{n+1}}$$

Check for whether damage has occurred or not

$\sigma_{\mathrm{d-virgin-trial}}^{\mathrm{t_{n+1}}} - Y_{flow}^{t_{n+1}} < 0$ then damage is zero

$\sigma_{\mathrm{d-virgin-trial}}^{\mathrm{t_{n+1}}} - Y_{flow}^{t_{n+1}} \geq 0$ then damage has occurred calculate damage

If damage has occurred then calculate equivalent damage

$$\Delta\beta^{t_{n+\frac{1}{2}}} = \Delta\lambda_{\mathrm{d}}^{t_{n+\frac{1}{2}}} = \frac{\Delta B}{dB/d\beta} = \frac{B^{t_{n+1}} - B^{t_n}}{dB/d\beta} = \frac{Y_{flow}^{t_{n+1}} - Y_{flow}^{t_n}}{dB/d\beta}$$

Where $dB/d\beta$ is the slope of β vs Y_{dam} or β vs Y_{flow}

Y_{dam} or Y_{flow} is the effective flow stress or damage threshold stress from the uniaxial experimental test

β is the effective damage from the uniaxial experimental test

If damage condition satisfy then

$$\Delta D^{t_{n+1}} = \frac{\Delta\beta^{t_{n+1}}}{\tilde{\sigma}_{\mathrm{D}}}[\tilde{J}][\sigma^{\mathrm{t_{n+1}}}]$$

Now we have the damage in terms current step are Chow's damages can be D_1, D_2, D_3 calculated.

Update damage parameters

$$D^{t_{n+1}} = D^{t_n} + \Delta D^{t_{n+\frac{1}{2}}}$$

The updated damage D^{n+1} is used in the beginning of the next step to update the parameters in terms of damage in Elastic and plastic part and the stress is updated.

Now update plastic strain

$$\varepsilon_p^{\mathrm{t_{n+1}}} = \varepsilon_p^n + \Delta\varepsilon_{\mathrm{p}}^{\mathrm{t_{n+1}}}$$

Now the stress is in the corrected Hill's surface with orthotropic material character.

9.2.5 Elastic plastic algorithm with inclusion of damage in current step

Use the calculated damage in the current step from the above procedure using equation (9.33).

$$\left[\tilde{\mathbf{C}}\right] = \{\mathbf{1} - \boldsymbol{D}^{\boldsymbol{t_{n+1}}}\}_{\boldsymbol{current}}[\mathbf{C}]\{\mathbf{1} - \boldsymbol{D}^{\boldsymbol{t_{n+1}}}\}_{\boldsymbol{current}} \qquad \text{(Eq. 9.33)}$$

Calculate trail stress with new damage again from the strain increment provided by Abaqus

$$\sigma_{trial}^{t_{n+1}} = \sigma^{t_n} + \widetilde{\boldsymbol{C}}\Delta\varepsilon^{t_{n+\frac{1}{2}}}$$

Correct the trail stress similar to the elastic plastic region correction along with the new damage in the current step.

$$\sigma^{t_{n+1}} = \sigma^{t_n} + \widetilde{\boldsymbol{C}}\Delta\varepsilon^{t_{n+\frac{1}{2}}} - \widetilde{\boldsymbol{C}}\Delta\varepsilon_p^{t_{n+\frac{1}{2}}}$$

9.3 Implementation of user subroutines, virtual tests and results

9.3.1 Isotropic material algorithm for elastic/plastic update

The explicit code is first tested for isotropic and kinematic hardening using one element test case. The steel material properties were used to check the results. Linear hardening conditions were provided in the user material input data. The Figure 9-2 shows the isotropic and kinematic hardening conditions for the steel material under similar loading conditions. The Abaqus/Explicit algorithm in VUMAT user subroutine is shown in Figure 9-3.

Table 9-1 Steel Material Properties

Steel Density	Young'sModulus	Poisson's Ratio	Yield Stress	Hardng Modulus
7800 kg/m^3	200 GPa	0.3	200 MPa	1.08 GPa

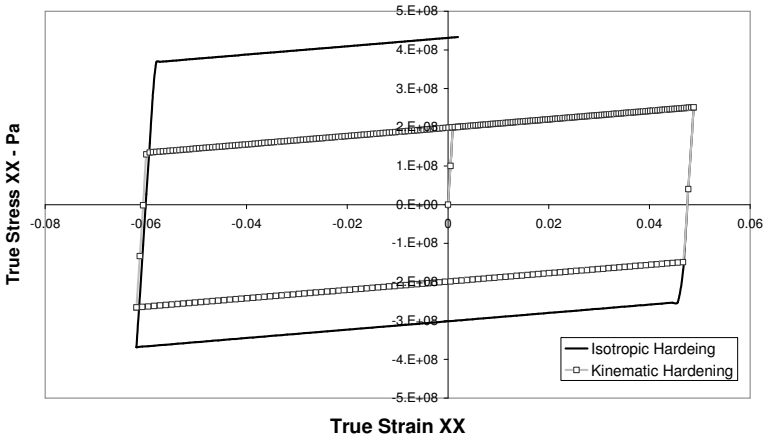

Figure 9-2 Isotropic and Kinematic hardening virtual test - user VUMAT subroutine

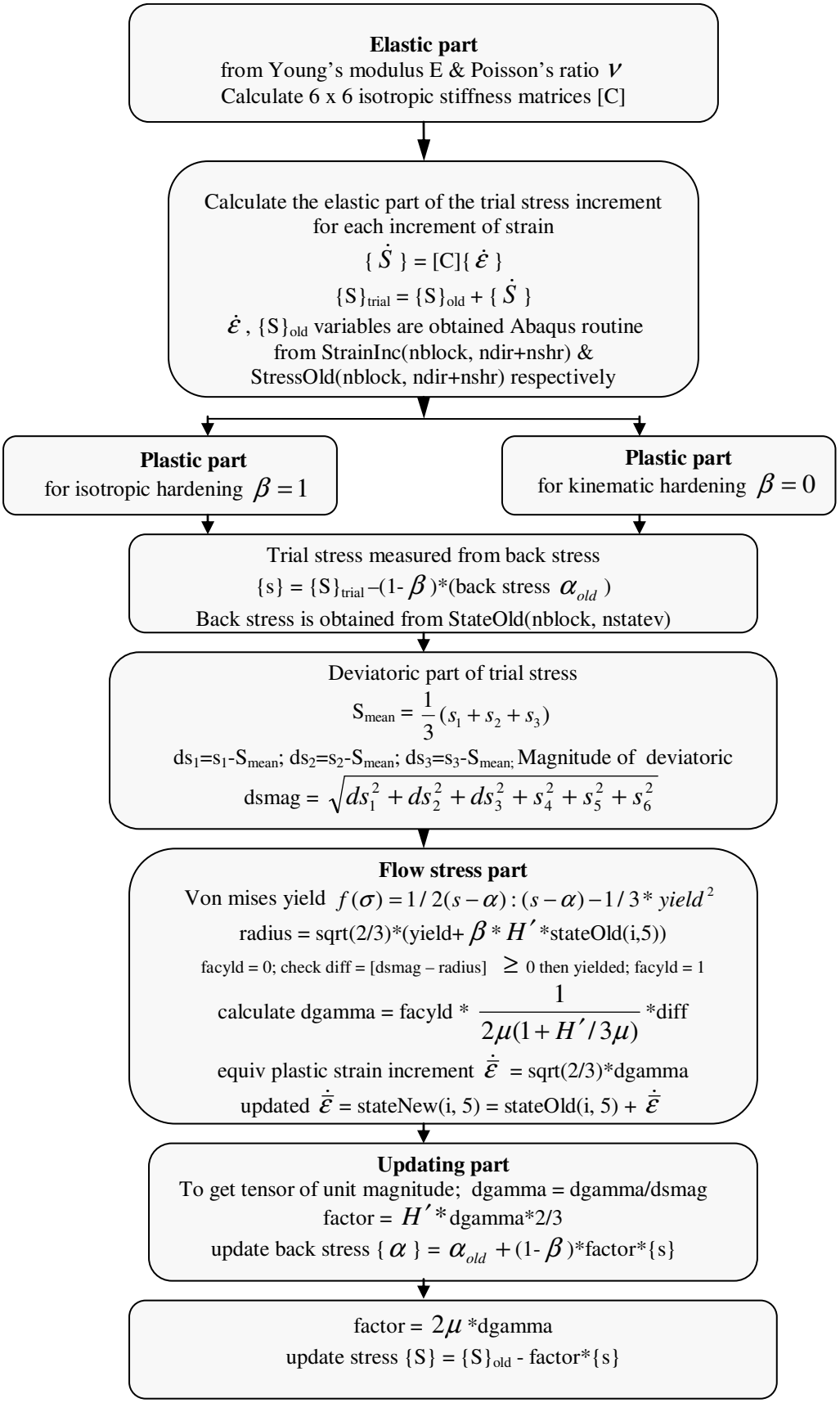

Figure 9-3 Isotropic and kinematic hardening Abaqus/Explicit user VUMAT subroutine algorithm

9.3.2 Simulation test to ascertain material orientation in user code

Software package such as LS-DYNA require inclusion of the update of material coordinate system in the user subroutine code, however Abaqus/Explicit manual states that it is not required to calculate the material coordinate system in their user subroutine. The aim of this virtual test was to confirm that all stresses, strains, stretches and state variables are passed to the user routine in the local (element) material coordinate system when we use Abaqus/Explicit. To do this an orthotropic model was created with material properties listed in **Table 9-2**. Next a virtual uniaxial tensile test case set up was constructed with displacement direction parallel to XX direction, thus it gives the Stress/Strain curve for material XX elastic material properties.

Table 9-2 Orthotropic Material Properties

Density	**Young's Modulus**		**Poisson's Ratio**			**Shear Modulus**
ρ kg/m^3	E1 Pa	E2=E3 Pa	$\nu 21$	$\nu 31$	$\nu 32$	G21=G23=G31 Pa
1600	1.60E+11	9.00E+09	0.0165	0.02	0.23	6.00E+09

From the above model a new model was created, without changing the boundary condition, in such a way that it is displaced along the material YY direction by only changing the material orientation. Now this model would use the YY direction properties and thus it would give the stress-strain curve for YY elastic material properties. The output results stress and strain were written from the user subroutine algorithm for each increment step. From this the virtual test Young's modulus can be compared with the actual material properties.

Following the above test the user material model was subjected to full cycle load with a combination of tension and compression parallel to XX axis, 45 degrees to XX axis, parallel to YY axis and 45 degrees to YY axis. The results are shown in **Figure 9-4**. A comparison was made between the Abaqus inbuilt model elastic results with the user subroutine algorithm model results and found that these results were almost identical. The above test establishes that Abaqus uses local material axes to update the results. Hence it is ascertained that the user has to specify only the orthotropic material orientation in input file and Abaqus/Explicit coding will use this local material axes as basis system.

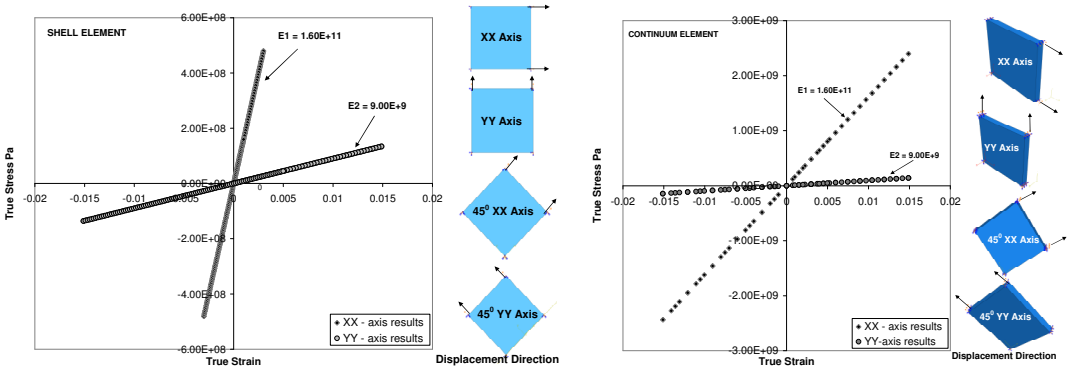

(a) Shell element (b) Continuum element

Figure 9-4 Elastic orthotropic material virtual test results to ascertain whether results are updated in local material orientation

9.4 Conclusion of orthotropic damage model algorithm implementation

The complete derivations of various equations were given in this chapter. The isotropic and kinematic hardening conditions and the material orientation were tested. The damage parameter calculated in the current step uses the information gathered from the previous step. Once the damage is calculated in the same step, Abaqus explicit allows recalculation of the stress from the newly damaged material with less resistance to loading due to damage. Thus the damage is calculated and implemented in the current step. The input data for the user VUMAT code are in the virgin material and hence the code need to switch back from virgin material state to damaged material state to calculate the parameters respectively. The material model was implemented on multi-element coupons and airframe structures. The results obtained through the simulation coupon tests were validated using the experimental results. The example input data and VUMAT code are given in the appendix.

10 Numerical test results and validation

The experimental results obtained from the material AA-2024-T3 and AA-7010-T7651 were used as material input parameters in Chow and Wang damage model numerical code exclusively developed in this thesis. Initially the virtual testing of orthotropic aluminium test coupons were checked for material behaviour in orthotropic case using a quarter specimen based on Alves and Jones (2000) geometry. Next simulation of orthotropic ductile elastic plastic model without damage subroutine in rolling, 90 to rolling, through thickness, 45^o to 0^o and 90^o and 45^o to all planes were tested and comparison were made with inbuilt model. An aircraft simple stringer model test results were obtained without damage to check the orthotropic behaviour of material.

The virtual test of isotropic elastic, plastic model with damage subroutine was implemented next using the VUMAT subroutine with damage model and compared with Chow and Wang (1987) experimental data from the literature. Single element one mm model, coarse multi-element coupon and fine mesh coupon were used to check and validate the damage model. Damage parameters were checked for consistence in an isotropic case. The models were then tested using multi-element virtual cyclic test. The results were obtained with similar procedures used for experimental results. The damage model was compared and validated using experimental results by comparing stress strain curve, damage curves and cyclic test curves. Simulation test of varying the damage parameter constants B_o and $dB/d\beta$ were completed and checked. Next the limitation of strain rate in the current model was tested by use of different speed of deformation in simulation. A multi-element model with one mm sized mesh and two mm sized mesh results were also compared for variation in results. A simple aircraft stringer along with damage parameters was also studied.

10.1 Virtual testing of coupons

10.1.1 Virtual testing of orthotropic Aluminium material

The virtual test of Aluminium material is carried out to understand and evaluate how the proposed experimental specimens would behave under similar loading and

boundary conditions. The material parameters are shown in **Table 10-1** from the experimental measurements. The values for Hill's F, G, H, L, M, N, co-efficient used here were obtained from Mirkovic (2004) work at Cranfield University using a thinner aluminium material with higher orthotropic material properties. The Hill's functions were then recalculated to facilitate their use in Abaqus/Explicit software in terms of R_{11}, R_{22}, R_{33}, R_{12}, R_{13} and R_{23} in consistence with the inbuilt Abaqus orthotropic material model (Abaqus analysis user's manual, 2007, pp 18.2.6). The calculated values are given in **Table 10-1** as the Abaqus plastic potential.

Table 10-1 Aluminium 2024-T3 orthotropic material properties, Mirkovic (2004)

Density	**Young's modulus**		**Poisson's ratio**			**Shear modulus**
ρ kg/m^3	E1 = E3 Pa	E2 Pa	$\nu 21$	$\nu 31$	$\nu 32$	G21=G23=G31 Pa
2700	7.2 E+10	6.60E+10	0.35	0.32	0.293	2.80E+10

Plastic strain	0	0.01	0.03	0.05	0.07	0.09	0.15	0.5	1
True stress MPa	340	370	410	430	440	450	460	465	467

Abaqus plastic potential	R_{11}	R_{22}	R_{33}	R_{12}	R_{13}	R_{23}
	1	0.8504	1.1506	1.1506	0.9515	0.8006

The specimen geometry is shown in Figure 10-1 (a). It is based on geometry studied by Alves and Jones (2000), the specimen width has been changed to 25 mm to work with tensile grips on CU test machine and consequently the length is also extended to 100 mm. The thickness has been changed to 2.5 mm size in consistent with previous test material supplied. The specimen is represented by 8 node C3D8R isoparametric elements with reduced integration type in ABAQUS/Explicit programme.

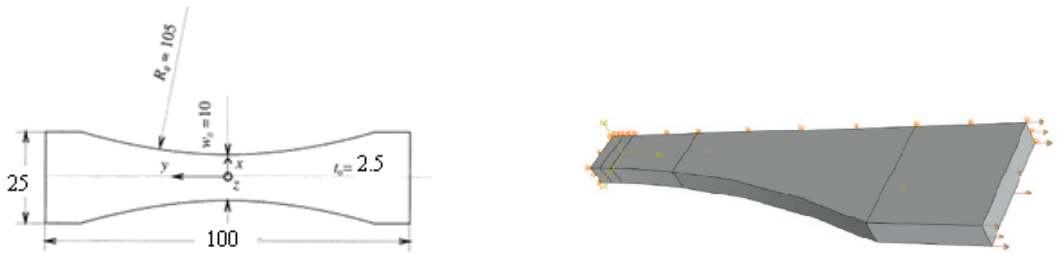

(a) Experimental test specimen (All dimension in mm)

(b) Virtual test specimen

Figure 10-1 A typical specimen used to measure damage variable D

The symmetry of the specimen has been exploited to model only one-fourth of the specimen as shown in Figure 10-1(b). A very fine mesh is used at the neck of the specimen. The results in

Figure 10-2 show results in 0 degrees to rolling direction and 90 degrees to rolling direction.

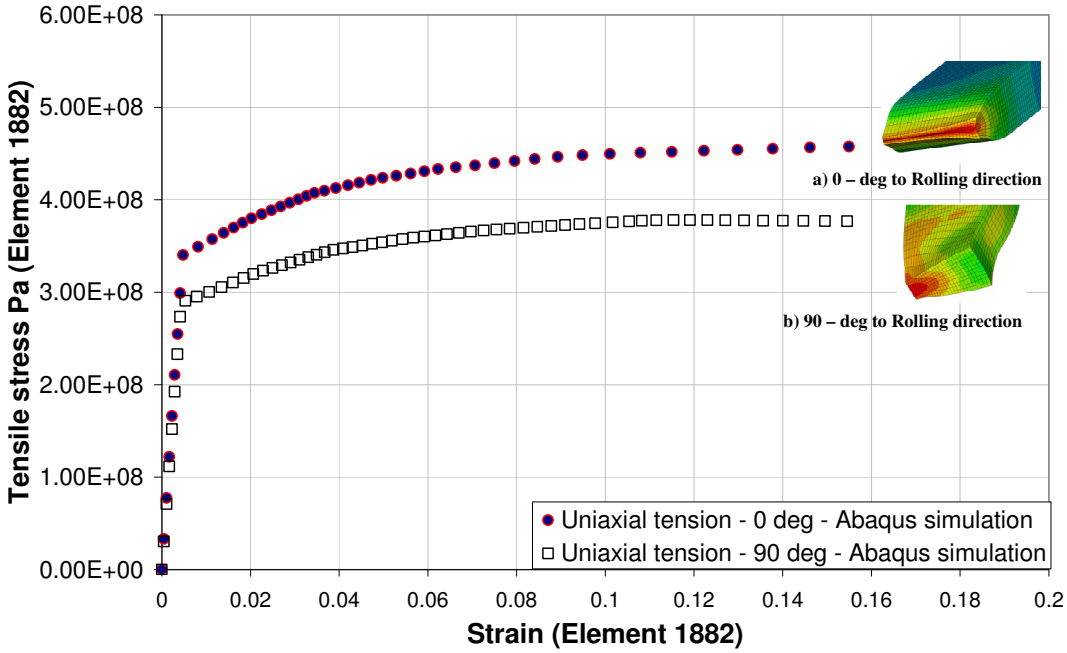

Figure 10-2 Uniaxial virtual test result of Aluminium 2024-T3 specimen with orthotropy – specimens were tested on 00 to rolling direction and 900 to rolling direction. The data for this specimen is taken from thinner Aluminium sheet hence orthotropy is significant

It can also be seen that material deformation varies in 0 degree and 90 degree direction. The more orthotropic behaviour of this material is due to the coupons used by Mirkovic (2004) for experimental tests were from thinner rolled material. The simulation quarters shown in figure are obtained just before failure to capture the material deformation differences due to orthotropy. The results show considerable amount of variation in material properties in the plastic region. Alves (2000) points out that the accurate elastic modulus of E is influenced by geometrical shape of a specimen at different deformation levels. The effect of geometrical effects on measurement of Young's modulus E and subsequent measurement of damage variable D and correction methods in case of measurement errors were discussed in Chapter 6 and Chapter 7. However the linear relationship of B versus β facilitates the prediction

of damage D beyond the necking region. The tests were completed with 45 degree to rolling direction test and obtain satisfactory results.

10.1.2 Test of orthotropic ductile elastic, plastic model without damage subroutine

The Chow's orthotropic ductile elastic plastic model without damage code was developed and the VUMAT subroutine was implemented in Abaqus explicit package. A single element cube model has been used here. The cube element is constrained to create uniaxial tensile test scenario. The element was tested in 1-direction, zero degree to rolling direction, having material axis 1' = global axis 1 (or X'=X), in 2-direction, 90 degree to rolling direction (through thickness direction), having material axis 2' = global axis 1 (or Y'=Y), and in 3-direction, 90 degree to rolling direction and through thickness direction having material axis 3' = global axis 1 (or Z'=1). The material is oriented to 45^0 in 1-2 plane by having material axis X'=[1,1,0] and in all 45^0 by having material axis X'=[1,1,1]. The results were verified by comparing Abaqus explicit inbuilt results for the same. The virtual simulation are shown in Figure 10-3 and validated by the experimental data. The results obtained from user subroutine VUMAT were verified with Abaqus inbuilt model. It could be inferred from the graphs that the user model developed in this research project produces exact results of Abaqus explicit inbuilt model results.

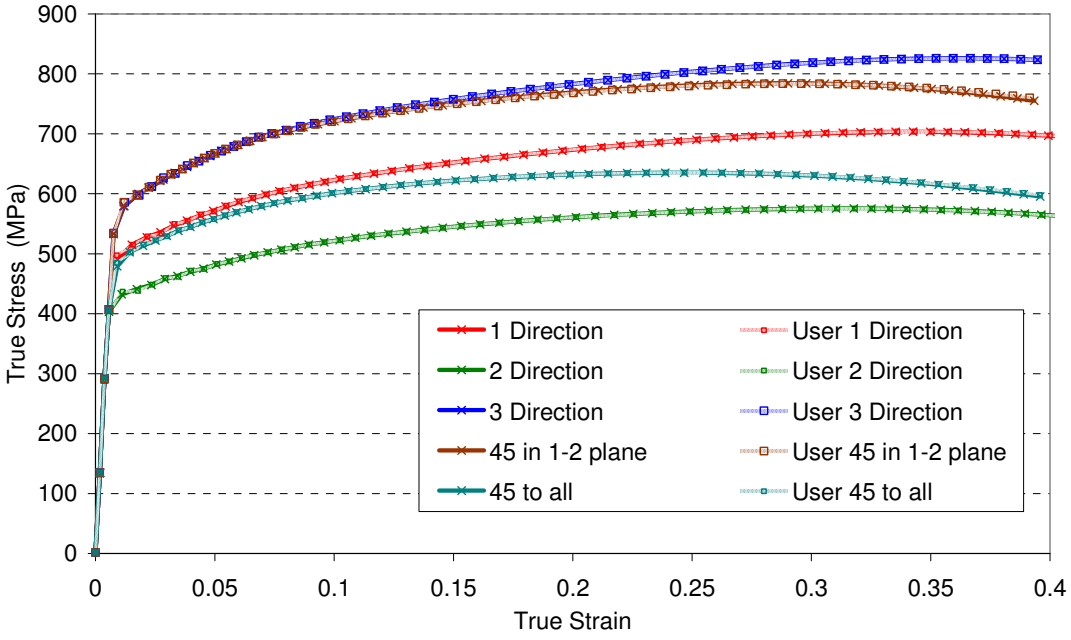

Figure 10-3 Uniaxial orthotropic ductile elastic plastic virtual test results

This subroutine has been submitted to Airbus-UK for large scale structural simulation. As a part of the ongoing testing of the new subroutine, a simple stringer buckling load case test was agreed with Airbus.

10.1.3 Standard tensile test of isotropic material with elastic, plastic and damage model subroutine

After thorough literature survey a complete new method was formulated in this research work to implement Chow's damage model in Abaqus Explicit as explained in Chapter 8. The uniaxial cyclic test case is used here with different cyclic load to the one done in the experiment to check the trend of FE model prediction with different cyclic load cases with more number of cycles. This method is followed throughout the FE model validation procedure. This allows to compare the multi-element model experimental results with single element results and their trends during different cyclic load case. The method of using different cyclic load case to the experimental study also provides information on the FE code's predictability of material character and its trends of experimental values.

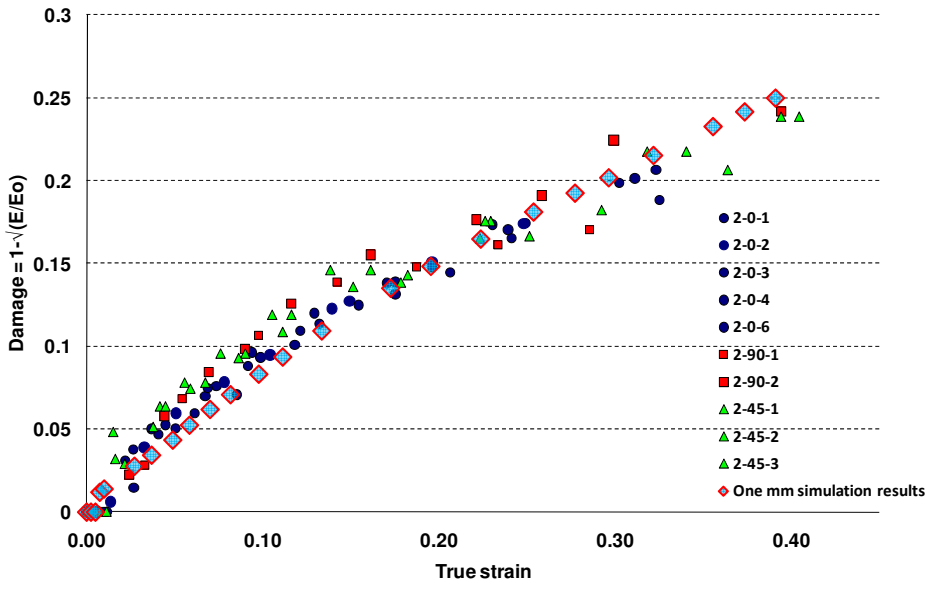

Figure 10-4 Validation of the model using CU experimental data AA2024 using one mm single element model with isotropic parameter, true strain versus damage for uniaxial cyclic loading case with good agreement with results

The newly formulated method has been added to the above VUMAT subroutine. To start with, the damage model was implemented with isotropic material behaviour to verify the numerical code in a single element case.

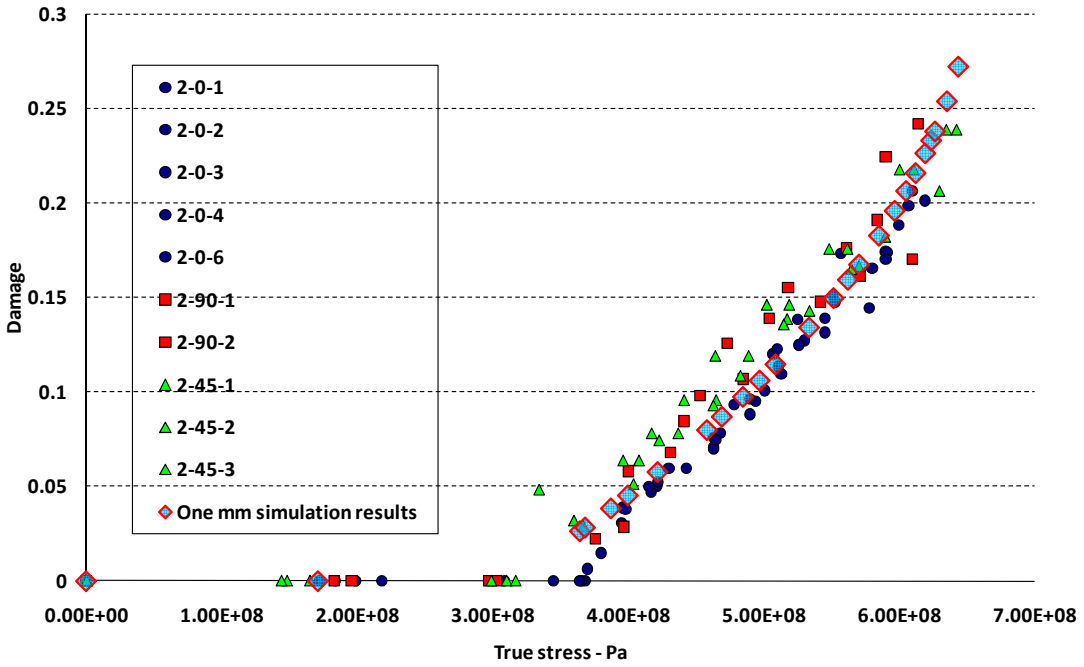

Figure 10-5 Validation of the model using CU experimental data AA2024 using one mm model with isotropic parameter, true stress versus damage for uniaxial cyclic loading case

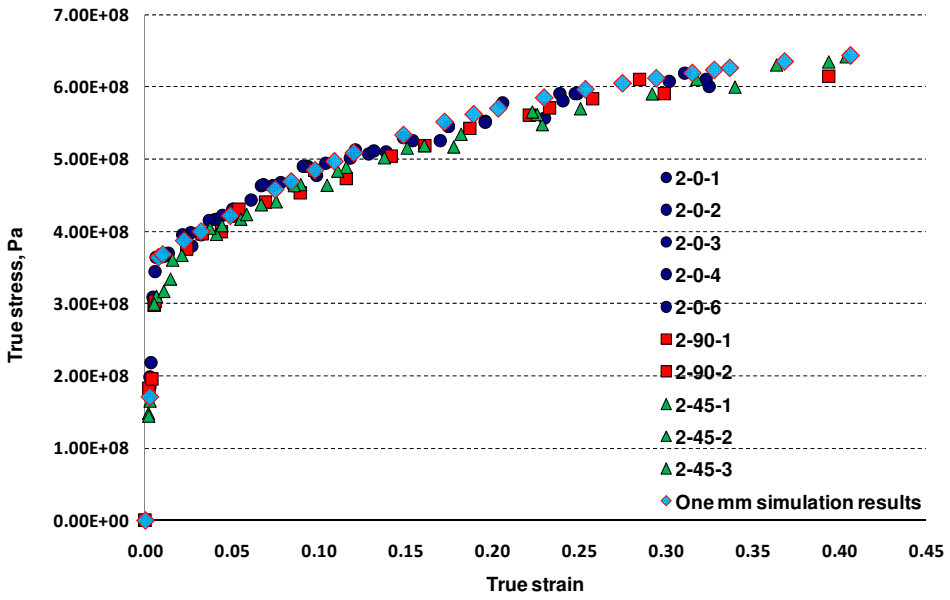

Figure 10-6 Validation of the model using CU experimental data AA2024 using one mm model with isotropic parameter, true stress versus true strain for uniaxial cyclic loading case

The material data required for isotropic case implementation in explicit code is shown in Table 6-4. The one mm model results are shown in Figure 10-4 to Figure 10-6. The single element model simulation results were incorporated in experimental true strain versus damage results Figure 10-4; the simulation results follow the trend of experimental curve. Similarly the comparison with true stress versus damage and stress-strain follow the trend of experimental curve.

The AA-7010 coupon test isotropic material constants were obtained from the material characterisation. The results from Table 6-6 were used in user subroutine VUMAT to check the results and validate the model. Series of virtual simple tensile coupon tests were performed. The results are presented in Appendix from Figure 13-8 to Figure 13-10. The results obtained from isotropic parameters VUMAT subroutine generate agreeable results.

10.2 Multi-element coupons for virtual testing

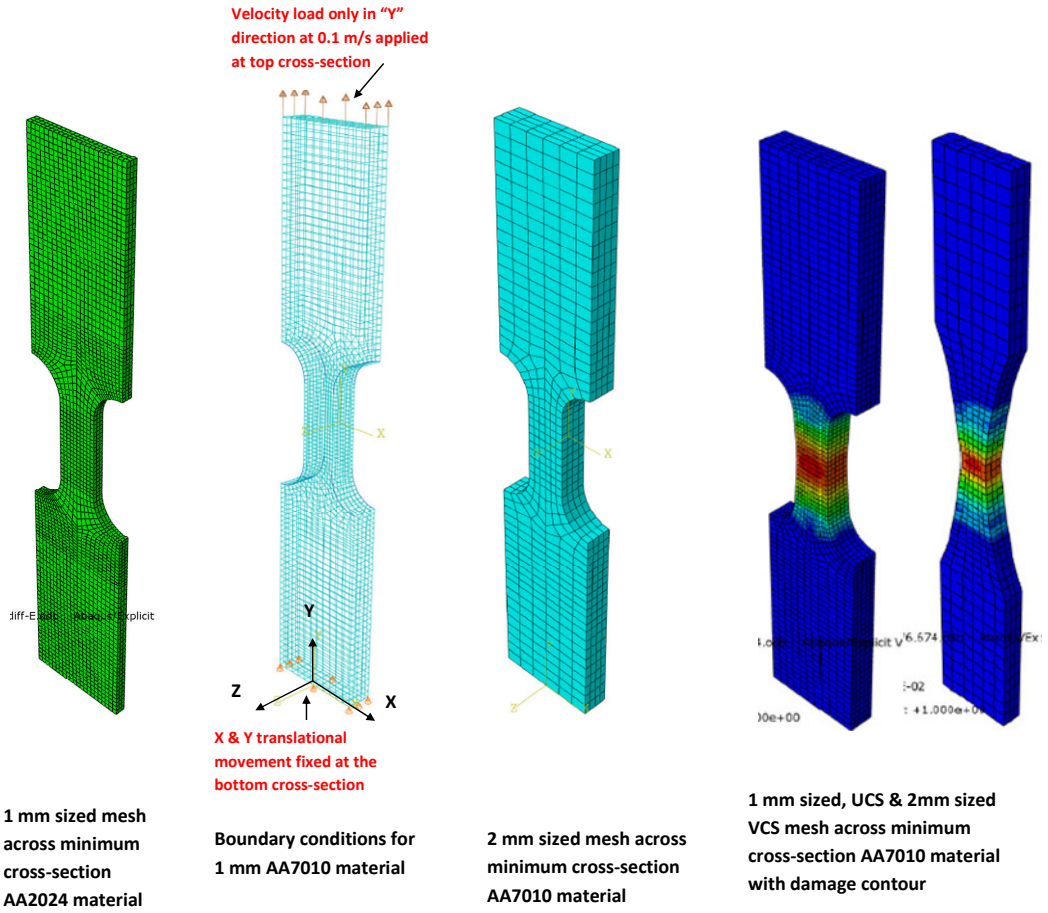

Figure 10-7 Example of virtual coupon mesh size, boundary conditions and damage contour output

The virtual model was created with multi-element model with one mm and two mm sized mesh, 3D with 8 node C3D8R isoparametric elements with reduced integration type is used for this analysis. The virtual coupons X and Y translation movement at the bottom were constrained; on top, a velocity load is applied at 0.1 m/s to achieve uniaxial loading conditions similar to the tensile testing machine. The number of elements for each simulation Abaqus CAE model was based on the cross section and thickness of the specimen. One mm or two mm sized mesh was used for the analysis. In some cases coarse mesh was also used to check the boundary condition and deformation velocities. As shown in Figure 10-7 a fine square mesh was created at the centre of the specimen where the deformation is likely to be maximum and the mesh sizes were gradually increased towards the grip end of the specimen.

As an example for AA7010 one mm sized UCS specimen the total number of elements were 5245 and for 2 mm sized specimen the total number of elements were 1408. Similarly a 1 mm sized AA2024 UCS coupon was created with 6924 elements to have better convergence of the mesh due to reduced thickness. Using the same criterion varying cross section specimens mesh were also created (AA7010 with 1 mm sized mesh with 3168 elements, 2 mm sized with 1044 elements and AA2024 1 mm sized mesh with 1024 elements).

10.3 Multi-element isotropic virtual tests

In a multi-element scenario, an evaluation procedure is required to check the code does not produce any anomalies before introducing orthotropy. Along with orthotropy present it will be difficult to check for anomalies of the code when we introduce multi-element scenario. One of the ways to check this is to assume the problem at a simpler level that is without orthotropy. To do this isotropic multi-element model could be created and checked in the virtual simulation test for the consistence of behaviour in all three directions. The methodology to do this is to introduce isotropic material character into the orthotropic VUMAT code. In principle the isotropic coupon model should produce identical results in all directions. With this principle in mind the isotropic multi-element model was created to analyse the multi-element coupon test cases.

10.3.1 Multi-element cyclic test of isotropic elastic, plastic without damage subroutine

The tensile or compressive load is applied at the top end of the specimen to mimic the experimental loading conditions. The FE model cyclic load was different from the experimental cyclic load to increase the number of cycles to check any anomalies in the FE model. Here the FE cyclic test case uses one of methods to calculate true stress strain curve using an extensometer type measurement. This method allows to check the of FE true stress and true strain results with the experimental results which are calculated using DIC procedure. Moreover using different cyclic load to obtain true stress and true strain data from FE provides the information how well FE model can predict the true stress and true stain trend when subject to different cyclic load cycles. Initially a cyclic test without damage parameter was carried out to check the behaviour. The results were then obtained using an extensometer points as show in Figure 10-8. The stress and strain were calculated from the extensometer reading at 2 mm and 6 mm from the centre and subsequent reaction forces at the end. It is clear from the Figure 10-8 the extensometer type measurement in FE model using 6 mm from the centre diverges due to necking and subsequent cushioning effect of the rectangular specimen. For the further FE cyclic tests the measurement of true stress and true strain are obtained directly from the FE model.

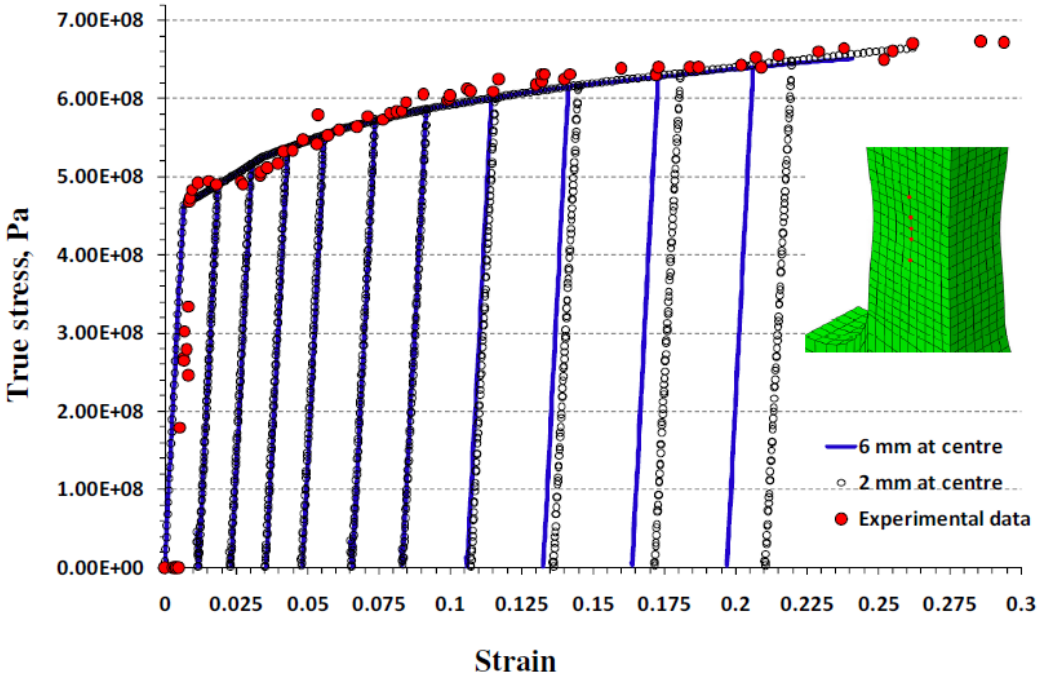

Figure 10-8 CU AA7010 uniaxial experimental data verification using one mm mesh UCS isotropic parameter without damage

10.3.2 Multi-element cyclic test of isotropic elastic, plastic with damage subroutine

The standard tensile test and low cycle cyclic tests were performed on simulation material coupons AA2024 and AA7010 using the isotropic damage material characteristic data obtained from experimental results. Tests were carried out on both uniform cross section and varying cross section specimens.

As shown in the Figure 10-7 damage appears to concentrate on the middle section of the model which follows the trend of the real specimen behaviour. The model also produces identical damage results in rolling direction, transverse direction and through thickness direction which is typical of isotropic material properties. The damage trend also follows the trend predicted by experimental results.

As a test of the characterisation procedure, a finite element model of the low cycle tension test specimen has been analysed using the Abaqus explicit code. The low cycle test allows the damage to be calculated similar to experimental material characterisation. The model includes the Chow and Wang (1988) damage model implemented as an Abaqus VUMAT routine. Standard tensile test are performed using simulation by holding one end of the specimen with appropriate constraints like in the actuator grip and moving the other end at constant speed with appropriate constraints to satisfy uniaxial tensile case. The specimen is tested until it fractured. The cyclic test is also performed in similar fashion but for every 2% to 5% of the strain the specimen is unloaded almost to zero load and reloaded to next 2% to 5% of the strain. This process is continued until the specimen reached critical damage level. The stress-strain curves were then calculated from the finite element model using the same process used for the experimental data, allowing β (Figure 10-10) and damage "***D***" to be calculated.

The procedure followed to calculate experimental results are used to calculate virtual test damage parameters. The elastic modulus degradation is used at each cycle to calculate the damage at that instance (Figure 10-9). The results were also verified using extensometer technique. In extensometer technique the displacement is measured between two points from the centre of the specimen and engineering strain and true strain are calculated, from the reaction forces at the end of specimen and

cross sectional area the engineering stress is calculated as in chapter 6.5 (Test procedure and measurements). Examples results of the two methods are shown in Figure 10-9 to Figure 10-11. The true stress is then calculated based on true strain.

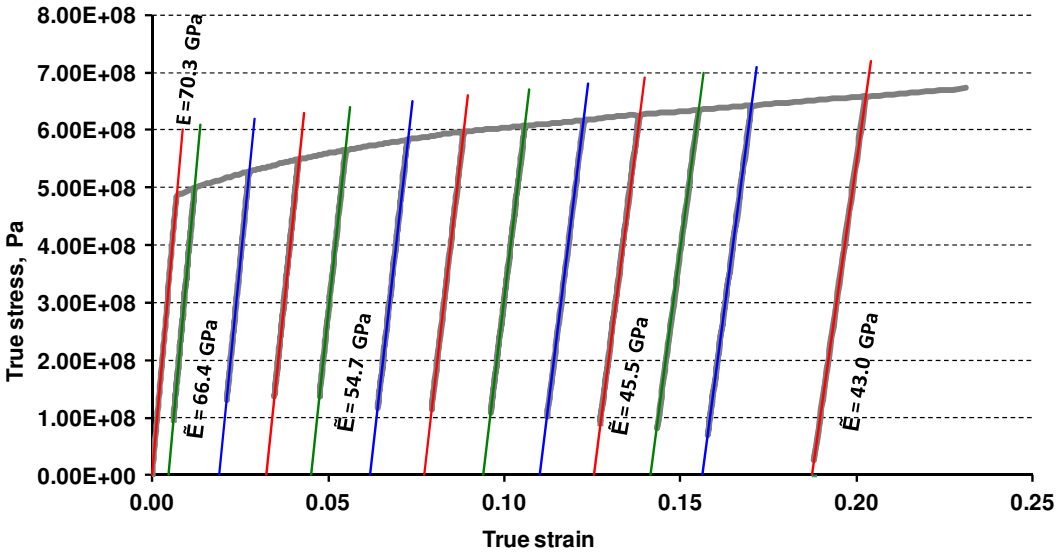

Figure 10-9 Simulation cyclic test results using the user code and material characterisation data for AA-7010 material results show similar elastic modulus degradation to experimental results for uniaxial loading case; the slope lines are highlighted with red, green and blue to show the Young's modulus degradation clearly

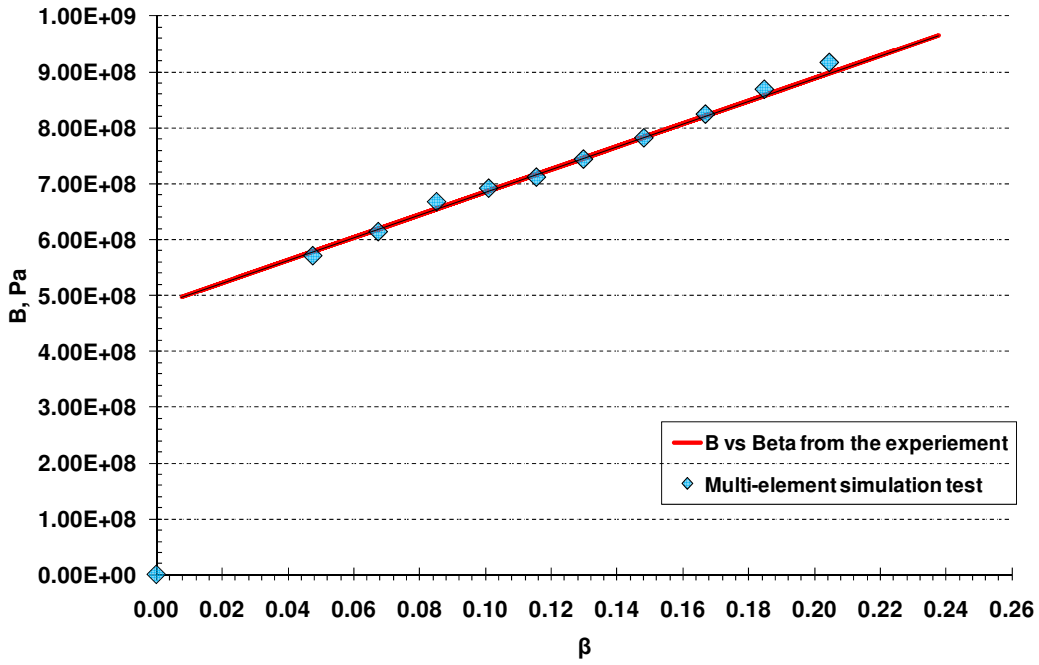

Figure 10-10 Simulation uniaxial cyclic test results using the user code and material characterisation data for AA-7010 material B (virgin material stress) versus β (overall damage), the R^2 value of B vs β fit is $R^2 = 1$

These results show good agreement with the experimental values, Figure 10-9 to Figure 10-11. The comprehensive comparative study done through various cyclic tests prove that the damage model created using the proposed numerical model is a good approximation of actual experimental result. Thus the simulated damage model VUMAT subroutine is validated by comparison with experimental results for an isotropic case.

Once the cyclic test regime and B (virgin material stress) versus β (overall damage) calculation were verified AA7010 cyclic tests were carried out using VUMAT code with isotropic parameters. The virgin material stress is denoted by Chow and Wang (1987) as B and during the damage calculation and the same notation is used here to keep the convention same. The results were compared and presented in Figure 10-11 and Figure 10-12. Similar to experimental calculation the damage values for D were obtained from the cyclic test elastic modulus degradation. The data obtained from the simulation produces agreeable results with the experimental values.

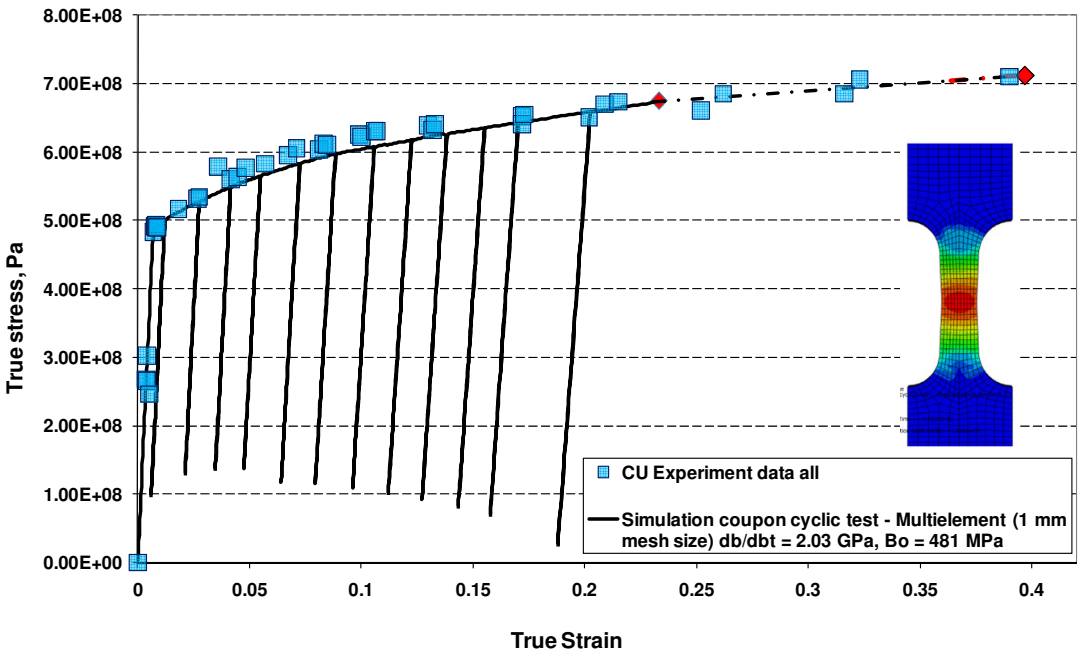

Figure 10-11 AA7010 simulation coupon test validation using experimental data verification using one mm mesh uniform cross section model with isotropic parameter for uniaxial loading case

The damage contours are shown (Figure 10-11 and Figure 10-12) along with the graph. The maximum damage occurs at the centre of the specimen which is coloured

in red. These results are similar to the experimental results where the centre of the specimen gets maximum strain and fails ultimately. As an additional check for the VUMAT code the experimental results obtained by Chow and Wang (1987) were also tested for isotropic case. The extensometer reading and surface strain measurement where obtained. The results obtained through both these methods are compared with Chow's experimental data. The results produced here agree with experimental results obtained by Chow. The graphs are presented in Appendix (Figure 13-5 to Figure 13-7).

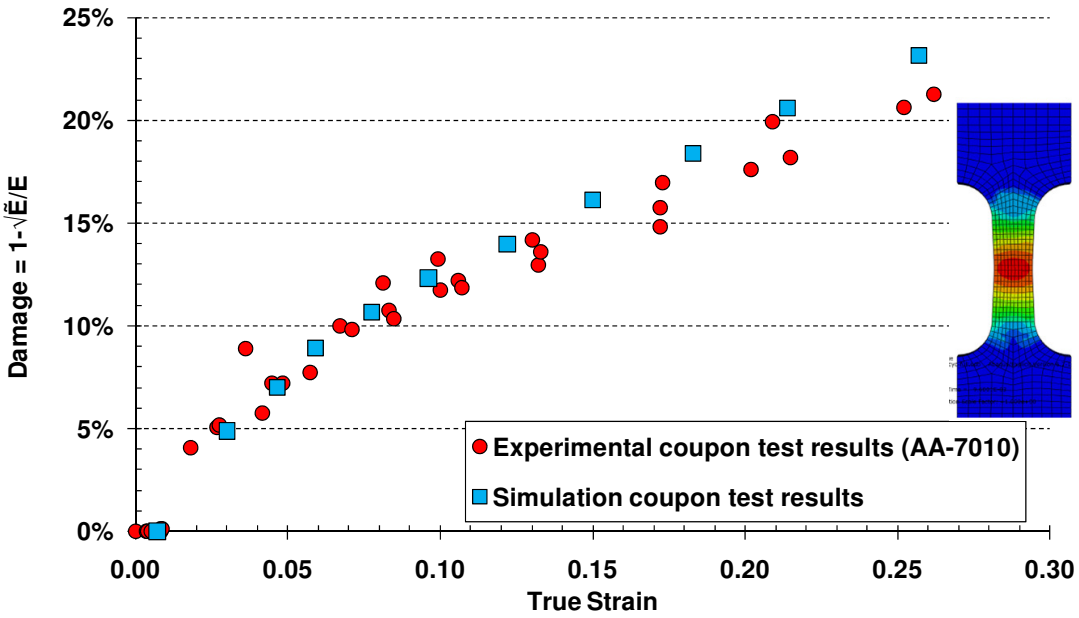

Figure 10-12 Simulation cyclic test results using the user code and material characterisation data for AA-7010 material results comparison of damage for uniaxial loading case

The damage contours are shown (Figure 10-11 and Figure 10-12) along with the graph. The maximum damage occurs at the centre of the specimen which is coloured in red. These results are similar to the experimental results where the centre of the specimen gets maximum strain and fails ultimately. As an additional check for the VUMAT code the experimental results obtained by Chow and Wang (1987) were also tested for isotropic case. The extensometer reading and surface strain measurement where obtained. The results obtained through both these methods are compared with Chow's experimental data. The results produced here agree with experimental results obtained by Chow. The graphs are presented in Appendix (Figure 13-5 to Figure 13-7).

The next level of experiments in AA2024 material is carried out using multi-element model with UCS specimen. Here the model has been subjected to strain levels above 45% to see the effect of damage growth. The damage values are calculated using the elastic modulus degradation technique and results are shown here. The results are compared with experimental values of stress-strain cyclic test (Figure 10-13 & Figure 10-16), true strain damage (Figure 10-14) and true stress damage (Figure 10-15). The results obtained from the numerical simulation agree well with experimental results.

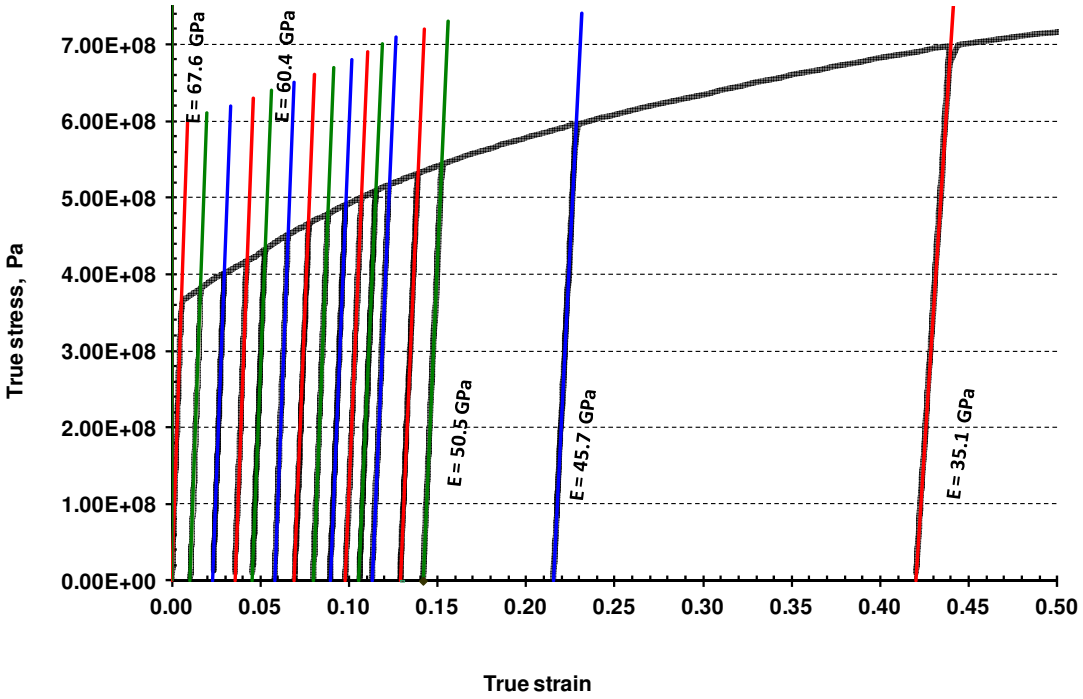

Figure 10-13 Simulation isotropic uniaxial cyclic test results using the user code and material characterisation data for AA-2024 material results show similar elastic modulus degradation to experimental results; the slope lines are highlighted with red, green and blue to show the Young's modulus degradation clearly

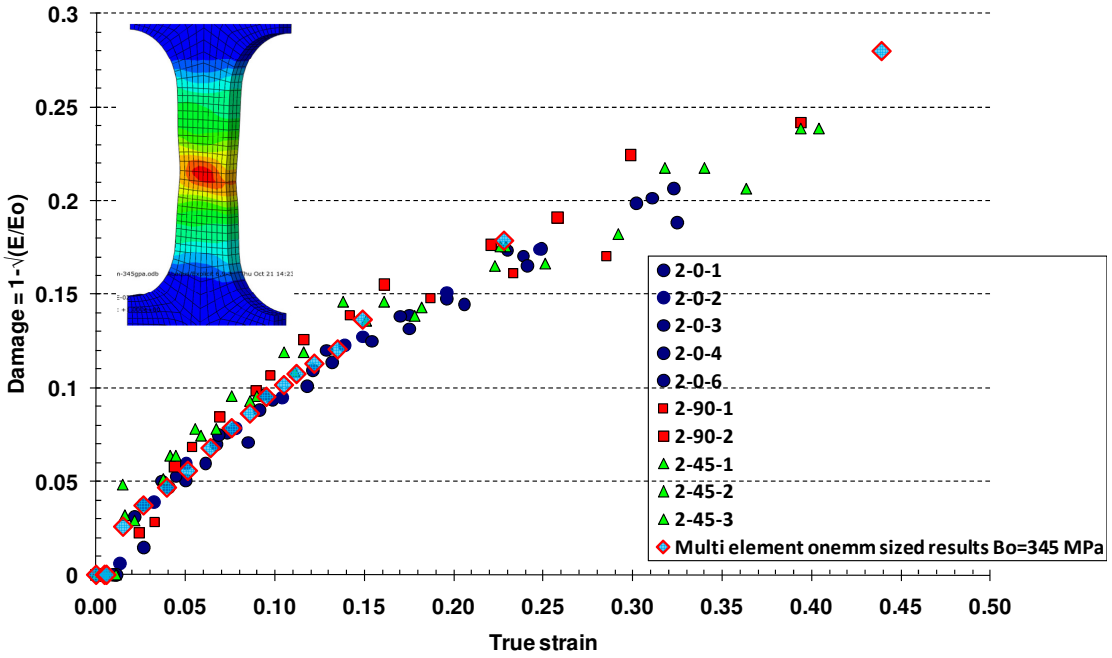

Figure 10-14 AA2024 model uniaxial cyclic test simulations result with isotropic parameter true strain versus damage

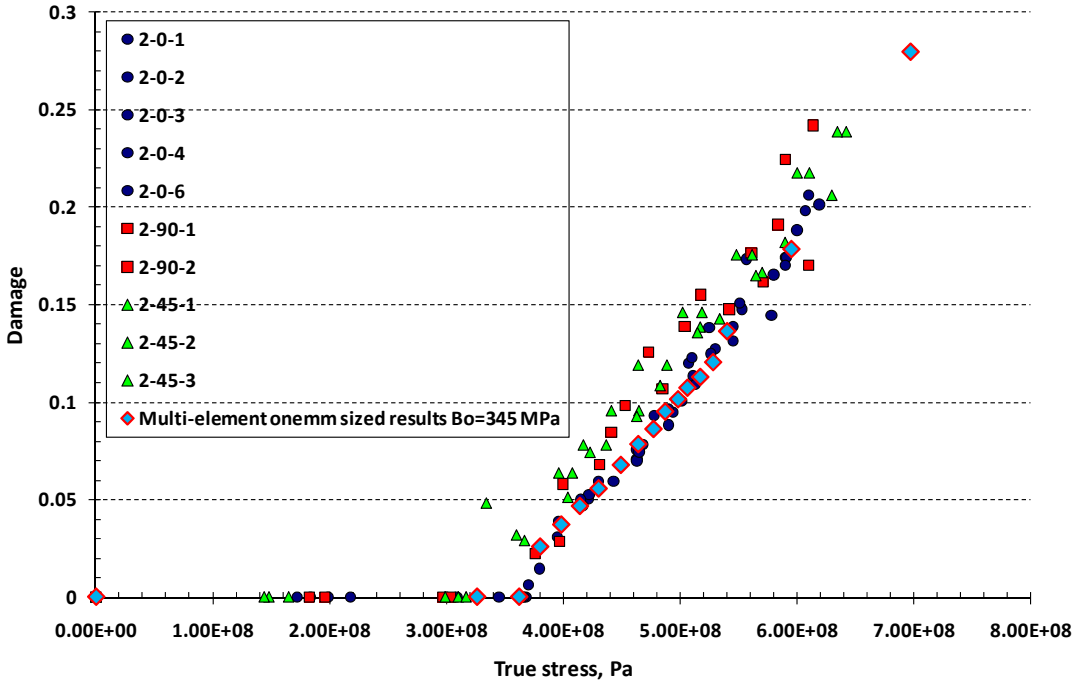

Figure 10-15 Validation of the model using Cranfield University uniaxial experimental data – proposed explicit damage model uniaxial cyclic test simulations result AA-2024 with introduced isotropic parameter true stress vs damage

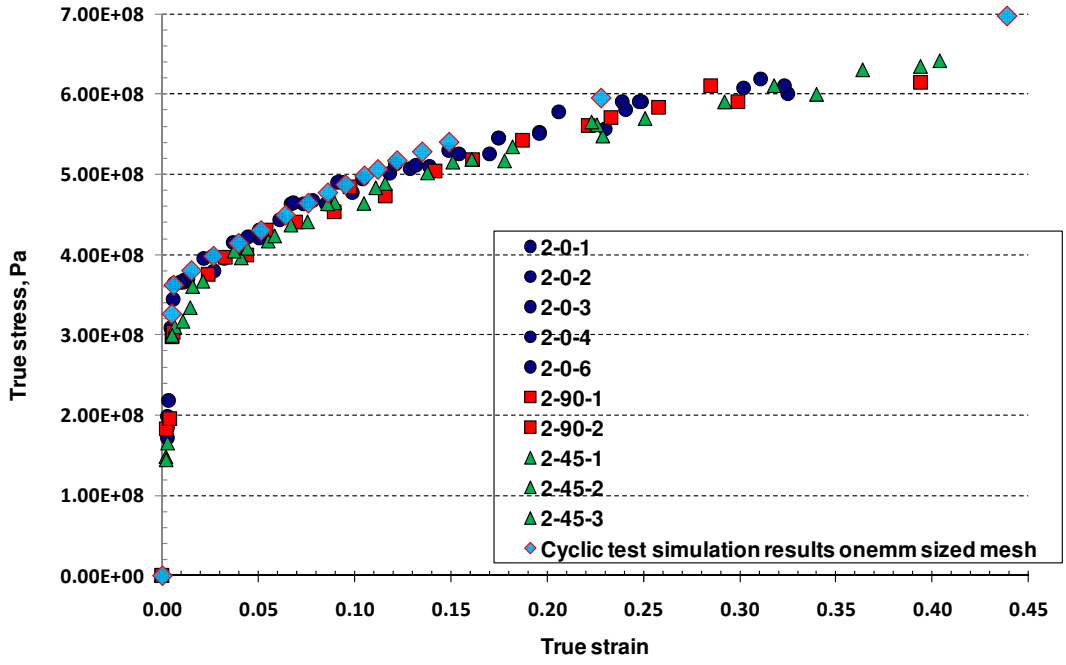

Figure 10-16 Validation of the model using Cranfield University uniaxial experimental data – proposed explicit damage model uniaxial cyclic test simulations result AA-2024 with introduced isotropic parameter true strain vs stress

The damage parameters are also calculated by the numerical code using the mathematical model explained in chapter 5. The contour of damage from the Abaqus output result is shown in Figure 10-14, the level of concentration at the middle of the specimen shows similar results to experimental behaviour.

10.3.3 Variation tests of Bo and $dB/d\beta$

The damage model uses the virgin material stress, virgin material strain as input along with other material characteristic constants from **Table 6-1**. The important damage parameter constants B_o and $dB/d\beta$ influence the damage growth and subsequent stress strain output from the user VUMAT. The effects of these changes are checked on the VUMAT subroutine by varying the parameters. The results are shown from Figure 10-17 to Figure 10-20. Three sets of data have been analysed in the simulations; first the Bo is kept constant and $dB/d\beta$ is varied, similarly the simulation is repeated by keeping $dB/d\beta$ constant and varying Bo. The results obtained show notable change in prediction of damage and subsequent prediction of stress and strain data. The simulations reveal that to get accurate prediction of material damage evolution and their stress and strain curve; exact values of these parameters should be obtained using the experimental tests. A slight change in these

parameters could influence the prediction results noticeably and lead to wrong prediction of material behaviour during its use.

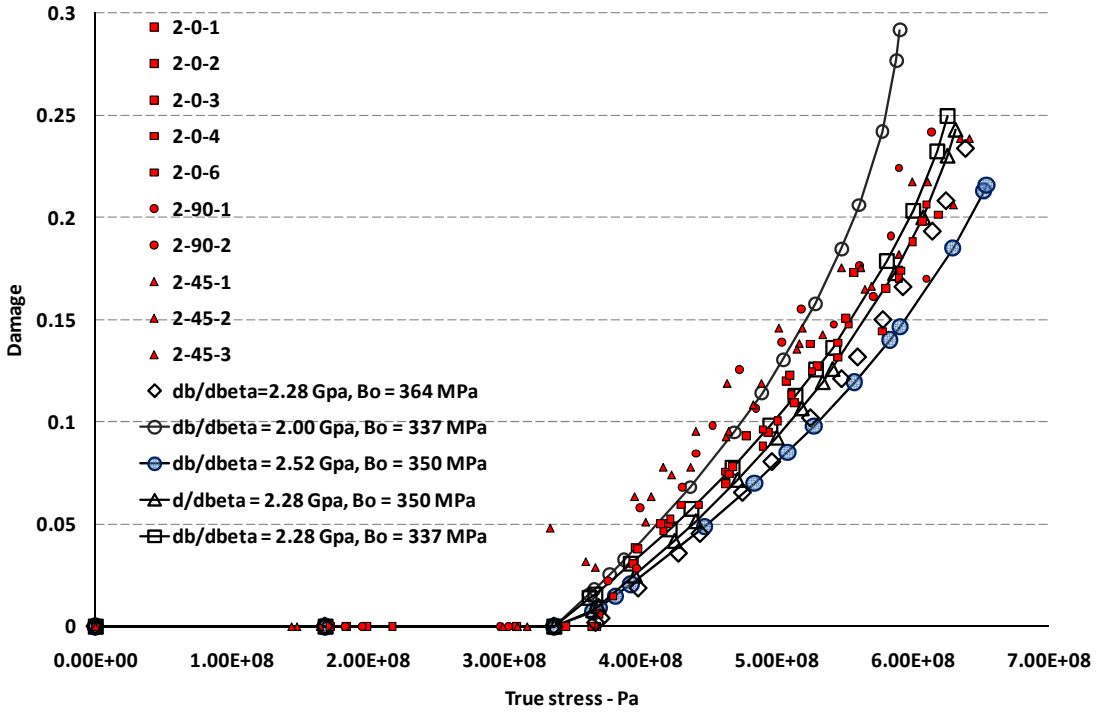

Figure 10-17 Simulation of AA-2024 with varying Bo and dB/dβ true stress vs damage compared with experimental coupon test results for uniaxial loading cases

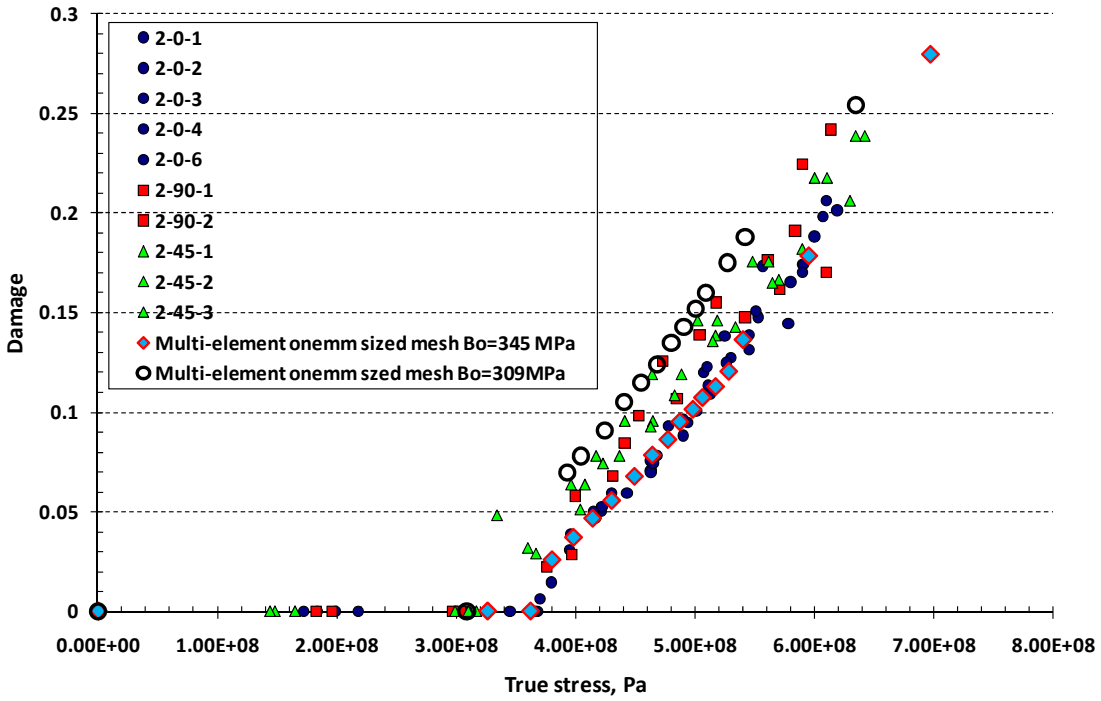

Figure 10-18 Uniaxial cyclic test simulations result AA-2024 comparison of Bo variation

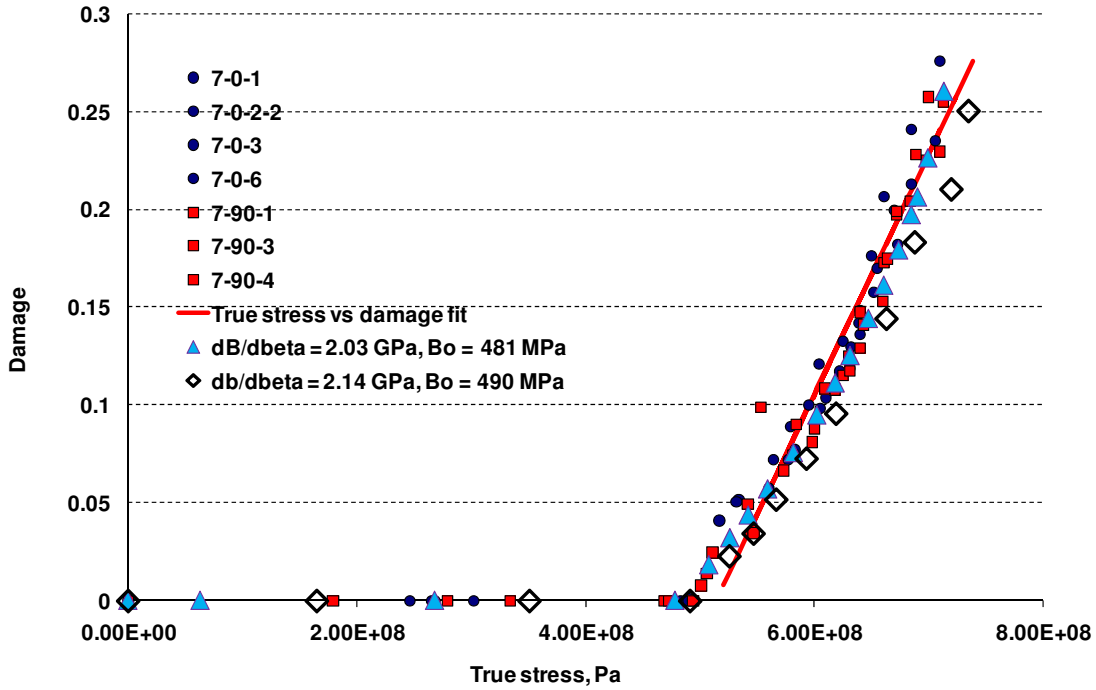

Figure 10-19 Simulation of AA-7010 with varying B_o and $dB/d\beta$ under uniaxial loading case - true stress vs damage compared with uniaxial experimental coupon test results, the R^2 value of Damage vs True stress fit is $R^2 = 1$

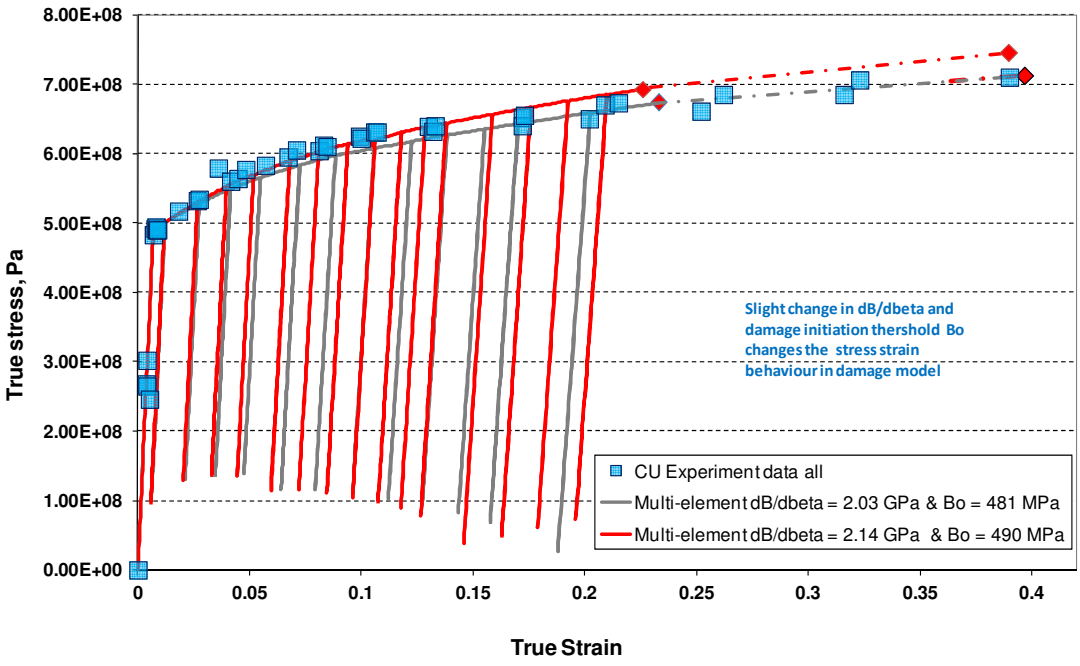

Figure 10-20 CU AA7010 simulation coupon test influence of $dB/d\beta$ and damage initiation threshold B_o under uniaxial cyclic test

The verification was done using one mm mesh uniform cross section model with isotropic parameter. The cyclic test simulation done in Abaqus explicit model with damage is presented in Figure 10-20, it shows a variation in the results produced.

Slight variation in $dB/d\beta$ and damage initiation stress B_o produces noticeable changes in prediction of stress, strain and damage values. Hence care should be taken while using the values for $dB/d\beta$ and B_o. Accurate determinations of these material parameters are essential for getting better results using material models with damage.

10.3.4 Influence due to mesh size and coupon cross section

The influence of mesh size is checked for 1 mm and 2 mm mesh for uniform cross section and varying cross section. The model is based on the multi-element mesh shown in Figure 10-7. The one mm sized varying cross-section with 3168 elements and two mm sized uniform cross-section with 1408 elements were constructed with of 8 node linear continuum solid element with reduced integration (C3D8R). The cyclic tests were carried out and the damage has been measured from the elastic modulus degradation. The damage data obtained from the results are presented here along with the experimental results for all AA7010 coupons. The difference between 1 mm and 2 mm results are shown in Figure 10-21 does not produce significant variation.

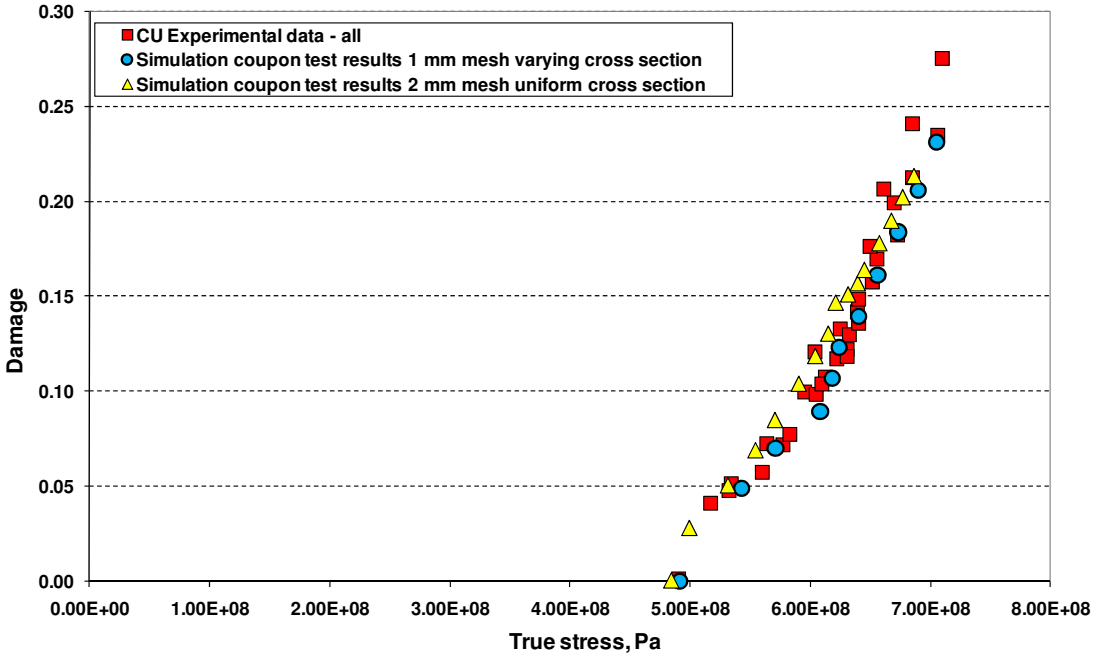

Figure 10-21 AA7010 simulation with 1 mm sized mesh versus 2 mm sized mesh under uniaxial loading case

10.3.5 Deformation speed test

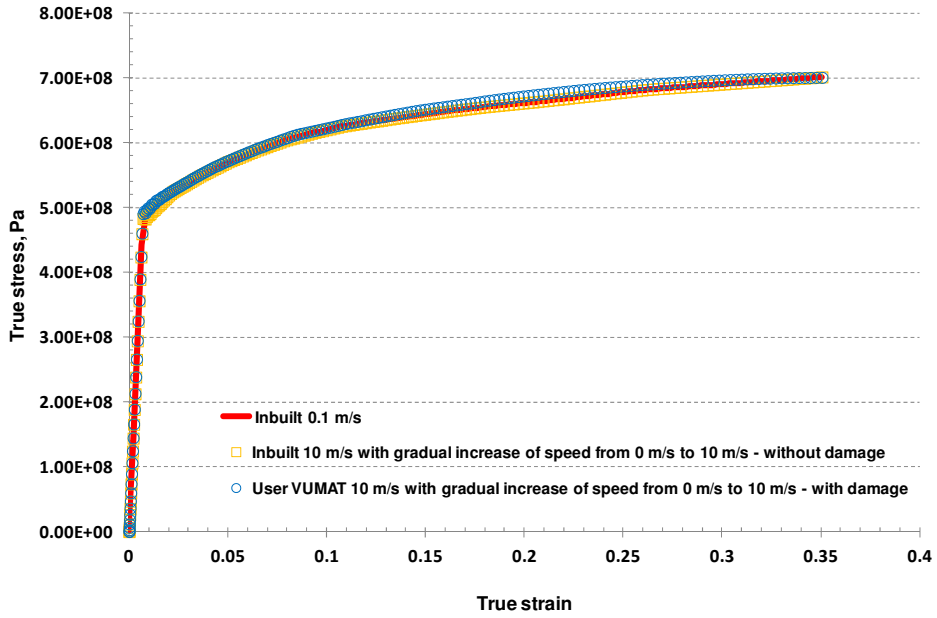

Figure 10-22 AA7010 simulation deformation speed test up to 10 m/s under uniaxial loading case

The VUMAT model was checked at various increasing deformation speed level from 0.1 m/s to 100 m/s against the inbuilt Abaqus material model to check for any inconsistency. To perform the test a single element model was used. The model was tested with uniaxial tensile condition for varying deformation speeds.

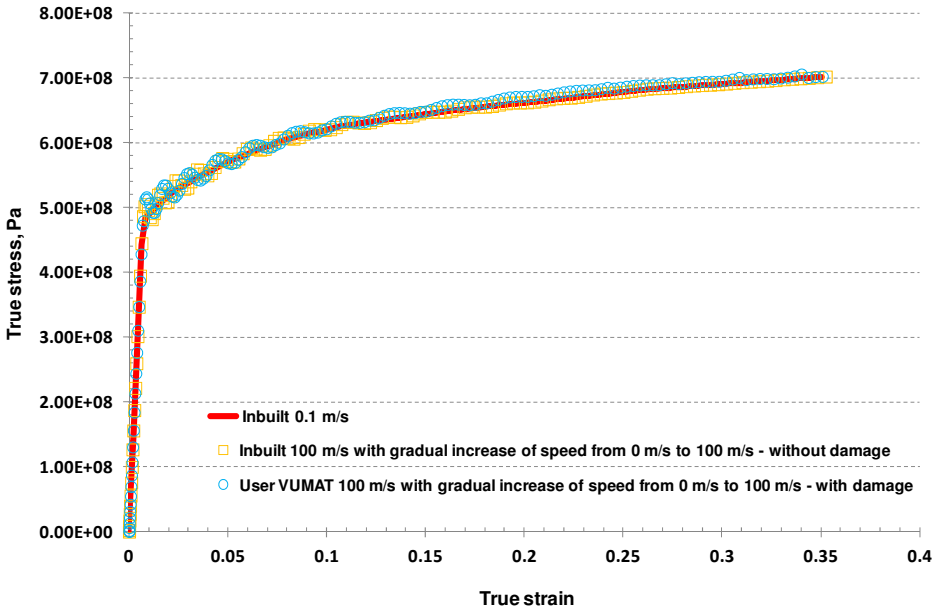

Figure 10-23 AA7010 simulation deformation speed test up to 100 m/s under uniaxial loading case

The VUMAT material model produces similar results suggesting that the user material model does not have other anomalies. The results in Figure 10-22 are for deformation speeds 0.1 m/s and 10 m/s. The user model produces similar results in this deformation speed ranges. The next Figure 10-23 shows test for 100 m/s and it proved to produce similar fluctuating results like the inbuilt model. This test proves that the material model could be used for deformation speeds of up to 10 m/s and beyond that caution should be taken in interpreting the results.

10.4 Multi-element orthotropic virtual tests

Upon satisfactory predictable results obtained on isotropic case, the new damage model was implemented on multi-element orthotropic model with identical geometry to the physical experiment model. The input data obtained from the experimental tests. The effective plastic strain and effective flow stress from one of the direction (rolling direction) uniaxial test case is used as input. Along with this the orthotropic material parameters for AA2024 materials are summarised in Table 6-5 and AA7010 material are summarised in Table 6-7. The value of B and $dB/d\beta$ provided in the input file is used to calculate the effective damage parameter β using equation (8.35) and individual orthotropic direction damage values D_1, D_2, D_3 based on Chow and Wang's damage model theory (1987) using equation (8.36). The model was then checked using single element orthotropic model after necessary verification in single element case the multi-element models virtual tests were performed. The multi-element results are shown from Figure 10-24 to Figure 10-33.

10.4.1 Orthotropic results for AA2024

The orthotropic results for AA2024 simulation results were obtained through cyclic tests. The damage parameter at each cycle is calculated using the elastic modulus degradation similar to experimental damage value calculations. The Figure 10-24 shows the orthotropic behaviour of AA2024 material. The Figure 10-25 shows one of the cyclic tests completed to calculate the damage parameter from simulation test. The damage values for each cycle were calculated in rolling direction and transverse direction. The calculated values were compared against experimental results stress-strain curve Figure 10-26, damage-strain curves Figure 10-27 and damage-stress

curves Figure 10-28. The simulation results produce predictable results in rolling directions and transverse directions.

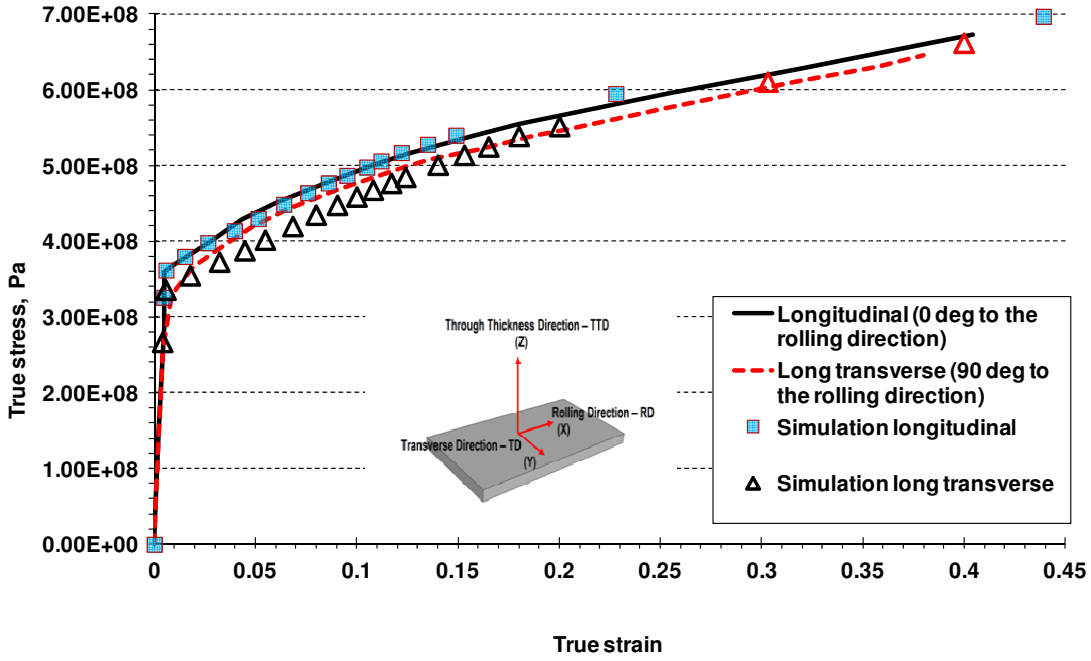

Figure 10-24 Orthotropic case simple tensile test experimental results versus simulation cyclic test results for uniaxial loading case

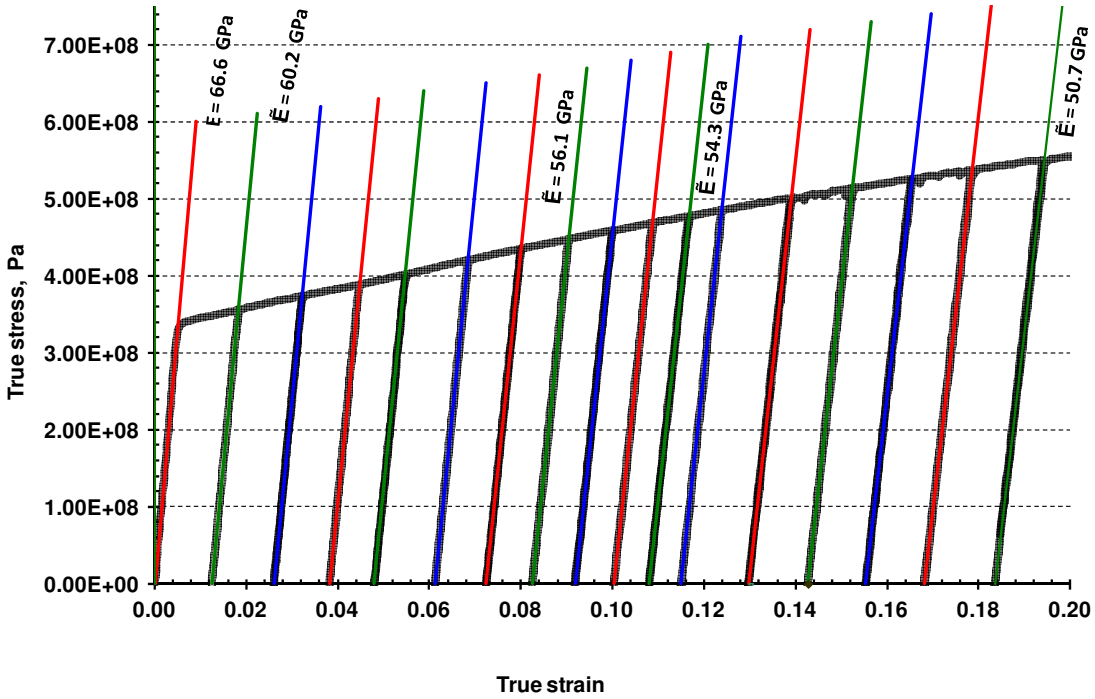

Figure 10-25 Simulation uniaxial cyclic test results using the user code with material AA 2024; the slope lines are highlighted with red, green and blue to show the Young's modulus degradation clearly

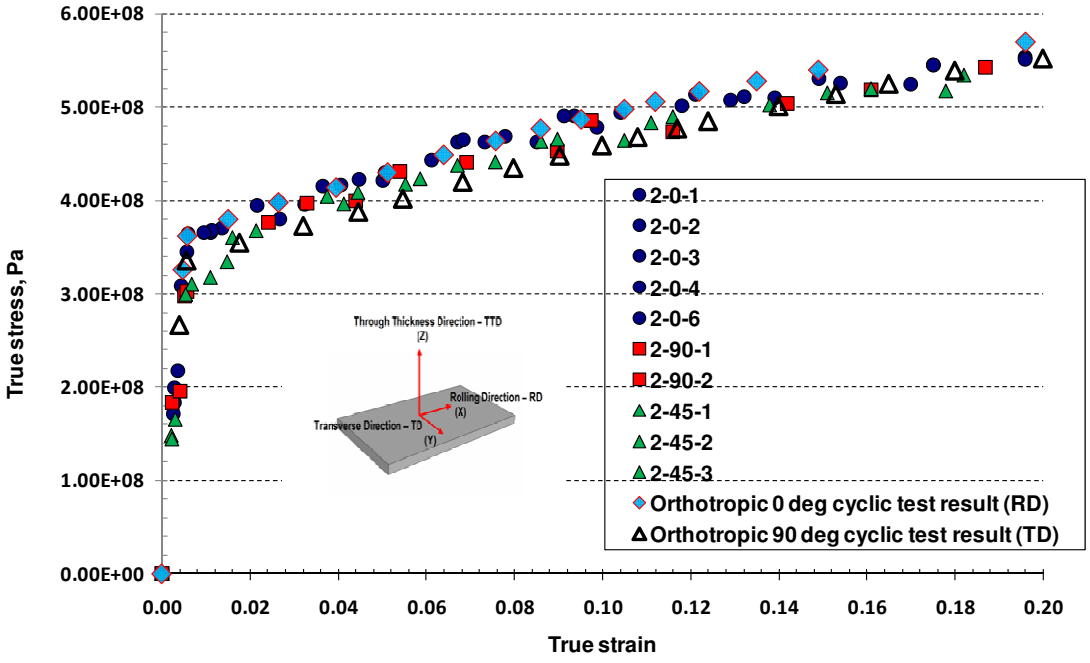

Figure 10-26 Orthotropic case uniaxial cyclic tensile test experimental results versus simulation cyclic test results

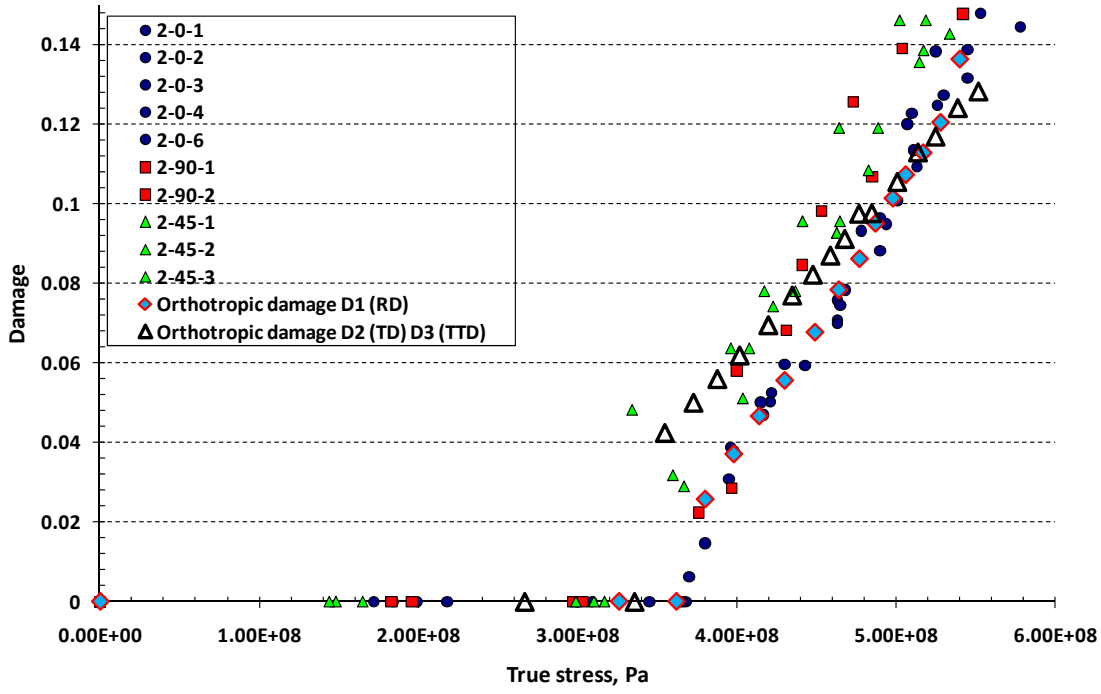

Figure 10-27 Simulation uniaxial cyclic test results using the user code and material characterisation data for AA-2024 material for orthotropic case damage vs stress

The damage values are calculated from rolling direction uniaxial test and transverse direction uniaxial tests using the same procedure applied in experimental results. The

difference in damage parameter between longitudinal direction (D_1) and in transverse direction (D_2) is also due to orthotropy nature of the AA2024 material. The damage parameter (D_3) can be directly obtained from the Abaqus output data. The Figure 10-27 and Figure 10-28 clearly shows the damage initiation points are not same for the rolling direction and transverse direction; this is due the plastic strain and damage starts at lower stresses for transverse direction compared to rolling direction. This also influences the growth of damage at initial stages which can be seen from the graph. As the damage grows in this way and dips lower than the rolling direction damage growth, this may be due to material grain sizes are smaller and packed well together in transverse direction than in the rolling direction. This in turn may not allow any further room for damage (or voids) to grow similar to rolling direction damage. Hence the damage in transverse lowers at critical levels of the material failure compared to rolling direction. It should be noted that in this orthotropic material scenario the material reaches critical damage level earlier in transverse direction compared to rolling direction. Alternatively the orthotropic behaviour might differ based on the grain sizes and distribution of grains, voids, impurities and growth of damage in each material based on the manufacturing process and life cycle loading conditions. The physical and experimental results obtained in this research work reflect the orthotropic behaviour of material recognized by other researcher (Hill (1948); Cordebois and Sidoroff (1980); Lemaitre (1985); Chow and Wang (1987); Hayakawa & Murakami (1998); Mirkovic (2004) and Panov (2006) and practical application problems in rolled aerospace aluminium alloy materials.

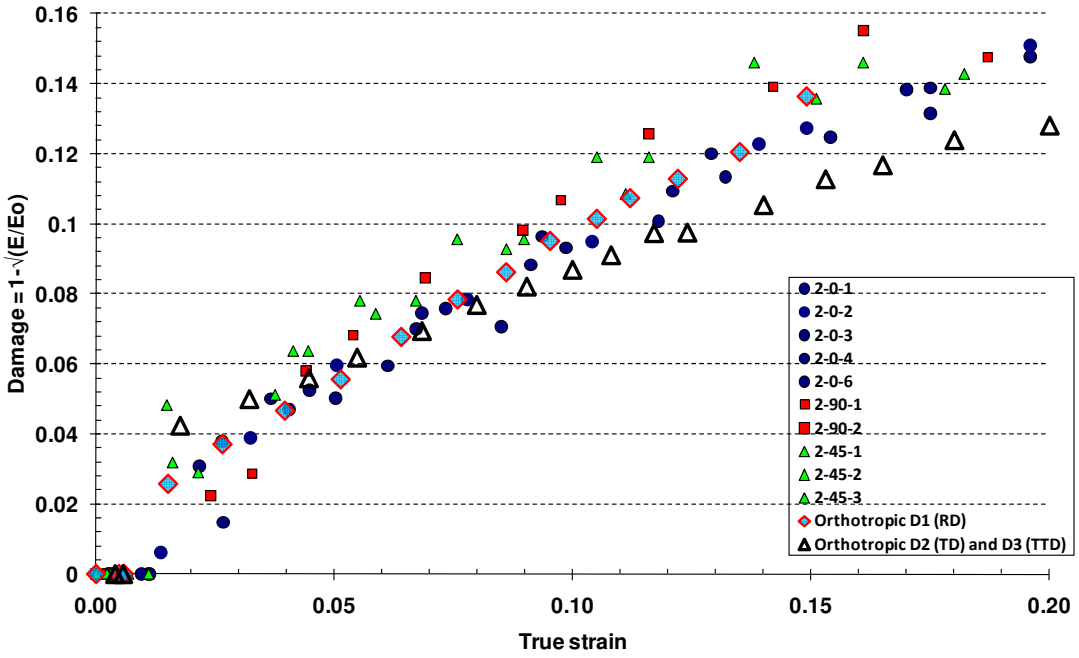

Figure 10-28 Simulation uniaxial cyclic test results for orthotropic case AA-2024 material for strain versus damage D_1, D_2, D_3

10.4.2 Orthotropic results for AA7010

The simulation results for AA7010 specimen are shown from Figure 10-29 to Figure 10-33. Initially a single element model was run with the VUMAT with orthotropic material data, the results are shown in Figure 10-29. The damage variables D_1, D_2 & D_3 produce similar results due to less orthotropy of the AA7010 material. The damage variables D_1, D_2 & D_3 are calculated based on equations (8.36) and (9.14). In Figure 10-29 the single element result show slight variation in the damage parameter. This may be due to the fact a single element with one mm cube might not produce the identical scenario of multi-element model used in experiment though this experiment checks the code for any discrepancies for further use in multi-element model. It is always a good practice to run single element analysis as explained in this research to ascertain the model behaviour before complex analysis.

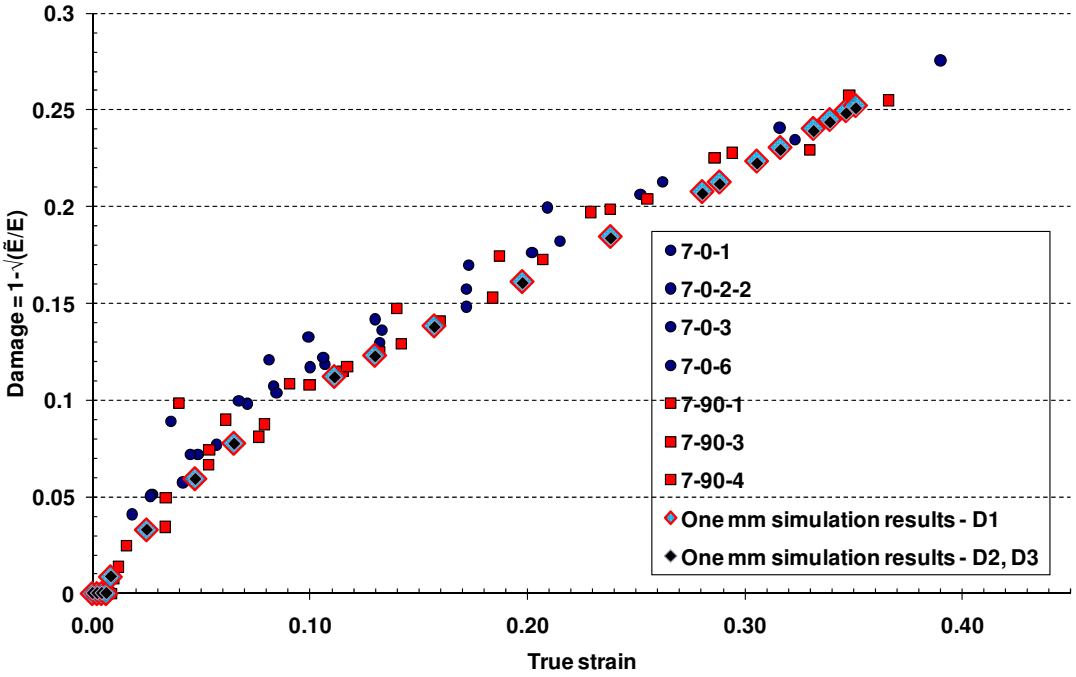

Figure 10-29 Simulation uniaxial cyclic test results using the user code and material characterisation data for AA-7010 material

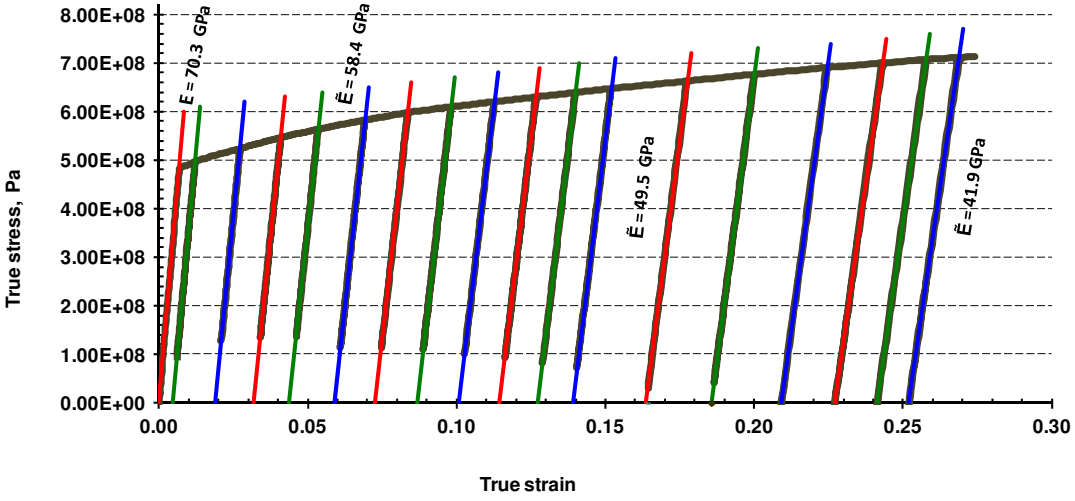

Figure 10-30 Simulation of orthotropic uniaxial cyclic test results using the user code and material characterisation data for AA-7010 material results show similar elastic modulus degradation to uniaxial cyclic test experimental results; the slope lines are highlighted with red, green and blue to show the degradation clearly

The multi-element model is next tested with cyclic test, for damage parameter determination. The Figure 10-30 shows the virtual cyclic test results and elastic modulus degradation. From the cyclic test damage parameters are obtained for rolling direction case and transverse direction case.

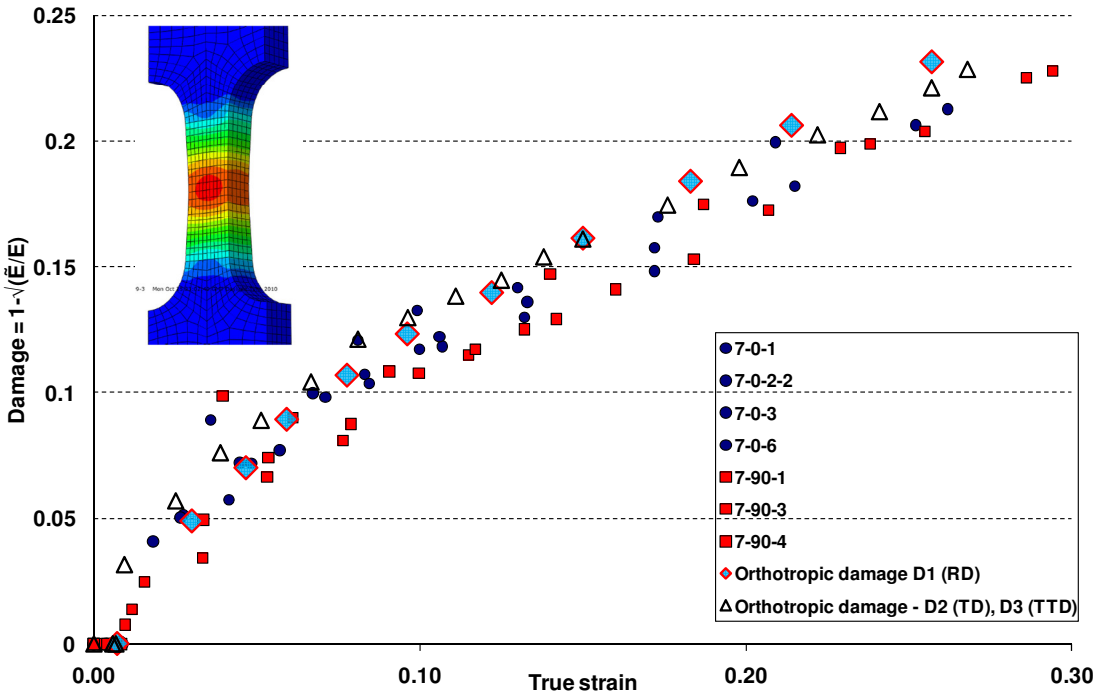

Figure 10-31 Simulation uniaxial cyclic test results using the user code and material characterisation data for AA-7010 material for orthotropic case damage vs strain

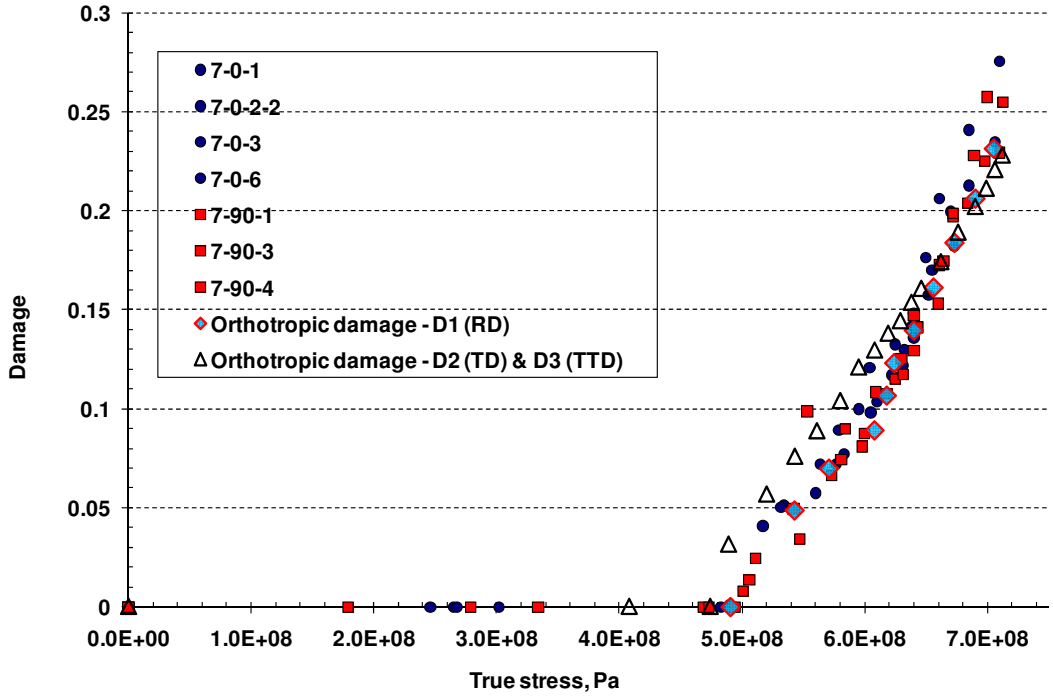

Figure 10-32 Simulation uniaxial cyclic test results using the user code and material characterisation data for AA-7010 material for orthotropic case damage vs stress

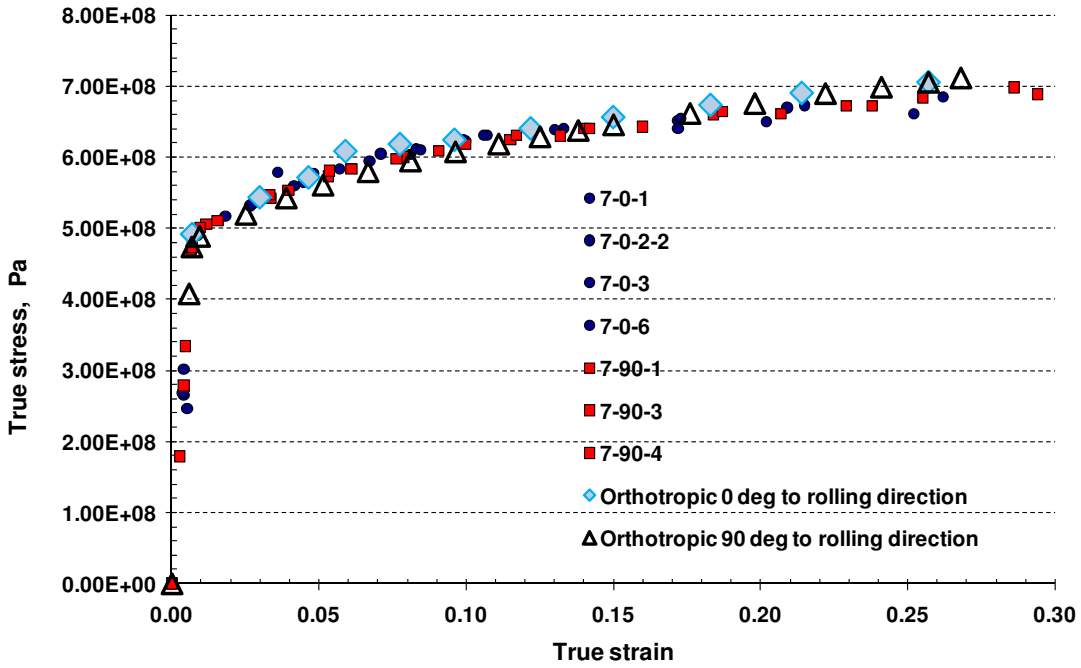

Figure 10-33 Simulation uniaxial cyclic test results using the user code and material characterisation data for AA-7010 material for orthotropic case stress vs strain

The results are shown in Figure 10-31 to Figure 10-33; similar to experimental tests the orthotropic behaviour of AA7010 material is not that significant from the result. The plasticity and damage initiation slightly differ from each other (Figure 10-31 to Figure 10-33). The damage (D_1) in rolling direction starts at a later level compared to transverse direction (Figure 10-32). The simulated damage curve also follows the trend of the experimental results. The damage D_2 starts at an earlier level of stress and it is also slightly higher than in the rolling direction but this difference is not significant. The curve of D_2 also follows the trend of the experimental curve but at initial stages it slightly over predicts the damage when compared to experimental results. However at the higher strains and stress the damage D_2 dips further due to slight orthotropic nature of the AA7010 material. The simulation results of true stress and true strain curves show in Figure 10-33 just follows the experimental curve throughout. The simulation tests results obtained using the new VUMAT code behaves similar to the experimental result trends. The identical methods of comparison of experimental results to simulation results confirm that the material model developed in this research work delivers expected results. The rigours verification and validation procedures followed during the analysis and comparison of simulation tests proves that the damage model has been successfully verified and validated using the coupons.

10.5 Virtual testing of aerospace simple stringer with damage

The airframe structures fail based on various mechanisms. One of the failure mechanisms is through damage, and in this virtual test the failure due to damage growth will be studied. The material damage model verification was planned using a simple aircraft structure. A representative of aircraft structure design was provided by one of the MUSCA partners Airbus. The agreed virtual test structure of simple stringer and skin is shown in Figure 10-34. The tests were carried out to check the code with two sets of different material combination. It was also tested for simultaneous application of inbuilt Abaqus code to represent the isotropic material model without damage and user VUMAT code to represent the orthotropic material with damage.

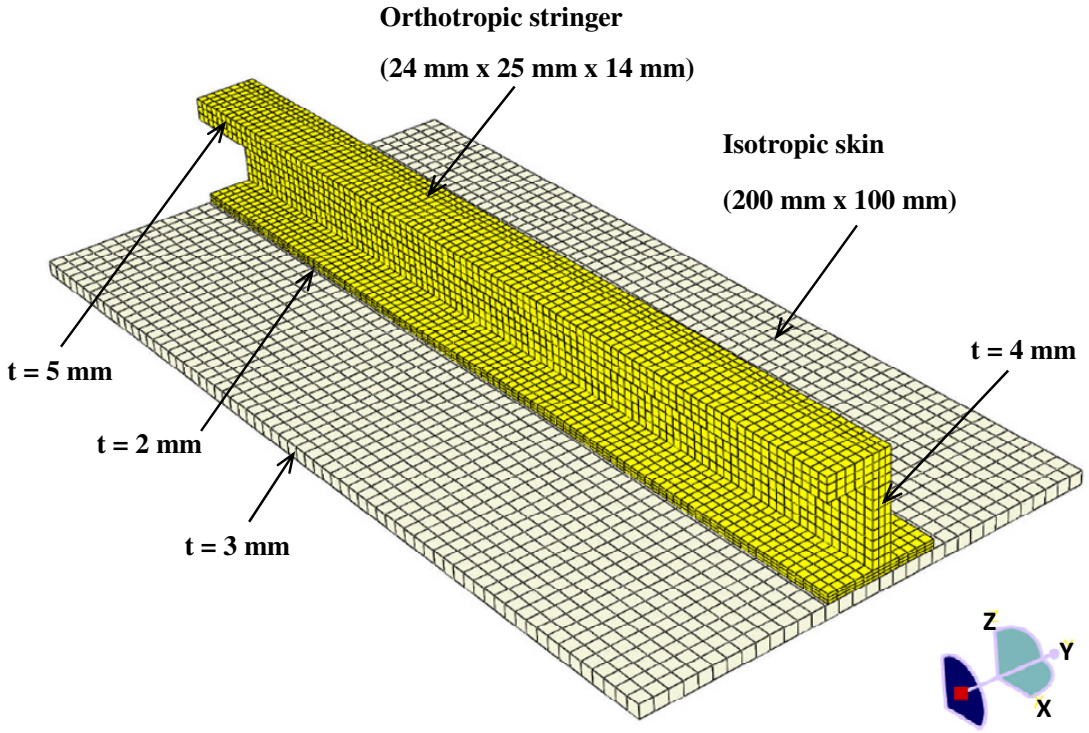

Figure 10-34 Aircraft simple skin and stringer with isotropic skin and orthotropic stringer material properties proposed by aerospace industry

The aim of the simulation tests is to check the code capability, robustness, applicability when used with different types of elements and their ability work when combination of inbuilt and user code material models were used. The model shown in Figure 10-34 is a similar aircraft structures simulated by the aerospace consortium. The simple aircraft skin and stringer model was provided by the aerospace consortium and the simulation tests were carried out to check the code. The results obtained here

were not compared with the experimental results due to the limitations and non-availability of test results from the commercial aerospace consortium. However positive feedbacks were provided by aerospace consortium after completing their independent review of the code and informed that the virtual simulations done using code provided results similar to experimental outcome. The simple stringer model was provided by the aerospace consortium and tested as it is modelled at the Cranfield university computing facility to check the new damage model code.

The skin of the model was represented by continuum brick element by the aerospace consortium when they provided the model for testing. The model has been tested as it was provided by aerospace consortium.

The tests were planned based on two different aspects of the practical application scenario of the code. In the first test case the airframe skin of the model was designated with titanium alloy with isotropic material properties and the stringer with orthotropic aluminium alloy material properties. The isotropic Titanium material parameters were provided by the Airbus and the orthotropic aluminium alloy (AA2024 and AA7010) material parameter were obtained from this research work. In the second test case the skin was designated with isotropic material properties of aluminium alloy and the stringer with orthotropic material properties of aluminium alloy. The simple aircraft structure is then tested with AA2024 and AA7010 along with Titanium. The finite element model developed using Abaqus CAE explicit. The skin was represented with 2211 elements of 8 node linear continuum shell type element with reduced integration (SC8R-explicit) and the stringer with 9000 elements of 8 node linear continuum solid element with reduced integration (C3D8R). The test requires approximately 1200 seconds of CPU time with single precision ABAQUS explicit executable analysis in single core processor. The overall geometry of the representative airframe is shown in Figure 10-34 and the boundary conditions and loading conditions are shown in Figure 10-35. On the one side of the structure all translational and rotational freedom were arrested for skin and stringer. On the other three sides (Figure 10-35) the translational movement of ZZ axis (U3) alone is arrested for the skin and stringer. The joints between the skin and stringer is represented with connector load of 1000 N applied at the joints in ZZ axis from the top and bottom (stringer side and skin side) to keep the skin and stringer together. The

opposite side of the fixed end is then applied with displacement in XX axis (U1) and YY axis (U2) direction. With this combination of boundary conditions the structure is subjected to end compression resulting in buckling of stringer and skin.

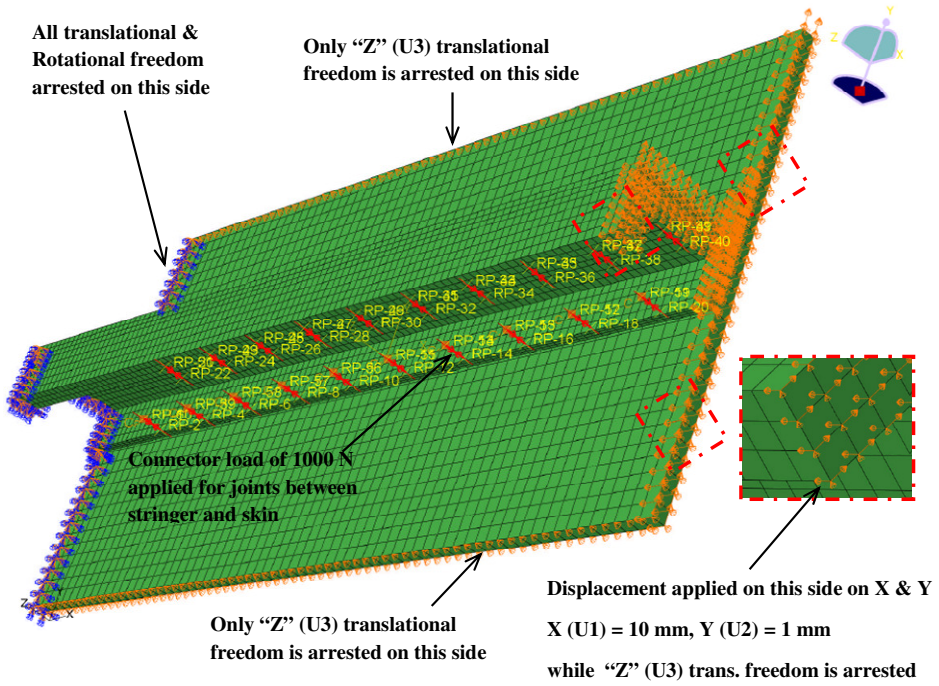

Figure 10-35 Aircraft simple skin and stringer structure boundary conditions and loads

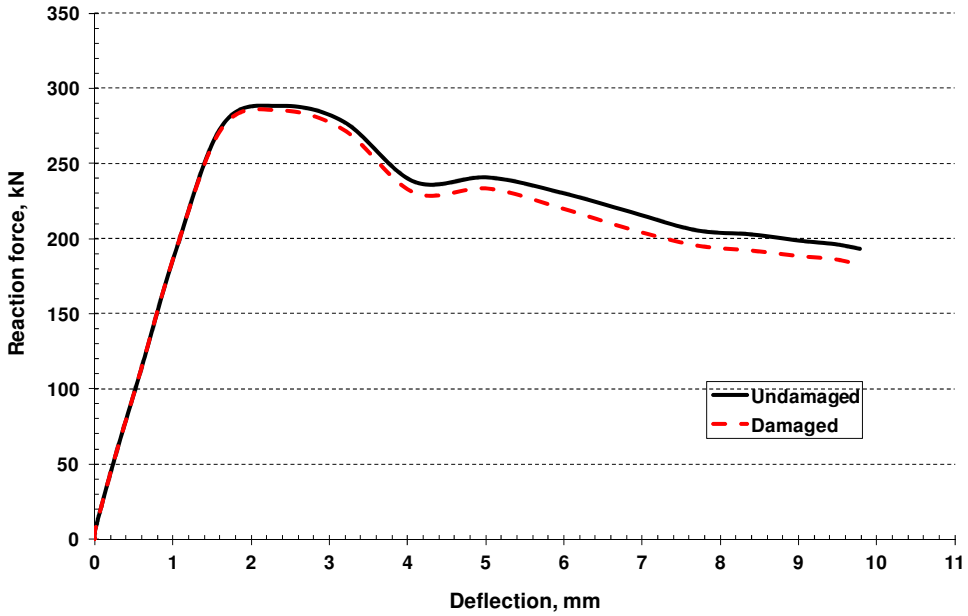

Figure 10-36 Aircraft simple skin (titanium alloy) and stringer (AA7010) structure force versus deflection curve

The reaction forces and deflection of the skin and the stringer are shown in the Figure 10-36. The force deflection curve contains some of the information about the propagation of damage. In this case the damage model is applied only for stringer of

the structure. When the structure reaches peak load, the damage starts to grow gradually in the stringer. In this case the application of the further load increases the damage in the stringer material gradually and damage grows up to 22% for plastic strain of 28% (Figure 10-38 and Figure 10-39).

10.5.1 AA-7010 aerospace simple stringer test

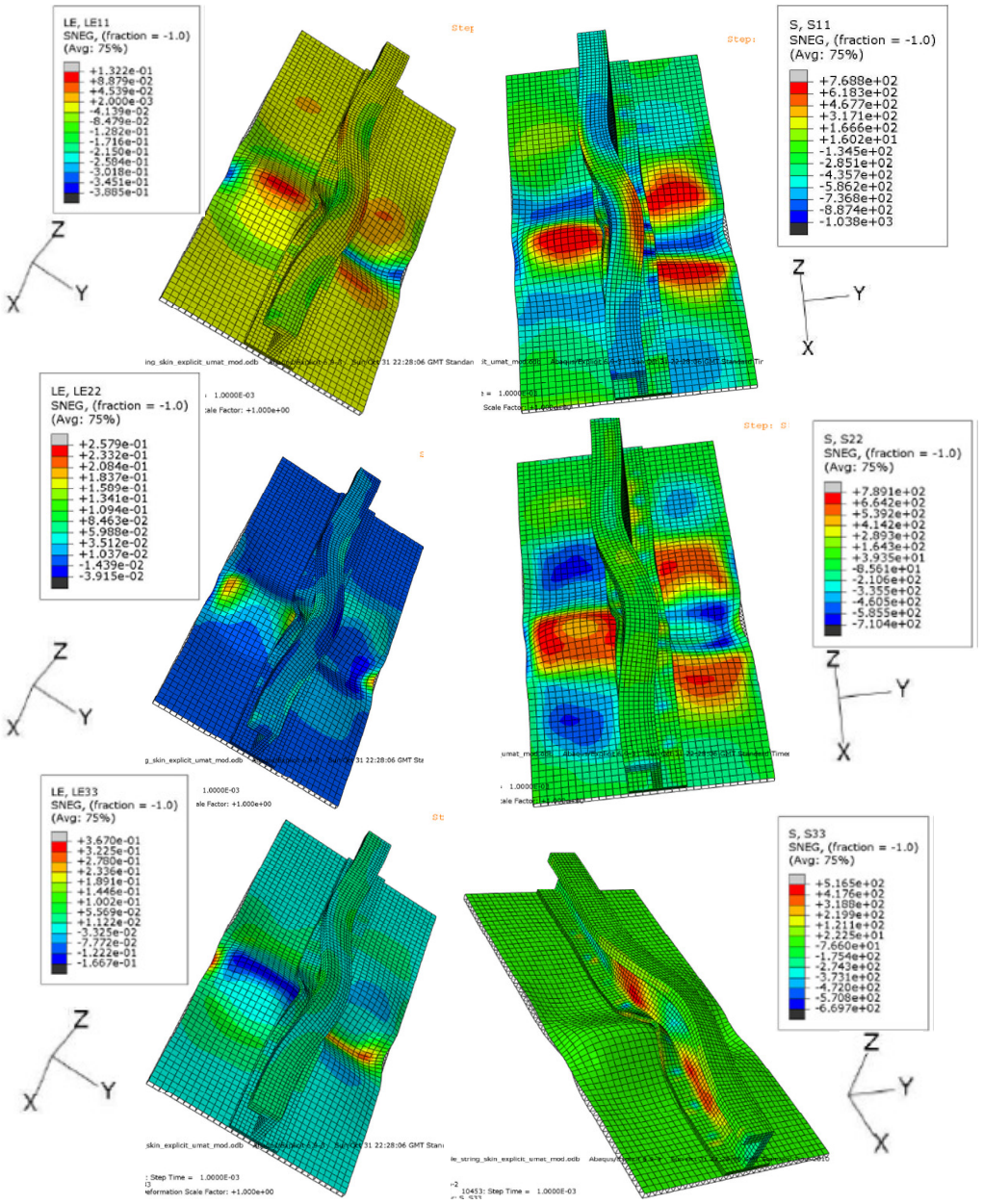

Figure 10-37 AA7010 isotropic skin and orthotropic stringer (aircraft structure) stringer with damage parameters in Rolling (11), long transverse (22) and transverse (33) direction (true strain notation LE, true stress notations S; true stress in N/mm^2)

The AA7010 material was analysed using the orthotropic parameters determined from the experimental results (Table 6-7) for the stringer and isotropic material parameters for the skin material. The complete assembly was subject to buckling loading and the results are shown Figure 10-37 to Figure 10-42. The combined isotropic and orthotropic simple stringer assembly results are shown in Figure 10-37. The stress strain contours based on tensile loading and compressive loading are shown for each rolling direction, transverse direction and through thickness direction.

The results show that the stress and strain variables are higher in transverse direction. The damage parameters are applicable only for the stringer portion of the analysis and the discussions of the results based on damage parameters are on the next paragraph.

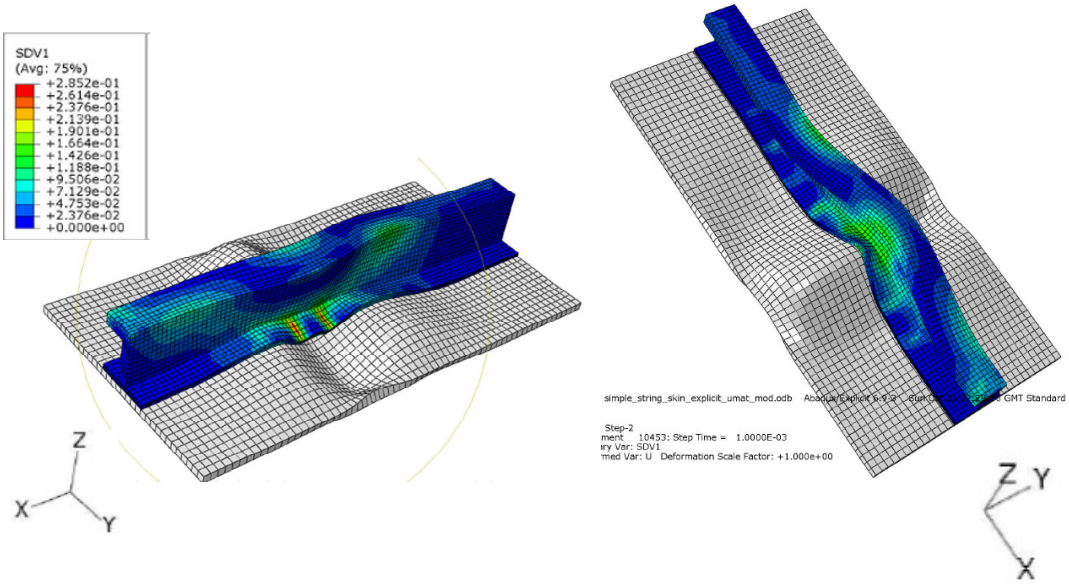

Figure 10-38 AA7010 Orthotropic stringer accumulated plastic strain (SDV1)

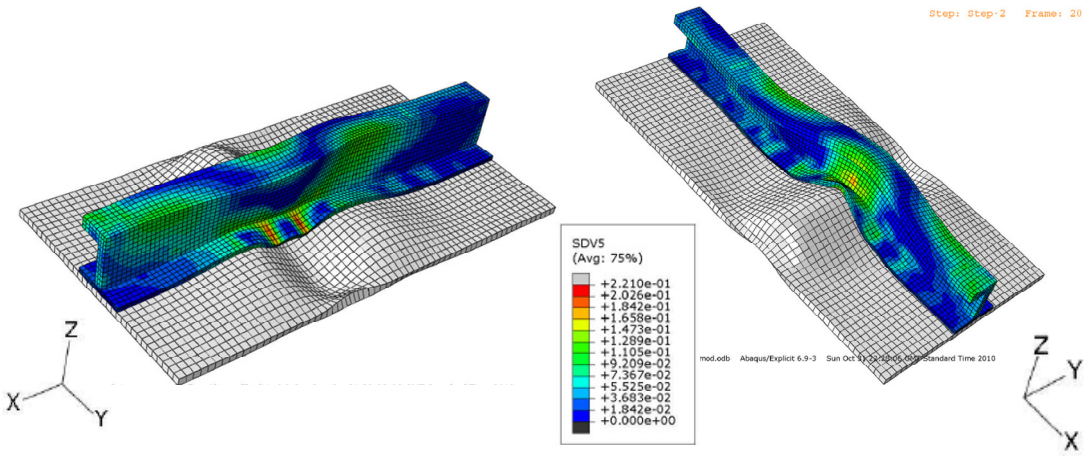

Figure 10-39 AA7010 Orthotropic stringer accumulated damage (SDV5)

The accumulated plastic strain and accumulated damage in the stringer material for a buckling loading are shown in Figure 10-38 and Figure 10-39. The damage parameters are shown here along with the plastic strain. The accumulated damage follows the trend of the plastic strain and show similar contour. It can be observed that the damage growth increases at various regions based on the tensile stresses induced in the stringer due to the loading condition. The area of maximum damages coincides with the maximum stresses and strains. The overall parameter obtained in this way gives a good understanding of material behaviour in actual loading conditions.

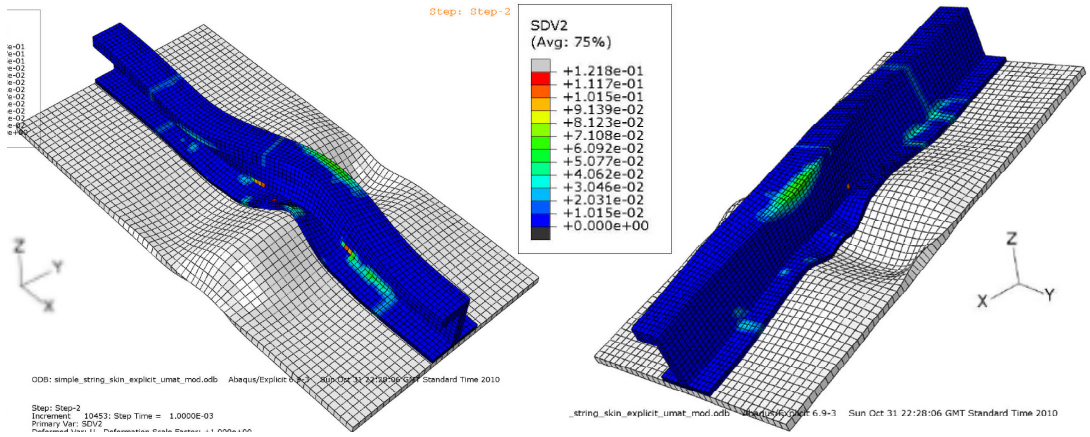

Figure 10-40 AA-7010 Orthotropic stringer test results - damage D_1 (rolling direction SDV2)

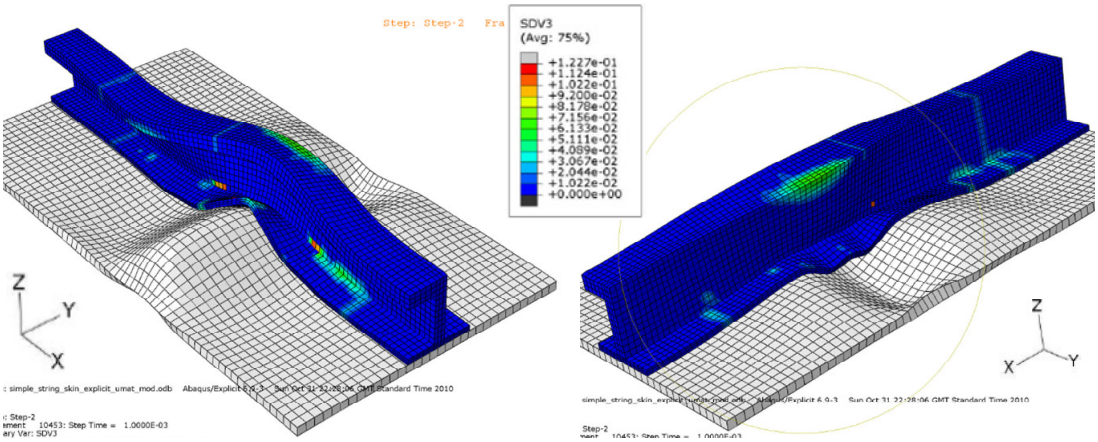

Figure 10-41 AA-7010 Orthotropic stringer test results - damage D_2 (90 deg to rolling direction SDV3)

The material damage in rolling direction is shown in Figure 10-40 the damage occurs at localised location along the flange of the stringer where it is connected to

the skin. The maximum damage peaks at about 12% at some of the locations . Similar to the rolling direction the transverse direction damage growth contours and transverse direction damage growth are shown in Figure 10-41 and Figure 10-42. The damage D_2 levels in transverse direction are similar to rolling direction D_1 levels. .

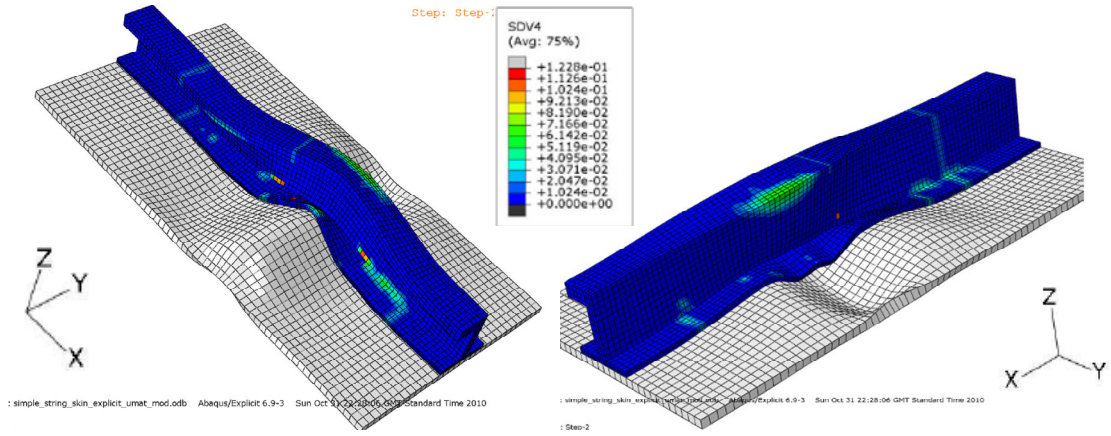

Figure 10-42 AA-7010 Orthotropic stringer test results - damage D_3 (through thickness direction SDV4)

10.5.2 Aerospace simple stringer with AA-2024 material

The test for AA2024 material was planned with less stiff aluminium material alloy compared to Titanium alloy provided by MUSCA partners, to check the response of the stringer with less stiff skin. The aluminium material parameters used in this test are based on the isotropic and orthotropic parameters determined in this research work. The simulation test for AA2024 isotropic material parameters were obtained from Table 6-4 for the skin material. The stringer orthotropic material properties were obtained from Table 6-5.

The user code tests were performed based on Chow and Wang damage model VUMAT code developed in this research. The combination of material used here are with isotropic and orthotropic material in nature. The isotropic analysis was performed by the inbuilt Abaqus explicit and the orthotropic model was run with the user explicit model. This test also proves that the combination of analysis can be performed using both Abaqus inbuilt and user explicit models at the same time. The Figure 10-43 shows the result of skin with isotropic values and stringer with orthotropic values for buckling test scenario. The high stress strain contours of skin

and stringer for rolling direction, transverse direction and through thickness directions are shown in the diagram. The higher tensile stress values are also seen on the skin as well as on the stringer. It should be noted that the skin stress strain values do not incorporate damage parameters.

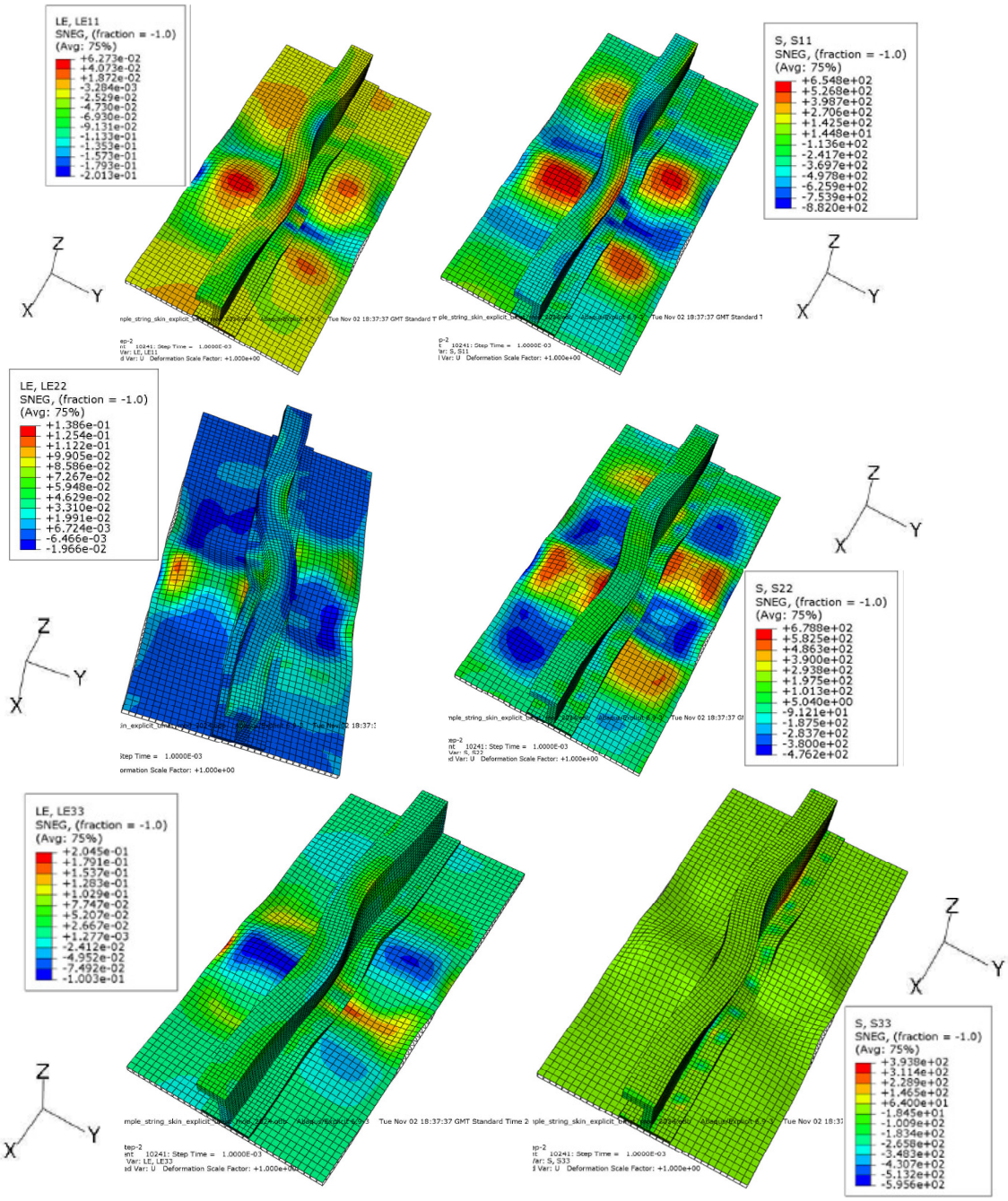

Figure 10-43 AA2024 isotropic skin without damage and orthotropic stringer with damage parameters in Rolling (11), long transverse (22) and transverse (33) direction (true strain notation LE, true stress notations S; true stress in N/mm^2)

The combined results are shown on the Figure 10-43. The stress and strain contours for AA2024 material combination shows lower values of stress and strain compare to AA7010 along with stiffer Titanium skin material combination discussed in the previous section. The less stiff skin of AA2024 isotropic material and AA2024 orthotropic stringer show around 10% reduction in accumulated plastic strain and subsequent 14% reduction of accumulated damage. The reduction in the damage growth on the stringer reveals a different contour of damage compared to pervious analysis of AA7010 material.

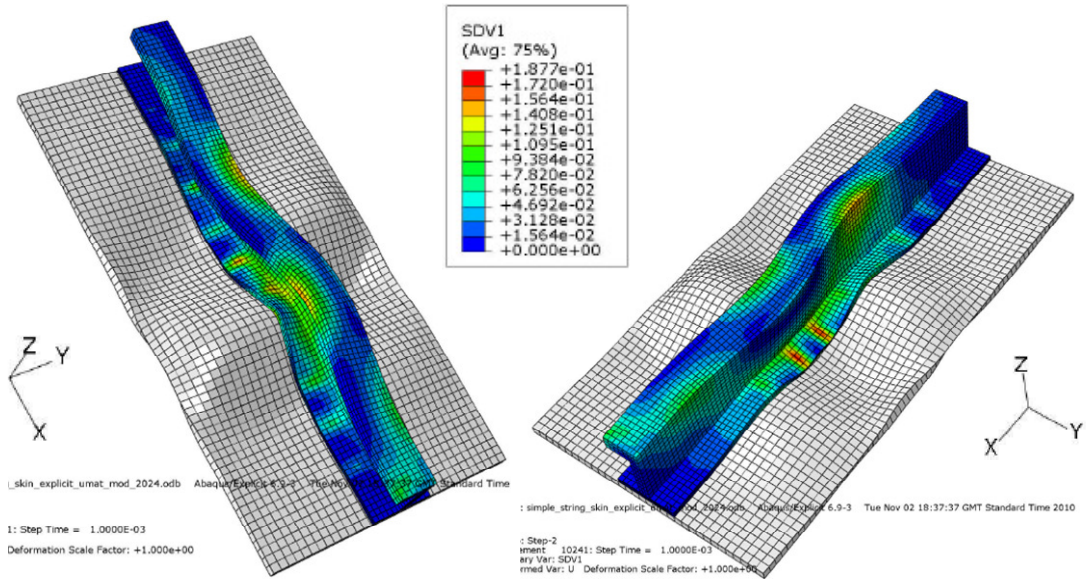

Figure 10-44 AA-2024 Orthotropic stringer accumulated plastic strain (SDV1)

The Figure 10-43 and Figure 10-44 show the accumulated plastic strain and accumulated damage in the stringer material for a buckling loading. The damage parameters are shown in conjunction with the plastic strain on the stringer in Figure 10-44. The accumulated damage or effective damage parameter from this analysis shows the overall damage as a cumulative combination of orthotropic effect in the individual material direction. This new accumulated damage term can be used to analyse the materials effects due to damage and predict the ultimate load for the structures.

The damage contours shown in Figure 10-44 gives the damage values at different area of the stringer geometry based on the tensile stresses and strains. Higher level of damage can be observed where the tensile parameters are high in the stringer. The

combined damage parameter shows where the material might fail in case if it is loaded further. The damage shows higher values at the joints between the stringer and skin. Similarly the damage values increase to higher levels at the corners of the material where the stresses are higher.

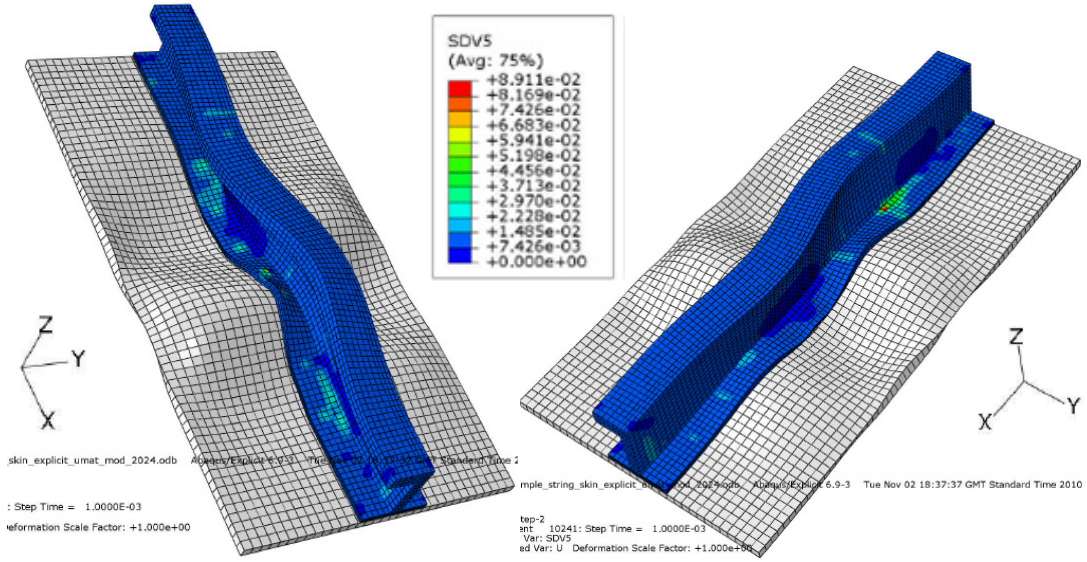

Figure 10-45 AA-2024 Orthotropic stringer results - accumulated damage (SDV5)

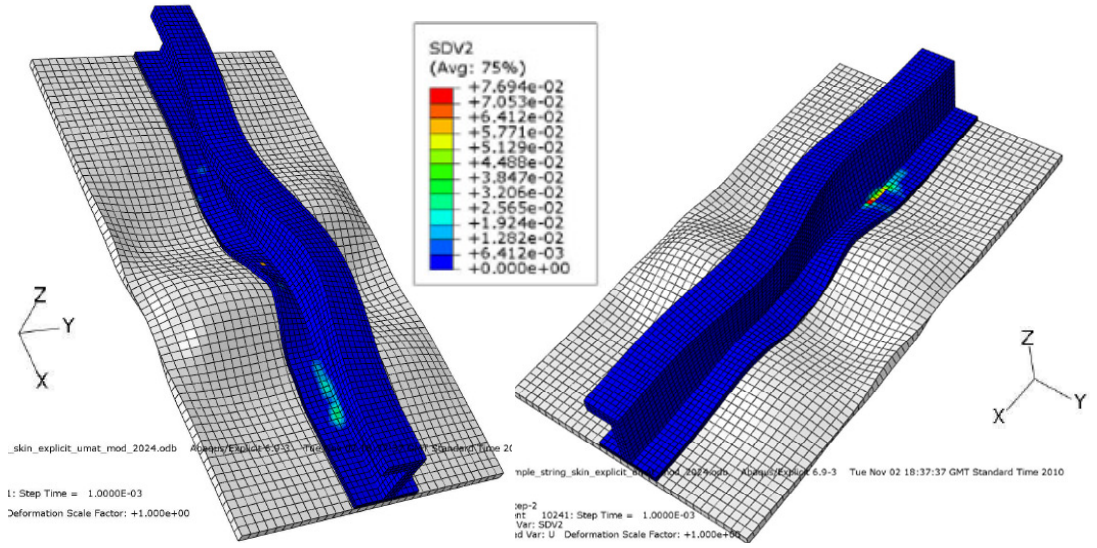

Figure 10-46 AA-2024 orthotropic stringer results - damage D_1 (rolling direction SDV2)

The individual damage growth parameters in the three orthotropic directions are shown from Figure 10-46 to

Figure 10-48. The damage growth in each direction depends on the loading condition in that particular region. In rolling direction of the material the damage growth is seen higher at the stringer joints where higher elongation takes place.

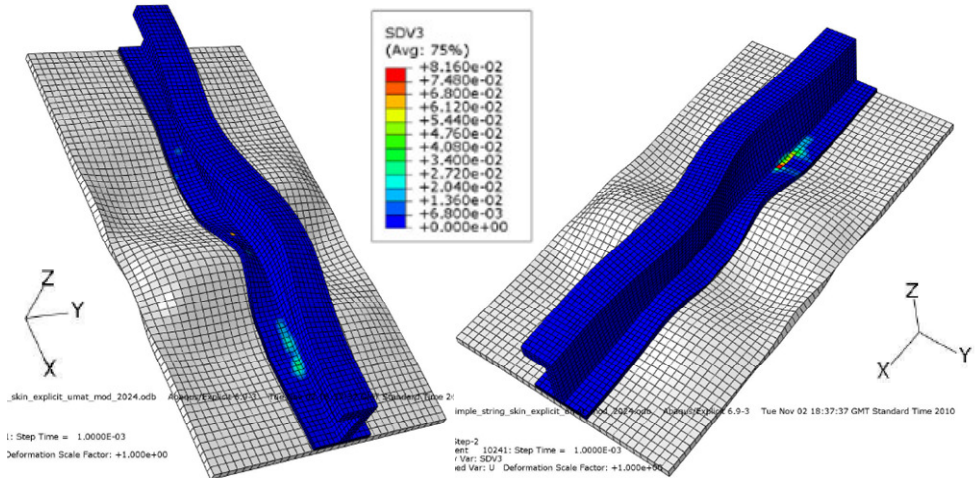

Figure 10-47 AA-2024 orthotropic stringer results - damage D_2 (90 deg to rolling direction SDV3)

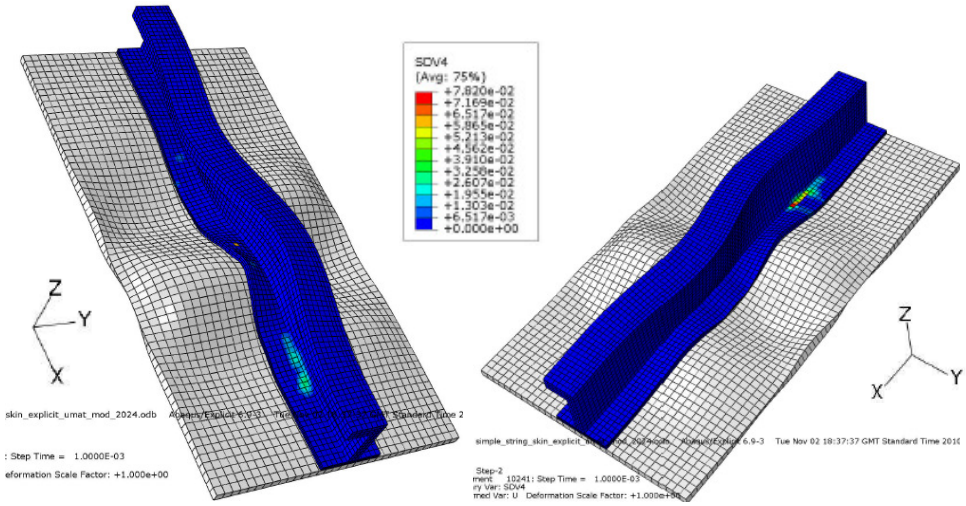

Figure 10-48 AA-2024 Orthotropic stringer results - damage D_3 (through thickness direction SDV4)

The localised nature of the damage growth shows similar behaviour of material when subjected to actual life cycle loading condition. The damage growth will be prominent if the material is subject to higher loads. The damage parameter evolution in this way can aid the engineers in identifying the weak areas of the section and take necessary steps to solve the problem. The Figure 10-46 shows the damage parameter in rolling

direction. The maximum damage of about 7.7% is seen near the joints of the stringer and skin. Similarly on Figure 10-47 the damage parameter in long transverse direction is about 8.2% which is slightly higher than in the rolling direction. The
Figure 10-48 shows the damage parameters for through thickness direction with a maximum of 7.8%. The variation in damage parameter in each direction is not that significant for AA2024 analysis. The damage concentrations on all three directions are almost similar in nature with slight variation in magnitude. This implies that the material damage might occur in areas where all the orthotropic damage growth accumulates and escalates the growth of damage. However individual orthotropic damage growth could also lead to material failure if pronounced effect on that particular direction is introduced due to a loading condition.

10.6 Numerical tests conclusion

The damage model along with the damage parameters determined from the experimental tests was successfully tested using single element isotropic models, multi-element isotropic models, multi-element orthotropic models and simple airframe structure. The damage parameters from the numerical tests were determined using identical methods used for experimental calculations. The simulation results were then verified and validated using the experimental results. The effects of variation in damage parameters such as damage initiation stress and damage evolution ratio and change in deformation speed were also successfully studied.

The individual damage in each orthotropic direction and accumulated damage growth determination using the damage model allows the researcher and engineers to predict the material damage in their respective applications. This also gives a great advantage to the engineer to identify localised damage growth for various loading condition and strengthen them during the design process. The application of damage along with elastic plastic stress strain curves also gives a powerful tool to get the materials strength during the loading history of the material. The virtual test also allows engineers to check the material ultimate load based on how much strain and stress are induced in the material during the loading condition in actual life cycle and predict failure during the use based on the present damage and successive damage growth values.

11 Conclusion

The main objective of the thesis is to develop a numerical testing tool to predict orthotropic metals behaviour in elastic loading condition, plastic deformation, initiation of damage, damage evolution and failure using simulation technique. The developed technique must be applicable in aerospace structures with noticeable level of orthotropy. The new numerical code should be developed using finite element software used/available in the EU aerospace industry. The Chow and Wang damage model was selected from the existing orthotropic model for developing the numerical model. MUSCA partners identified that explicit solvers gave better behaviour of dynamic processes for large scale structure in quasi-static test regime. The material model was developed for quasi-static strain rate regime as per MUSCA project partners requirement and implemented in Abaqus VUMAT explicit user code. Experiments were carried out with standard uniform cross-section specimens and varying cross section specimens to obtain the damage model material constants. The orthotropic materials were characterised using relatively new non contact type digital image correlation technique using standard dog bone specimen. The developed code was verified and validated using the experimental results. The methodologies to develop the material model and the conclusions of the research work are summarised here.

- A quasi-static Chow and Wang damage model was selected for the development of numerical model. A new implementation procedure with plastic multiplier and damage multiplier were derived for numerical calculation of damage parameters compatible with Abaqus explicit VUMAT code in this thesis.

- An iterative material model development procedure has been followed in this research work. Initially a verification of material co-ordinate transformation is checked in Abaqus. The material model is then developed for use for elastic region and plastic region with isotropic material character. A single element uniaxial tensile test model was developed and tested with known material values. After that multi-element tensile test models were developed and test with isotropic material properties.

- Experimental tests have been conducted using the new digital image correlation technique. This technique is used for obtaining the stress strain values for standard tensile test and cyclic test from the uniform cross section and varying cross section specimens. Using the data obtained from DIC a new procedure has been developed to characterise damage parameters in this research. The possibility of identifying maximum strain to obtain damage parameter from a uniform cross section specimen after completion of the cyclic test is checked thoroughly in this research work. The procedure uses DIC equipment available in the industry.

- The Chow and Wang damage parameter are identified and calculated using the elastic modulus degradation of material during the damage process. A method has been established and verified to determine all damage parameters from the initial experimental values obtained through the DIC. The procedures to obtain the Chow and Wang damage parameters are explained in this research work. Using the procedure aerospace Aluminium alloy AA-2024-T3 and AA-7010-T7651 orthotropic parameters were characterised.

- It was also established during the isotropic simulation testing that in some material where there is less orthotropy behaviour, isotropic damage parameters are more than sufficient as the input parameters.

- The numerical model iterative step is then introduced with orthotropic yield criteria with damage evolution and failure using Hill's orthotropic co-efficient. The numerical model is then implemented first on a single element and checked and verified with experimental values. Multi-element isotropic and orthotropic tests were then carried out and the damage parameters were calculated similar to the experimental test. The simulation values were verified and validated by comparing with the experimental test data.

- The simulation with combination of user code and inbuilt analysis done in aircraft simple stringer and skin proves that the newly developed VUMAT code can be used in combination with inbuilt material models.

There are lot of advanced complicated material models available in the damage mechanics area without clear strategy to calibrate them. However in this research the combination of experimental work and numerical analysis with clear and simpler calibration strategy for damage model is demonstrated. This is the important contribution of this research work and the streamlined procedures are vital for the industry to utilise the new damage prediction tools.

The damage model implementation and test procedures developed through this research provide information and processes involved in fundamentally predicting the ductile damage in metals and metal alloys. The numerical damage model developed using the well defined verification and validation procedures explained in this research work with new streamlined damage material characterisation using recent contact less DIC technique has wider implication in the material model development for ductile metals in general.

- The validation and verification procedure can be used in developing other ductile materials such as Titanium, Copper, Steel and similar metals and metal alloys.

- The damage material characterisation test procedure has been well streamlined in this research for immediate industrial applications with existing equipment and it could be adopted in characterising similar metals and metal alloys.

- The streamlined experimental laboratory and virtual laboratory set up explained in this research work and the research methodology in developing numerical model can be followed by other researchers in this field.

The optical contact less method used by DIC technique allows the researchers and engineers in the industry to characterise the damage parameters for practical application. A standard specimen can be used during the cyclic test. The maximum strain location can be identified after completion of the experiment and subsequent damage values can be determined. The verification and validation process and the relatively simple damage parameter characterisation using new DIC technique

delivered a robust numerical damage model for practical application in the aerospace industry.

The advantage of using damage along with the existing stress stain curve allows the engineers and researchers to predict and establish the structural ultimate load at known interval. During the design phase the engineers can develop their new structures and testing them along with damage model will be vital in new product development. The identification of damage concentration and localised directional values based on orthotropy will allow the engineers to improve the product in design phase itself. The rigorous checking and designing of new products using damage model will reduce the overall cost and time of superior product delivery.

11.1 Future work

Future work should be carried out to improve the present model; some of the ways to improve the model and further research work based on this present model are listed here:

- The present model is verified and validated in quasi-static region; the AA2024 material and AA7010 material also have verified and validated intermittent strain rate test data (Panov, 2006). To extent dynamic case using these quasi-static experimental data and transient dynamic rate dependent experimental data and result findings (Panov, 2006). To create a combination of this two to the material model and use this for complete analysis at various strain rates at practical industrial applications.
- The dynamic range of the material model could be improved further using new material testing at higher strain rates and temperature loading. This will enable the application of the simulation to complex engineering structures with different dynamic load and subjected to different strain rates and temperature.
- The present material model could be developed into DYNA3D to extend the possibility of application.
- The present model is developed based on isotropic strain hardening criterion. A combined isotropic and kinematic strain hardening can be developed in the continuum mechanics principle to extent model for engineering materials that show kinematic strain hardening behaviour.

12 References

AKINIWA, Y., TANAKA, K. and MATSUI, E., 1988. Statistical characteristics of propagation of small fatigue cracks in smooth specimens of aluminium alloy 2024-T3. *Materials Science & Engineering A: Structural Materials: Properties, Microstructure and Processing,* **A104**, pp. 105-115.

ALLEN, D.H., HARRIS, C.E. and GROVES, S.E., 1987. A thermomechanical constitutive theory for elastic composites with distributed damage-I. Theoretical development. *International Journal of Solids and Structures,* **23**(9), pp. 1301-1318.

ALVES, M., YU, J. and JONES, N., 2000. On the elastic modulus degradation in continuum damage mechanics. *Computers and Structures,* **76**(6), pp. 703-712.

ARETZ, H., HOPPERSTAD, O.S. and LADEMO, O.-., 2007. Yield function calibration for orthotropic sheet metals based on uniaxial and plane strain tensile tests. *Journal of Materials Processing Technology,* **186**(1-3), pp. 221-235.

BENALLAL, A., BILLARDON, R. and LEMAITRE, J., 1985. Finite analysis of structure by continuum damage mechanics. *Proc. ICF-6, Advances in Fracture Research,* **5**, pp. 3669-3676.

BETTEN, J., 1983. Damage tensors in continuum mechanics. *Journal de mecanique theorique et appliquee,* **2**(1), pp. 13-32.

BRIDGMAN, P.W., 1952. *Studies in Large Plastic Flow and Fracture.* Newyork: McGraw-Hill.

BRÜNIG, M., 2003. Numerical analysis of anisotropic ductile continuum damage. *Computer Methods in Applied Mechanics and Engineering,* **192**(26-27), pp. 2949-2976.

CAMPBELL, J.C., VIGNJEVIC, R. and MIRKOVIC, J., 2006. A damage model for orthotropic metals, *Journal de physique IV (2006)*, pp. 481-486.

CHABOCHE, J.L., 1993. Development of continuum damage mechanics for elastic solids sustaining anisotropic and unilateral damage. *Int. J. Damage Mech.,* **2**(4), pp. 311-329.

CHABOCHE, J.L., 1984. Anisotropic creep damage in the frame work of continuum damage mechanics *Nuclear Engineering and Design,* **79**(3), pp. 309-319.

CHEN, S.R. and GRAY, G.T., Constitutive behaviour of Tantalum and Tantalum-Tungsten alloys. *Metallurgical Transactions 24A,* **27A**, pp. 2994-3006.

CHOW, C.L. and JIE, M., 2004. Forming limits of AL 6022 sheets with material damage consideration - Theory and experimental validation. *International Journal of Mechanical Sciences,* **46**(1), pp. 99-122.

CHOW, C.L. and LU, T.J., 1992. A comparative study of continuum damage models for crack propagation under gross yielding. *International Journal of Fracture,* **53**(1), pp. 43-75.

CHOW, C.L., TAI, W.H. and CHU, E., 2003. Computer simulation of sheet metal forming based on damage mechanics approach. *Journal of Materials Processing Technology,* **139**(1-3 SPEC), pp. 553-558.

CHOW, C.L. and WANG, J., 1988. A finite element analysis of continuum damage mechanics for ductile fracture. *International Journal of Fracture,* **38**, pp. 83-102.

CHOW, C.L. and WANG, J., 1987. An anisotropic continuum damage theory and its application to ductile crack initiation *Damage mechanics in composites; Proceedings of the Winter Annual Meeting,* 13-18 Dec 1987, , pp. 1-9.

CHOW, C.L. and WANG, J., 1987. An anisotropic theory of continuum damage mechanics for ductile fracture. *Engineering Fracture Mechanics,* **27**(5), pp. 547-558.

CHOW, C.L. and WANG, J., 1987. An anisotropic theory of elasticity for continuum damage mechanics. *International Journal of Fracture,* **33**(1), pp. 3-16.

CHOW, C.L. and YANG, X.J., 2003. Prediction of forming limit diagram with mixed anisotropic kinematic-isotropic hardening plastic constitutive model based on stress criteria. *Journal of Materials Processing Technology,* **133**(3), pp. 304-310.

CHOW, C.L., YU, L.G. and DEMERI, M.Y., 1997. A unified damage approach for predicting forming limit diagrams. *Journal of Engineering Materials and Technology, Transactions of the ASME,* **119**(4), pp. 346-353.

CHUNG, K. and SHAH, K., 1992. Finite element simulation of sheet metal forming for planar anisotropic metals. *International journal of plasticity,* **8**(4), pp. 453-476.

CORDEBOIS, J.P. and SIDOROFF, F., 1980. Anisotropic damage in elasticity and plasticity. *Journal de mecanique theorique et appliquee,* , pp. 45-59.

CRISFIELD, M.A., 2000. *Non-linear finite element analysis of solids and structures - Volume 2 - Advanced topics.* England: John Wiley & Sons.

CRISFIELD, M.A., 1997. *Non-linear finite element analysis of solids and structures - Volume 1.* England: John Wiley & Sons.

DANTEC DYNAMICS, 2006. *Advanced full-field displacement and strain analysis - Digital 3D correlation system Q-400-II.* Germany: .

DAVIES, H.E., TROXELL, G.E., HAUCK, G.F.W., 1982. *The testing of engineering materials* New York: McGraw Hill.

DE BORST, R. and FEENSTRA, P.H., 1990. Studies in anisotropic plasticity with reference to the hill criterion. *International Journal for Numerical Methods in Engineering,* **29**(2), pp. 315-336.

DE VUYST, T., 2003. *Hydrocode modeling of water impact*, PhD Thesis, Cranfield University.

Dieter, G.E., 1989. *Mechanical Metallurgy, Third Edition, McGraw-Hill Series in Materials Science and Engineering*, USA: McGraw-Hill, Inc.

FOLLANSBEE, P.S. and KOCKS, U.F., 1988. A constitutive description of the deformation of copper based on use of mechanical threshold stress as an internal state variable *Acta Metallurgica,* **36**, pp. 81-93.

FONSEKA, G.U. and KRAJCINOVIC, D., 1981. Continuous damage theory of brittle materials - 2. Uniaxial and plane response modes *Journal of Applied Mechanics, Transactions ASME,* **48**(4), pp. 816-824.

GAUDREAULT, P., BOUAMOUL, A., DUROCHER, R. and ST-JEAN, B., 2005. Finite element modelling of light armoured vehicle welds heat affected zone subjected to an anti-vehicular blast landmine loading, A summary of numerical model and field experiment, *22 International symposium on ballistics,* 14-18 November 2005 2005, Vancouver, BC, Canada, pp. 1079-1087.

GERMAIN, P., NGUYEN, Q.S. and SUQUET, P., 1983. Continuum thermodynamics. *Journal of Applied Mechanics, Transactions ASME,* **50**(4 b), pp. 1010-1020.

GOURDIN, W.H. and LASSILA, D.H., 1991. Flow stress of OFE copper at strain rates from 10^{-3} to 10^{4} s^{-1}: Grain-size effects and comparison to the mechanical threshold stress model. *Acta Metallurgica Et Materialia,* **39**(10), pp. 2337-2348.

GRAY, G.T., MAUDLIN, P.J., HULL, L.M., ZUO, Q.K. and CHEN, S., 2005. Predicting material strength, damage and fracture - The synergy between experiment and modeling. *Los Almos Science,* (29), pp. 80-93.

HALPHEN, B. and NGUYEN QUOC SON, 1975. On generalized standard materials. *J Mec,* **14**(1), pp. 39-63.

HAO LEE, KE PENG and JUNE WANG, 1985. Anisotropic damage criterion for deformation instability and its application to forming limit analysis of metal plates. *Engineering Fracture Mechanics,* **21**(5), pp. 1031-1054.

HAYAKAWA, K., MURAKAMI, S. and LIU, Y., 1998. An irreversible thermodynamics theory for elastic-plastic-damage materials. *European Journal of Mechanics - A/Solids,* **17**(1), pp. 13-32.

HILL, R., 1990. Constitutive modelling of orthotropic plasticity in sheet metals. *J. Mech. Phys. Solids,* **38**(3), pp. 405-417.

HILL, R., 1948. A theory of the yielding and plastic flow of anisotropic materials. *Proc. Roy. Soc.,* **A193**, pp. 189-297.

HILL, R., 1993. User-friendly theory of orthotropic plasticity in sheet metals. *International Journal of Mechanical Sciences,* **35**(1), pp. 19-25.

HILL, R., 1964. *The mathematical theory of plasticity.* Oxford university press, Amen house, london: The Oxford engineering science series.

HOLMQUIST, T.J. and JOHNSON, G.R., 1991. Determination of constants and comparison of results for various constitutive models. *Journal De Physique,* **IV**, pp. C3 853-C3 860.

HUTCHINSON, J.W., 1987. Alteration of stress-strain behaviour of structural material due to nucleation of microscopic damage *Proceeding of eighth Riso international symposium on metallurgy and material science* 1987, , pp. 95-105.

JANSSON, S. and STIGH, U., 1985. Influence of cavity shape on damage parameter *Journal of Applied Mechanics,* **52**(3), pp. 609-614.

JOHN, V., 1992. *Testing of materials.* Houndmills: Macmillan Education Ltd.

JOHNSON, G.R. and COOK, W.H., 1983. A constitutive model and data for metals subjected to large strains, high strain rates and high temperatures *Proceedings of the seventh international symposium on ballistics,* 1983, , pp. 541-547.

JOHNSON, G.R. and HOMQUIST, T.J., 1988. Evaluation of cylinder-impact test data for constitutive model constants. *Journal of applied physics,* **64**(8), pp. 3901-3910.

JOHNSON, G.R., HOEGFELDT, J.M., LINDHOLM, U.S. and NAGY, A., 1983. Response of various metals to large torsional strains over a large range of strain rates - part 1: ductile metals; part 2: less ductile metals. *Journal of Engineering Materials and Technology, Transactions of the ASME,* **105**(1), pp. 42-53.

JONAS, A.Z., 1982. *Impact Dynamics.* New York: Wiely Intersicience.

JU, J.W., 1989. Energy-based coupled elastoplastic damage models at finite strains. *Journal of Engineering Mechanics,* **115**(11), pp. 2507-2525.

KACHANOV, L.M., 1958, 2007-last update, Fundamentals of the theory of plasticity.

KACHANOV, M., 1993. Elastic solids with many cracks and related problems. *Advances in Applied Mechanics,* **30**, pp. 259-445.

KAWAMOTO, T., ICHIKAWA, Y. and KYOYA, T., 1988. Deformation and fracturing behaviour of discontinuous rock mass and damage mechanics theory. *International Journal for Numerical and Analytical Methods in Geomechanics,* **12**(1), pp. 1-30.

KRAJCINOVIC, D., 1985. Continuous damage mechanics revisited: Basic concepts and definitions 1985, .

KRAJCINOVIC, D. and FONSEKA, G.U., 1981. Continuous damage theory of brittle materials - 1. General theory. *Journal of Applied Mechanics, Transactions ASME,* **48**(4), pp. 809-815.

KRAJCINOVIC, D. and LEMAITRE, J., eds, 1987. *Continuum Damage Mechanics: Theory and Application.* New York: Springer.

LADEVÈZE, P., 1983. On an anisotropic damage theory. *Failure Criteria of Structured Media,* , pp. 355-363.

LADEVÈZE, P. and LEMAITRE, J., 1984. Damage effective stress in quasi unilateral conditions. *The 16th International Congress of Theoretical and Applied Mechanics,* .

LE ROY, G., EMBURY, J.D., EDWARDS, G. and ASHBY, M.F., 1981. A model of ductile fracture based on the nucleation and growth of voids. *Acta Metallurgica,* **29**(8), pp. 1509-1522.

LECKIE, F.A. and ONAT, E.T., 1981. Tensorial nature of damage measuring internal variables, J. HULT and J. LEMAITRE, eds. In: *Proc. IUTAM Symp. on Physical Non-Linearities in Structural Analysis,* 1981, Springer, pp. 140-155.

LEMAITRE, J., 1972. Evaluation of dissipation and damage in metals submitted to dynamic loading *Mechanical behavior of materials; Proceedings of the First International Conference* 15-20 Aug, 1971 1972, , pp. 540-549.

LEMAITRE, J., DESMORAT, R. and SAUZAY, M., 2000. Anisotropic damage law of evolution. *European Journal of Mechanics, A/Solids,* **19**(2), pp. 187-208.

LEMAITRE, J., 1985. Continuous damage mechanics model for ductile fracture. *Journal of Engineering Materials and Technology, Transactions of the ASME,* **107**(1), pp. 83-89.

LITEWKA, A., 1986. On stiffness and strength reduction of solids due to crack development. *Engineering Fracture Mechanics,* **25**(5-6), pp. 637-643.

Liu, P.F. , and Zheng, J.Y., 2010. Recent developments on damage modelling and finite element analysis for composite laminates: A review, *Materials and Design* 31 (2010) 3825–3834

LU, T.J. and CHOW, C.L., 1990. On constitutive equations of inelastic solids with anisotropic damage. *Theoretical and Applied Fracture Mechanics,* **14**(3), pp. 187-218.

MAUDLIN, P.J., GRAY III, G.T., CADY, C.M. and KASCHNER, G.C., 1999. High-rate material modelling and validation using the Taylor cylinder impact test. *Philosophical Transactions of the Royal Society A: Mathematical, Physical and Engineering Sciences,* **357**(1756), pp. 1707-1729.

MIRKOVIC, J., 2004. *Modelling of nonlinear behaviour of metallic structure components*, PhD Thesis, Cranfield University.

MURAKAMI, S., 1988. Mechanical modeling of material damage *Journal of Applied Mechanics, Transactions ASME,* **55**(2), pp. 280-286.

MUSCA Multiscale Analysis of Large Aerostructures, European Commission, Research and innovation, Transport Project (Air, Economic aspects, Vehicle technology), European 6th RTD Framework Programme, Duration 09/2005 to 03/2009 date. http://ec.europa.eu/research/transport/projects/items/musca_en.htm

ONAT, E.T. and LECKIE, F.A., 1988. Representation of mechanical behavior in the presence of changing internal structure *Journal of Applied Mechanics, Transactions ASME,* **55**(1), pp. 1-10.

PRAGER, W., 1972. CONVEXITY IN PLASTICITY. *Arch Mech - Arch Mech Stosow,* **24**(5-6), pp. 827-836.

RABOTNOV, Y.N., 1969. *Creep problems in structural members* Amsterdam: North Holland publishing company.

SCHREIER, H.W., BRAASCH, J.R., and SUTTON, M.A. , "Systematic errors in digital image correlation caused by intensity imterpolation", Opt. Eng. 39(11), 2006, 2915- 2921

SIDOROFF, F., 1981. Description of anisotropic damage application to elasticity. *Proceedings of the IUTAM Symposium on Physical Non-Linearities in Structural Analysis - Senlis (France) - 1980, .*

STEINBERG, D.J., COCHRAN, S.G. and GUINAN, M.W., 1980. A constitutive model for metals applicable at high strain rate. *Journal of applied physics,* **3**(1498), pp. 1504.

STEINBERG, D.J. and LUND, C.M., 1989. A constitutive model for strain rates from 10^{-4} to 10^{6} s^{-1}. *Journal of Applied Physics,* **65**(4), pp. 1528-1533.

VAKULENKO, A.A. and KACHNOV, M., 1971. Continuum theory of a medium with cracks *Mech. Solids, .*

WEITSMAN, Y., 1988. Damage coupled with heat conduction in uniaxially reinforced composites. *Journal of Applied Mechanics, Transactions ASME,* **55**(3), pp. 641-647.

ZERILLI, F.J. and ARMSTRONG, R.W., 1987. Dislocation mechanics based constitutive relations for material dynamics calculations. *Journal of applied physics,* **61**(5), pp. 1816-1825.

ZHANG, Z.L., HAUGE, M., ØDEGÅRD, J. and THAULOW, C., 1999. Determining material true stress-strain curve from tensile specimens with rectangular cross-section. *International Journal of Solids and Structures,* **36**(23), pp. 3497-3516.

ZHANG, Z.L., ØDEGÅRD, J. and SØVIK, O.P., 2001. Determining true stress-strain curve for isotropic and anisotropic materials with rectangular tensile bars: Method and verifications. *Computational Materials Science,* **20**(1), pp. 77-85.

ZUREK, A.K., RICHARDS, W.T., TRUJILLO, C.P., TONKS, D.L., HENRIE, B.L. and KEINIGS, R.K., 2003. Damage evolution in ductile metals. *Los Almos Science,* (28), pp. 111-113.

13 Appendix

13.1 Aluminium alloy material properties

The other aluminium alloy material properties used in this thesis report are given in this section of the appendix.

Table 13-1 Aluminium alloy isotropic material properties

Density	**Young's modulus**		**Poisson's ratio**			**Shear modulus**
ρ kg/m^3	E1 = E2 = E3 Pa		$\nu 21$	$\nu 31$	$\nu 32$	G21=G23=G31 Pa
2770	7.2 E+10		0.32	0.32	0.32	2.80E+10

Plastic strain	0	0.0019	0.025	0.0787	0.117	0.18	0.262	0.394	
True stress MPa	366	369	402	477	516	561	605	672	

Abaqus plastic potential	R_{11}	R_{22}	R_{33}	R_{12}	R_{13}	R_{23}
	1	1	1	1	1	1

Table 13-2 Aluminium 2024-T3 orthotropic material properties

Density	**Young's modulus**		**Poisson's ratio**			**Shear modulus**
ρ kg/m^3	E1 = E3 Pa	E2 Pa	$\nu 21$	$\nu 31$	$\nu 32$	G21=G23=G31 Pa
2770	6.78 E+10	6.66E+10	0.326	0.347	0.326	2.80E+10

Plastic strain	0	0.0019	0.025	0.0787	0.117	0.18	0.262	0.394	
True stress MPa	366	369	402	477	516	561	605	672	

Abaqus plastic potential	R_{11}	R_{22}	R_{33}	R_{12}	R_{13}	R_{23}
	1	0.8504	1.1506	1.1506	0.9515	0.8006

13.2 Additional numerical test results

The additional numerical test results are given in this section of the appendix. This section should be read in conjunction with Chapter 10.

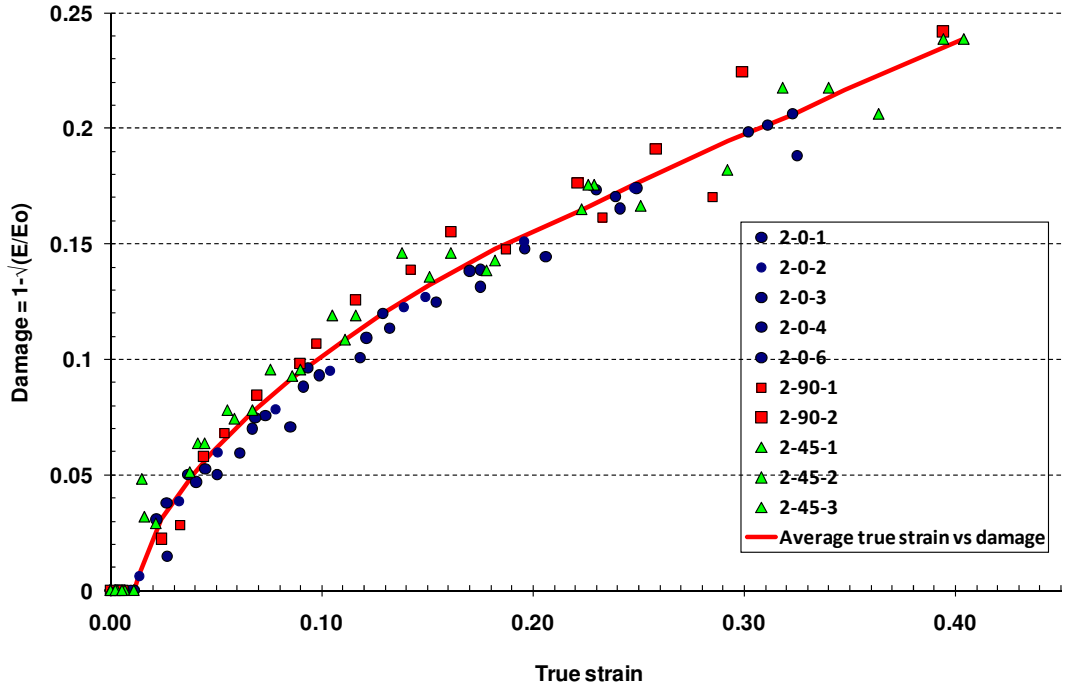

Figure 13-1 Aluminium AA2024-T3 damage calculation using degradation of elastic modulus from the uniaxial cyclic test

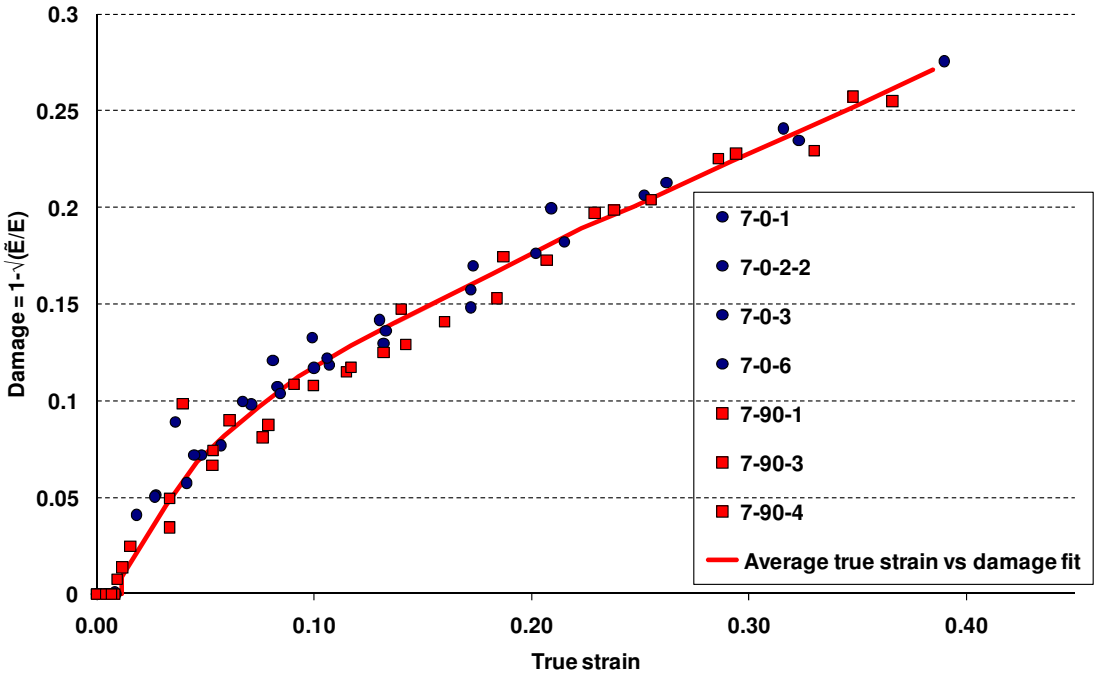

Figure 13-2 Damage calculated from cyclic test of Aluminium AA7010 uniaxial experimental data

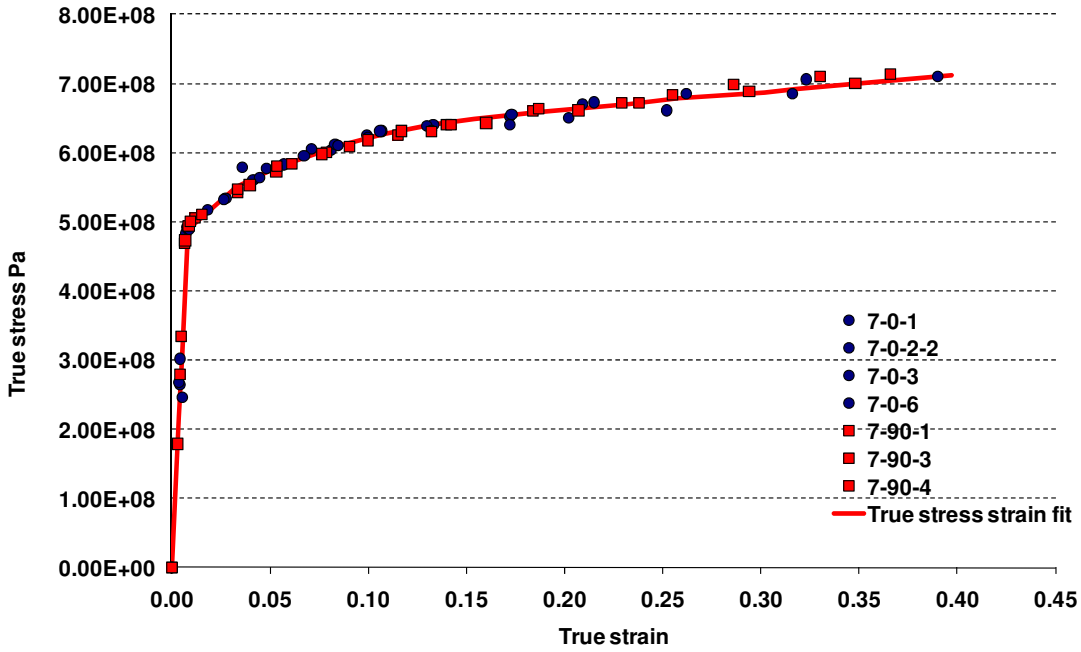

Figure 13-3 True stress strain curve extracted from uniaxial cyclic tensile test of Aluminium AA7010 experimental data

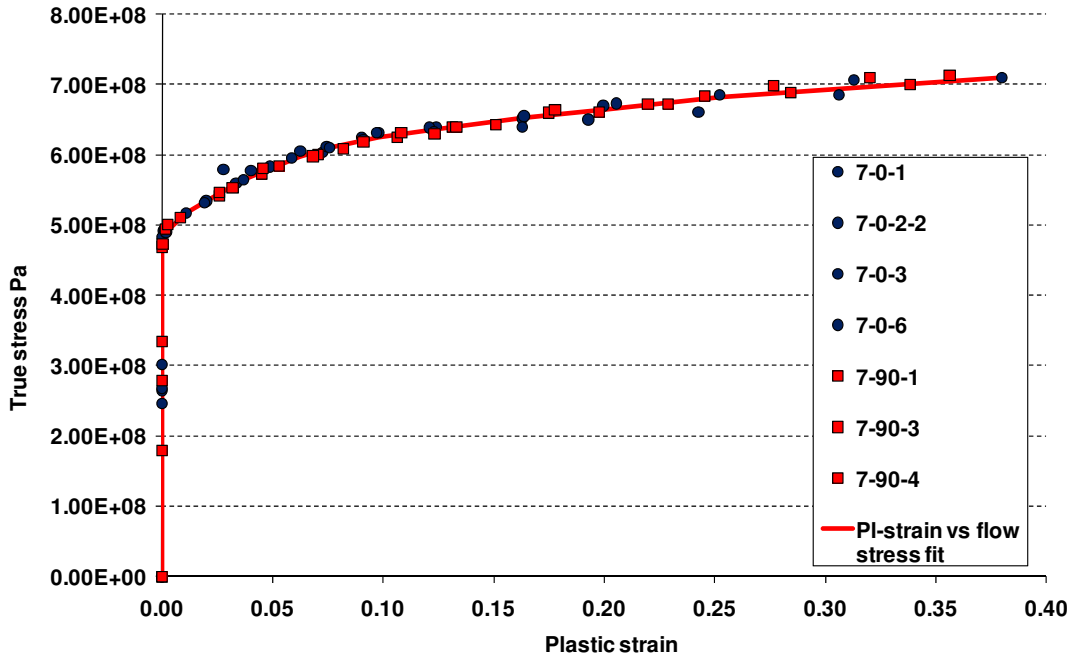

Figure 13-4 Flow stress versus plastic strain curve extracted from uniaxial cyclic tensile test of Aluminium AA7010 experimental data

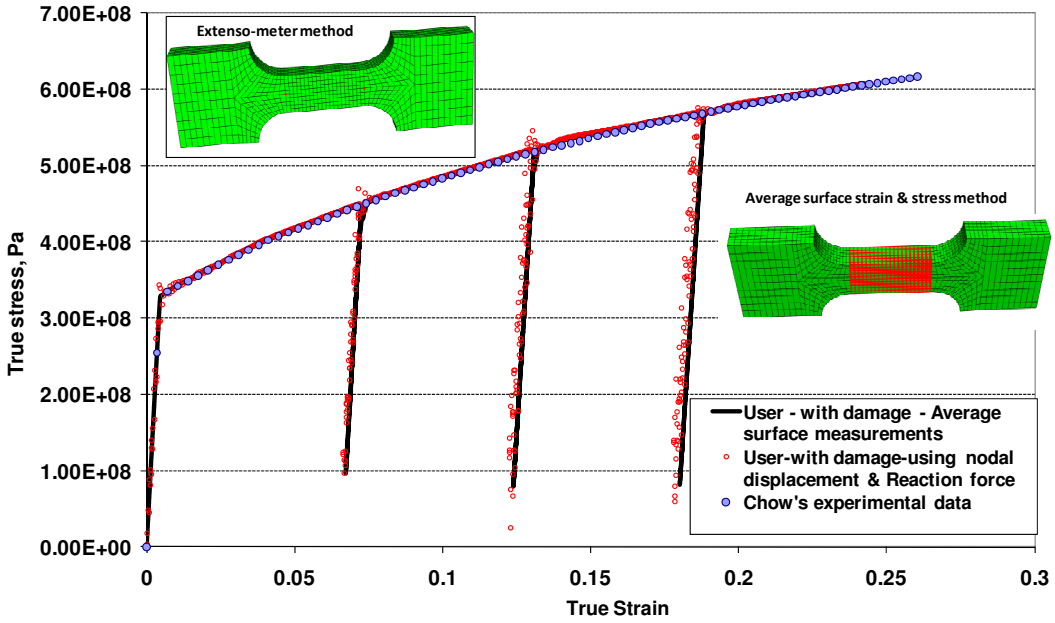

Figure 13-5 Validation of the model using Chow and Wang (1988) uniaxial experimental data - Averaged value for the model (highlighted in boxes), extenso-meter results (highlighted in dots) – Elastic modulus degradation shown in cyclic test case due to damage present for AA-2024 with introduced isotropic parameter

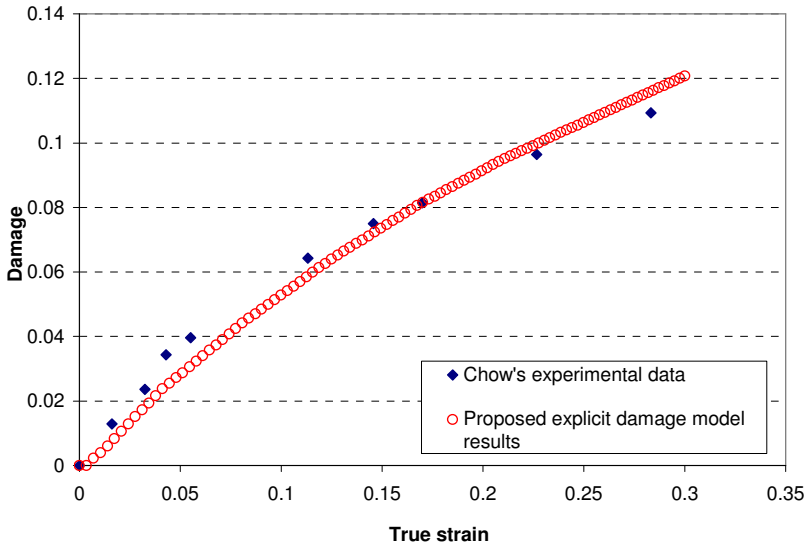

Figure 13-6 Validation of the model using Chow and Wang (1988) uniaxial experimental data – proposed explicit damage model simulations result AA-2024 with introduced isotropic parameter true strain vs damage

The experimental results obtained by Chow and Wang (1987) were also tested using the numerical code and extensometer reading and surface strain measurement where obtained. The results obtained through both these methods are compared with Chow's

experimental data. The results produced here agree with experimental results obtained by Chow (Figure 13-5 to Figure 13-7)

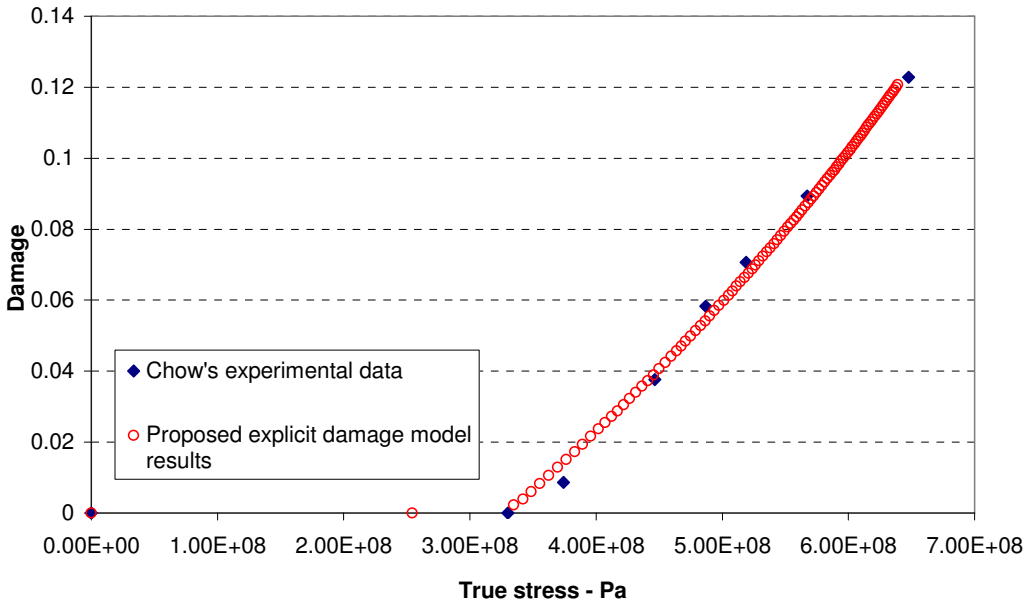

Figure 13-7 Verification of the model using Chow and Wang (1988) uniaxial experimental data – proposed explicit damage model simulations result AA-2024 with introduced isotropic parameter true stress vs damage

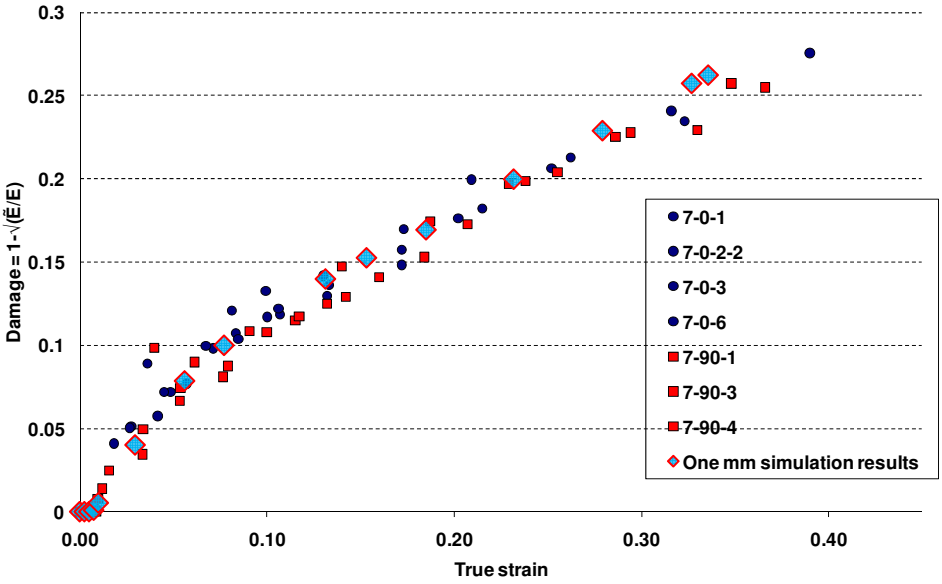

Figure 13-8 CU AA7010 simulation coupon test validation using uniaxial experimental data verification using one mm sized model with isotropic parameter – uniaxial cyclic test simulation done in Abaqus user explicit model with damage present

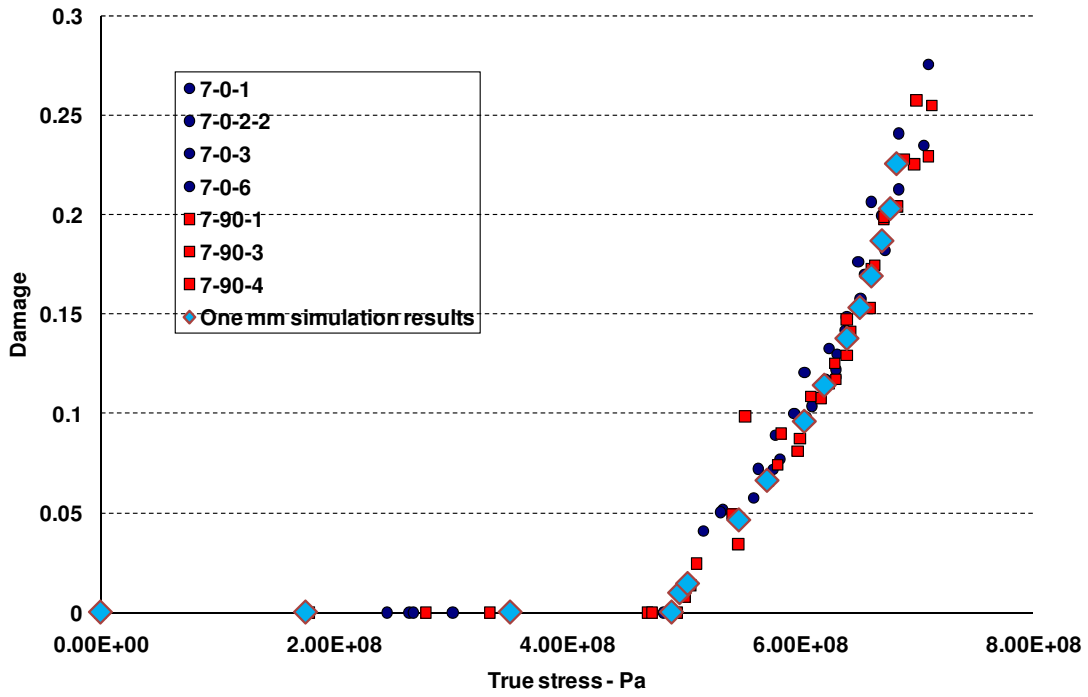

Figure 13-9 Validation of the model using CU uniaxial experimental data AA7010 using one mm single element model with isotropic parameter, true stress versus damage

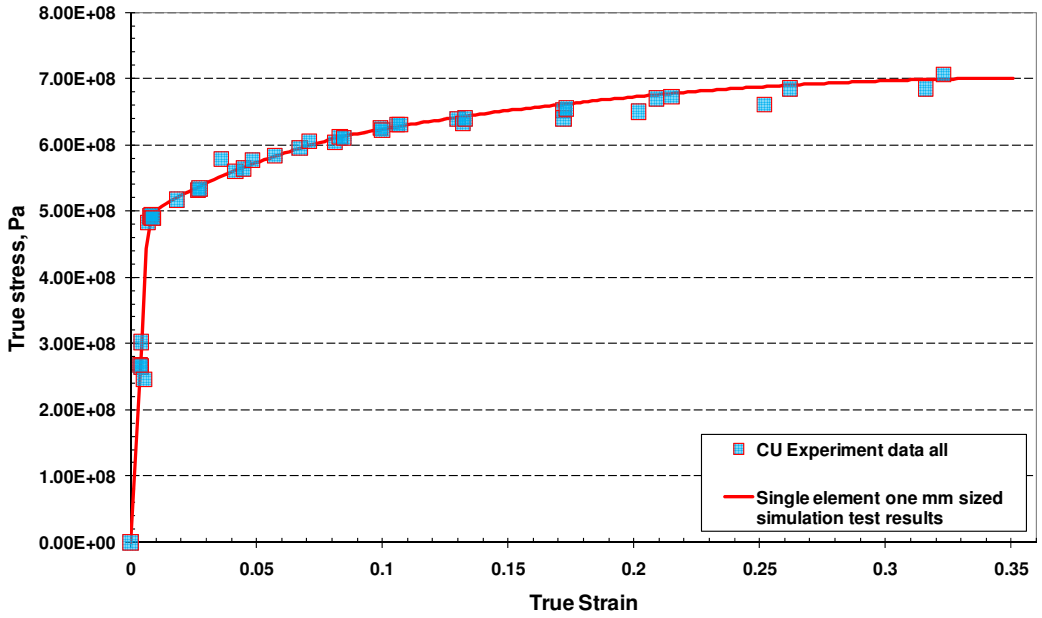

Figure 13-10 CU AA7010 simulation coupon test validation using uniaxial experimental data verification using one mm sized model with isotropic parameter – uniaxial simple tensile test simulation done in Abaqus user explicit model with damage present

13.3 Orthotropic ABAQUS VUMAT with damage a user information

The VUMAT is an implementation of an orthotropic elastic-plastic material model. It is suitable for use within an explicit analysis only as it assumes that the strain increment within a single step is small. The routine is for continuum elements.

Elastic behaviour

The material assumes linear elasticity with the material properties defined using the 'engineering constants': the three moduli E_1, E_2, E_3; Poisson's ratios v_{12}, v_{13}, v_{23}; and the three shear moduli G_{12}, G_{13} and G_{23}. All of there properties are defined with respect to the material principal directions.

Plastic Behaviour

The orthotropic plastic behaviour of the material is modelled using Hill's potential function for the virgin material stress. It is assumed that the material principal directions for plasticity are the same as the principal directions for elasticity. The yield surface is defined through the six yield stress ratios R_{ij}.

The hardening behaviour is rate-independent and defined through a piecewise linear yield stress vs. plastic strain function, combined with an isotropic hardening model. The yield stress vs. plastic strain curve should be defined for the material reference direction (the 1 direction).

Damage

The damage behaviour of the material is modelled using Chow's damage model which uses energy equivalence principle.

The Chow's damage behaviour is rate-independent and defined through linear damage threshold (B) vs effective damage (β) function and the material coefficient (μ) which can be determined based on the uniaxial test results. The damage D_1, D_2, D_3 in three

principle directions can be calculated and using damage parameters the (μ) and its co-efficient matrices (J) can be calculated.

where

$$D_1 = 1 - \sqrt{\frac{\tilde{E}_1}{E_1}}$$

The material co-efficient μ can be determined based on the uniaxial test results of effective mechanical properties D_1 and D_2.

$$\mu = \frac{D_2\left[1-\frac{D_2}{2}\right]}{D_1\left[1-\frac{D_1}{2}\right]}$$

From Chow's experiment AL-2024-T3 series the value for μ from the measured value of D_1 and D_2 is 0.579 over a linear relationship of 70 percent of damage critical value in 1-1 direction D_{1C} and 85 percent of damage critical value in 2-2 direction $D_{2C.}$ In Chow's examination the effect of the degree of anisotropic damage on the crack initiation load revealed that for isotropic case with $\mu = 1$ yielded the lowest fracture load and at the highest degree of anisotropy for $\mu = -0.5$ resulted in the highest facture load.

When damage is used in the analysis the effective yield stress ($\tilde{\sigma}$) and effective plastic strain $\tilde{\varepsilon}_p$ should be used in the input file instead of yield stress (σ) and plastic strain (ε_p). The effective yield stress can be calculated from the yield stress (σ) and plastic strain (ε_p) using the damage D calculated in the respective co-ordinate.

Here if the uniaxial test is done in 1-1 direction then

Effective yield stress $\tilde{\sigma} = \frac{\sigma}{1 - D_1}$ and

Effective plastic strain $\tilde{\varepsilon}_p = (1 - D_1)\varepsilon_p$

The damage threshold can be obtained from the uniaxial loading test using the equation $B = \tilde{\sigma} - B_0$ where B_0 is the initial damage threshold (stress) at which

damage starts to evolve. B_0 is similar to yield stress in plasticity and B_0 can be obtained from the uniaxial test.

The overall damage parameter β can be obtained from uniaxial test using the relationship $\beta = D_1 - \frac{D_1^2}{2}$.

The slope $\frac{dB}{d\beta}$ of curve $B - \beta$ can be readily established.

The element deletion option can be invoked using any one of the critical damage value D_{1C} ($D_{1\text{-critical}}$) or D_{2C} ($D_{2\text{-critical}}$) or D_{3C} ($D_{3\text{-critical}}$) or overall damage critical β_c (β_{critical}) values in the respective material parameter definition in Line 3.

The value of damage critical can be obtained from uniaxial test and the overall damage critical $\beta_C = D_{1C} - \frac{D_{1C}^2}{2}$

Input format

This routine uses one state variable, which is effective plastic strain. DEPVAR must be set to 5 using the *DEPVAR keyword if delete element keyword is not used. If delete keyword is used then the *DEPVAR, DELETE=6 should be used and DEPVAR should be set to 6.

The analysis can be performed with or without damage using a switch SWDAM (props(16)) in the VUMAT code. In the input file for the entry value as material parameters for 16^{th} value; one (1.) means the damage switched on and it is present and Zero (0.) means damage is switched off.

A material density must be defined using the *DENSITY keyword.

All other material parameters are defined using the *USER MATERIAL keyword. Following the keyword the data is supplied with eight constants per line, using as many lines as necessary. A minimum of four lines (24 constants + 2 constants (one effective yield stress & corresponding effective plastic strain)) are required for this model.

Line 1

Entry	1	2	3	4	5	6	7	8
Value	E_1	E_2	E_3	v_{12}	v_{13}	v_{23}	G_{12}	G_{13}

Line 2

Entry	1	2	3	4	5	6	7	8
Value	G_{23}	R_{11}	R_{22}	R_{33}	R_{12}	R_{13}	R_{23}	Damage switch

Line 3

Entry	1	2	3	4	5	6	7	8
Value	μ	$\frac{dB}{d\beta}$	Bo	$D_{critical-1}$	$D_{critical-2}$	$D_{critical-3}$	$\beta_{critical}$	Blank

Line 4

Entry	1	2	3	4	5	6	7	8
Value	Effective true stress 1	Effective Plastic strain 1	Effective true stress 2	Effective Plastic strain 2	Effective true stress 3	Effective Plastic strain 3	Effective true stress 4	Effective Plastic strain 4

Use as many lines as are necessary to define the complete curve. At least one yield stress – plastic strain pair must be defined. If only one pair is given the material will be perfectly plastic. The curve must represent the relationship for the material 1 direction.

The first nine entries (the elastic properties) are identical to the properties required for the *ELASTIC, TYPE=ENGINEERING CONSTANTS keyword. The six yield stress ratios are the same as required for the *POTENTIAL keyword. The yield stress – plastic strain points are the same as required for the *PLASTIC, HARDENING=ISOTROPIC keyword except it should be replaced with effective yield stress and effective plastic strain.

Example

The VUMAT routine with the following input keywords for Chow's damage model with orthotropic material character:

```
** MATERIALS
**
*Material, name=AA7010
*Density
2770.,
*Depvar, Delete=6
6,
*User Material, constants=80
7.04e+10,7.04e+10,7.04e+10,0.327,0.327,0.327,2.67e+10,2.67e+10
2.67e+10, 1., 0.9961, 0.9547, 0.9547, 0.9838, 1., 1.
0.995, 2.0342e+09, 4.817e+08, 0.75, 0.32, 0.32, 0.32, 0.32
4.9e+08, 0., 4.97e+08, 0.00017, 5e+08, 0.0015, 5.2e+08, 0.006
5.26e+08, 0.008, 5.32e+08, 0.01, 5.72e+08, 0.0238, 5.95e+08,0.032
6.12e+08, 0.0389, 6.45e+08, 0.0526, 5e+08, 0.0706, 7.03e+08,  0.0826
7.17e+08, 0.0913, 7.37e+08, 0.1051, 7.65e+08, 0.1235, 7.94e+08, 0.1459
8.13e+08, 0.1581, 8.39e+08, 0.1764, 8.71e+08, 0.1982,9.16e+08,      0.231
9.53e+08, 0.2548, 9.8e+08, 0.2716, 1.e+09, 0.2847, 1.16e+09, 0.3915
1.2e+09, 0.4213, 1.35e+09, 0.5312, 1.48e+09, 0.624, 1.7e+09, 0.7832
```

Isotropic material behaviour

Isotropic elastic behaviour can be represented by defining the elastic input parameters as follows:

$$E_1 = E_2 = E_3 = E \text{ (Young's Modulus)}$$

$$v_{12} = v_{13} = v_{23} = v \text{ (Poisson's ratio)}$$

$$G_{12} = G_{13} = G_{23} = G = \frac{E}{2(1+v)}$$

Isotropic plastic behaviour (Mises yield surface) can be obtained by setting

$$R_{11} = R_{22} = R_{33} = R_{12} = R_{13} = R_{23} = 1$$

Isotropic damage behaviour can be obtained by setting

$$\mu = 1$$

13.4 ABAQUS VUMAT subroutine

```
      subroutine vumat(
C Read only -
     1  nblock, ndir, nshr, nstatev, nfieldv, nprops, lanneal,
     2  stepTime, totalTime, dt, cmname, coordMp, charLength,
     3  props, density, strainInc, relSpinInc,
     4  tempOld, stretchOld, defgradOld, fieldOld,
     3  stressOld, stateOld, enerInternOld, enerInelasOld,
     6  tempNew, stretchNew, defgradNew, fieldNew,
C Write only -
     5  stressNew, stateNew, enerInternNew, enerInelasNew )
C
      include 'vaba_param.inc'
C*************************************************************************
C VUMAT for an orthotropic elastic-plastic material.  Yield is determined
C  using Hill's virgin material stress.  Hardening is piecewise linear using a curve
C  defined in the input file.
C
C History variables:
C   1: Effective plastic strain
C
C*************************************************************************
      dimension props(nprops), density(nblock),
     1  coordMp(nblock,*),
     2  charLength(*), strainInc(nblock,ndir+nshr),
     3  relSpinInc(*), tempOld(*),
     4  stretchOld(*), defgradOld(*),
     5  fieldOld(*), stressOld(nblock,ndir+nshr),
     6  stateOld(nblock,nstatev), enerInternOld(nblock),
     7  enerInelasOld(nblock), tempNew(*),
     8  stretchNew(*), defgradNew(*), fieldNew(*),
     9  stressNew(nblock,ndir+nshr), stateNew(nblock,nstatev),
     1  enerInternNew(nblock), enerInelasNew(nblock)
C
      dimension curve_ep(nprops), curve_fs(nprops)
C
      character*80 cmname
C
      parameter( zero = 0., one = 1., two = 2., three = 3.,
     1  third = one/three, half = .5, twoThirds = two/three,
     2  threeHalfs = 1.5 )
C*************************************************************************
C  Get input properties
C*************************************************************************
C  Properties to be specified in user input file
C  User Material, Constants = 42
C  e1 = Young's modulus in 11 direction
C  e2 = Young's modulus in 22 direction
```

```
C  e3 = Young's modulus in 33 direction
C  v21 = Poisson's ratio in 21 direction
C  v31 = Poisson's ratio in 31 direction
C  v32 = Poisson's ratio in 32 direction
C  shr12 = shear modulus in 12 direction
C  shr23 = shear modulus in 23 direction
C  shr31 = shear modulus in 31 direction
C  r11 to r23 = Orthotropic yield coefficients
C  The following define the stress strain curve of the material
C  curve_fs = Flow stress in uniaxial stress for reference direction
C  curve_ep = Plastic strain in uniaxial stress for reference direction
C
      e1     = props(1)
      e2     = props(2)
      e3     = props(3)
      v21    = props(4)
      v31    = props(5)
      v32    = props(6)
      shr12  = props(7)
      shr23  = props(8)
      shr31  = props(9)
C
      r11    = props(10)
      r22    = props(11)
      r33    = props(12)
      r12    = props(13)
      r13    = props(14)
      r23    = props(15)
      swdam  = props(16)   ! used as damage switch this time, to switchoff/on the
damage
      xmu    = props(17)   ! material constant for mu for AL2024 0.582 for isotropic
xmu = 1.
      dbdbt  = props(18)   ! material constant db/dbeta
      bnot   = props(19)   ! Bnot stress at damage initiation under uniaxial tensile test
      dcr1   = props(20)   ! critical damage material data in rolling direction
      dcr2   = props(21)   ! critical damage material data in LT direction
      dcr3   = props(22)   ! critical damage material data in ST direction
      bcr    = props(23)   ! critical effective damage
      delsw  = props(24)   ! delete element switch
C
      npoints = nprops-24
      if(mod(npoints,2).gt.0) then
       write(6,50)
  50    format(//30X,'*** VUMAT ERROR ***,'/,
     1 30X,'Stress vs. Strain values must be given as data pairs')
       call XPLB_EXIT
      endif
      npoints = npoints/2
      do i=1,npoints
       j = 24 + 2*(i-1)
```

```
       curve_fs(i) = props(j+1)
       curve_ep(i) = props(j+2)
      enddo
C*************************************************************************
C  Calculate elastic and plastic coefficient matrices before processing elements
C*************************************************************************
     twoshr  = shr12
     threshr = threeHalfs * twoshr
     con1   = sqrt( twoThirds )
C
C Calculation of Hill's anisotropic coefficients F,G,H,L,M,N
C
       rr11 = one/(r11**2)
       rr22 = one/(r22**2)
       rr33 = one/(r33**2)
       df = half*(rr22+rr33-rr11)
       dg = half*(rr33+rr11-rr22)
       dh = half*(rr11+rr22-rr33)
       dl = three/(two*(r23**2))
       dm = three/(two*(r13**2))
       dn = three/(two*(r12**2))
C
C*************************************************************************
C Process element block
C*************************************************************************
     do 100 i = 1,nblock
C
C Damage parameters d1, d2, d3 and xmu
C
          d1 = stateOld(i,2)
          d2 = stateOld(i,3)
          d3 = stateOld(i,4)
C*************************************************************************
C  xmu = one for isotropic material
C*************************************************************************
C
C  Elastic co-efficient matrix
C
       d1sqr = (one - d1)**2
       d2sqr = (one - d2)**2
       d3sqr = (one - d3)**2
       d1d2  = (one - d1)*(one - d2)
       d1d3  = (one - d1)*(one - d3)
       d2d3  = (one - d2)*(one - d3)
C
C Calculate coefficients of H matrix
C
       H11 = (dg+dh)/(1-d1)**2
       H22 = (df+dh)/(1-d2)**2
       H33 = (df+dg)/(1-d3)**2
```

```
      H12 = -dh/((1-d1)*(1-d2))
      H13 = -dg/((1-d1)*(1-d3))
      H23 = -df/((1-d2)*(1-d3))
      H44 = two*dn/((1-d1)*(1-d2))
      H55 = two*dm/((1-d1)*(1-d3))
      H66 = two*dl/((1-d2)*(1-d3))
C
C  Elastic co-efficient matrix multiplied by damage parameters
C
      v12 = (e1/e2)*v21
      v13 = (e1/e3)*v31
      v23 = (e2/e3)*v32
      A    =  1./(1.-v12*v21-v23*v32-v13*v31-2*v21*v32*v13)
      C11  = (e1*A)*(1.-v23*v32)*d1sqr
      C22  = (e2*A)*(1.-v13*v31)*d2sqr
      C33  = (e3*A)*(1.-v12*v21)*d3sqr
      C12  = (e1*A)*(v21+v31*v23)*d1d2
      C13  = (e1*A)*(v31+v21*v32)*d1d3
      C23  = (e2*A)*(v32+v12*v31)*d2d3
      C44  = shr12*d1d2
      C55  = shr23*d1d3
      C66  = shr31*d2d3
C
C Elastic stress increment
C
     s11 = C11*strainInc(i,1) + C12*strainInc(i,2)+C13*strainInc(i,3)
     s22 = C12*strainInc(i,1) + C22*strainInc(i,2)+C23*strainInc(i,3)
     s33 = C13*strainInc(i,1) + C23*strainInc(i,2)+C33*strainInc(i,3)
     s12 = 2*C44*strainInc(i,4)
     s23 = 2*C55*strainInc(i,5)
     s13 = 2*C66*strainInc(i,6)
C
C Trial Stress
C
     sig11 = stressOld(i,1) + s11
     sig22 = stressOld(i,2) + s22
     sig33 = stressOld(i,3) + s33
     sig12 = stressOld(i,4) + s12
     sig23 = stressOld(i,5) + s23
     sig13 = stressOld(i,6) + s13
C
C  Introduce fixed value damage and check the code
C
C       write (*,*) d1, d2, d3
C
C       sig11 = sig11/(1.-d1)
C       sig22 = sig22/(1.-d2)
C       sig33 = sig33/(1.-d3)
C       sig12 = sig12/sqrt((1.-d1)*(1.-d2))
C       sig23 = sig23/sqrt((1.-d2)*(1.-d3))
```

```
C       sig13 = sig13/sqrt((1.-d1)*(1.-d3))
C
C*************************************************************************
C  Calculate Hill's virgin material stress from trial stress
C*************************************************************************
       b1 = H11*sig11 + H12*sig22 + H13*sig33
       b2 = H12*sig11 + H22*sig22 + H23*sig33
       b3 = H13*sig11 + H23*sig22 + H33*sig33
       b4 = H44*sig12
       b5 = H55*sig13
       b6 = H66*sig23
C
       hill = b1*sig11 + b2*sig22 + b3*sig33 +
     1         b4*sig12 + b5*sig13 + b6*sig23
       sigbar = sqrt(hill)
       fltminsigbar = tiny(sigbar)
       sigbar = max(sigbar,fltminsigbar)
C
C*************************************************************************
C Calculate flow stress in reference direction (assumed to be material 1)
C*************************************************************************
      call flow_stress(stateOld(i,1),yflow,npoints,curve_ep,curve_fs,
     1                 hard)
C Where
C       yflow is the flow stress
C       hard is the tangent modulus of the uniaxial stress/plastic strain curve at yflow
C
C*************************************************************************
C Check for yield
C*************************************************************************
C
C
          f_yield = sigbar - yflow
          facyld = zero
      if(f_yield .ge. zero ) facyld = one
C*************************************************************************
C If yield then caalculate increment in plastic strain (Lambda dot)
C*************************************************************************
      if(facyld.gt.0.5) then
       denom1 = C11*b1 + C12*b2 + C13*b3
       denom2 = C12*b1 + C22*b2 + C23*b3
       denom3 = C13*b1 + C23*b2 + C33*b3
       denom4 = C44*b4
       denom5 = C55*b5
       denom6 = C66*b6
C
       denom = (1.0/sigbar**2) * (b1*denom1 + b2*denom2 + b3*denom3 +
     1                    b4*denom4 + b5*denom5 + b6*denom6)
       rlambda = f_yield/(denom-hard)
C
```

```
      factor = rlambda/sigbar
     endif  ! if facyld.gt.0.5 statement
C
C*********************************************************************
C Store new stress and history varaible
C*********************************************************************
C Note that if yield has not occurred facyld = 0.0 and the new stress is set to the
C  elastic trial stress
     stressNew(i,1) = sig11 - facyld*factor*denom1
     stressNew(i,2) = sig22 - facyld*factor*denom2
     stressNew(i,3) = sig33 - facyld*factor*denom3
     stressNew(i,4) = sig12 - facyld*factor*denom4
     stressNew(i,5) = sig23 - facyld*factor*denom6
     stressNew(i,6) = sig13 - facyld*factor*denom5
     stateNew(i,1) = stateOld(i,1) + facyld*rlambda
C
C*********************************************************************
C  DAMAGE PARAMETERS CALCULATION
C*********************************************************************
C
C*********************************************************************
C  J Matrix
C*********************************************************************
      DJ11  = one/d1sqr
      DJ22  = one/d2sqr
      DJ33  = one/d3sqr
      DJ12  = one*xmu/d1d2
      DJ13  = one*xmu/d1d3
      DJ23  = one*xmu/d2d3
      DJ44  = one*(one-xmu)/d1d2
      DJ55  = one*(one-xmu)/d1d3
      DJ66  = one*(one-xmu)/d2d3
C
C*********************************************************************
C Calculation of effective damage stress
C*********************************************************************
     sn11 = stressNew(i,1)
     sn22 = stressNew(i,2)
     sn33 = stressNew(i,3)
     sn12 = stressNew(i,4)
     sn23 = stressNew(i,5)
     sn13 = stressNew(i,6)
C
     DJ1 = DJ11*sn11+DJ12*sn22+DJ13*sn33
     DJ2 = DJ12*sn11+DJ22*sn22+DJ23*sn33
     DJ3 = DJ13*sn11+DJ23*sn22+DJ33*sn33
     DJ4 = DJ44*sn12
     DJ5 = DJ55*sn23
     DJ6 = DJ66*sn13
C
```

```
      sdam1=DJ1*sn11+DJ2*sn22+DJ3*sn33+DJ4*sn12+DJ5*sn23+DJ6*sn13
      sdam = sqrt(sdam1)
      fltminsdam = tiny(sdam)
      sdam = max(sdam,fltminsdam)
C       sdam = sdam+one
C*********************************************************************
C  Calculate Ydam from corrected stress
C*********************************************************************
      ydam = bnot + stateOld(i,5)*dbdbt
      facdam = zero
       if (sdam .ge. ydam) facdam = one
C*********************************************************************
C  Calculate Hill's matrices from corrected stress
C*********************************************************************
        bn1 = H11*sn11 + H12*sn22 + H13*sn33
        bn2 = H12*sn11 + H22*sn22 + H23*sn33
        bn3 = H13*sn11 + H23*sn22 + H33*sn33
        bn4 = H44*sn12
        bn5 = H55*sn13
        bn6 = H66*sn23
C*********************************************************************
C  Calculate right hand of beta equation from corrected stress
C*********************************************************************
       if(facyld.gt.0.5) then
       denew1 = C11*bn1 + C12*bn2 + C13*bn3
       denew2 = C12*bn1 + C22*bn2 + C23*bn3
       denew3 = C13*bn1 + C23*bn2 + C33*bn3
       denew4 = C44*bn4
       denew5 = C55*bn5
       denew6 = C66*bn6
C
       djdenew  = facdam*(DJ1*denew1+DJ2*denew2+DJ3*denew3+
     1            DJ4*denew4+DJ5*denew5+DJ6*denew6)
       djdenew1 = djdenew*stateOld(i,1)/(sdam*sigbar)
C
C*********************************************************************
C  Calculation of B and effective damage (lamdad-dot)
C*********************************************************************
C
         bee = facdam*(yflow - ydam - djdenew1)
         fltminbee = tiny(bee)
         bee = max(bee,fltminbee)
         rlamdam = bee/dbdbt
C
C*********************************************************************
C  Calculation of db/2sigd
C*********************************************************************
        dbsigd = swdam*facdam*rlamdam/(sdam)
C
C*********************************************************************
```

```
C Calculation of damage
C*****************************************************************
      dam1 = DJ1*dbsigd
      dam2 = DJ2*dbsigd
      dam3 = DJ3*dbsigd
      dam4 = DJ4*dbsigd
      dam5 = DJ5*dbsigd
      dam6 = DJ6*dbsigd
      endif ! if facyld.gt.0.5 statement
C
      if (dam1 .le. zero) dam1 = 0
      if (dam2 .le. zero) dam2 = 0
      if (dam3 .le. zero) dam3 = 0
      if (dam4 .le. zero) dam4 = 0
      if (dam5 .le. zero) dam5 = 0
      if (dam6 .le. zero) dam6 = 0
C
C       if (dam1 .ge. 0.85) dam1 = 0.85
C       if (dam2 .ge. 0.85) dam2 = 0.85
C       if (dam3 .ge. 0.85) dam3 = 0.85
C       if (dam4 .ge. 0.85) dam4 = 0.85
C       if (dam5 .ge. 0.85) dam5 = 0.85
C       if (dam6 .ge. 0.85) dam6 = 0.85
C
    stateNew(i,5) = stateOld(i,5) + facdam*rlamdam
    stateNew(i,2) =  stateOld(i,2) + dam1
    stateNew(i,3) =  stateOld(i,3) + dam2
    stateNew(i,4) =  stateOld(i,4) + dam3
C
C=============================================================
C Convergence check (to be implemented with 10 iterations)
C=============================================================
C     stateNew(i,7) = half*(stateOld(i,5) + stateNew(i,5))
C     stateNew(i,8) = stateNew(i,5) - stateNew(i,7)
C     if (stateNew(i,8) .ge. 0.0001) then
C     goto 60
C     end if! for checking the effective damage
C
    stateNew(i,6) = 1
     if (stateNew(i,2) .gt. dcr1) stateNew(i,6)= 0
C=============================================================
C New damage update for new stress calculation
C=============================================================
        d1 = stateNew(i,2)
        d2 = stateNew(i,3)
        d3 = stateNew(i,4)
C*****************************************************************
C  xmu = one for isotropic material and xmu = 0.582 for AL-2024 orthotropic mat
C*****************************************************************
C
```

```
C  Elastic co-efficient matrix
C
      d1sqr = (one - d1)**2
      d2sqr = (one - d2)**2
      d3sqr = (one - d3)**2
      d1d2  = (one - d1)*(one - d2)
      d1d3  = (one - d1)*(one - d3)
      d2d3  = (one - d2)*(one - d3)
C
C Calculate coefficients of H matrix
C
      H11 = (dg+dh)/(1-d1)**2
      H22 = (df+dh)/(1-d2)**2
      H33 = (df+dg)/(1-d3)**2
      H12 = -dh/((1-d1)*(1-d2))
      H13 = -dg/((1-d1)*(1-d3))
      H23 = -df/((1-d2)*(1-d3))
      H44 = two*dn/((1-d1)*(1-d2))
      H55 = two*dm/((1-d1)*(1-d3))
      H66 = two*dl/((1-d2)*(1-d3))
C
C  Elastic co-efficient matrix multiplied by damage parameters
C
      v12 = (e1/e2)*v21
      v13 = (e1/e3)*v31
      v23 = (e2/e3)*v32
      A    =  1./(1.-v12*v21-v23*v32-v13*v31-2*v21*v32*v13)
      C11  = (e1*A)*(1.-v23*v32)*d1sqr
      C22  = (e2*A)*(1.-v13*v31)*d2sqr
      C33  = (e3*A)*(1.-v12*v21)*d3sqr
      C12  = (e1*A)*(v21+v31*v23)*d1d2
      C13  = (e1*A)*(v31+v21*v32)*d1d3
      C23  = (e2*A)*(v32+v12*v31)*d2d3
      C44  = shr12*d1d2
      C55  = shr23*d1d3
      C66  = shr31*d2d3
C
C Elastic stress increment
C
     s11 = C11*strainInc(i,1) + C12*strainInc(i,2)+C13*strainInc(i,3)
     s22 = C12*strainInc(i,1) + C22*strainInc(i,2)+C23*strainInc(i,3)
     s33 = C13*strainInc(i,1) + C23*strainInc(i,2)+C33*strainInc(i,3)
     s12 = 2*C44*strainInc(i,4)
     s23 = 2*C55*strainInc(i,5)
     s13 = 2*C66*strainInc(i,6)
C
C Trial Stress
C
     sig11 = stressOld(i,1) + s11
     sig22 = stressOld(i,2) + s22
```

```
      sig33 = stressOld(i,3) + s33
      sig12 = stressOld(i,4) + s12
      sig23 = stressOld(i,5) + s23
      sig13 = stressOld(i,6) + s13
C
C  Introduce fixed value damage and check the code
C
C       write (*,*) d1, d2, d3
C
C       sig11 = sig11/(1.-d1)
C       sig22 = sig22/(1.-d2)
C       sig33 = sig33/(1.-d3)
C       sig12 = sig12/sqrt((1.-d1)*(1.-d2))
C       sig23 = sig23/sqrt((1.-d2)*(1.-d3))
C       sig13 = sig13/sqrt((1.-d1)*(1.-d3))
C
C*********************************************************************
C  Calculate Hill's virgin material stress from trial stress
C*********************************************************************
        b1 = H11*sig11 + H12*sig22 + H13*sig33
        b2 = H12*sig11 + H22*sig22 + H23*sig33
        b3 = H13*sig11 + H23*sig22 + H33*sig33
        b4 = H44*sig12
        b5 = H55*sig13
        b6 = H66*sig23
C
        hill = b1*sig11 + b2*sig22 + b3*sig33 +
     1         b4*sig12 + b5*sig13 + b6*sig23
        sigbar = sqrt(hill)
        fltminsigbar = tiny(sigbar)
        sigbar = max(sigbar,fltminsigbar)
C
C*********************************************************************
C Calculate flow stress in reference direction (assumed to be material 1)
C*********************************************************************
      call flow_stress(stateOld(i,1),yflow,npoints,curve_ep,curve_fs,
     1                 hard)
C Where
C       yflow is the flow stress
C       hard is the tangent modulus of the uniaxial stress/plastic strain curve at yflow
C
C*********************************************************************
C Check for yield
C*********************************************************************
C
C
          f_yield = sigbar - yflow
          facyld = zero
      if(f_yield .ge. zero ) facyld = one
```

```
C*************************************************************************
**************
C If yield then calculate increment in plastic strain (Lambda dot)
C*************************************************************************
**************
      if(facyld.gt.0.5) then
       denom1 = C11*b1 + C12*b2 + C13*b3
       denom2 = C12*b1 + C22*b2 + C23*b3
       denom3 = C13*b1 + C23*b2 + C33*b3
       denom4 = C44*b4
       denom5 = C55*b5
       denom6 = C66*b6
C
       denom = (1.0/sigbar**2) * (b1*denom1 + b2*denom2 + b3*denom3 +
     1                      b4*denom4 + b5*denom5 + b6*denom6)
       rlambda = f_yield/(denom-hard)
C
       factor = rlambda/sigbar
      endif  ! if facyld.gt.0.5 statement

C
C*************************************************************************
C Store new stress and history varaible
C*************************************************************************
C Note that if yield has not occured facyld = 0.0 and the new stress is set to the
C  elastic trial stress
      stressNew(i,1) = sig11 - facyld*factor*denom1
      stressNew(i,2) = sig22 - facyld*factor*denom2
      stressNew(i,3) = sig33 - facyld*factor*denom3
      stressNew(i,4) = sig12 - facyld*factor*denom4
      stressNew(i,5) = sig23 - facyld*factor*denom6
      stressNew(i,6) = sig13 - facyld*factor*denom5
      stateNew(i,1) = stateOld(i,1) + facyld*rlambda
C
C
    !
  100 continue
C
C
      return
      end
!
!=============================================================
!
      subroutine flow_stress(eqplas,sigflow,npoints,curve_ep,curve_fs,
     1          E_tan)
      !
      ! Calculate current flow stress from input curve
      !
      include 'vaba_param.inc'
```

```
      !
      real deqp, dsig
      !
      dimension curve_ep(npoints),curve_fs(npoints)
      !
      if(npoints.eq.1) then
       sigflow = curve_fs(1)
       E_tan = 0.0
       return
      endif
      if(eqplas.gt.curve_ep(npoints)) then
       ! If plastic strain exceeds the extent of the curve, follow ABAQUS convention
       !  and have perfectly plastic behaviour.  This will also cover the case where
       !  only one poitn is defined in the curve.
       sigflow = curve_fs(npoints)
       E_tan = 0.0
      else
       do i=1,npoints-1
        if(eqplas-curve_ep(i+1).le.0.0) then
         if(curve_ep(i+1).le.curve_ep(i)) then
          write(6,100)
  100      format(//30X,'*** VUMAT ERROR ***,'/,
     1 30X,' Plastic strain values must be entered in ascending order.')
          call XPLB_EXIT
         endif
         dsig = curve_fs(i+1)-curve_fs(i)
         deqp = curve_ep(i+1)-curve_ep(i)
         E_tan = dsig/deqp
         sigflow = curve_fs(i) + E_tan*(eqplas-curve_ep(i))
         exit
        endif
       enddo

      endif
      !
      return
      !
      end subroutine flow_stress
```